

INFORMATION TO USERS

This manuscript has been reproduced from the microfilm master. UMI films the text directly from the original or copy submitted. Thus, some thesis and dissertation copies are in typewriter face, while others may be from any type of computer printer.

The quality of this reproduction is dependent upon the quality of the copy submitted. Broken or indistinct print, colored or poor quality illustrations and photographs, print bleedthrough, substandard margins, and improper alignment can adversely affect reproduction.

In the unlikely event that the author did not send UMI a complete manuscript and there are missing pages, these will be noted. Also, if unauthorized copyright material had to be removed, a note will indicate the deletion.

Oversize materials (e.g., maps, drawings, charts) are reproduced by sectioning the original, beginning at the upper left-hand corner and continuing from left to right in equal sections with small overlaps.

Photographs included in the original manuscript have been reproduced xerographically in this copy. Higher quality 6" x 9" black and white photographic prints are available for any photographs or illustrations appearing in this copy for an additional charge. Contact UMI directly to order.

ProQuest Information and Learning
300 North Zeeb Road, Ann Arbor, MI 48106-1346 USA
800-521-0600

UMI[®]

**ANALYSIS AND MODELING OF TRANSIENT PHENOMENA IN BORON-DOPED
SILICON**

By

AARON D. LILAK

**A DISSERTATION PRESENTED TO THE GRADUATE SCHOOL
OF THE UNIVERSITY OF FLORIDA IN PARTIAL FULFILLMENT
OF THE REQUIREMENTS FOR THE DEGREE OF
DOCTOR OF PHILOSOPHY**

UNIVERSITY OF FLORIDA

2001

UMI Number: 3027545

UMI[®]

UMI Microform 3027545

Copyright 2002 by Bell & Howell Information and Learning Company.

All rights reserved. This microform edition is protected against
unauthorized copying under Title 17, United States Code.

Bell & Howell Information and Learning Company
300 North Zeeb Road
P.O. Box 1346
Ann Arbor, MI 48106-1346

Copyright 2001

by

Aaron D. Lilak

To my parents

ACKNOWLEDGMENTS

This work would have been impossible to complete without the help, advice, and support of countless individuals. There are many people I need to thank for my success and all I have been able to accomplish. If I have omitted someone, I apologize.

Dr. Mark E. Law has been the greatest advisor one could ever wish for. Dr. Law possesses the rare ability to comprehend a difficult idea and express it in simple language, this is reflected in his many awards for teaching excellence. Dr. Law has been there through it all; from bleeding on the soccer field, pounding beers at Ale House, to the conferences and reviews. I am indebted to him for all he has done for me.

Dr. Kevin S. Jones has also been a great co-advisor for this work. His advice has helped mold the experimental portions of this work, improved my talks and also motivated me to get out of a rut and finish this. I also need to thank Kevin for the barbeques. Kevin also has three of the coolest kids in the world; I will remember Ryan and Sean and their wars with the whiteboard erasers.

I am also indebted to Dr. Pearton and Dr. Bosman for being on my committee and teaching two classes which have been of immense help to me. Dr. Bosman's device physics class has been of great help in trying to understand the odd Hall effect results we obtained. Dr. Pearton's semiconductor processing class has been of help on many occasions in understanding this material. However bad one's mood before Dr. Pearton's

lectures, one always walks out with a smile and usually laughing. I never looked at physical plant the same way again.

The members of the SWAMP center have been there for this all. Many people have come and gone and I miss them a great deal. I need to acknowledge Hernan Rueda for all the soccer games and the beers we drank together. Holly Miller has been a friend, Wings fan, kick-boxing and euchre buddy; and sent me countless encouraging emails after she left. Raghu Raman was always a quiet voice of sanity. Hugo Saleh always had a different point of view; sometimes he was right. Yasser Hadara helped make sense of it all. Current members of the SWAMP center helped me get through this. I especially need to thank Richard “Chummy” Brindos for being a friend, quarterback, neighbor, answering the phone for three years in the office; and for making the go-cart race a little more interesting. Ibo Avci has been my baklava connection for the past couple of years and also has the inside scoop on fine hotels in Reno, NV. Patrick Keys let me show him up on the soccer field (just kidding), snow-boarded through broken ribs, and will soon be my co-worker at Intel. Dr. Wish Krishnamoorthy helped me in countless ways during this work and supplied many a keg of Guinness. Chad Lindfors has helped with the Hall effect samples and was there to watch many a Wings game. I also need to thank Ljuba, Lance, Erik, Mark, Pladdy, Susan, and Dr. Chen who have all helped me at some time or another.

I have also been very fortunate to have great industrial/governmental mentors and contacts throughout this work. I would like to thank Steve Cea (Intel), Stephen Morris (Intel), Hal Kennel (Intel), Paul Packan (Intel), Samir Chaudhry (Agere), John McMacken (Agere), Wolfgang Windl (Motorola), Matthew Laudon (Motorola), Mark Johnson (LLNL), Tomas Diaz de la Rubia (LLNL), Maria Caturla (LLNL), Jing Zhu (LLNL), and

Silva Theiss (LLNL). I especially need to thank Martin Giles of Intel Corporation for mentoring me during two internships, advising me out of many tough situations, and convincing me that Intel was where I wanted to work.

I thank my good friend Effie Phillipakos for always being there and for her good call of avoiding the police on Archer road by taking Hull road.....NOT!!! I should have listened to her about more than I did (and she should have listened to me about UPD). Laura, Katie, Jelly, and Heather have been the coolest friends and neighbors a guy could have, drank up all my Black Haus when I decided I no longer liked it and driving me around when my new car broke. Juan Sanchez was always ready to go out for a beer and watch a game (we used to joke about him having the psychotic girlfriend).

Most importantly, I need to thank my family. Without my parents, I would not be where I am today. I am grateful to my brother and for the wisdom of my Grandma and Grandpa Gidley and my Grandma Lilak. It's been fun.

TABLE OF CONTENTS

	<u>page</u>
ACKNOWLEDGMENTS	iv
LIST OF TABLES	ix
LIST OF FIGURES.....	x
ABSTRACT	xviii
 1 INTRODUCTION.....	 1
1.1 Motivation.....	1
1.1.1 Conductivity Modulation: Semiconductors and Dopants	1
1.1.2 Building Blocks of Integrated Circuits: MOS Transistors	2
1.1.3 Moore's Law	3
1.2 Analysis Techniques.....	4
1.2.1 Transmission Electron Microscopy	4
1.2.2 Secondary Ion Mass Spectroscopy, SIMS	5
1.2.3 Spreading Resistance Profilometry.....	6
1.2.4 Hall Effect Analysis.....	7
1.3 Diffusion Processes	9
1.3.1 Fickian Diffusion Theory	10
1.3.2 Point-Defect Diffusion Theory	11
1.3.3 Fermi-Level and High Concentration Effects	11
1.4 Conductivity Modulation of Silicon: Dopant Incorporation and Activation	13
1.5 Ion Implantation	14
1.5.1 Dopant Distribution from Ion Implantation Process.....	15
1.5.2 Channeling.....	18
1.5.3 Implantation Damage.....	18
1.5.4 Amorphization	19
1.5.5 Damage Profiles.....	20
1.6 Point-Defect Interactions and Recombination	20
1.7 Thermal Activation of Dopants.....	22
1.8 Transient Diffusion Phenomena.....	23
1.8.1 Extended Defects from Ion Implantation Damage	24
1.8.2 Uphill Diffusion and Surface Dose Loss	25
1.8.3 Transient Enhanced Diffusion as a Function of Implant Energy	26
1.8.4 Transient Enhanced Diffusion as a Function of Implanted Dose.....	27
1.8.5 Transient Enhanced Diffusion as a Function of Temperature.....	27

1.8.6	Transient Diffusion in Absence of Extended Defects.....	28
1.8.7	Minimization of Transient Enhanced Diffusion.....	28
1.9	Transient Clustering Processes.....	30
1.10	Influence of Impurities upon Boron Transient Processes	32
1.11	Prior Boron Clustering/Activation/Diffusion Experimental Work	33
1.11.1	MBE DSL Experiments	33
1.11.2	TEM Defect Count Experiments	34
1.11.3	SIMS Experiments.....	34
1.11.4	Activation Experiments SIMS vs. SRP.....	34
1.12	Statement of Thesis.....	34
2	DEVELOPMENT OF PREDICTIVE MODELS	55
2.1	Modeling of Intrinsic Diffusion	55
2.2	Modeling of Interstitial System.....	56
2.3	Transient Enhanced Diffusion and Clustering.....	57
2.4	Applications to Electrical Activation and Reverse Annealing.....	59
2.5	Reduced Cluster Model	60
2.6	High Concentration Effects.....	61
3	EXPERIMENTAL INVESTIGATION OF BORON CLUSTERING KINETICS AND PROCESSES	86
3.1	Outline of Experiments.....	86
3.2	Boron Well Experiment	85
3.3	Boron Implant Study.....	89
3.3.1	Qualification of Hall Effect Measurements: Comparison to SRP	91
3.3.2	Observed Reactivation Behavior	93
3.3.3	Reactivation of Boron as a Function of Implanted Dose	94
3.3.4	Reactivation as a Function of Implant Energy	95
3.3.5	Reactivation at Similar Chemical Dopant Concentration	96
3.3.6	Mobility Data.....	97
4	ANALYSIS AND SIMULATION OF EXPERIMENTAL FINDINGS	144
4.1	Simulation of Boron Well Experiment	144
4.2	Qualitative Comparison to Boron Implant Study.....	145
4.3	Qualitative Correlation to Boron Activation Work.....	145
4.4	Quantitative Comparison of Simulated Results to SRP Profiles.....	146
4.5	Time Constant to Boron Activation and Possible Binding Energies	147
4.6	Correlating Observed Dissolution Kinetics to Cluster System	153
5	SUMMARY OF FINDINGS AND FUTURE WORK	173
5.1	Summary	173
5.2	Future Work	175
	APPENDIX A: SUPPLEMENTAL DATA FROM BORON IMPLANT STUDY	177
	APPENDIX B: SAMPLE INPUT SCRIPTS	197

LIST OF TABLES

<u>Table</u>	<u>page</u>
1-1	Relative energies of differing boron/interstitial clusters. Energies are computed through the local density approximation relative to isolated substitutional boron and doubly charged tetrahedral configuration interstitials. Energy of most stable configuration is in bold for each case.31
3-1	Implant matrix used in boron implant study. A 'x' indicates that condition was processed.89
3-2	Anneal matrix of boron implant study. Wafers in table 3.1 were diced into several pieces with a piece of each wafer being subjected to the twelve anneals as illustrated here. An 'x' indicates given split was subjected to this anneal step.....91
4-1	Exponential decay fits to the concentration of clustered boron for various implant conditions followed by anneals at 750°C. 149
4-2	Exponential decay fits to the concentration of clustered boron for various implant conditions followed by anneals at 850°C. 150
4-3	Calculated barriers to hypothetical BIC cluster dissolution reactions from experimental dissolution data 151

LIST OF FIGURES

<u>Figure</u>	<u>page</u>
1-1 Schematic of MOS transistor	36
1-2 .Projected scaling of the junction depth until the year 2014.....	37
1-3 Projected sheet resistance of the extension region.	38
1-4 Illustration of a hall effect structure (left) and a Van der Pauw structure (right).	39
1-5 Illustration of Fick's first law.....	40
1-6 Illustration of Fick's second law.	41
1-7 Two basic point defects:.....	42
1-8 Point-defect mediated diffusion mechanisms	43
1-9 Coordinated push mechanism.	44
1-10 Relative energies of differently configured interstitials.	45
1-11 Intrinsic interstitial density (cm^{-3}) as a function of boron doping level.....	46
1-12 Interstitial diffusivity as a function of boron concentration.	47
1-13 Simplified schematic of an ion implanter.	48
1-14 Residual damage arising from 40 keV $2 \times 10^{14} \text{ cm}^{-2}$ boron implant	49
1-15 40 keV $2 \times 10^{14} \text{ cm}^{-2}$ boron implant annealed at 700°C	50
1-16 A 20 keV $2 \times 10^{15} \text{ cm}^{-2}$ boron implant subjected to a 800°C 60 minute anneal. ..	51
1-17 Binding energies and reactions in the boron cluster system.	52
1-18 SIMS profiles of a doped super-lattice structure.....	53
1-19 Comparison of electrical and chemical measurements.....	54
2-1 Boron diffusion system under intrinsic conditions.....	63

2-2	Comparison of the intrinsic diffusion of a 80 keV $2 \times 10^{12} \text{ cm}^{-2}$ boron implant for two hours at 1000°C simulated with a model as in Figure 2-1.	64
2-3	Comparison of the intrinsic diffusion of a 80 keV $2 \times 10^{12} \text{ cm}^{-2}$ boron implant for one hour at 1100°C simulated with a model as in Figure 2-1.....	65
2-4	Interstitial cluster system utilized in this work.....	66
2-5	Dissolution of interstitials trapped in {311} defects simulated as a function of time.	67
2-6	Transient progression of interstitial clusters following the anneal at 815°C of a $5 \times 10^{13} \text{ cm}^{-2}$ silicon implant.....	68
2-7	Interstitial system at a time of one micro-second following the anneal at 705°C of a $5 \times 10^{13} \text{ cm}^{-2}$ silicon implant..	69
2-8	Interstitial system at a time of 1.44×10^5 seconds following the anneal at 705°C of a $5 \times 10^{13} \text{ cm}^{-2}$ silicon implant..	70
2-9	Full BIC cluster system used in this work..	71
2-10	A 40 keV $2 \times 10^{14} \text{ cm}^{-2}$ boron implant following the anneal at 700°C for a time of one hour simulated with FLOOPS using full cluster model.	72
2-11	A 40 keV $2 \times 10^{14} \text{ cm}^{-2}$ boron implant following the anneal at 700°C for a time of two hours simulated with FLOOPS using full cluster model.	73
2-12	Simulation of a 40 keV $2 \times 10^{14} \text{ cm}^{-2}$ boron implant following the anneal at 700°C for a time of one hour. All cluster species are shown in this plot.....	74
2-13	Transient progression of the boron clusters following a 700°C anneal of a 40 keV $2 \times 10^{14} \text{ cm}^{-2}$ boron implant..	75
2-14	Interstitial supersaturation as a function of depth following the 700°C anneal of a 40 keV $2 \times 10^{14} \text{ cm}^{-2}$ boron implant for a time of one hour.....	76
2-15	Simulation of diffusion enhancement exhibited by 40keV $2 \times 10^{14} \text{ cm}^{-2}$ boron implant at various times following anneal at 700°C	77
2-16	Simulation of transient nature of boron diffusion enhancement resulting from a 40keV $2 \times 10^{14} \text{ cm}^{-2}$ boron implant annealed at 700°C	78
2-17	Fractional activation of a 40 keV $2 \times 10^{14} \text{ cm}^{-2}$ boron implant following the anneal at 700°C for a time of one hour.	79
2-18	Reverse anneal effect as simulated by FLOOPS.....	80

2-19	Activation of a 40keV $6.6 \times 10^{14} \text{ cm}^{-2}$ boron implant following anneals of 1 hour at various temperatures (as in figure 2-18).....	81
2-20	Reduced boron cluster model as used in this work.....	82
2-21	Simulation with the reduced cluster model of a 40 keV $2 \times 10^{14} \text{ cm}^{-2}$ boron implant following the anneal at 700°C for a time of one hour.....	83
2-22	Simulation with the reduced cluster model of a 40 keV $2 \times 10^{14} \text{ cm}^{-2}$ boron implant following the anneal at 700°C for a time of two hours.....	84
2-23	Simulation of a 40 keV $2 \times 10^{14} \text{ cm}^{-2}$ boron implant following the anneal at 700°C for a time of one hour accounting for various concentration dependent effects and differing charge states present in the interstitial system.....	82
2-21	Simulation of a 40 keV $2 \times 10^{14} \text{ cm}^{-2}$ boron implant following the anneal at 700°C for a time of two hours accounting for various concentration dependent effects and differing charge states present in the interstitial system.....	83
2-22	Simulation with the reduced cluster model of a 40 keV $2 \times 10^{14} \text{ cm}^{-2}$ boron implant following the anneal at 700°C for a time of two hours.....	84
2-23	Simulation of a 40 keV $2 \times 10^{14} \text{ cm}^{-2}$ boron implant following the anneal at 700°C for a time of one hour accounting for various concentration dependent effects and differing charge states present in the interstitial system.....	85
3-1	Process flow of boron-doped well experiment.....	98
3-2	Plan view TEM micrographs from the boron well experiment.....	99
3-3	Results of defect counts from the boron-doped well experiment.....	100
3-4	Process sequence for boron implant experiment.....	101
3-5	Comparison of the integrated spreading resistance profile and sheet number obtained from Hall effect measurement for anneals conducted at 750°C and 850°C for up to one hour.....	102
3-6	Comparison of the integrated spreading resistance carrier profile and the sheet number obtained from Hall effect measurements for anneals at 850°C for times of greater than one hour, at 950°C and 1000°C	103
3-7	Plot showing the variation from run to run in hall effect measurements.....	104
3-8	Reactivation of a boron implants following a 750°C 30 minute anneal as seen through the spreading resistance profiles.....	105
3-9	Reactivation process at 750°C	106

3-10	Reactivation at 850 ⁰ C..	107
3-11	SRP profiles of the reactivation process at 850 ⁰ C for a 20 keV 8x10 ¹⁴ cm ⁻² boron implant reactivated at various times at 850 ⁰ C.....	108
3-12	Reactivation of a 20 keV 4x10 ¹⁴ cm ⁻² boron implant at 950 ⁰ C as seen through the spreading resistance profiles.....	109
3-13	Reactivation of a 40 keV 1.6x10 ¹⁵ cm ⁻² boron implant at 850 ⁰ C as seen through the spreading resistance profiles.....	110
3-14	Reactivation at 850 ⁰ C of 40 keV boron implants of various doses.....	111
3-15	Activation of 10 keV boron implants at various doses at 750 ⁰ C.	112
3-16	Activation of 20 keV boron implants at various doses at 750 ⁰ C.	113
3-17	Activation of 40 keV boron implants at various doses at 750 ⁰ C.	114
3-18	Activation of 80 keV boron implants at various doses at 750 ⁰ C.	115
3-19	Activation of 10 keV boron implants at various doses at 850 ⁰ C.	116
3-20	Activation of 20 keV boron implants at various doses at 850 ⁰ C.	117
3-21	Activation of 40 keV boron implants at various doses at 850 ⁰ C.	118
3-22	Activation of 80 keV boron implants at various doses at 850 ⁰ C.	119
3-23	Activation of boron implants at various doses following a 10 minute anneal at 950 ⁰ C.	120
3-24	Activation of boron implants at various doses following a 20 minute anneal at 950 ⁰ C.	121
3-25	Activation of boron implants at various doses following a 2 minute anneal at 1000 ⁰ C.	122
3-26	Reactivation process of 4x10 ¹⁴ cm ⁻² boron implants as the implant energy is varied.	123
3-27	Reactivation process of 8x10 ¹⁴ cm ⁻² boron implants as the implant energy is varied.	124
3-28	Reactivation process of 1.6x10 ¹⁵ cm ⁻² boron implants as the implant energy is varied.	125
3-29	Reactivation of 2x10 ¹⁴ cm ⁻² boron implants at 750 ⁰ C.....	126

3-30	Reactivation of $4 \times 10^{14} \text{ cm}^{-2}$ boron implants at 750°C	127
3-31	Reactivation of $8 \times 10^{14} \text{ cm}^{-2}$ boron implants at 750°C	128
3-32	Reactivation of $1.6 \times 10^{15} \text{ cm}^{-2}$ boron implants at 750°C	129
3-33	Reactivation of $4 \times 10^{14} \text{ cm}^{-2}$ boron implants at 850°C	130
3-34	Reactivation of $4 \times 10^{14} \text{ cm}^{-2}$ boron implants at 850°C	131
3-35	Reactivation of $8 \times 10^{14} \text{ cm}^{-2}$ boron implants at 850°C	132
3-36	Reactivation of $1.6 \times 10^{15} \text{ cm}^{-2}$ boron implants at 850°C	133
3-37	Reactivation of boron implants by the 950°C 10 minute anneal from the clustered state as a function of implant energy.	134
3-38	Reactivation of boron implants by the 950°C 20 minute anneal from the clustered state as a function of implant energy.	135
3-39	Reactivation of boron implants by the 1000°C 2 minute anneal from the clustered state as a function of implant energy.	136
3-40	Reactivation of the $1.6 \times 10^{15} \text{ cm}^{-2}$ boron implants as a function of implant energy from the clustered state by the 950°C 10 minute anneal.	137
3-41	Activation of boron from the clustered state by the 850°C 10 minute anneal. ...	138
3-42	Electrical activation of samples with similar chemical boron concentrations... ..	139
3-43	Activation of boron samples with similar chemical dopant concentrations from the clustered state by a 850°C 10 minute anneal.	140
3-44	Hole mobility as a function of hole density. Note that the hole mobility decreases with increasing hole density due to impurity scattering.	141
3-45	Hole mobility as a function of clustered boron density. There is no clear trend directly evident from this plot.	142
3-46	Hole mobility as a function of clustered boron concentration. At lower clustered boron densities, the hole mobility appears to decrease with increasing clustered boron density.	143
4-1	Simulation of boron well experiment.	154
4-2	Simulation of a 10 minute anneal at 740°C of a 40 keV $4 \times 10^{14} \text{ cm}^{-2}$ silicon implant into a boron-doped well of $1 \times 10^{19} \text{ cm}^{-3}$ concentration.	155

4-3	Simulation of a 10 minute anneal at 740°C of a 40 keV $4 \times 10^{14} \text{ cm}^{-2}$ silicon implant into a boron-doped well of $1 \times 10^{16} \text{ cm}^{-3}$ concentration.	156
4-4	Simulation of a 40 keV $4 \times 10^{14} \text{ cm}^{-2}$ boron implant annealed for 30 minutes at a temperature of 750°C.	157
4-5	Simulation of a 40 keV $4 \times 10^{14} \text{ cm}^{-2}$ boron implant annealed for 30 minutes at a temperature of 750°C (state of Figure 4-4) with an additional 10 minute anneal at 850°C.	158
4-6	Simulation illustrating the levels of boron substitutionality following a 750°C anneal for 30 minutes of a 40 keV boron implant of varying dose.	159
4-7	Simulation of the boron activation from a 40 keV $4 \times 10^{14} \text{ cm}^{-2}$ boron implant annealed at 750°C for 30 minutes.	160
4-8	Direct comparison of the activation exhibited by the model developed through this work and electrical measurement from SRP.	161
4-9	Direct comparison of the activation exhibited by the model developed through this work and electrical measurement from SRP. A 40 keV $1.6 \times 10^{15} \text{ cm}^{-2}$ boron implant was subjected to a 30 minute 750°C Anneal (state of Figure 4-8) followed by a 10 minute anneal at 850°C.	162
4-10	Direct comparison of the activation exhibited by the model developed through this work and electrical measurement from SRP. A 40 keV $1.6 \times 10^{15} \text{ cm}^{-2}$ boron implant was subjected to a 30 minute 750°C Anneal (state of Figure 4-8) followed by a 120 minute anneal at 850°C.	163
4-11	Direct comparison of the activation exhibited by the model developed through this work and electrical measurement from SRP. A 40 keV $4 \times 10^{14} \text{ cm}^{-2}$ boron implant was subjected to a 30 minute 750°C anneal.	164
4-12	Direct comparison of the activation exhibited by the model developed through this work and electrical measurement from SRP. A 10 keV $4 \times 10^{14} \text{ cm}^{-2}$ boron implant was subjected to a 30 minute 750°C anneal.	165
4-13	Direct comparison of the activation exhibited by the model developed through this work and electrical measurement from SRP. A 10 keV $4 \times 10^{14} \text{ cm}^{-2}$ boron implant was subjected to a 30 minute 750°C anneal (state of Figure 4-12) followed by a 850°C anneal for a time of 10 minutes.	166
4-14	Direct comparison of the activation exhibited by the model developed through this work and electrical measurement from SRP. A 20 keV $8 \times 10^{14} \text{ cm}^{-2}$ boron implant was subjected to a 30 minute 750°C anneal.	167
4-15	Direct comparison of the activation exhibited by the model developed through this work and electrical measurement from SRP. A 20 keV $8 \times 10^{14} \text{ cm}^{-2}$ boron	

	implant was subjected to a 30 minute 750°C anneal (state of Figure 4-14) followed by a 850°C anneal for a time of 10 minutes.	168
4-16	Calculated binding energy to dissociation of a boron interstitialcy from a BIC- like cluster as calculated from anneals at 750°C as a function of implant energy.....	169
4-17	Calculated binding energy to dissociation of a boron interstitialcy from a BIC- like cluster as calculated from anneals at 850°C as a function of implant energy.....	170
4-18	Calculated binding energy to dissociation of a boron interstitialcy from a BIC- like cluster as calculated from anneals at 750°C as a function of implant dose..	171
4-19	Calculated binding energy to dissociation of a boron interstitialcy from a BIC- like cluster as calculated from anneals at 850°C as a function of implant dose..	172
A-1	10 keV as-implanted profiles.	178
A-2	20 keV as-implanted profiles.	179
A-3	40 keV as-implanted profiles.	180
A-4	80 keV as-implanted profiles.	181
A-5	Exponential best fits to the 750°C BIC cluster dissolution observed from implants performed at 10 keV.....	182
A-6	Exponential best fits to the 750°C BIC cluster dissolution observed from implants performed at 20 keV.....	183
A-7	Exponential best fits to the 750°C BIC cluster dissolution observed from implants performed at 40 keV.....	184
A-8	Exponential best fits to the 750°C BIC cluster dissolution observed from implants performed at 80 keV.....	185
A-9	Exponential best fits to the 850°C BIC cluster dissolution observed from implants performed at 10 keV.....	186
A-10	Exponential best fits to the 850°C BIC cluster dissolution observed from implants performed at 20 keV.....	187
A-11	Exponential best fits to the 850°C BIC cluster dissolution observed from implants performed at 40 keV.....	188
A-12	Exponential best fits to the 850°C BIC cluster dissolution observed from implants performed at 80 keV.....	189

A-13	Time constant to boron reactivation from clustered state following 10 keV implants at temperatures of 750C and 850C.....	190
A-14	Time constant to boron reactivation from clustered state following 20 keV implants at temperatures of 750C and 850C.....	191
A-15	Time constant to boron reactivation from clustered state following 40 keV implants at temperatures of 750C and 850C.....	192
A-16	Time constant to boron reactivation from clustered state following 80 keV implants at temperatures of 750C and 850C.....	193
A-17	Time constant to boron activation for $4 \times 10^{14} \text{ cm}^{-2}$ boron implants.....	194
A-18	Time constant to boron activation for $8 \times 10^{14} \text{ cm}^{-2}$ boron implants.....	195
A-19	Time constant to boron activation for $1.6 \times 10^{15} \text{ cm}^{-2}$ boron implants.....	196

Abstract of Dissertation Presented to the Graduate School
of the University of Florida in Partial Fulfillment of the
Requirements for the Degree of Doctor of Philosophy

ANALYSIS AND MODELING OF TRANSIENT PHENOMENA IN BORON-DOPED
SILICON

By

Aaron D. Lilak

August 2001

Chairman: Mark E. Law

Major Department: Electrical and Computer Engineering

Boron is currently the dominant p-type dopant utilized in silicon processing technologies due primarily to the high electrical solubility level which it allows. Unfortunately, boron's low mass and small size make it highly susceptible to transient diffusion and activation effects which are mediated by the implantation process. These effects degrade the ability to form ultra-shallow p⁺/n junctions, such as those required for the source/drain region of a metal oxide semiconductor (MOS) structure. Prior research has largely focused on understanding the transient diffusion behavior, neglecting the study of the transient activation behavior. It is believed that this transient activation behavior is mediated via a boron clustering process in which boron atoms are bound to silicon interstitials into thermally stable and immobile complexes. Recent first-principles calculations performed by Lawrence Livermore National Laboratories have also attempted to elucidate the structure and energetics involved in these clustering processes. The first goal of this work is to experimentally investigate the kinetics of the boron

clustering and activation processes. This was investigated via two experiments. The first of these utilized boron-doped wells of 5×10^{16} to $1.2 \times 10^{18} \text{ cm}^{-3}$ concentration which were subjected to a 40 keV silicon implant followed by low temperature anneals. A study of the residual {311} type defects in these samples helps elucidate the mechanisms of boron clustering processes. The second experiment utilized Hall effect and spreading resistance measurements to study the activation of a boron implant at 10 keV to 80 keV with dose of 2×10^{14} to $1.6 \times 10^{15} \text{ cm}^{-2}$, which illustrates a cluster dissolution process governed by a binding energy of approximately 2.7 eV.

The second goal of this work was to develop a continuum model within the FLOOPS process simulation software capable of predicting several transient phenomena in boron-doped silicon. This model was based upon the theoretical calculations performed at Lawrence Livermore National Laboratories and has been found to be fairly consistent with the experimental work obtained as part of this work and also results of previous researchers. The 2.5 to 2.8 eV dissolution energy, which was determined as part of this work, is roughly the dissolution energy of the B3I complex via the B2 intermediary. This binding energy was also found to be a weak function of implant energy and dose with higher concentration material providing a higher energy to dissolution. This result is indicative of multi-cluster or fermi-level effects becoming important at higher boron concentrations. The modeling work also indicates that the substitutional boron profile is a reasonable depiction of the electrically active boron profile, while the B3I complex with 33% fractional activation leads to an overestimate of the electrically active boron profile in many instances.

CHAPTER 1 INTRODUCTION

1.1 Motivation

Smaller, faster and cheaper: Three words which have governed the semiconductor industry for the past 30 years. The transistor, invented by Bell Labs in 1947, has progressed from a device approximately the size of an apple to modern devices with feature sizes smaller than 100nm. This level of scaling allows over one billion of these transistors to be placed on a single chip approximately 1 cm^2 with corresponding computational power undreamed of only a few years ago.

1.1.1 Conductivity Modulation: Semiconductors and Dopants

Solids may be characterized as either insulators, metals or semiconductors based upon the type of chemical bonding which holds them together. This bonding determines how the material will react to applied electrical forces or voltages as well as other physical properties.

Insulators are very resistive to applied electrical voltages. These materials have very large bandgaps with very tightly bound electrons and are utilized in semiconductor processes to physically separate regions conducting charge. Common insulators utilized in silicon semiconductor processes are SiO_2 and Si_3N_4 .

Metals are very conductive, meaning they have many free electrical carriers. The valence electrons in a metal are typically not localized to any one atom. Rather, they are free to move about within the solid making them very conductive media to the transport

of electrical charge. Metals are typically utilized in semiconductor processes as conduits for electrical charge between adjacent devices. Typical metals used in silicon CMOS processes are Ti, W, Al, Au, and Cu.

Semiconductors in their pure form are most like an insulator. Without impurities, a semiconductor is very resistive to applied voltages and a poor material for the transport of electrical charge. However, what makes semiconductors unique, is that they may be transformed into a metal-like material by the addition of impurities. Homogeneous semiconductor materials such as silicon and germanium are from the fourth column of the periodic table. Each atom has four shared valence bonds with its neighbors and there are no free carriers in an intrinsic, un-doped, semiconductor. Elements from Columns III and V are typically utilized as dopants in silicon CMOS technology. A Column V element has five valence electrons and is referred to as an electron donor. If this atom replaces a silicon lattice atom, four of the valence electrons will be utilized in order to bond the atom to the four nearest silicon neighbors and one electron will be free to move about the crystal and contribute to electrical conduction. Similarly, if an atom of Column III is used to replace a lattice atom, the three valence electrons will be shared amongst the nearest neighbors and one bond will be incomplete. This incomplete bond, or lacking electron, may also contribute to electrical conduction. For obvious reasons, elements of Column III are referred to as electron acceptors.

1.1.2 Building Blocks of Integrated Circuits: MOS Transistors

The MOS, metal oxide semiconductor, transistor is the component from which most integrated circuits are currently constructed. A simple schematic of this is shown in Figure 1-1. Integrated circuit applications typically utilize this device as a voltage-

controlled switch; although it may also be used as an amplifier. Such applications are beyond the scope of this work.

The MOS transistor is classified by both the type of doping in the source/drain region as either a PMOS or NMOS device. In this device, the gate voltage is utilized to charge-couple a conducting channel in the silicon region immediately below the insulating oxide. If a voltage is then applied between the source and drain, current will flow in the device. If the voltage on the gate region sufficient to maintain a conducting channel is removed, the current will essentially cease. In this manner, the MOS device operates as a switch with the gate voltage determining whether the device is “on” or “off.” While this description of MOS transistor operation is very brief and entirely incomplete, it is sufficient background for this work.

1.1.3 Moore’s Law

Gordon Moore, a one-time Intel CEO, observed that silicon integrated circuits roughly double in terms of number of transistors and speed every 1.5 to 2 years. This trend has held true for the past 30 years. The corollary to this rule is that only those companies which have met or stayed ahead of this trend have been long-term successful!

In order to continue to achieve this rate of growth to the semiconductor industry, many challenges must be overcome. The semiconductor companies have addressed this by the formation of Sematech. This company is funded by a consortium of semiconductor companies with the sole goal of conducting research into areas critical to the future development of semiconductor processing technologies. As part of this task, Sematech has published the International Technology Roadmap for Semiconductors, or ITRS. This document identifies both projected growth within the semiconductor industry and also

areas forecast to limit future growth. One area of particular concern is the formation of very shallow source/drain extensions (SDE) with very high regions of acceptor-type dopants. For reasons soon to be discussed, the formation of such regions is not a trivial matter. Figures 1-2 and 1-3 illustrate the Sematech projections of the junction depth and the sheet resistance of the extension regions in a CMOS device.

1.2 Analysis Techniques

Throughout this work, a series of measurement techniques were utilized in order to study the transient properties of boron in doped silicon. A brief overview of each technique is presented here.

1.2.1 Transmission Electron Microscopy

Transmission electron microscopy provides information from very thin samples through which energetic electrons are transmitted. The TEM provides useful information regarding the location, composition, and quantity of crystalline defects. The TEM can be utilized to monitor the progression of these defects with processing steps.

The TEM samples may be classified as either plan-view or cross-sectional. A plan-view image is taken on a sample prepared perpendicular to the wafer surface and a cross-sectional sample is prepared parallel to the surface. Plan-view samples provide information regarding the areal density of damage and type of damage, but provide very little information regarding the location of the damage in regards to the crystalline surface. Cross-sectional samples provide information regarding the thickness of the damaged region and its separation from the surface. Cross-sectional samples provide a much less accurate measure of the defect density. Plan-view samples were sufficient for most of this work.

The TEM images may be classified as either bright field or dark field. The bright field image is formed from the transmitted beam of electrons and the dark field image is formed from the diffracted beam of electrons. Dark field images generally provide higher resolution and were used in most of this work.

Preparation of a plan-view sample is a somewhat tedious task of first cutting out a small piece of material from the sample to be analyzed. This piece is then mounted face down on a polishing jig with crystal bond and ground from the back side until it is approximately the thickness of a thin sheet of paper. This sample is then removed from the polishing jig with the aid of heat and mounted with wax upon a Teflon holder face down. Wax is formed into a circular region on the surface and the sample is slowly etched with a solution of $\text{HF:HNO}_3=25\%:75\%$ until the sample just forms a very small hole. The thin regions surrounding this hole are the areas which are analyzed by the transmission electron microscope.

Plan-view TEM can be used to analyze defects as small as a few atoms. Defect densities as small as roughly $1 \times 10^{12} \text{ cm}^{-3}$ can be determined. Error from a PTEM count is quite substantial. It is not unreasonable to assume a 50% error on any PTEM defect count given the methods which must be used to analyze the micrograph. This error, however, should be fairly consistent from sample to sample. A PTEM measurement is somewhat inaccurate, however, it can be considered reasonably precise or reproducible if recounted from same image with same counting methodology.

1.2.2 Secondary Ion Mass Spectroscopy, SIMS

SIMS is a method of determining the chemical impurity concentration as a function of depth within the wafer. SIMS provides no electrical information regarding the state of the impurity. SIMS provides a 1-D profile and is not normally useful for 2-D

analysis. A SIMS machine is much like an ion implanter in that highly energetic beams of ions are impinged upon the surface of the wafer. Typical ions utilized are Cs^+ , O_2^+ , O^+ , and Ar^+ at energies of 2keV to 20 keV. These ions will physically remove, or sputter, material from the surface at a relatively constant rate, some of which will be in the form of ions. These sputtered ions are then fed into a mass analyzer which determines the species present and number of counts of each material. The depth within the material may be determined by analyzing the depth of the sputtered crater. The chemical concentration at a given point may be determined by the area of the beam and the counts of a given ion specie in comparison to those of a known reference sample.

Many tricks are employed in order to use SIMS for very shallow regions. These are beyond the level of understanding required here. In general, SIMS depth measurements are fairly accurate. Concentration results may have some error due to the fact that this method compares results to those of another sample. Resolution varies depending upon the analysis and operator. For deeper implants used in this study, it is reasonable to expect minimal concentration resolution of approximately $1 \times 10^{17} \text{ cm}^{-3}$. There are many errors and artifacts native to SIMS measurements especially at the surface or at an interface such as the Si/SiO₂ interface. For more information please consult a reference.

1.2.3 Spreading Resistance Profilometry

Spreading resistance profilometry, or SRP, is a means of measuring the electrically active fraction of a dopant profile as a function of spatial position and depth. No direct information is provided regarding inactive dopants. To measure an electrically active dopant profile, the sample is first beveled and then the differential resistance is determined between adjacent positions from which the carrier concentration may be

inferred. The resolution of the SRP profile is determined, in large part by the size of the probe tip used for the analysis and the angle of the bevel.

Spreading resistance analysis requires an electrical junction be present in the material. In order to accomplish this, all of the boron implants used in this study were performed into a phosphorus-doped n-type wafer. SRP profiles measure only the net differential resistivity as a function of depth, therefore, no meaningful measurements below the background doping concentration may be made and the profile near the electrical junction has a degree of inaccuracy. Spatial resolution of around 10 to 20 nm is possible with this technique depending upon the bevel angle and size of probes utilized.

In order to convert the spreading resistance into a dopant concentration it is necessary to infer a carrier mobility. The carrier mobility is generally treated as a function of just the carrier concentration. As will be shown in this work, additional dependencies may need to be addressed for inactive structures. In this work, all of the spreading resistances were converted to resistivities according to the Schumann-Gardner theory. The conversion of the resistivity to the carrier concentration was done according to ASTM standard F723 which is based upon a great deal of experimental work. In the future, if mobility models are developed which incorporate other scattering mechanisms, it would be an easy matter to substitute in these dependencies.

1.2.4 Hall Effect Analysis

Hall effect measurements provide the carrier type, the carrier mobility and the sheet resistance for the sample. From the sheet resistance, it is possible to infer the carrier concentration or the net number of electrically active dopant impurities. Hall effect is a means of gauging the degree to which implanted dopants are electrically active as well as

monitoring the mobility degradation due to impurity scattering from both the incorporated dopants and any extended defects.

This work involved hundreds of hall effect measurements. These samples were prepared on a 4 contact Van der Pauw structure approximately 14.4 mm square as shown in Figure 1-4. Aluminum/Silicon alloy contacts were used for this structure and all samples were treated with a 450⁰C 30-minute contact-hardening anneal.

In Hall effect measurement, a known voltage is applied between two of the ohmic contacts. Since the distance between these contacts is known, the resistance of the material may be determined from Ohm's law. This resistance may easily be converted into a carrier density. The mobility is computed by applying a magnetic field perpendicular to the direction of current flow. This magnetic field introduces a Lorentz force which will act upon the electrons as:

$$\text{Force}_{\text{Lorentz}} = q * (\text{velocity} \times B) \quad (1.1)$$

Since there is no path for current to flow in a perpendicular direction, this force must be exactly cancelled by a voltage acting in the perpendicular direction. This is referred to as the Hall Voltage. For the bulk crystal sample, this voltage will have magnitude of:

$$V_{\text{Hall}} = \frac{1}{q * P, N} * \text{MagneticField} * \frac{\text{Current}}{\text{Thickness}} \quad (1.2)$$

with orientation to oppose the Lorentz force. The carrier type is determined by the sign of the Hall voltage.

The modification of these equations to the Van der Pauw structure is fairly straightforward. With respect to Figure 1-4 where a current, I_{AB} , refers to a current flowing from Contact A to Contact B and a voltage, V_{AB} , is the potential difference of

Contact A relevant to Contact contact B the following equations apply to the Van der Pauw structure:

$$\exp(-pR_A / R_S) + \exp(-pR_B / R_S) = 1 \quad (1.3)$$

which is referred to as the Van der Pauw equation where R_S is the sheet resistance of the material and R_A and R_B are determined from:

$$R_A = V_{43} / I_{12} \quad (1.4)$$

$$R_B = V_{14} / I_{23} \quad (1.5)$$

It is then possible to determine the sheet resistance from equations 1.3 to 1.5. The carrier mobility may be determined from:

$$\mu = \text{mag}(V_H) / (R_S * I * B) \quad (1.6)$$

1.3 Diffusion Processes

The diffusivity of an impurity describes its tendency to move about in the presence of thermal energy. The general diffusivity may be expressed in an arrhenius form as:

$$D = D_0 * \exp\left(\frac{-E_m}{kT}\right) \quad (1.7)$$

Where D_0 is the diffusivity prefactor, E_m is the migrational energy of the impurity, and KT is the product of kelvin temperature and boltzman's constant. The diffusion process is governed by both defect and impurity gradients with the impurities tending diffuse from areas of higher concentration to areas of lower concentration much like a drop of dye will disperse to tint a glass of water. Other factors such as the presence and proximity of extended defects, presence of trap species, presence of stress fields and proximity of the crystalline surface or an interface are becoming important to highly scaled devices.

1.3.1 Fickian Diffusion Theory

At low concentrations, the diffusion behavior of many impurities is governed by Fick's laws. The first law states that the impurities will move from areas of higher concentration to areas of lower concentration with a flux, J , proportional to the concentration gradient of the impurity as shown in Figure 1-5. This constant of proportionality is the diffusivity of the dopant.

$$J = D * \nabla C \quad \text{Equation (1.8)}$$

The second of these laws states that there is a conservation of impurity particles. For a simple 1-D dopant flux:

$$\text{Volume} * \frac{dC}{dt} = \text{Area} * (J_{in} - J_{out}) \quad (1.9)$$

Taken differentially, this will become:

$$\frac{dC}{dt} = \frac{dJ}{dx} \quad (1.10)$$

Or generalized to a 3-D flux as shown in Figure 1-6:

$$\frac{dC}{dt} = \nabla J \quad (1.11)$$

The expression of Fick's first law can be substituted into Fick's second law to obtain the form:

$$\frac{dC}{dt} = D * \nabla^2 C \quad (1.12)$$

Which makes the additional assumption that the diffusivity is independent of position.

These models treat all of the impurity as being mobile with a given diffusivity and produces dopant profiles which are gaussian in nature. Fickian diffusion models are adequate in the description of low concentrations of impurities subjected to very long

thermal cycles at high temperatures. Unfortunately, this is not the case in modern silicon CMOS processing technology.

1.3.2 Point-Defect Diffusion Theory

Crystalline silicon possesses a number of atomistic lattice imperfections called point defects which may take the form of either an interstitial or a vacancy as shown in Figure 1-7. The equilibrium concentration of such point-defects is governed by the disorder or entropy of the material. A vacancy is simply the lack of a lattice atom and an interstitial is an atom which occupies a site within the interstices of the lattice.

By examining the diffusion processes at the microscopic level, several diffusion mechanisms become evident involving these point-defects. Examples of these are illustrated in Figure 1-8. Boron is known to form stable complex by binding to a silicon interstitial and diffusing as an interstitialcy via the hexagonal site of the lattice. Recent work has also indicated another means of boron diffusion, the coordinated push effect, in which a silicon tetrahedral interstitial becomes interstitial by pushing a substitutional boron atom to a neighboring lattice site [Liu00]. The silicon atom displaced is then pushed to a neighboring tetrahedral site as shown in Figure 1-9.

1.3.3 Fermi-Level and High Concentration Effects

At high doping levels, the point-defects and interstitialcies will begin to take on different charge states [Gil89, Zhu97, Len00]. Each of these different charge states can possess a different migrational energy and the net point-defect or interstitialcy population is actually composed of several components. Empirically, these effects are considered by the modification of the net dopant point diffusivity to a form similar to the following:

$$D_{\text{NET}} = D^0 + D^+ * \left(\frac{p}{n_i}\right) + D^{++} * \left(\frac{p}{n_i}\right)^2 \quad (1.13)$$

This may be alternately expressed as:

$$D_{\text{NET}} = \sum_i (D_i * f_i) \quad (1.14)$$

Where D_{net} is the total diffusivity, f_i is the fractional component of each charge state with diffusivity of D_i . The net effect of these fermi-level effects is to generally increase the dopant diffusivity with increasing doping concentration.

The physical explanation for this concentration dependent diffusivity is related to the fact that the relative energies of the different defect configurations is a function of the fermi-level in the material [Zhu97]. Figure 1-10 illustrates the relative energies of the different interstitial charge configurations and that of the boron interstitialcy charge states as a function of the Fermi-level which in turn is directly determined by the doping level [Sze81]. It is important to account for these effects as the different interstitial and interstitialcy charge states may have different migrational energies and hence different diffusivities. This implies concentration dependence to the point-defect and interstitialcy diffusivities and the intrinsic carrier density.

For the case of heavily boron-doped silicon, there are three interstitial configurations and two interstitialcy configurations [Zhu97]. The relative populations of each are given by the following expressions [Gil89]:

$$C_i^+ = C_i^0 * \left(\frac{p}{n_i}\right) * \exp\left(\frac{E^+ - E_i}{kT}\right) \quad (1.15)$$

$$C_i^{++} = C_i^0 * \left(\frac{p}{n_i}\right)^2 * \exp\left(\frac{E^{++} - E_i}{kT}\right) \quad (1.16)$$

Detailed calculations leading to results such as those shown in Figure 1-10 can lead to the following expressions for the case of boron if it is assumed that the relative energy levels will track the valence band edge with increasing temperature.

$$E^+ - E_i \approx \frac{E_f}{E_g} * 1.25 - \frac{E_g}{2} \quad (1.17)$$

$$E^{++} - E_i \approx -1 + \frac{E_f}{E_g} * 2.6 - \frac{E_g}{2} \quad (1.18)$$

Where E_f is the fermi energy level as determined by Maxwell-boltzman statistics for the heavily doped cases, E_g is the temperature dependent energy gap of the semiconductor and E^{++} and E^+ are the relative energies of the singly and doubly positively charged interstitial configurations.

Figure 1-11 shows the relative populations of interstitials for a highly boron-doped sample with the corresponding interstitial diffusivity shown in Figure 1-12, which accounts for differing migrational energies of the differently charged interstitials [Zhu97, Len00]. Note the influence of the doping level on the determination of the interstitial population within the peak region of the implant. It is also necessary to account for the electric field term in heavily doped material. For more information please consult a reference or see an example script in Appendix B.

1.4 Conductivity Modulation of Silicon: Dopant Incorporation and Activation

As previously mentioned, pure silicon is a highly resistive material. Without the addition of dopants, it is possible to find silicon with resistivities of 2.5×10^5 ohm-cm. Dopants, incorporated within the silicon crystal, may modify this conductivity by several orders of magnitude. However, the mere presence of a dopant atom is not sufficient for it to contribute to conduction within the crystal. Rather, only activated dopants and possibly fractionally activated dopant complexes may participate in this electrical conduction. This activation process involves both the atom occupying a substitutional site via a kick-out mechanism and either donating an electron to the silicon crystal for the case of a

donor-type impurity or accepting an electron from the silicon crystal for acceptor-type dopants. The process of either donating or accepting this electron requires a small amount of energy as well; however, for common dopants in silicon such as boron, phosphorus, and arsenic this process is easily mediated with ambient thermal energy.

There is a limit as to how much of an impurity which may be incorporated within the silicon lattice and still remain electrically active under equilibrium conditions. At extremely high doping levels, the further addition of dopants will lead to the formation of electrically inactive precipitates. These precipitates are not only electrically inactive, but also degrade the carrier mobility through scattering mechanisms affecting several device parameters in a derogatory manner. This “solubility limit” is a strong function of both temperature and impurity specie and places an upper bound on the quantity of dopant impurity which normally may become electrically active within the silicon crystal.

The solid solubility of common dopants in silicon as a function of temperature is very well known. Arsenic’s high solid solubility and high mass make it the predominant n-type dopant in silicon. Boron is also the only p-type dopant in silicon with high enough solid solubility to be useful in the formation of highly-doped regions.

1.5 Ion Implantation

By far, the most common means of introducing dopant atoms within the silicon crystal is ion implantation. The chief advantages to ion implantation are the precise control it gives you over dopant positioning and the degree to which this process is understood. Figures of merit from an ion-implantation process are the tilt of the wafer, rotation of the wafer, temperature of implant, current density, ion species, implanted dose and implant energy. A schematic of a basic ion implanter is shown in Figure 1-13. In the

most simple form, an ion implanter may be thought of as a device which utilizes electrical energy to accelerate ions and direct them towards the wafer. The ions come from an ion source and are then filtered to remove any unwanted contaminant ions. This separation takes place according to the mass to charge ratio of the ion. The filtered ions are then directed into an acceleration tube where they acquire kinetic energy given by following formula [Wol86]:

$$\text{Energy} = q * \text{AcceleratingVoltage (eV)} \quad (1.19)$$

They are then directed through a series of deflection plates which steers the ion beam across the wafer in a uniform manner providing roughly constant exposure to all areas of the wafer. An integrator circuit is connected between the wafer and ground potential which is utilized to determine the beam current which has impinged upon the wafer. From this beam current, it is possible to determine the total implanted dose of dopants as follows:

$$\text{Dose} = \int_{t=0}^t \text{BeamCurrent} * \frac{\text{Ionization}}{q * \text{Area}} dt \quad (1.20)$$

where the ionization is one for a singly ionized impurity, two for a doubly ionized impurity, etc..

1.5.1 Dopant Distribution from Ion Implantation Process

Having knowledge of the spatial location of the implanted ions is of paramount importance to the determination of the device behavior. Analytical expressions for the determination of implantation profiles have been developed and are remarkably accurate. As the implanted ions impinge on the surface of the wafer, they lose energy in collisions

with atoms and electrons within the crystal. The rate at which an ion loses energy is given by the following:

$$\frac{dE}{dx} = S_n(E) + S_e(E) \quad (1.21)$$

Where $S_n(E)$ is the nuclear stopping component which is related to atomic collisions and $S_e(E)$ is due to the interaction of the ion with the electrons of the crystal. Values of $S_n(E)$ and $S_e(E)$ have been computed for various dopants/energies, or it is possible to compute them for low doses from:

$$S_n \approx 2.8 * 10^{-5} * \frac{Z_1 * Z_2 * N * M_1}{\left(\frac{Z_1^2}{2} + \frac{Z_2^2}{2}\right) * (M_1 + M_2)} \text{ (eV/Angstrom)} \quad (1.22)$$

$$S_e = 1.22 * 10^{-16} * N * \sqrt{\frac{\text{Energy}}{M_1}} \text{ (ev/Angstrom)} \quad (1.23)$$

where z_1 and m_1 refer to the implanted ion and z_2 , m_2 refer to the crystal ion and N is the atomic density of the crystal, $5 \times 10^{22} \text{ cm}^{-3}$ for silicon. It is not typically necessary to calculate these values since they have been tabulated and plotted for most dopants.

The point at which the stopping mechanisms is equal for a given dopant is referred to as the critical energy and may be expressed as:

$$E_{\text{crit}} = (S_n * K)^2 \quad (1.24)$$

It is now possible to write an expression for the total range of the implant, or the distance a given ion will travel before it comes to rest. It is important to note that this is a net distance and not a vector quantity. The ion may come to rest directly beneath its point of impingement or to the side.

$$\text{Range} = \int_0^{\text{Energy}} \frac{dE}{-\frac{dE}{dR}} \quad (1.25)$$

This may be approximated as:

$$\text{Range} = \frac{\text{Energy}_{\text{ion}}}{S_n} \quad (\text{if below } E_{\text{crit}}) \quad (1.26)$$

or

$$\text{Range} = \frac{\text{Energy}_{\text{ion}}}{S_e} \quad (\text{if above } E_{\text{crit}}) \quad (1.27)$$

It is possible to then determine the average depth at which an ion will come to rest. This quantity is referred to as the projected range and may be expressed as:

$$\text{Range}_{\text{projected}} = \frac{\text{Range}}{1 + \frac{M_2}{3 * M_1}} \quad (1.28)$$

The distribution of the doping profile about the projected range is given by the straggle of the implant which may be expressed as:

$$\Delta R_p = \frac{2}{3} * R_p * \frac{\sqrt{M_1 M_2}}{(M_1 + M_2)} \quad (1.29)$$

It is now possible to write an expression for a gaussian distribution to describe the implanted profile:

$$n(x) = \frac{\text{Dose}}{\sqrt{2\pi} * \Delta R_p} \exp\left(-\frac{(x - R_p)^2}{2 * \Delta R_p^2}\right) \quad (1.30)$$

The lateral straggle of the implant may be accounted for by the following equation:

$$n(x, y) = n(x) * \exp\left(-\frac{y^2}{2 * \Delta R_p^2}\right) \quad (1.31)$$

This lateral straggle is becoming increasingly important for highly scaled devices as the degree to which an ion travels horizontally below a mask layer approaches the total lateral separation of the mask layer.

1.5.2 Channeling

Certain implanted ions will land in the channels of the crystal. These ions will experience only electronic stopping and will travel a very long distance before they come to rest. At low implanted doses the channeling component is very important. As the dose is increased, the implanted ion will displace lattice atoms which will destroy the long-range order of the crystal and block the channels limiting the distance an ion may travel within a channel before it encounters a nuclear stopping event. Channeling is generally controlled through the variation of the wafer tilt and rotation.

1.5.3 Implantation Damage

As the implanted ions come to rest in the silicon crystal and they disperse their kinetic energy to the lattice, they may locally disrupt the symmetry of the lattice by displacing lattice atoms. The typical energy required to displace a silicon atom from a bound lattice site is 15eV. With typical implant energies of .5keV to 100 keV it is easy to see how a single implanted ion may cause several such displacements. The process of removing a silicon atom from a lattice site is referred to as the Frenkel process. The silicon atom removed from the lattice site is referred to as an interstitial and the lattice site left unoccupied is referred to as a vacancy. These interstitials and vacancies are the basic point-defects.

For low energies, below the critical energy as is typical of modern CMOS processes, it is possible to determine the energy dispersed per length within the crystal as:

$$\frac{dE}{dx} = S_n \quad (1.32)$$

it is then possible to evaluate the energy displaced per atomic plane as:

$$\frac{dE}{\text{latticeplane}} = S_n * \text{spacing} \quad (1.33)$$

Typical displacement energies are 15eV for the Frenkel process and the excess energy transferred to the displaced ion may cause secondary displacements. These secondary displacements are significant for heavier ions such as Arsenic with large nuclear stopping components. For lighter ions such as boron, most of the damage is due to the original displacement and is referred to as primary damage.

1.5.4 Amorphization

At high levels of implantation damage, the long-range order of the crystal begins to be eroded. It is generally assumed that once 10% of the lattice atoms are displaced, that the material is no longer crystalline and is referred to as amorphous. The implanted dose necessary to achieve this is referred to as the amorphization dose. This is a strong function of the ion mass. Heavy ions such as Arsenic create a number of secondary collisions and a relatively few ions may destroy the order to the lattice. Lighter ions such as boron create few, if any, secondary displacements and it is next to impossible to amorphize a silicon crystal by implanting boron at practical doses. Ions which are implanted into an amorphous region generally exhibit very low channelling and higher nuclear stopping coefficients which limit the penetration of the ions within the crystal. In addition to this, when the crystal is reformed by a low temperature anneal, it has been shown that higher levels of activation are possible for certain dopants than normally is the case [Lam99]. For this reason, amorphous implants are used within certain processing

steps with the crystal often being amorphized by electrically neutral species such as silicon or germanium if the implanted dopant is light in mass such as boron. The principle disadvantage to this is that amorphization followed by regrowth of the crystal introduces a number of extended defects near the projected range of the amorphizing implant. These extended defects may induce leakage currents or scatter carriers if they are not properly located.

1.5.5 Damage Profiles

The location of the residual implant damage is of critical importance to the diffusion of the dopants. Software tools such as UT-Marlowe are invaluable for predicting the final damage profiles following an implant. In general, the vacancy profile is deeper than the interstitial profile since some of the displaced lattice atoms will simply be knocked-on into the lattice and not cause additional displacements. Since the silicon vacancies and silicon interstitials are created in the same process, the numbers of these defects created by the implant step is identical and their integrated populations from the damage profile must be identical neglecting any other reactions which may occur during the implant. Sample damage profiles from UT-Marlowe are shown in Figure 1-14.

1.6 Point-Defect Interactions and Recombination

Point-defects, both interstitials and vacancies, must be removed or they will have derogatory effects upon the distribution of the dopants as will be discussed shortly in the following pages. There are two processes by which the point defects may be removed from the crystal. One of these is recombination at the surface and the other is recombination with the opposite point defect.

Thermodynamic equilibrium demands a certain amount of disorder to the lattice. This disorder creates stable populations of interstitials and vacancies referred to as Cistar

and C_{vstar} . Recombination at the surface will seek to equilibrate these populations to the equilibrium value.

$$\frac{dInt}{dt}(\text{surface}) = K_{ri} * (C_{Int} - C_{Istar}) \quad (1.34)$$

$$\frac{dVac}{dt}(\text{surface}) = K_{rv} * (C_{Vac} - C_{Vstar}) \quad (1.35)$$

where k_{ri} and k_{rv} are the recombination rates and are given by:

$$K_{ri} = 4 * \pi * D_i * \rho_{oi} * a_{si} \quad (1.36)$$

$$K_{rv} = 4 * \pi * D_v * \rho_{ov} * a_{si} \quad (1.37)$$

where ρ_{oi} and ρ_{ov} are the surface site density, or the atomic density to the 2/3 power.

Note that these reactions may either inject or remove point defects.

The other point-defect annihilation mechanism is IV recombination in which an interstitial and vacancy recombine to recreate a lattice atom. This occurs at the rate:

$$\frac{dInt}{dt} = K_{rIV} * (Int * Vac - C_{Istar} * C_{Vstar}) = \frac{dVac}{dt} \quad (1.38)$$

where k_{riv} is expressed as:

$$k_{riv} = 4 * \pi * (D_i + D_v) * a_{si} * C_{silicon} \quad (1.39)$$

IV recombination is a much faster process than surface annihilation. In general, a majority of the implantation induced point defects will be destroyed by recombining with their opposite defect. Vacancies, which have a higher diffusivity than an interstitial, are more prone to recombine at the surface. This can have some effect on the final damage profile following IV recombination for deeper implants as fewer vacancies are available to recombine with the interstitials at a given location.

If it is assumed that a majority of the implant-induced point-defects recombine via an IV recombination process, it is possible to approximate the final damage profile as an interstitial profile approximately equal to the implanted profile. This is because the implanted ions will displace a silicon atom from a lattice site as they move to substitutional positions. This approximation is frequently used in TCAD simulations of ion implantations and is referred to as the “Plus one” model. In certain experiments, the residual damage profile is treated as a non-unity scalar of the implant profile. In these cases, this is referred to as the “Plus X” approximation where ‘X’ refers to the scalar constant [Pel98].

1.7 Thermal Activation of Dopants

Immediately following ion implantation very few of the implanted dopants are electrically active, or able to contribute to the movement of charge within the crystal. Following implantation, most of the implanted ions are electrically worthless. In order for these dopant atoms to contribute to conduction within the crystal, they must generally occupy substitutional sites within the lattice. This process requires some amount of thermal energy. For this reason, there is generally an annealing step at some point following an ion-implantation step.

This anneal typically takes place in a furnace, in a rapid thermal process, or as part of another process. It is generally the case that you want as little movement, or diffusion, of the dopants as possible. For this reason, the thermal budget, or allowed thermal energy which is provided to the wafer is very low and precisely controlled.

Once the dopants occupy substitutional sites, they may become ionized at which point they will release a carrier to contribute to the conduction within the crystal. This is

also a thermal process, however, the ambient thermal energy at room temperature is sufficient to ionize most common dopants used in silicon CMOS technology. It is interesting to note, however, that at higher temperatures silicon devices will fail. This is due to both the higher concentrations of holes and electrons at higher temperatures as well as due to fact other deeper level impurities will begin to be ionized. The energy required to ionize a dopant atom is referred to as an ionization potential and has been computed for most common dopants and contaminants.

1.8 Transient Diffusion Phenomena

By examining the mechanisms through which boron diffuses [Sto97], all of which involve interstitials, it is easy to see that boron diffusion might be enhanced by excess point-defects from an implantation process. This is the case. For a given dopant which is assumed to diffuse via both vacancy and interstitial or interstitialcy mechanisms, it is possible to express the equilibrium diffusion as:

$$D = f_i \cdot D_i + f_v \cdot D_v \quad (1.40)$$

where f_i and f_v are the fraction of total diffusivity which is due to the interstitial or interstitialcy and the fraction due to the vacancy mechanism. D_i and D_v are the diffusivities of these mechanisms and may be concentration dependent with respect to the dopant specie. Under non-equilibrium, this diffusivity may be expressed as:

$$D = f_i \cdot (C_i/C_{i\text{star}}) \cdot D_i + f_v \cdot (C_v/C_{v\text{star}}) \cdot D_v \quad (1.41)$$

In these equations, the quantities $C_i/C_{i\text{star}}$ and $C_v/C_{v\text{star}}$ are referred to as the interstitial and vacancy supersaturations. This non-equilibrium diffusion will last so long as the point-defect supersaturation is maintained.

Dopants with fractional interstitialcies of close to unity, such as boron, will exhibit transient enhanced diffusion or TED in the presence of implant damage. The magnitude of this diffusivity enhancement, D/D^* , is often very large. In fact, for modern CMOS processes, the depth of the dopant profile in the source/drain region is more a function of the transient diffusion parameters than that of the implantation parameters. In other words, CMOS technology has progressed to the point where the diffusion length for the impurity atoms far exceeds the projected range of the implant in the source/drain regions of the device. Figure 1-15 shows a boron implant which exhibits strong transient diffusion behavior.

Transient enhanced diffusion is most severe at lower temperatures [Cow90]. The primary reasons this is true are because the recombination reactions which annihilate point-defects are stronger at high temperatures which will minimize the period of time during which transient diffusion may occur and the fact that at higher temperatures the value D^* is higher which will lower the D/D^* ratio.

1.8.1 Extended Defects from Ion Implantation Damage

At high concentrations of point-defects it is energetically favorable for the point-defects to form extended defects [Ben97]. These extended defects may take the form of rod-like defects, dot-type defects, submicroscopic defects, dislocation loops, etc.. These defects have been extensively studied and characterized within silicon.

Recently, work at Bell labs has shown that rod-type defects which form in the $\{311\}$ planes dissolve with a time constant approximately equivalent to the time constant of TED. These $\{311\}$ defects may be imaged using plan view TEM. Theoretical calculations determined the structure of the loop which forms the $\{311\}$ defect and from

this, the number of trapped interstitials per unit length may be determined to be approximately 26 interstitials per nm of length of defect. In this manner, the areal density of interstitials trapped in {311} defects may be determined from PTEM micrographs. This was done for a variety of silicon self implants and anneals over a range of temperatures and times. From these studies, the binding energy of the {311} defect was determined to be approximately 3.7eV.

Recent work has also suggested that other defects may play a role in storing the interstitials for TED. Work by Saleh et al. Has shown that the time constant to {311} dissolution is not necessarily consistent with TED at all implant energies. Rather, it is likely that other submicroscopic defects also contribute to the TED. As will be discussed shortly, enhanced diffusion may occur without extended defects entirely.

1.8.2 Uphill Diffusion and Surface Dose Loss

The diffusion of interstitialcy diffusers such as boron can also be driven by a gradient in the defect concentration and not just a gradient in the boron concentration.

$$J_{\text{boron}} = D_{\text{Bi}} * K_{\text{Bif}} * (\text{Int} * \text{grad}(C_{\text{boron}}) + C_{\text{boron}} * \text{grad}(\text{Int})) \quad (1.42)$$

The silicon surface acts as a very strong sink for excess point defects to recombine through the Schottky process. This can potentially lead to large point-defect gradients towards the surface which may mediate a phenomena known as uphill diffusion in which the impurity diffuses to regions of greater concentration due to the defect gradient. It is also very possible that this may lead to a pile-up of dopants at a surface or interface. Reactions of this type may potentially lead to a large flux of dopant to the surface, and possibly some dose loss to an interface dopant spike [Vuo99].

1.8.3 Transient Enhanced Diffusion as a Function of Implant Energy

For a given implant which produces damage approximately given by the “Plus X” model, the majority of this damage will be removed via recombination at the surface [Cow00]. The flux to the surface will be approximately $D_I \cdot I_e / R_p$ where R_p is the projected range of the implant and I_e is the quasi equilibrium interstitial population given by a reaction of form

$$D_{311} \cdot I_{nt} \cdot K_f = D_{311} \cdot K_r \quad (1.43)$$

or

$$I_e \sim K_r / K_f \quad (1.44)$$

Therefore, the time required to remove the excess point-defects is approximately proportional to the energy of the implant for non-amorphizing implants well below the critical energy. If we assume that any other reactions may be neglected the time required to quench the diffusion transient is approximately:

$$\tau = \frac{4\pi\alpha_{si} R_p \cdot \text{Dose}}{D_o \cdot N_{\text{silicon}}} \exp\left(\frac{E_m + E_b}{KT}\right) \quad (1.45)$$

In fact, this is exactly what does occur. Liu, et al have shown through a series of silicon implants into a MBE grown structure that transient enhanced diffusion is enhanced by deeper implants [Liu96]. Studies by Packan have also verified that point-defect profiles with greater separation from the surface will result in greater diffusion enhancements [Pac91]. In Packan’s experiment, a boron implant was subjected to a silicon implant at differing energy. The higher energy silicon implant resulted in greater diffusion of the boron spike.

1.8.4 Transient Enhanced Diffusion as a Function of Implanted Dose

Generally, increasing the dose of an implant will increase the damage density and provide more point-defects for driving the transient diffusion behavior. At low damage densities, the point-defects will not form extended defects and the transient diffusion behavior will be relatively short-lived. However, at higher damage densities, the point-defects will find it more energetically favorable to form extended defects such as $\{311\}$'s and dislocation loops. Both of these types of defects may drive enhanced diffusion. Because of this, in general, for higher dose implants, you'd expect the diffusion transient to be longer lived.

Again, Liu has studied TED as a function of implanted dose as well as study the extended defects which form as a result of boron implantation. Her results were in general agreement with this theory. It is important to note that we have not yet accounted for any clustering behaviors which will slow the diffusion at higher implanted doses. From her work, the diffusion length appears to saturate as the implanted dose in increased; this is due to this boron clustering which will be discussed in a future section. Packan has also investigated this with a similar experiment where he performed a silicon self-implant into a structure containing a boron-doped region. Packan noted additional diffusion of the boron layer with increasing dose of the silicon implant. It is important to note that Packan's boron concentration is well below the clustering threshold.

1.8.5 Transient Enhanced Diffusion as a Function of Temperature

The transient diffusion is driven by point-defects and the release of point-defects from extended defects. The diffusion transient should last so long as there are extended defects remaining in the crystal. Therefore, the diffusion transient should be shorter at

higher temperatures. Further, the intrinsic diffusivity increases with temperature, therefore, one would expect the magnitude of the diffusivity enhancements to decrease with increasing temperature.

This was investigated experimentally by Liu. She found that higher temperatures do lead to lower diffusivity enhancements and these enhancements are shorter lived than for lower temperature anneals.

1.8.6 Transient Diffusion in Absence of Extended Defects: Boron Enhanced Diffusion

As previously discussed, work has shown that transient enhanced diffusion is generally decreased for lower implant energies. Recently, however, it has been found that for very high dose and low energy implants transient diffusion exists which is not mediated by extended defects. This effect has been termed boron enhanced diffusion, BED. There are two major theories on the origin of this phenomena: one is that this effect is normal charge-dependent diffusion which is enhanced because of the high concentration of acceptor dopants, and the other is that the boron reacts at higher concentrations to form a phase or a boron-vacancy cluster which injects interstitials in this region driving the diffusion transient.

1.8.7 Minimization of Transient Enhanced Diffusion by Thermal Cycle Engineering

Much work has been focused upon the minimization of the transient diffusion of dopants by tailoring the thermal cycle to rapidly eliminate the point-defects and extended defects or to activate the dopants without eliminating the extended defects [Cow00, Ler99, Osb96, Sch99]. By eliminating the point-defects before TED can occur or reach it's full potential, it is possible to minimize the enhanced diffusivity. By eliminating the extended defects, you have a means of controlling the duration of the diffusion

enhancement. By activating the dopants without eliminating the extended defects, it is possible to also limit the duration of the diffusion transient.

One popular means of limiting the amount of transient diffusion is the use of spike anneals in a rapid thermal process, or RTP. In this system a series of lamps are used to heat the wafer in a very rapid fashion. The duration of this anneal is typically very brief and the wafer is essentially brought to temperature and immediately cooled off via a radiative cooling method where the thermal energy is dissipated to the surrounding air. This method can activate the dopant without allowing the extended defects to form. These anneals are typically at very high temperatures so the diffusion enhancement is lower. The radiative cooling process provides a lower bound to the net thermal budget from this type of anneal. While the wafer may be heated at several hundred degrees per second, it can only be cooled at a maximum rate of 70 degrees celcius per second. It is often the case where the ramp-down of the thermal spike determines the amount of enhanced diffusion.

Means of utilizing laser energy to activate dopants have been investigated. Laser processing has advantages in that the laser energy has a fixed penetration depth and only heats a small fraction of the wafer while the RTP process heats the full wafer. The laser annealed wafer is then radiatively cooled, although, this occurs as a much faster rate than for RTP processed material since the volume of material heated is much less than for the RTP treated case. This is a relatively new technology and it remains to be seen whether this will become part of the CMOS fabrication process. Many drawbacks must still be addressed such as the uniformity of the laser, and integration within existing process without additional lithography steps.

1.9 Transient Clustering Processes

Many researchers have observed that boron at high concentrations in the presence of silicon interstitials is fairly immobile and not fully electrically active [Cow94, Wan00]. Recent research has also shown that {311} defects dissolve at a higher rate in heavily-doped boron environments. This has led engineers to speculate that boron is clustering with the interstitials from the implant damage to form stable complexes. Since this time, Ab-Initio calculations have supported this hypothesis. An example of a boron implant exhibiting strong clustering at high concentrations is shown in Figure 1-16.

A group at Lawrence Livermore National Laboratories has calculated the binding energies of different boron cluster complexes [Len00, Zhu97]. This group of cluster complexes is based upon the premise that a substitutional boron atom may capture either an interstitial, vacancy or boron interstitialcy. The reactions generally are diffusion limited in terms of formation, that is to say that there is no energetic barrier to their formation aside from the migrational energy of the diffusive specie. Similar calculations have been performed by other groups [Lus98, Liu00, Ras98]

$$K_{\text{forward}} = 4 * \pi * D * \text{radius}_{\text{capture}} \quad (1.46)$$

The dissolution of these clusters is determined by the binding energy of the cluster. For this system, the B3I complex was found to be the most energetically favorable.

$$K_{\text{release}} = C_{\text{Si}} * D * 4 * \pi * a_{\text{Si}} * \exp\left(\frac{-E_b}{kT}\right) \quad (1.47)$$

where E_b is the energy required to break up a cluster. The following table illustrates the relative energies of these clusters in differing charge states.

From this table, it can be seen that the boron only clusters are unbound. When this table is plotted and the binding energies are illustrated, as shown in Figure 1-17, it can be

seen that the B₃I cluster is unusually stable. For this reason, it is used as the jump point to larger clusters in many simulation methodologies.

Table 1-1 Relative energies of differing boron/interstitial clusters. Energies are computed through the local density approximation relative to isolated substitutional boron and doubly charged tetrahedral configuration interstitials. Energy of most stable configuration is in bold for each case.

	+1	0	-1	-2	-3
B _{sub}		0			
B ₂		1.38	.96	.93	
B ₃		1.54	1.03	.89	1.14
BI	-1.02	-.79			
B ₂ I	-1.43	-2.12	-1.60		
B ₃ I	-1.95	-2.72	-3.09		
B ₄ I	-1.00	-1.85	-2.32	-2.40	
BI ₂	-2.35	-2.24	-1.89		
B ₂ I ₂	-3.22	-3.24	-2.79		
B ₃ I ₂	-3.87	-4.41	-3.57		
B ₄ I ₂	-4.20	-4.80	-4.73		

Work performed at Lawrence Livermore National Laboratories has indicated that some of these boron complexes are fractionally active. This is important, because it has implications for the net activation which may be achieved within the substrate and also will determine the rate at which the boron is deactivated and the rate at which it may be reactivated. Previous work has hypothesized that the B₃I and B₄I clusters are the dominant residual species following high-dose implantation and annealing at relatively low temperatures. The B₃I and B₄I clusters are believed to have fractional activities of

33% and 50% respectively; thus, one hole from the B3I cluster contributes to electrical conduction and two do so for the B4I cluster. It is then possible to obtain the rate prefactor to deactivation as:

$$K_{\text{deactivation}} = (1 - f_{\text{active}}) * 4 * \pi * \alpha_{\text{cluster}} * D_{\text{capture}} \quad (1.48)$$

and the rate prefactor to reactivation as:

$$k_{\text{reactivation}} = (1 - f_{\text{active}}) * 4 * \pi * \alpha_{\text{cluster}} * D_{\text{release}} * \exp\left(\frac{-E_{\text{binding}}}{kT}\right) \quad (1.49)$$

$$\text{Rate}_{\text{reactivation}} = \sum_{\text{clusters}} (C_{\text{cluster}} * (1 - f_{\text{active}}) * 4 * \pi * \alpha_{\text{cluster}} * D_{\text{release}} * \exp\left(\frac{-\min(\sum E_{\text{binding}})}{kT}\right)) \quad (1.50)$$

From this, it can be seen that a thorough physical understanding of the clustering physics is necessary in order to accurately model these phenomena. This must account for the actual clustering pathways, barriers and recombination pathways experienced within the material.

1.10 Influence of Impurities upon Boron Transient Processes

Typical substrate material is formed by either a Czochralski or a Float-zone process. Contamination from elements such as carbon and oxygen varies greatly between these processes and to a lesser degree with wafer batch. These contaminants are known to affect the diffusion transient of boron, and recently have been shown to affect the activation transient [Nap99]. This must be considered when comparisons are made in terms of absolute quantities between experiments which were conducted on different substrate materials. For instance, it may not be justifiable to compare the activation or diffusion results from a highly contaminated MBE grown sample to those obtained from

a high purity epi layer. Research with other impurities and dopants is also being pursued [Hua97, Li00].

1.11 Prior Boron Clustering/Activation/Diffusion Experimental Work

To date, a great deal of experimental work has been done investigating the processes and mechanisms of boron transient processes. These may generally be classified into one of several types of experiments.

1.11.1 MBE DSL Experiments

A group at Lucent Technologies, now Agere Semiconductor, has extensively studied the transient diffusion and clustering phenomena exhibited by a doped superlattice, DSL, structure grown by molecular beam epitaxy. This DSL structure was then subjected to a silicon self implant and various anneals. The transient diffusion phenomena were measured with SIMS as shown in Figure 1-18 and the degree to which the various spikes were clustered were extracted by fitting gaussians to the immobile portion of each peak. The chief advantage to this approach is that it allows for the determination of the depth dependence to the transient phenomena along with the very sharply delineated doping spikes which MBE produces which are not generally producible by an implant process. Some of the disadvantages to this experiment are due to the uncertainties regarding the level of contaminants in MBE grown material. Experiment has shown that this material exhibits transient enhanced diffusion in an as-grown state and it is difficult to extract the contributions due to these different sources.

1.11.2 TEM Defect Count Experiments

Several previous studies have correlated the results of TEM pictures to the observed transient behaviors. Liu correlated the $\{311\}$ defect to transient enhanced diffusion over a range of implant energies, doses and anneals.

Another interesting experiment was performed by Haynes, et al. In this experiment a fairly uniform highly boron-doped region was implanted with silicon and annealed. Haynes observed that the more heavily doped the region, the fewer residual $\{311\}$ defects. This experiment has been repeated and modified as part of this work. Similar results have been obtained for the case of phosphorus and arsenic, although the $\{311\}$ suppression is weaker in these cases.

1.11.3 SIMS Experiments

The classical means of studying transient enhanced diffusion is to perform an implant and anneal sequence. The amount of diffusion and clustering may then be obtained from SIMS profiles. A large matrix of SIMS data from experiment such as this is available from Intel Corporation and prior experiments by other groups.

1.11.4 Activation Experiments SIMS vs. SRP

A series of partially deactivated boron implants were analyzed with both SIMS and SRP by Cowern, et al. By directly comparing the chemical and the electrical profiles, it is possible to determine the inactive boron profile. A similar method was utilized as part of this work in order to determine the kinetics of reactivation. An example of this is shown in Figure 1-19.

1.12 Statement of Thesis

This work has contributed to the following areas:

- First principles based calculations have been implemented into predictive process simulation models for transient diffusion and activation effects exhibited by boron in silicon.
- Correlation has been demonstrated between kinetic monte carlo and continuum modeling approaches.
- $\{311\}$ defect formation has been studied in the presence of differing boron concentrations.
- Experimental investigation of boron activation as a function of implanted boron dose, implant energy and anneal temperature.
- Experimental determination of the energy to activation and determination of binding energy of BIC cluster which limits reactivation of boron.
- Experimental work provides some support for the idea of fractionally active boron complexes.
- Modeling work indicates that the substitutional boron profile provides a reasonable depiction of the carrier profile for many instances.

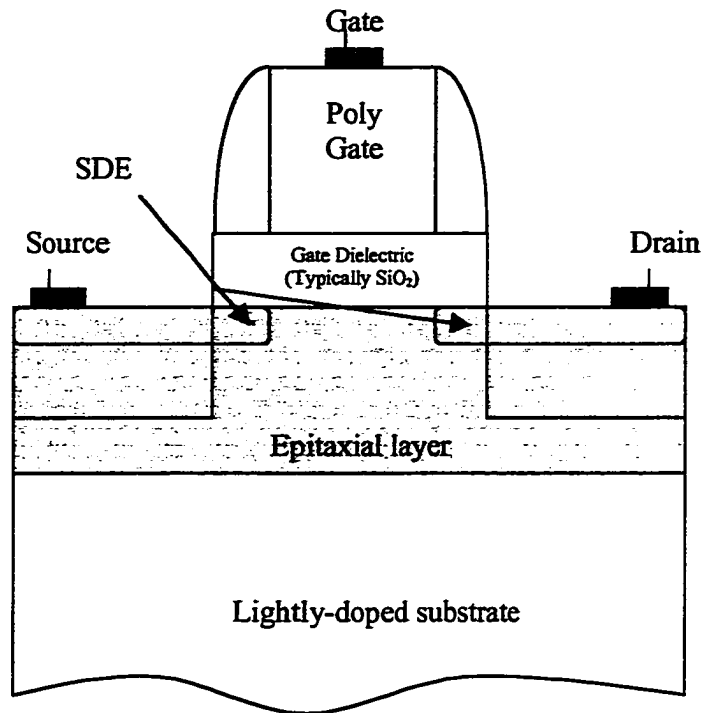


Figure 1-1 Schematic of a MOS transistor.

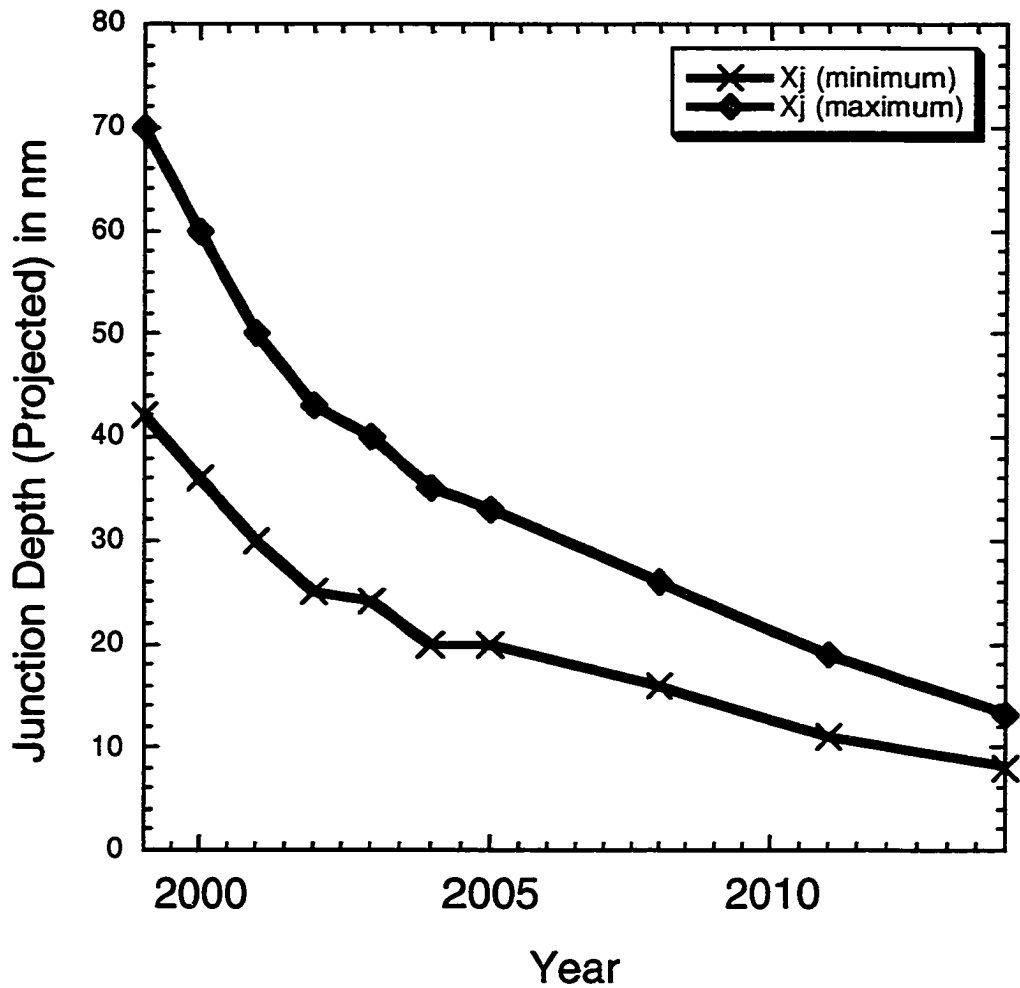


Figure 1-2 Projected scaling of the junction depth until the year 2014. The two lines reflect the maximum allowed value and minimal anticipated value. Future technologies will require much shallower SDE regions.

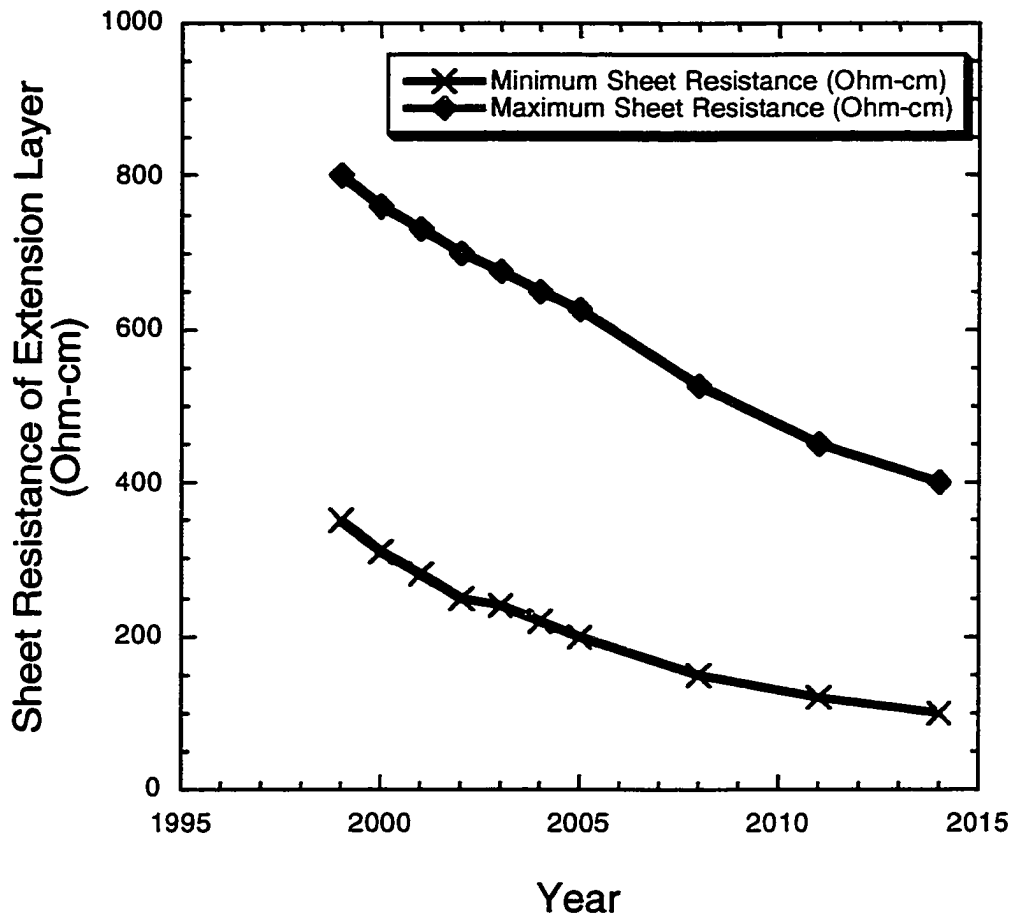


Figure 1-3 Projected sheet resistance of the extension region. Future technologies will require more heavily-doped layers.

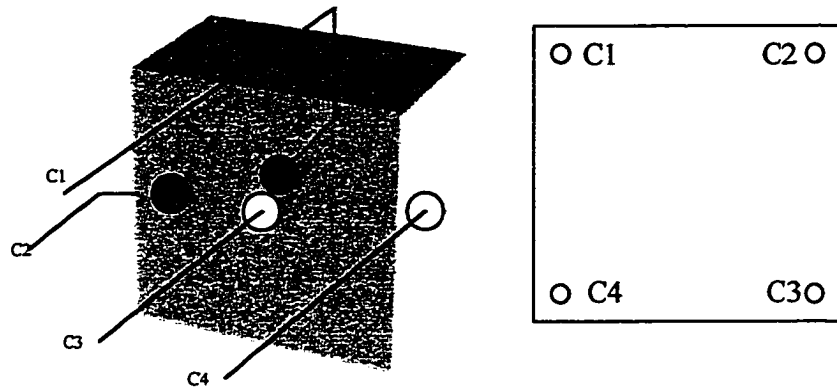


Figure 1-4 Illustration of a hall effect structure (left) and a Van der Pauw structure (right) which is applicable to measurements on a geometry essentially 2-D in nature such as a silicon wafer. Van der Pauw structures used in this work were 14.4 mm square.

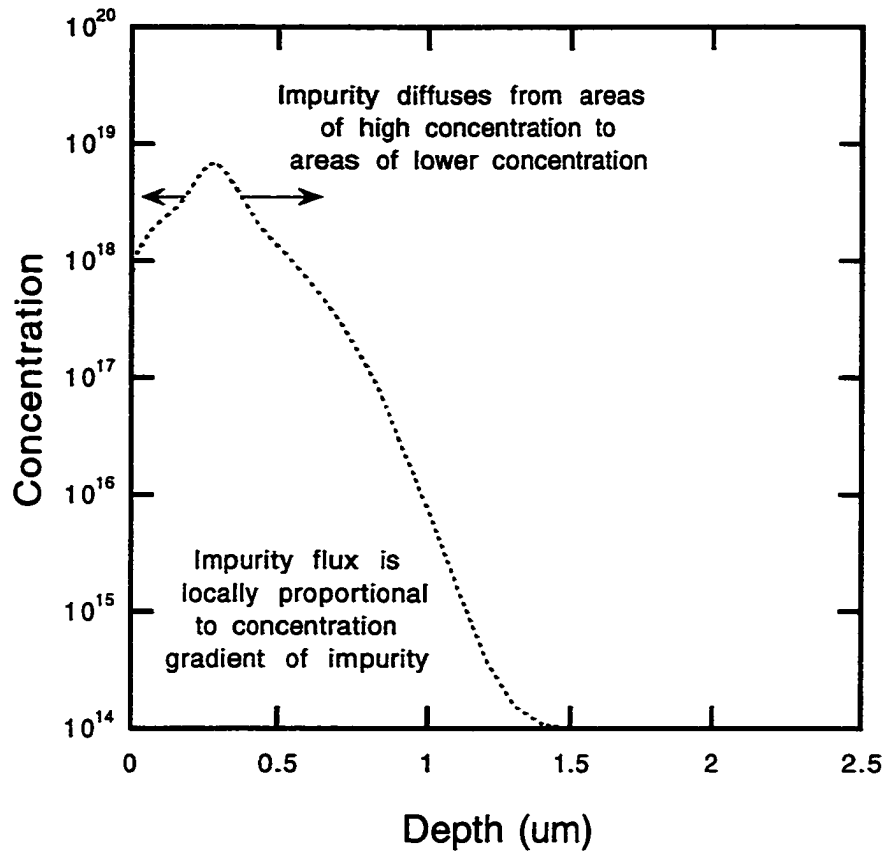


Figure 1-5 Illustration of Fick's first law governing the diffusion of particles. Particles will diffuse from areas of higher concentration to areas of lower concentration at a rate which is locally proportional to the dopant gradient.

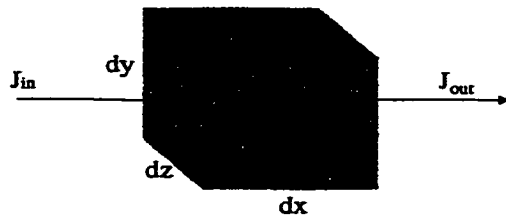


Figure 1-6 Illustration of Fick's second law. Particles are conserved such that for a differential element (dx, dy, dz) the divergence in flux is equivalent to the rate of concentration change for the element.

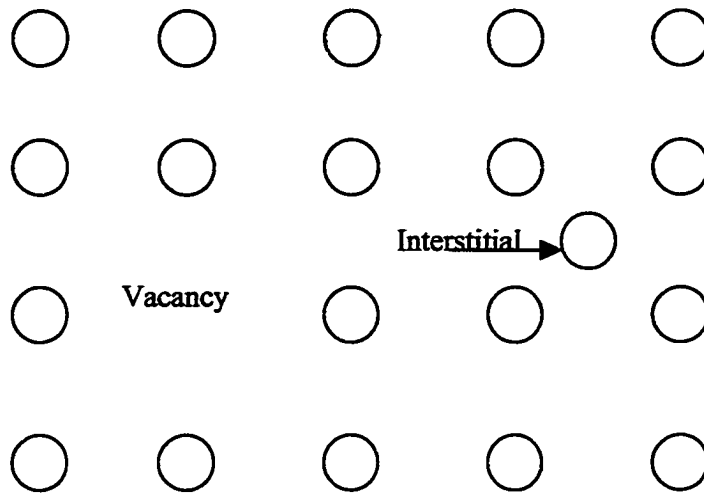


Figure 1-7 Two basic point defects: interstitials and vacancies.

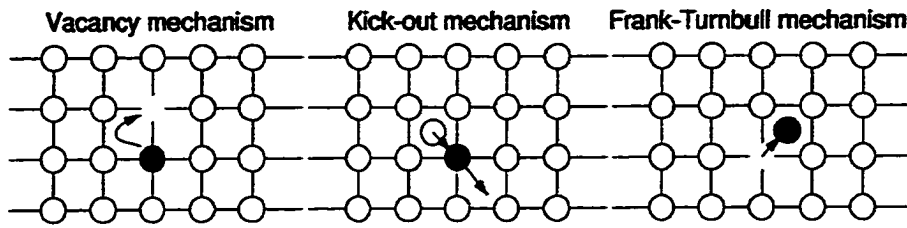


Figure 1-8 Point-defect mediated diffusion mechanisms. (a) Vacancy mechanisms involve dopant atoms interchanging spaces with lattice vacancies. (b) Kick-out mechanisms (and interstitialcy mechanisms) involve self-interstitials displacing dopant atoms from lattice which are then free to diffuse through the crystal either as a free dopant or as an interstitialcy. (c) Frank-Turnbull mechanism involves dopant atoms moving to interstitial sites and diffusing within the interstices of the lattice.

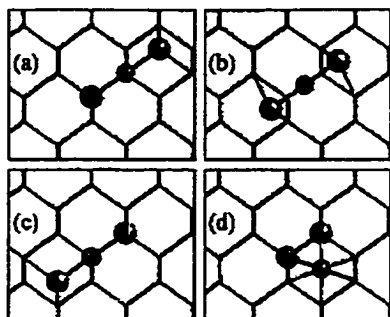


Figure 1-9 Coordinated push mechanism. Boron is animated as the smaller ball while silicon is animated as the larger ball.

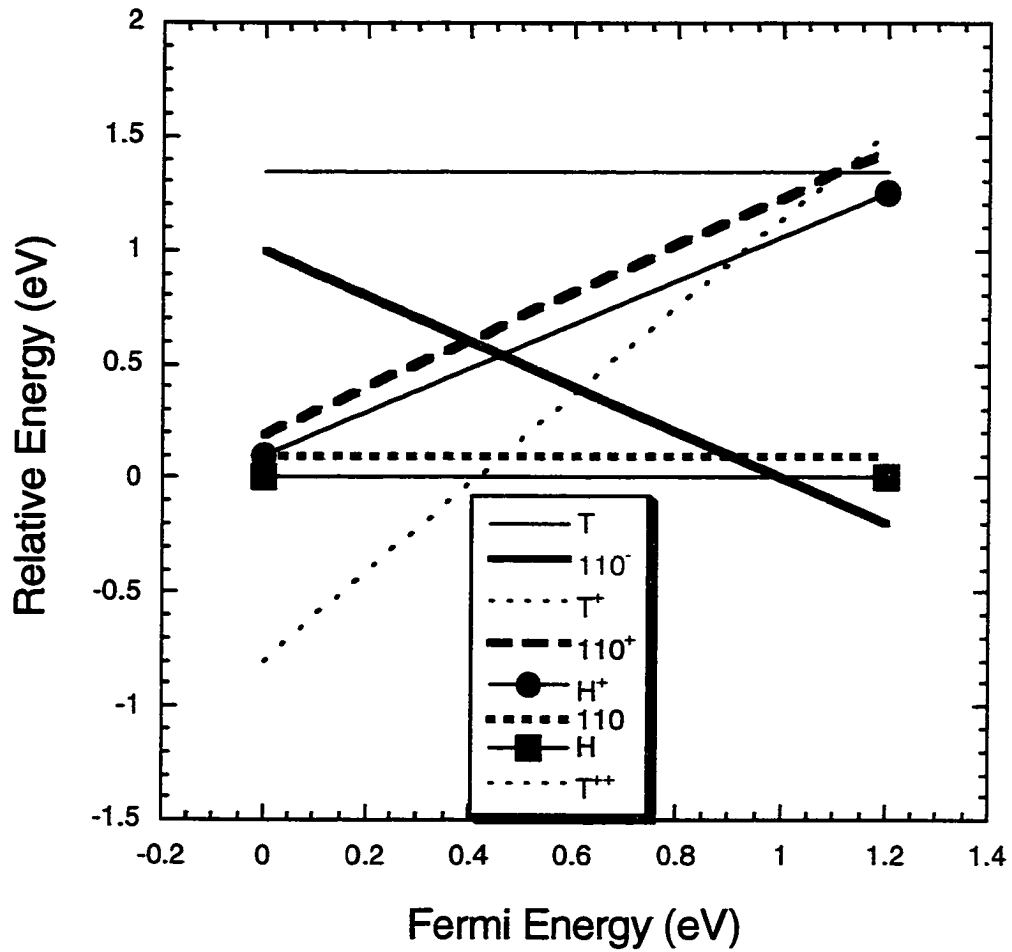


Figure 1-10 Relative energies of differently configured interstitials. Plots such as these are useful in determining the net charge state of the interstitials at a given fermi-level. This, in turn, determines the net diffusivity of the interstitials.

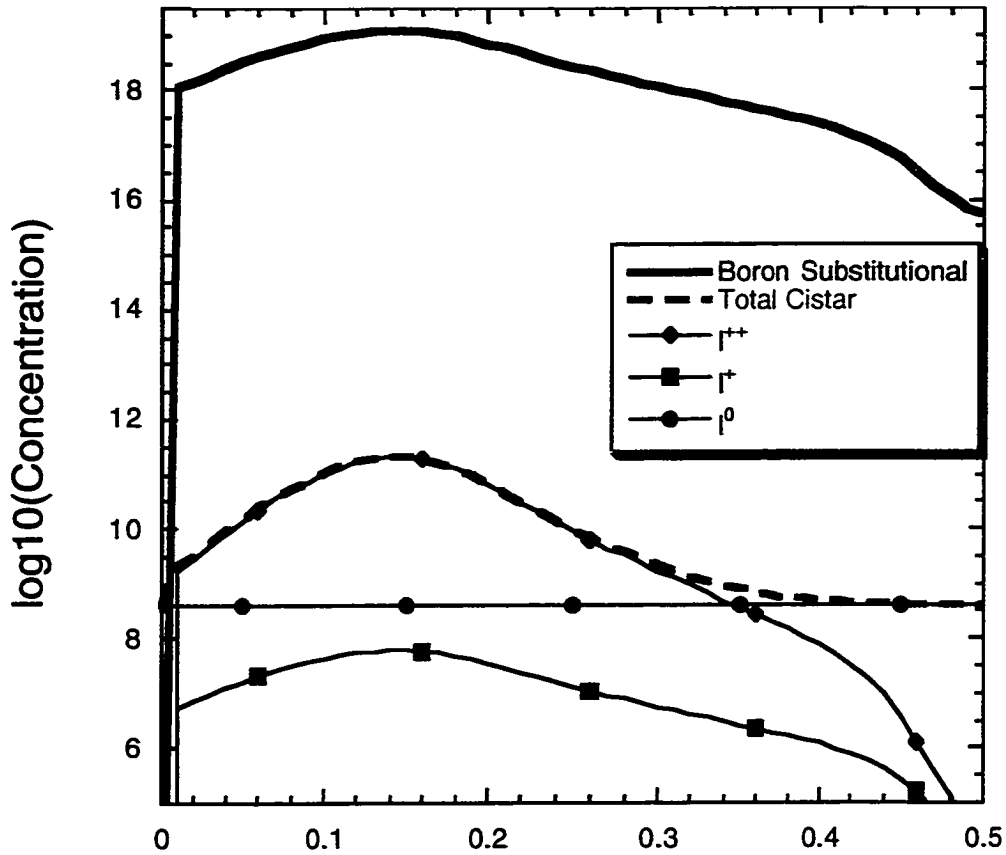


Figure 1-11 Intrinsic interstitial density (cm^{-3}) as a function of boron doping level. Under slight interstitial saturations, such effects must be accounted for in simulations. Shown are the components to the interstitial profile as determined from energetics of Figure 1-10. Note here that the majority of interstitials in the peak region are doubly charged (T^{++} configuration) which is the lowest energy configuration at energies near the valence band edge.

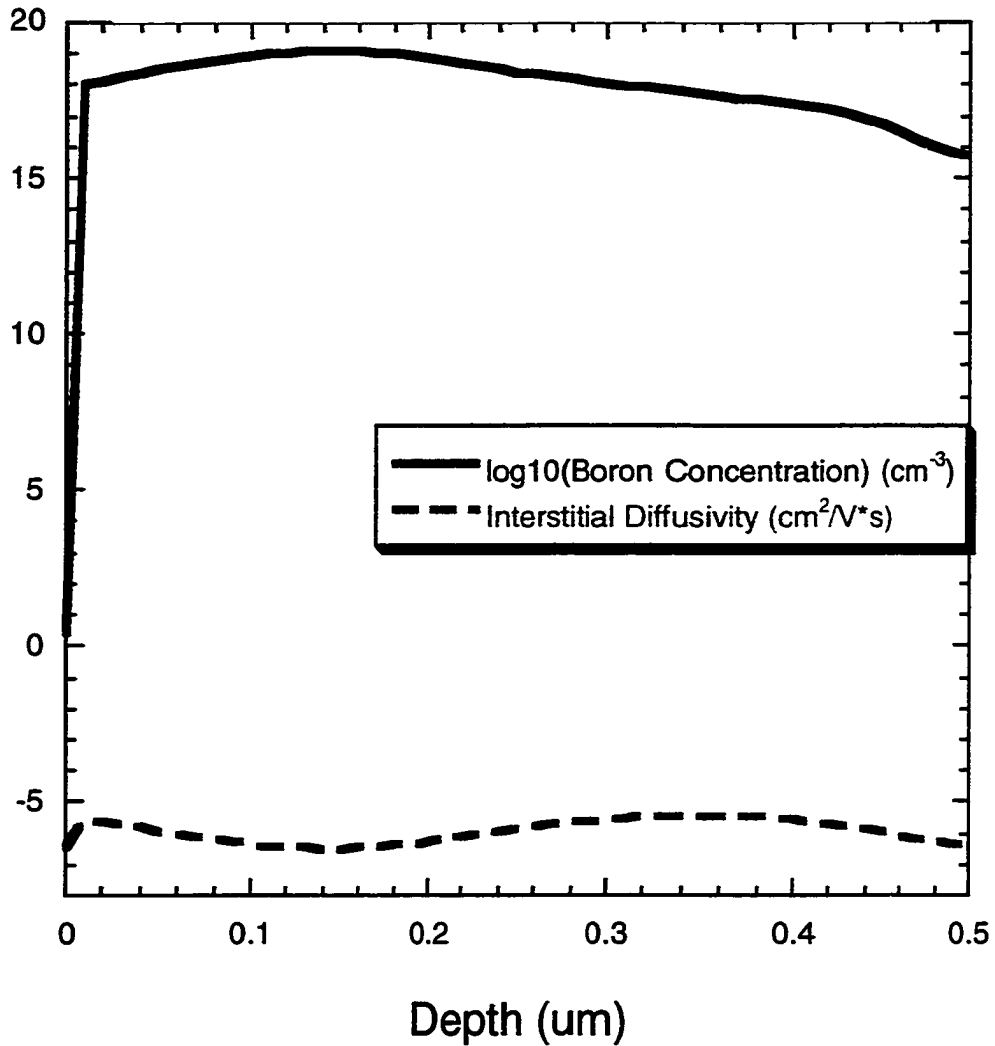


Figure 1-12 Interstitial diffusivity as a function of boron concentration. Intrinsic diffusivity is enhanced throughout a majority of the region of the boron implant by a small factor due to differences in the migrational energies of the interstitial configurations.

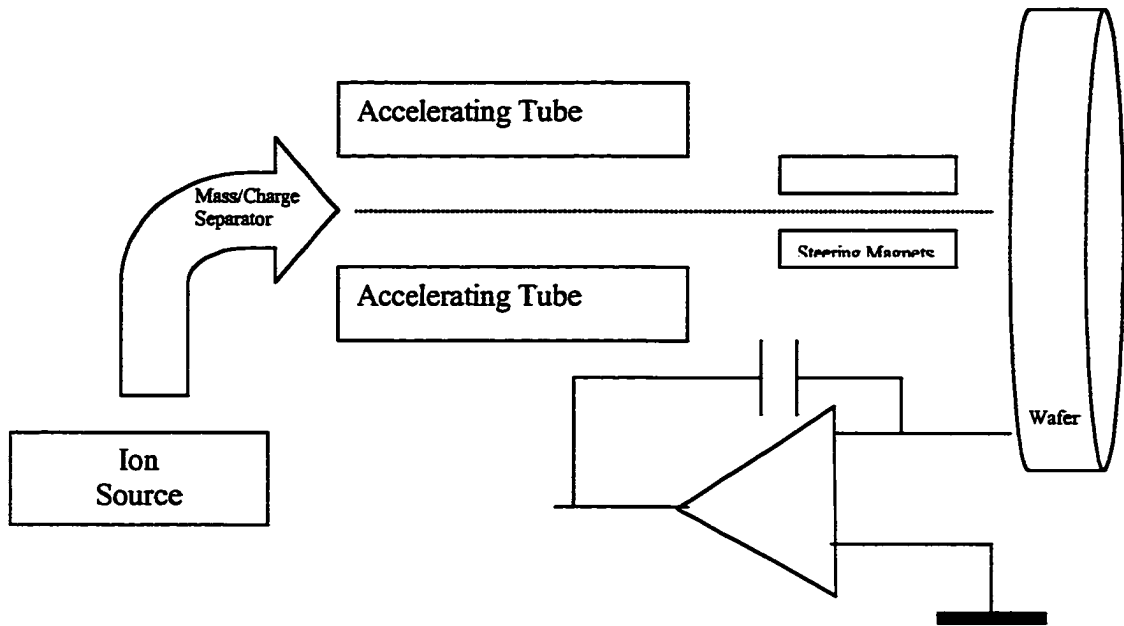


Figure 1-13 Simplified schematic of an ion implanter. Shown are the ion source, mass/charge separator, accelerating tube, steering magnets, integrator circuit and wafer in process.

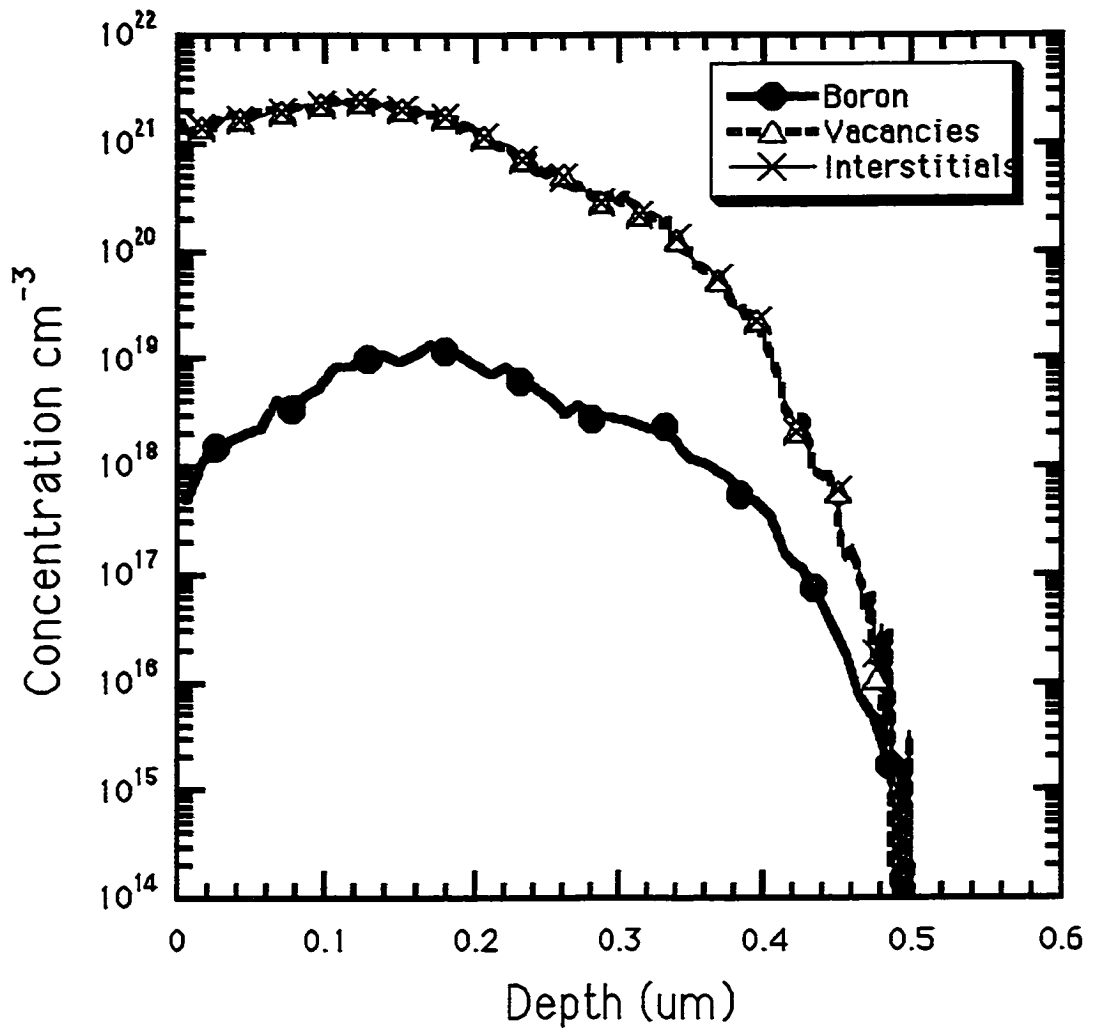


Figure 1-14 Residual damage arising from a 40 keV $2 \times 10^{14} \text{ cm}^{-2}$ boron implant as determined by UT-Marlowe. Note that the interstitial and vacancy profiles are nearly equivalent following implant, and that both the interstitial and vacancy concentrations far exceed the boron concentration.

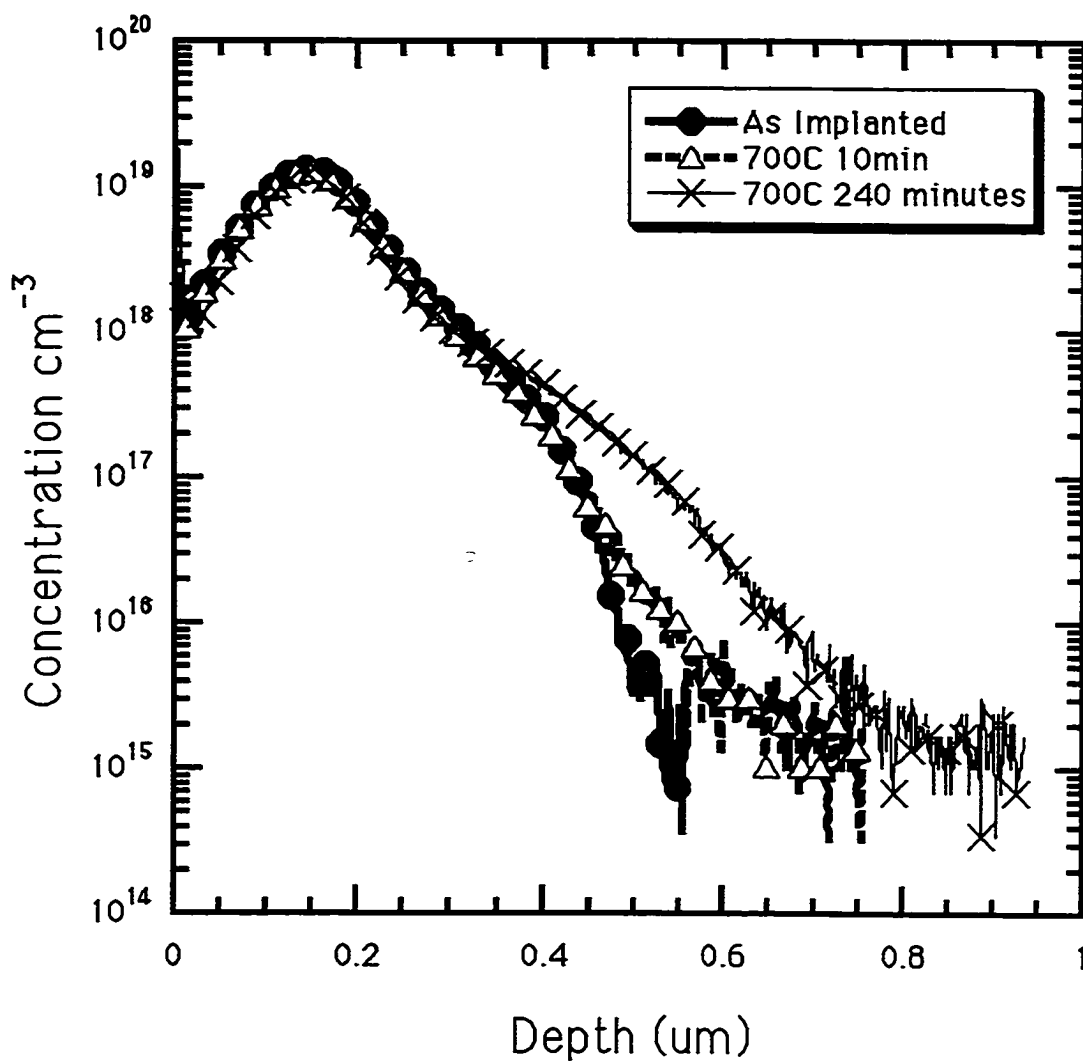


Figure 1-15 40 keV $2 \times 10^{14} \text{ cm}^{-2}$ boron implant annealed at 700°C following implant. Intrinsic diffusion at this temperature is negligible in comparison to the transient effects shown here.

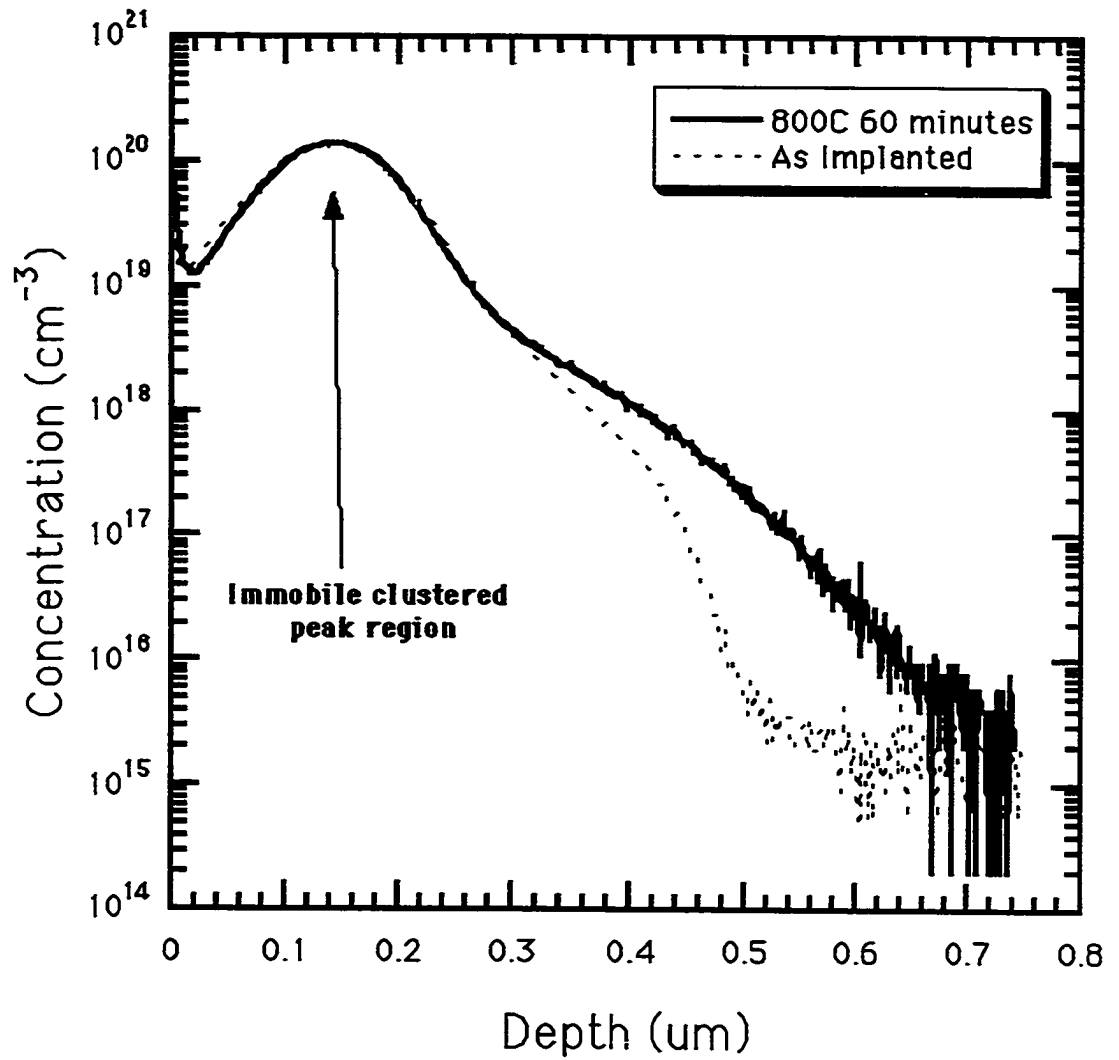


Figure 1-16 A $20 \text{ keV } 2 \times 10^{15} \text{ cm}^{-2}$ boron implant subjected to a 800°C 60 minute anneal. Note the formation of a highly immobile region in the peak of this implant. This is the region which is heavily clustered.

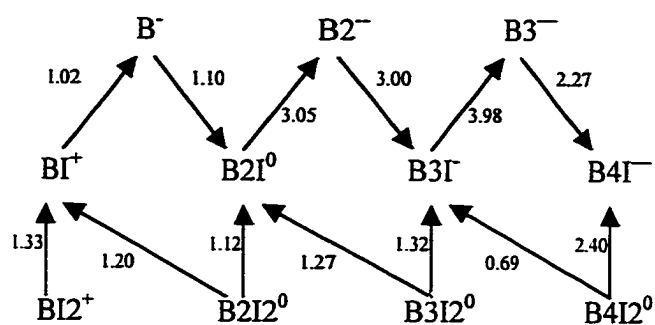


Figure 1-17 Binding energies and reactions in the boron cluster system. $B3I$ cluster is unusually stable. $B3$ and $B2$ clusters are unbound.

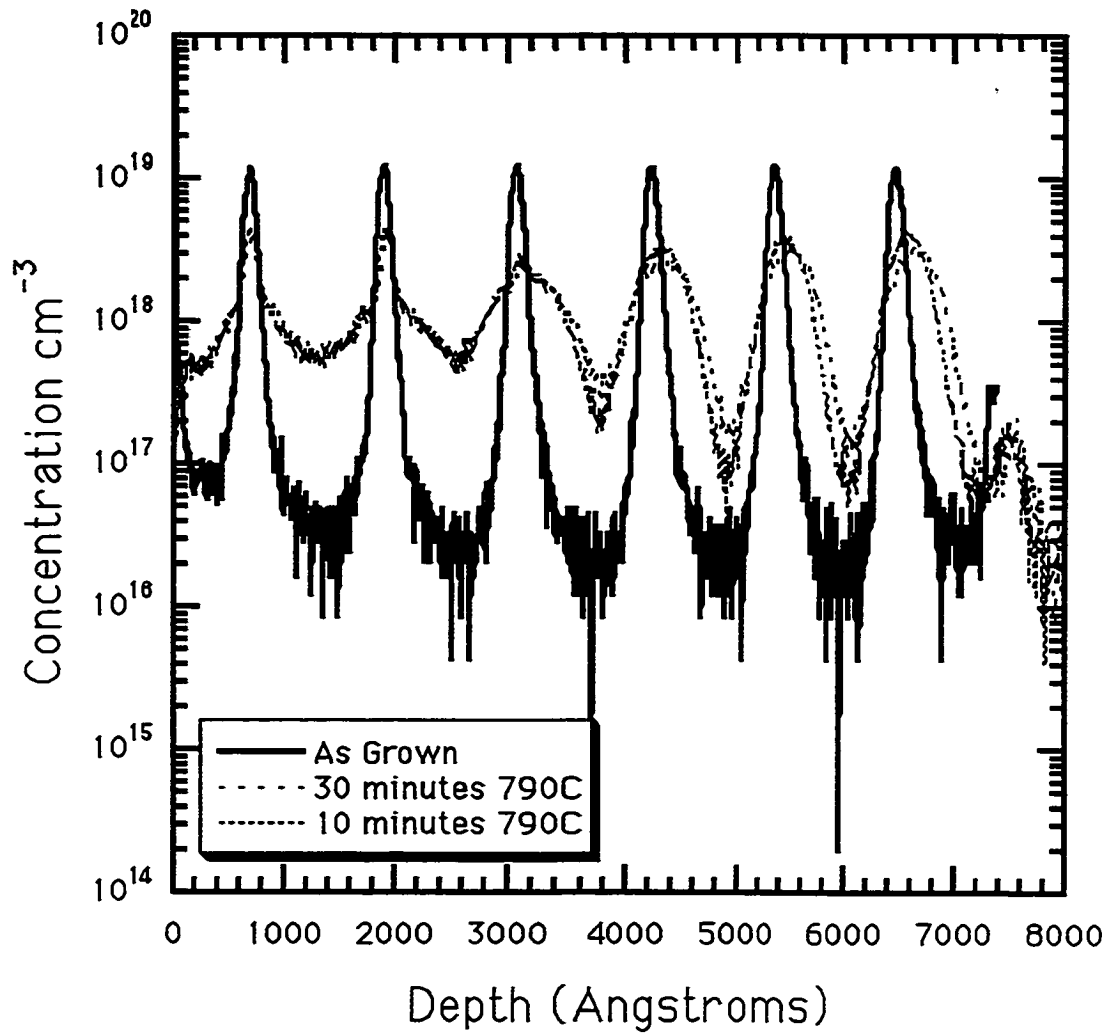


Figure 1-18 SIMS profiles of a doped super-lattice structure in the as-implanted form along with the profiles resulting following a 40 keV $5 \times 10^{13} \text{ cm}^{-2}$ silicon implant and anneals at 790°C for 10 minutes and 30 minutes. Note the strongly clustered peak regions of the first few spikes and the simultaneous transient diffusion exhibited at lower concentrations.

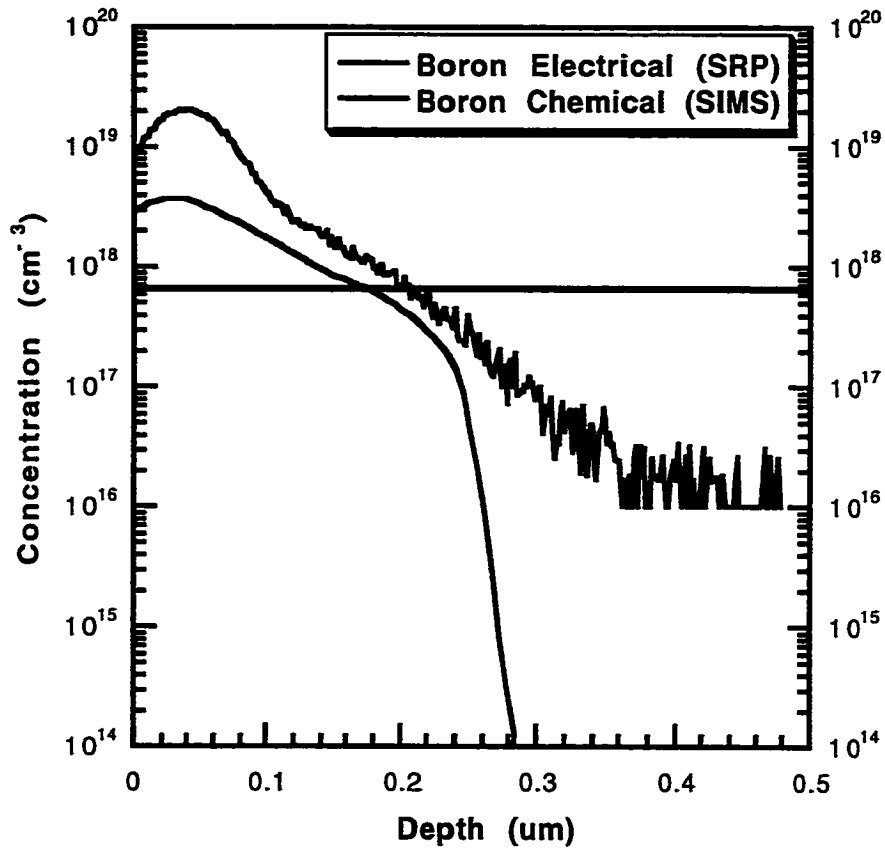


Figure 1-19 Comparison of electrical and chemical measurements of a 40 keV $2 \times 10^{14} \text{ cm}^{-2}$ boron implant annealed at 740°C for 40 minutes. Note that a significant fraction of boron in the peak region is deactivated.

CHAPTER 2 DEVELOPMENT OF PREDICTIVE MODELS

As part of this work a comprehensive physics-based model has been developed which is capable of accurately predicting several transient phenomena. This model is based upon the energetic calculations as performed by Lawrence Livermore National Laboratory as described in Chapter 1.

2.1 Modeling of Intrinsic Diffusion

In the development of this model the first case considered was that of intrinsic diffusion. Under these conditions, the concentration of interstitials deviates very slightly from the thermal equilibrium value and the boron concentration was assumed to be fairly low in order to minimize any charge effects which were not yet accounted for. Under these conditions, diffusion of the boron is accomplished via the boron pairing to an interstitial to form a boron interstitialcy by using the boron interstitial complex as an intermediary. This is accomplished with a rate prefactor of:

$$KB_{if} = 4 * \pi * a_{\text{silicon}} * C_{\text{silicon}} * \exp(-E_{Bi}^F / KT) * D_{Bi} \quad (2.1)$$

The amount of diffusion can be controlled by very small adjustments to the rate at which boron pairs with the interstitial to form the boron interstitialcy. The necessity of small adjustments such as these are not surprising as a very small variation in the energetics of the system could produce an identical effect. Energetic Calculations from Lawrence Livermore National Laboratories have also shown that the boron interstitialcy diffuses with a migrational energy of approximately .3 eV with a prefactor of roughly $1e-3$. The simplified system utilized for the simulation of intrinsic diffusion is shown in Figure 2-1. Verification

of the correct boron diffusion behavior under intrinsic conditions is necessary because it provides verification that the jump rate from the boron interstitial complex to the boron interstitialcy is approximately correct. It is necessary to accurately describe both the population and diffusivity of these boron interstitialcies since they present the only path to boron diffusion in our model and also account for subsequent boron clustering, as will be discussed.

Ideally, the diffusion under these circumstances will be equivalent to that as determined by experiment. The diffusion behavior exhibited by this model was verified by comparison to the default FLOOPS simulations of a boron implant subjected to various high temperature anneals. Results of this nature are shown in Figures 2-2 and 2-3.

2.2 Modeling of Interstitial System

The importance of the interstitials to the transient diffusion and clustering processes is understood. With the release of the interstitials from $\{311\}$ defects governing the diffusion process, the ability to accurately predict the dissolution of these clusters is of paramount importance. Further, at shorter times, the boron forms a competitive system for the available interstitials. Therefore, it is not accurate to simply apportion the interstitials to the $\{311\}$ defects as part of the initial conditions. Rather, it is necessary to account for the cluster nucleation in the presence of the boron.

Lawrence Livermore National Laboratories has calculated the binding energies of interstitial-type defects up to size of 300 interstitials which they solve for as part of their kinetic monte carlo diffusion simulations. Unfortunately, including this many equations in a continuum model would make the model prohibitively slow to compute. The compromise used in this work is that I2 and I3 cluster species are included to allow for nucleation of the

larger $\{311\}$ defect as shown in Figure 2-4. Simulation results using this model allow for the interstitials to be available to react with boron at short times to form either BIC's or SMIC's.

The dissolution of interstitials from $\{311\}$ defects has been experimentally investigated by several groups as shown in Chapter 1 of this work. Simulation of such results is the easiest way to validate the system. Small changes to the $\{311\}$ binding energy and the rate at which the surface sinks/injects interstitials and vacancies were the only calibrations performed upon the reactions involved in these processes. Simulation of the experimental results for the dissolution of $\{311\}$ defects, such as those obtained by Eaglesham, provide validation for this system. Figure 2-5 illustrates simulation results of the $\{311\}$ cluster dissolution as compared to the data of Eaglesham. Figure 2-6 shows the transient progression of the clusters in this system at 815°C . This figure shows that at very short times, the small interstitial clusters hold a majority of the interstitials. As time progresses the majority of the interstitials are contained in the $\{311\}$ defects which are highly thermally stable. Population profiles of the interstitial and interstitial clusters is shown in Figures 2-7 during the time period in which the SMIC clusters are predominant and in Figure 2-8 during which time the $\{311\}$ cluster contains the majority of the silicon interstitials.

2.3 Transient Enhanced Diffusion and Clustering

With the verification of the correct behavior under intrinsic diffusion conditions and also the verification of the correct $\{311\}$ dissolution behavior, simulation of the transient enhanced diffusion behavior were attempted. Under these conditions it was necessary to include the full system of boron clusters as shown in Figure 2-9. Under these conditions, the dominant residual cluster was found to be the B3I complex.

Intel has performed a series of transient enhanced diffusion experiments to which we have verified this model. Results of the diffusion at 700°C for 60 minutes of a $2 \times 10^{14} \text{ cm}^{-2}$

boron implant are shown in Figure 2-10 and for a 700°C anneal for 120 minutes in Figure 2-11. This model clusters sufficient boron in the peak region while simultaneously providing sufficient boron to match the diffusion in the tail. Results of this model were verified against a series of transient enhanced diffusion experiments resulting from boron implants in the 20 keV to 80 keV energy range with doses of $2 \times 10^{14} \text{ cm}^{-2}$ at temperatures of 700°C and 800°C with good results obtained across the dose/energy range. Generally, one is most interested in the final boron profile, however, it is also possible to solve for each of the individual boron clusters as shown in Figure 2-12, and the time progression of the boron clusters as shown in Figure 2-13. This time progression shows that the precursor clusters of B2I, BI2 and BI are formed and lead to the formation of the larger and more thermally stable B3I cluster. The B3I cluster continues to form at times of several hundred seconds as shown in Figure 2-13 at a temperature of 700°C.

Further analysis of these simulation results can lead to great insight into the transient diffusion process. Neglecting boron clustering, the interstitial super-saturation, as shown in Figure 2-14 is normally equal to the diffusion enhancement. It is interesting to note from this figure that the supersaturation extends a great distance into the bulk of the wafer and transient diffusion will also be exhibited there if there is no mechanism to trap the interstitials. It is also possible that this exodus of interstitials from the implanted region could also lead to lateral diffusion of the dopants, although only the 1-D case is presented here. If one accounts for the clustering of the boron, which will trap some of the boron interstitials providing a much lower net diffusivity, the instantaneous diffusion enhancement at any given time may be expressed by the following equation:

$$\frac{D_B}{D_B^*} = \frac{DBi}{D_B(\text{fickian})} * \frac{C_{Bi}}{C_{\text{Boron}}} \quad (2.2)$$

Using this simulation methodology it is also possible to simulate the duration of the transient diffusion phenomena and the instantaneous diffusion enhancement. By again approximating the diffusion enhancement by equation 2.2, the instantaneous diffusion enhancement exhibited by a 40 keV $2 \times 10^{14} \text{ cm}^{-2}$ boron implant was simulated as shown in figure 2-15 and 2-16 following anneals at 700°C . While $\{311\}$ defects are present, roughly to time of 20,000 seconds, the diffusion enhancement is largely mediated by the release of interstitials from the $\{311\}$ defects and this enhancement is very large. Following the dissolution of the $\{311\}$ defects, this diffusion enhancement is largely mediated by the release of interstitials from the BIC clusters, which is a much slower process than the release of interstitials from $\{311\}$ defects. Thus, for times greater than approximately 20,000 seconds, the instantaneous diffusion enhancement is much lower, however, it extends for times approaching 10^6 seconds as the BIC (B3I) clusters are dissolved.

2.4 Applications to Electrical Activation and Reverse Annealing

Boron, immediately following ion implantation, is largely electrically inactive. Recent work has also shown that certain boron interstitial clusters may also be fractionally electrically active. Therefore, it is possible to directly simulate the electrically active fraction of the boron profile. Under all instances, it is assumed that the substitutional boron is fully ionized, thereby contributing a single hole to the electrical conduction for each substitutional boron atom. If the substitutional boron is the only electrically active specie, the fractional activation as a function of depth may be obtained from these simulations as shown in Figure 2-18. Similar comparisons may also be made if it is assumed that certain boron interstitial complexes are also fractionally active.

Prior researchers have noted that ion implanted boron will exhibit a negative or near-zero differential activation in the temperature range of 500°C to 800°C [Bic70, Sei71]

followed by monotonically increasing activation above this temperature until full activation is achieved. This effect has been termed “reverse annealing” and has been attributed to the clustering of the boron deactivating the boron. This effect was simulated by performing a 1 hour anneal on a 40 keV $2 \times 10^{14} \text{ cm}^{-2}$ boron implant at temperatures of 400°C to 900°C as shown in figure 2-19 and 2-20. These results qualitatively agree with prior observations.

2.5 Reduced Cluster Model

Each cluster specie requires a separate differential equation to be solved and adds additional terms to the others. Great savings in computational time may be realized by eliminating only a few cluster species. Further, if different cluster species are in approximate equilibrium, it should be possible to combine the reactions into a single cluster with an effective clustering and dissolution rate. In this work, the simplified cluster system shown in Figure 2-21 was utilized. By using this system, five boron cluster species are eliminated. Effective reaction rates are computed by taking the product over the sum of the rates of formation and nucleation for cluster reactions which occur in a series fashion and by reciprocally adding the reaction rates for those which occur in parallel. Care must also be taken to compute all of the rates into a form of:

$$\frac{d(C_{BIC})}{dt} = k_f * C_{\text{precursor}} \quad (2.3)$$

where k_f is not necessarily equal to k_f of the full model, rather, this effective k_f may also include the interstitial or boron interstitialcy concentration which is necessary to formulate the given reaction into the form of equation 2.3. Following this formulation, the B3I cluster is differential in time as:

$$\frac{dC_{B3I}}{dt} = \frac{C_{B_{\text{sub}}} * C_{B_i}^2 * K_{B2If} * K_{B3If}}{K_{B2Ir} + K_{B3Ir}} - \frac{C_{B3I} * K_{B2Ir} * K_{B3Ir} * C_{\text{Int}}}{K_{B2Ir} + K_{B3Ir}} \quad (2.4)$$

Results of this model are in very good agreement with both the full model and experiment. For the case of the 40 keV $2 \times 10^{14} \text{ cm}^{-2}$ boron implant used for comparison purposes herein, diffusion simulations at an anneal temperature of 700°C are shown in Figures 2-19 for times of one hour and in Figure 2-22 for an anneal time of two hours.

2.6 High Concentration Effects

As mentioned in Chapter 1, at high doping levels, the charge-state effects begin to become more important. This is important because interstitials with differing charge states may diffuse at different rates due to differing migrational energies. The treatment of the boron interstitialcy is somewhat easier in that theoretical work has shown that the charge-neutral configuration is not stable and it is assumed that the singly negative configuration does not exist in any appreciable concentrations in the highly p-type region. Different charge state effects are not included in the binding energies of the cluster system since they have not all been computed as a function of the fermi-level of the material. If charge neutrality is assumed, and charge exchange is assumed to be instantaneous, it is not necessary to solve for the individual charge states of each.

Equations of the form of 1.15 to 1.18 have been implemented within the full cluster model for the interstitial system and also within the rate prefactors for the various clusters as:

$$K_{\text{Icapture}} = 4 * \pi * C_{\text{silicon}} * \frac{C_{\text{I}}^+ * D_{\text{I}}^+ + C_{\text{I}}^{++} * D_{\text{I}}^{++} + C_{\text{I}}^0 * D_{\text{I}}^0}{C_{\text{I}}^0 + C_{\text{I}}^+ + C_{\text{I}}^{++}} * a_{\text{silicon}} \quad (2.5)$$

with a similar result for the rate prefactor for a process involving the release of an interstitial. The net result of this is generally a lower interstitial diffusivity in the highest region of boron doping due to the 1.4 eV migrational energy of the doubly positive silicon interstitial. This lower diffusivity serves to maintain a population of interstitials for a longer period of time in the region of highest boron doping density, however, the rate prefactors to interstitial capture

are also lower due to the higher migrational energy of the doubly positive silicon interstitial. This provides a net result of a slower cluster dissolution process in a highly p-type environment than in a lightly p-type environment. At high doping levels, it is also more important to consider the electric field term to the interstitial and vacancy diffusivity. This is accomplished via an expression of form:

$$J_I = -\nabla\left(\frac{C_I}{C_I^*}\right)(D_I)(C_I^*) \quad (2.6)$$

The net effect of these charge-state effects and adding the electric field term to the interstitial diffusivity is shown in Figure 2-23 for the 40 keV $2 \times 10^{14} \text{ cm}^{-2}$ boron implant used as an example in the previous sections annealed for one hour.

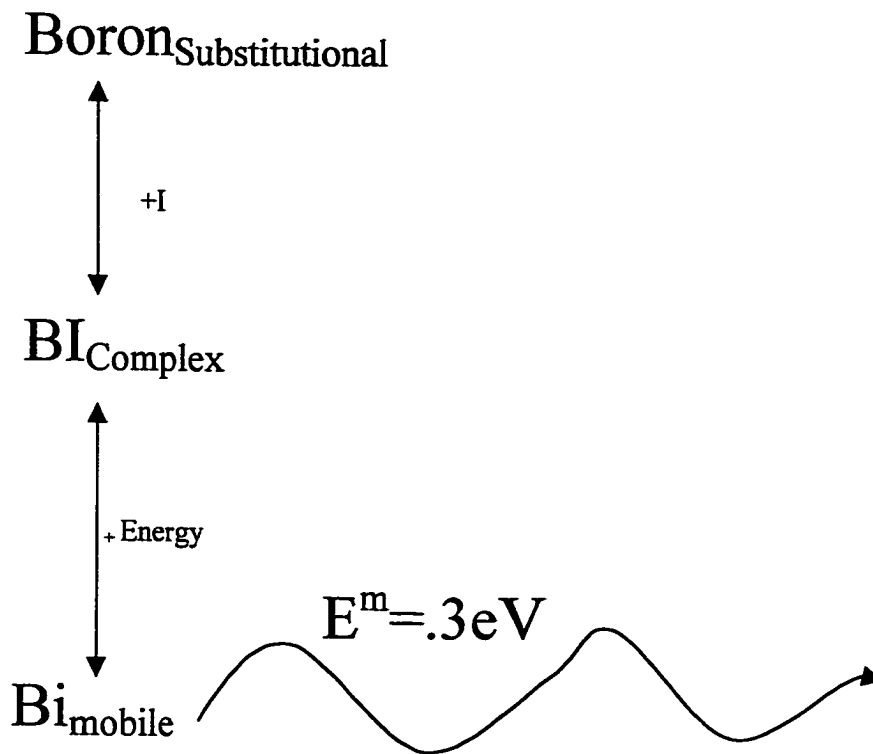


Figure 2-1 Boron diffusion system under intrinsic conditions. All BIC clusters, aside from BI complex, are neglected as are all interstitial clusters.

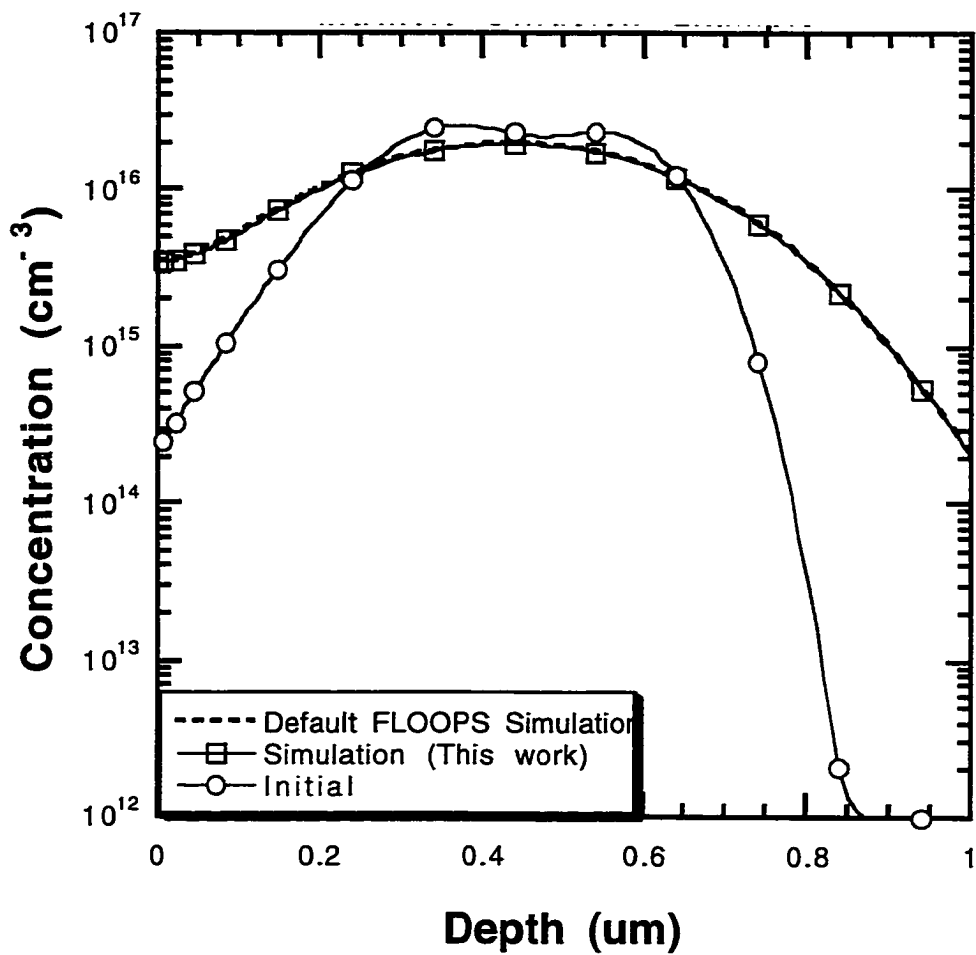


Figure 2-2 Comparison of the intrinsic diffusion of a 80 keV $2 \times 10^{12} \text{ cm}^{-2}$ boron implant for two hours at 1000°C simulated with a model as in Figure 2-1. The simulated profile is nearly identical to the FLOOPS default.

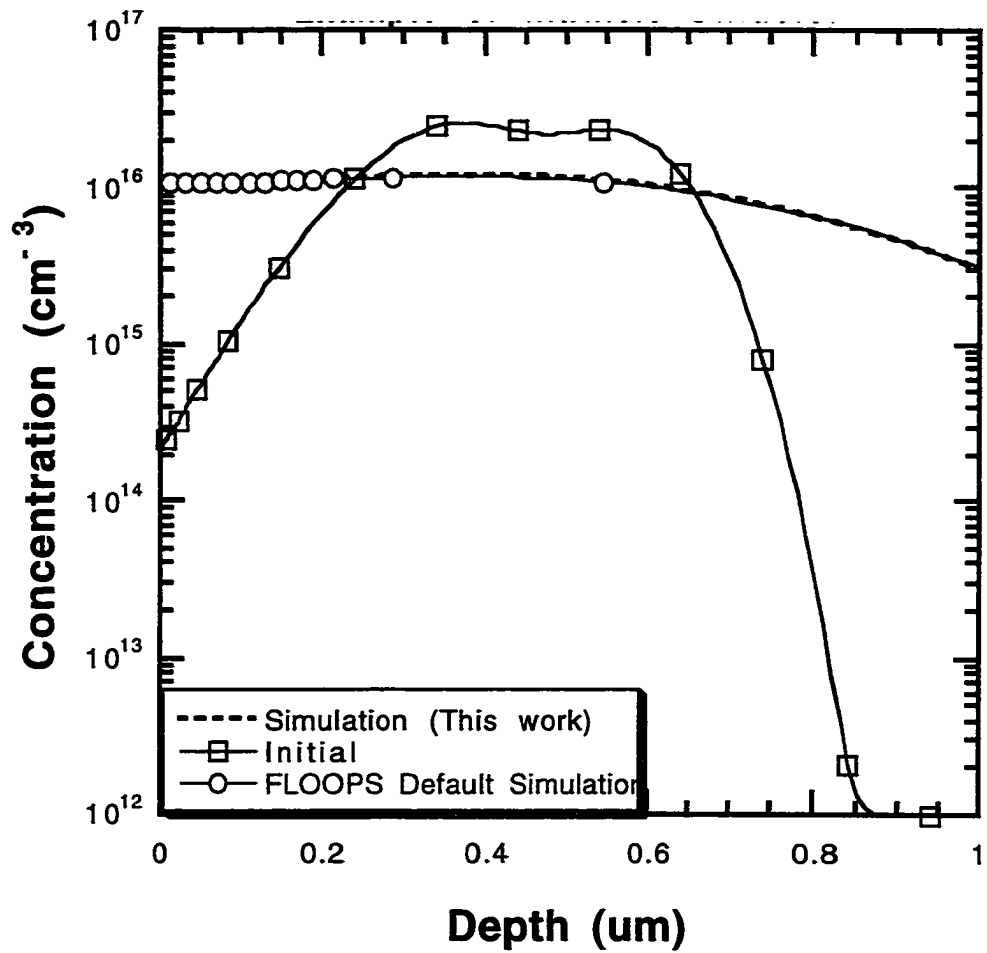


Figure 2-3 Comparison of the intrinsic diffusion of a 80 keV $2 \times 10^{12} \text{ cm}^{-2}$ boron implant for one hour at 1100°C simulated with a model as in Figure 1. The simulated profile is nearly identical to the FLOOPS default.

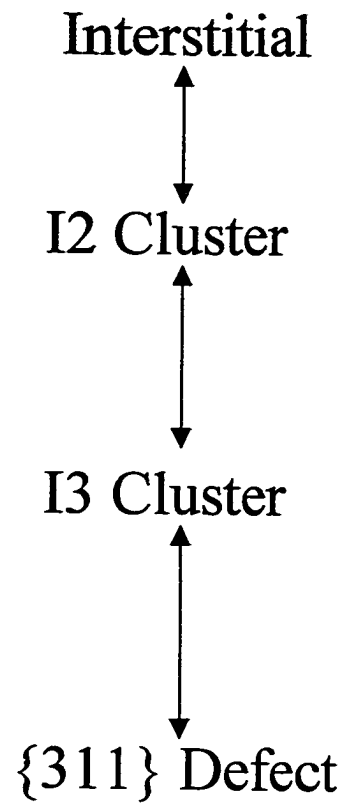


Figure 2-4 Interstitial cluster system utilized in this work. Interstitials may nucleate into I2 clusters which then ripen into I3 clusters and ultimately {311} defects.

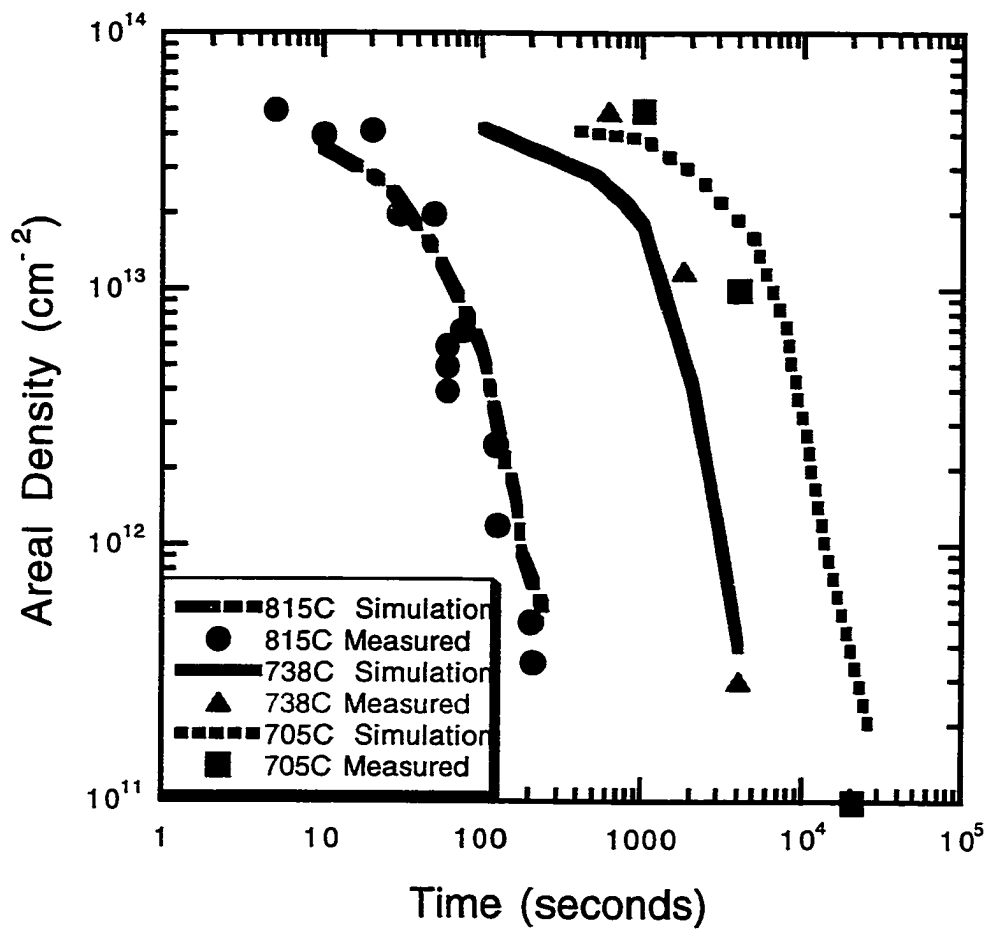


Figure 2-5 Dissolution of interstitials trapped in {311} defects simulated as a function of time and anneal temperature compared to experimental values for a 40 keV $5 \times 10^{13} \text{ cm}^{-2}$ silicon implant.

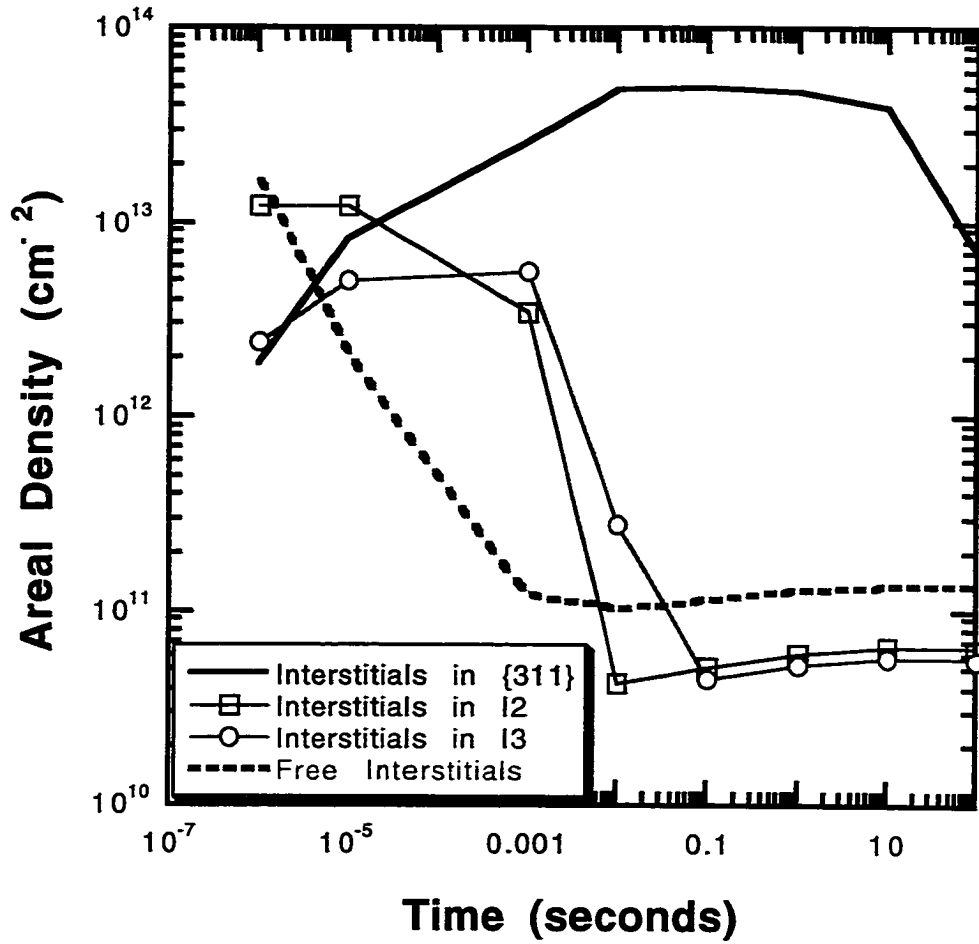


Figure 2-6 Transient progression of interstitial clusters following the anneal at 815°C of a $5 \times 10^{13} \text{ cm}^{-2}$ silicon implant. Note that at very short times, the interstitials are contained in I2 and I3 clusters which rapidly ripen to the more energetically favorable {311} defect.

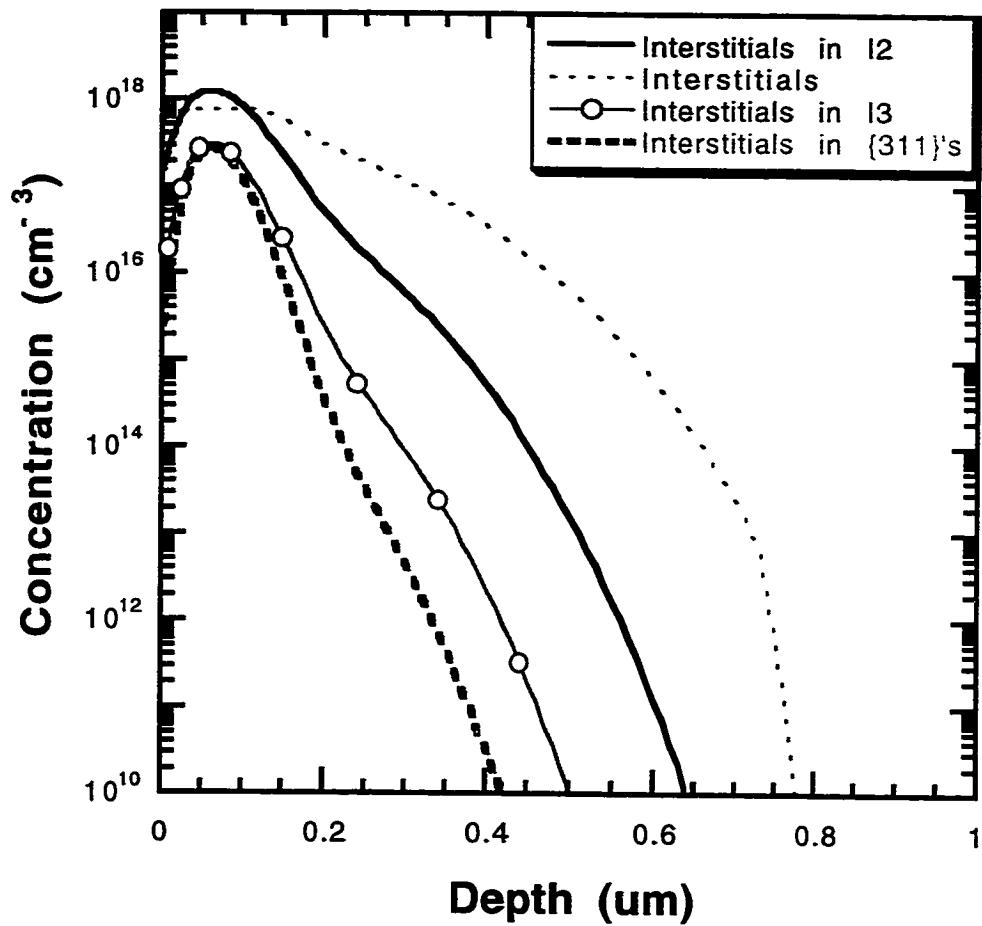


Figure 2-7 Interstitial system at a time of one micro-second following the anneal at 705°C of a $5 \times 10^{13} \text{ cm}^{-2}$ silicon implant as simulated by FLOOPS. Note how the sub-microscopic interstitial clusters contain the majority of the implant damage (interstitials).

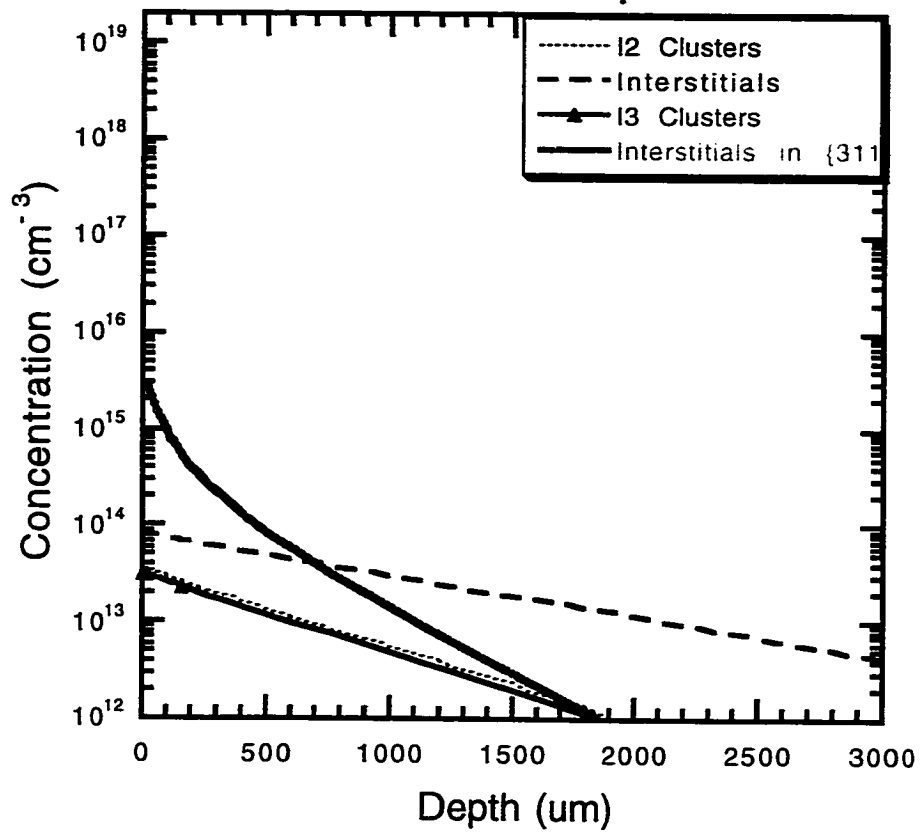


Figure 2-8 Interstitial system at a time of 1.44×10^5 seconds following the anneal at 705°C of a $5 \times 10^{13} \text{ cm}^{-2}$ silicon implant as simulated with FLOOPS. Note that the majority of the $\{311\}$ defects have been dissolved.

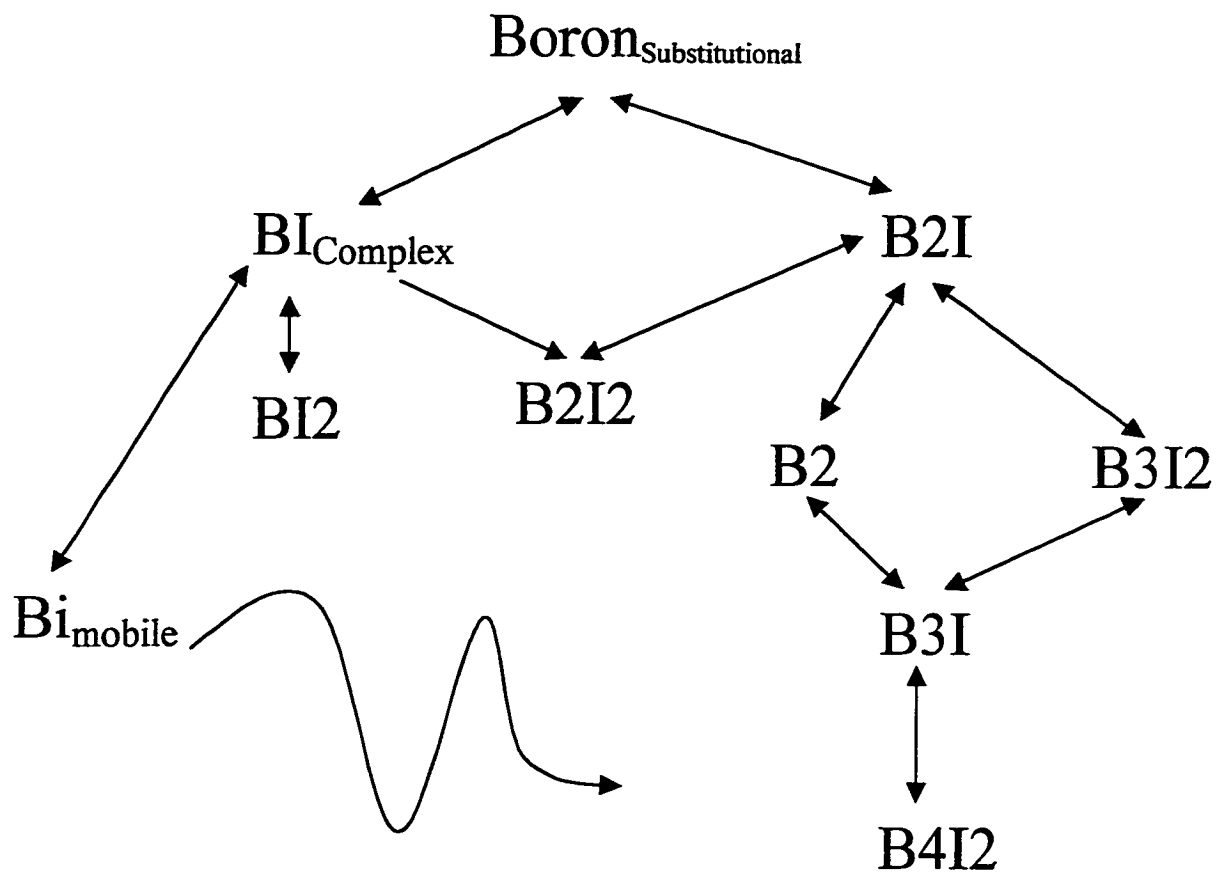


Figure 2-9 Full BIC cluster system used in this work. B₃I was found to be the most energetically stable complex.

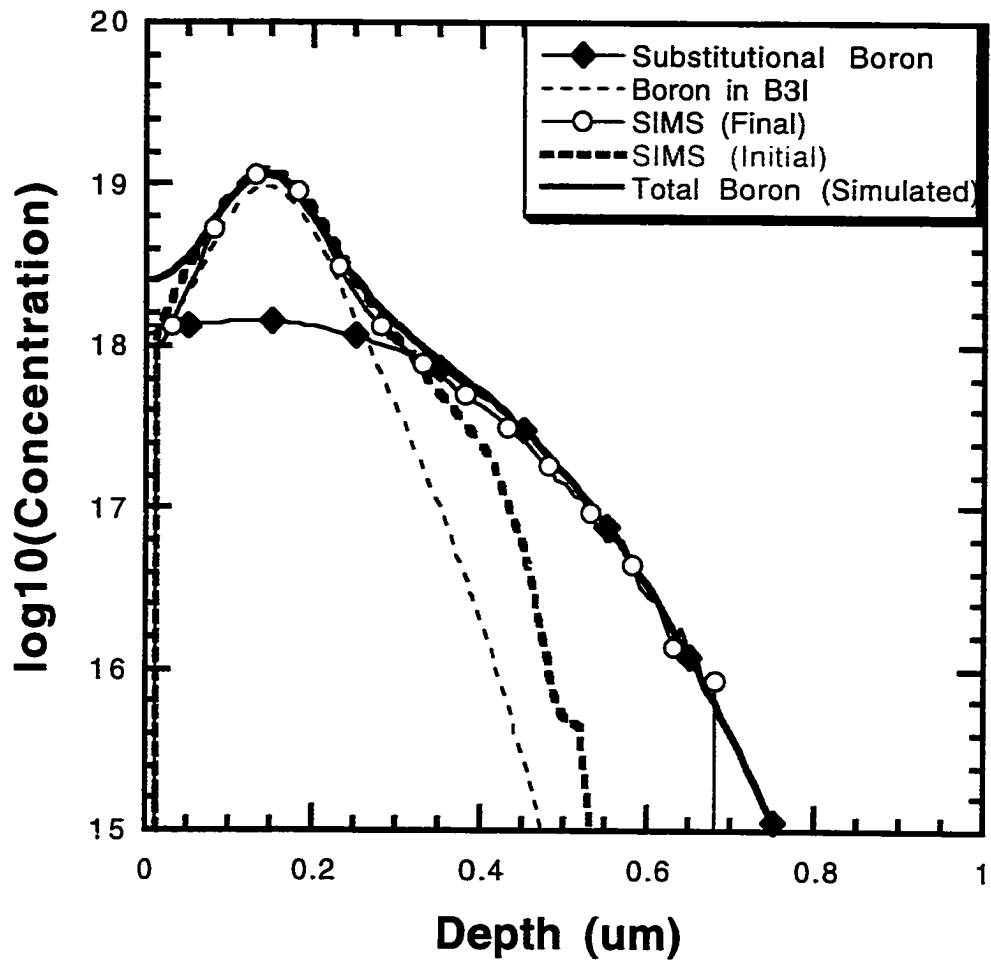


Figure 2-10 A 40 keV $2 \times 10^{14} \text{ cm}^{-2}$ boron implant annealed at 700°C for a time of one hour as simulated with FLOOPS using full cluster model.

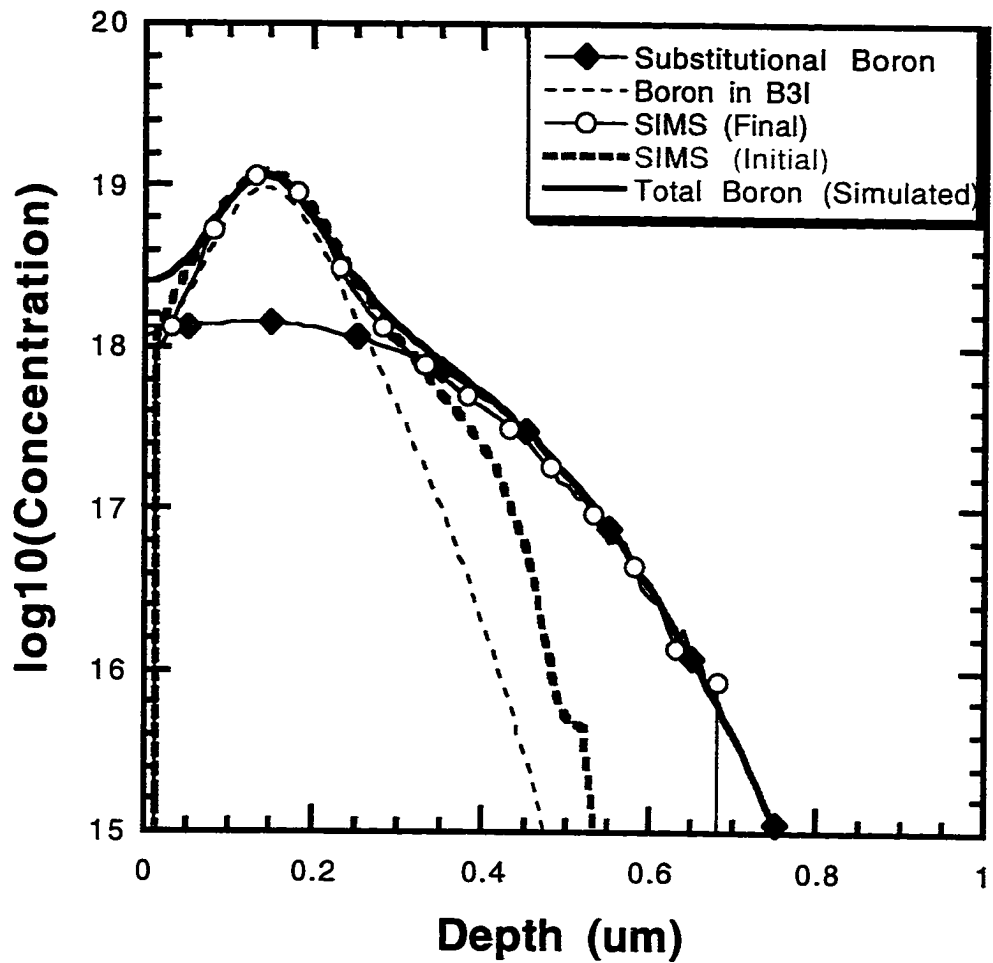


Figure 2-11 A 40 keV $2 \times 10^{14} \text{ cm}^{-2}$ boron implant annealed at 700°C for a time of two hours as simulated with FLOOPS using full cluster model.

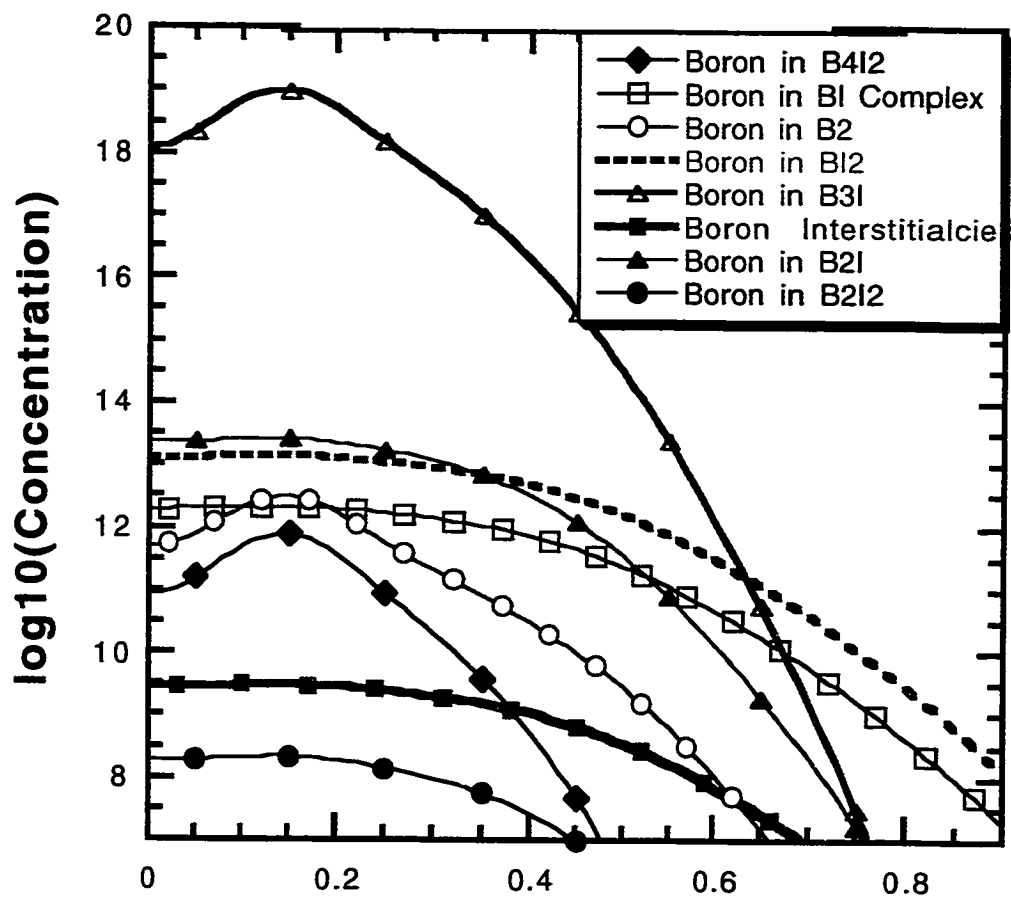


Figure 2-12 Simulation of a $40 \text{ keV } 2 \times 10^{14} \text{ cm}^{-2}$ annealed at 700°C for one hour. All cluster species are shown in this plot. Note that the boron interstitialcy represents only a small fraction of the total boron, but is responsible for all diffusion. Note also that relatively (compared to B3I complex) boron is contained in the precursor clusters at these times. Plots like this justify the development of reduced models.

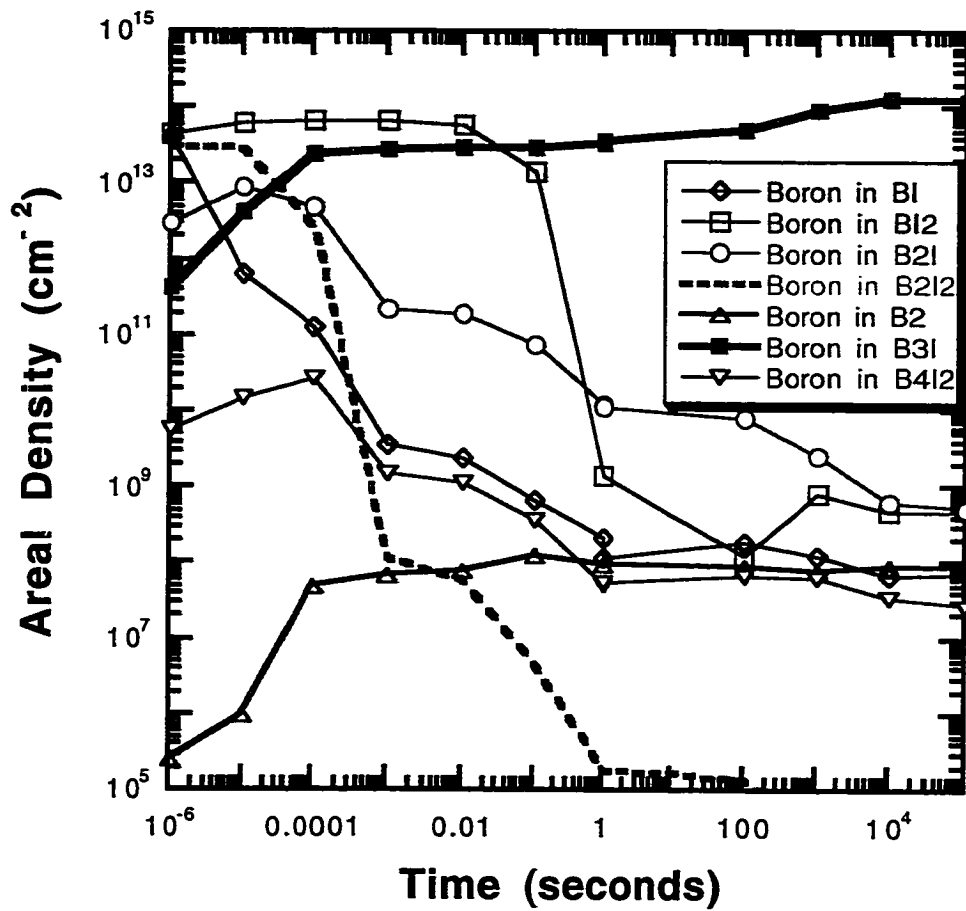


Figure 2-13 Transient progression of the boron clusters following a 700°C anneal of a $40\text{ keV } 2 \times 10^{14}\text{ cm}^{-2}$ boron implant. Note that the areal density of the boron trapped in the precursor clusters rapidly drops off as the B3I clusters are formed.

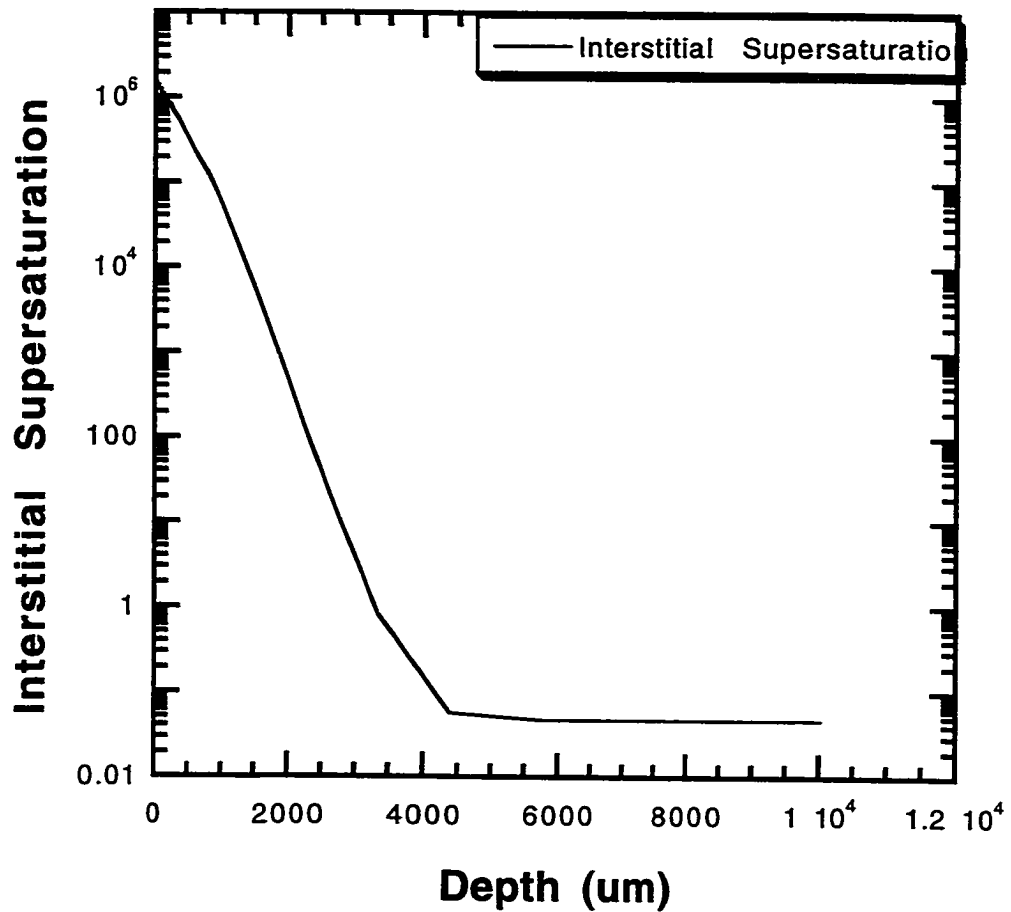


Figure 2-14 Interstitial supersaturation as a function of depth following the 700°C anneal of a $40 \text{ keV } 2 \times 10^{14} \text{ cm}^{-2}$ boron implant for a time of one hour. Note that the region of interstitial supersaturation reaches far outside the region of the boron implant.

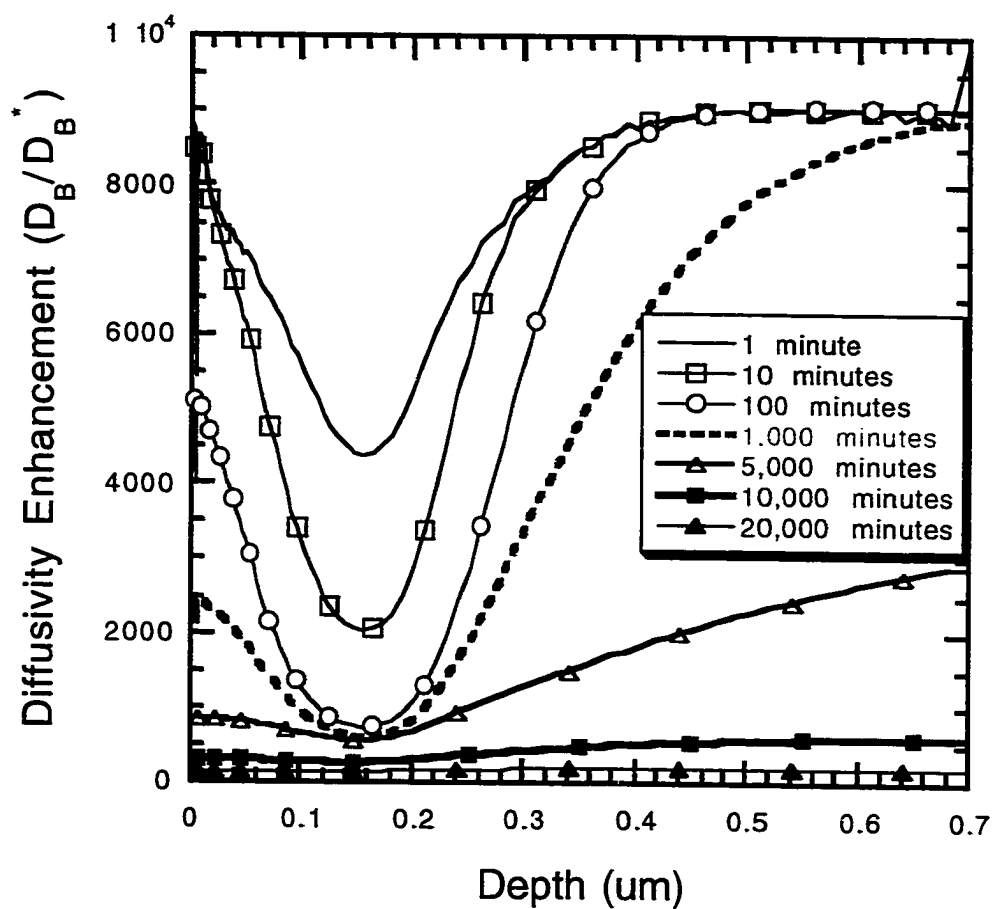


Figure 2-15 Simulation of diffusion enhancement exhibited by $40\text{keV } 2 \times 10^{14}\text{cm}^{-2}$ boron implant at various times following anneal at 700°C .

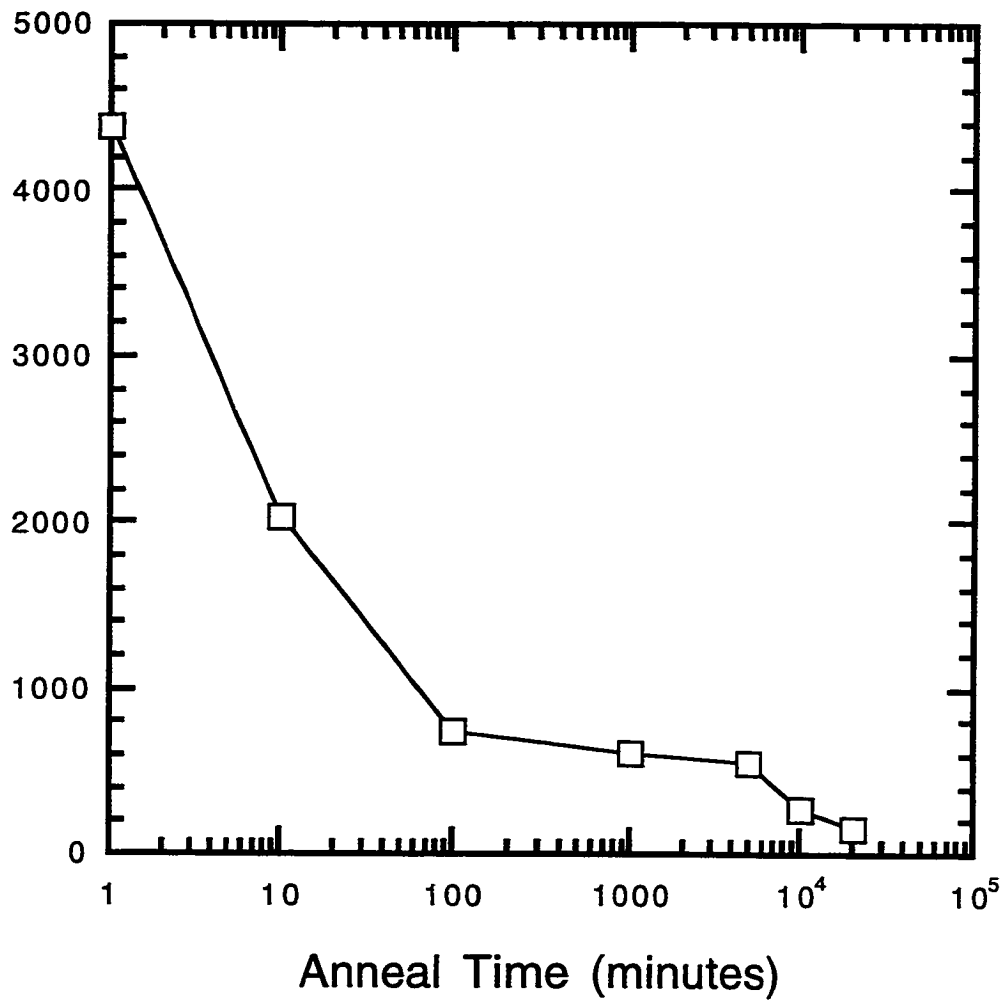


Figure 2-16 Simulation of transient nature of boron diffusion enhancement resulting from a 40keV $2 \times 10^{14} \text{ cm}^{-2}$ boron implant annealed at 700°C. Plotted are values at the peak of the implanted profile.

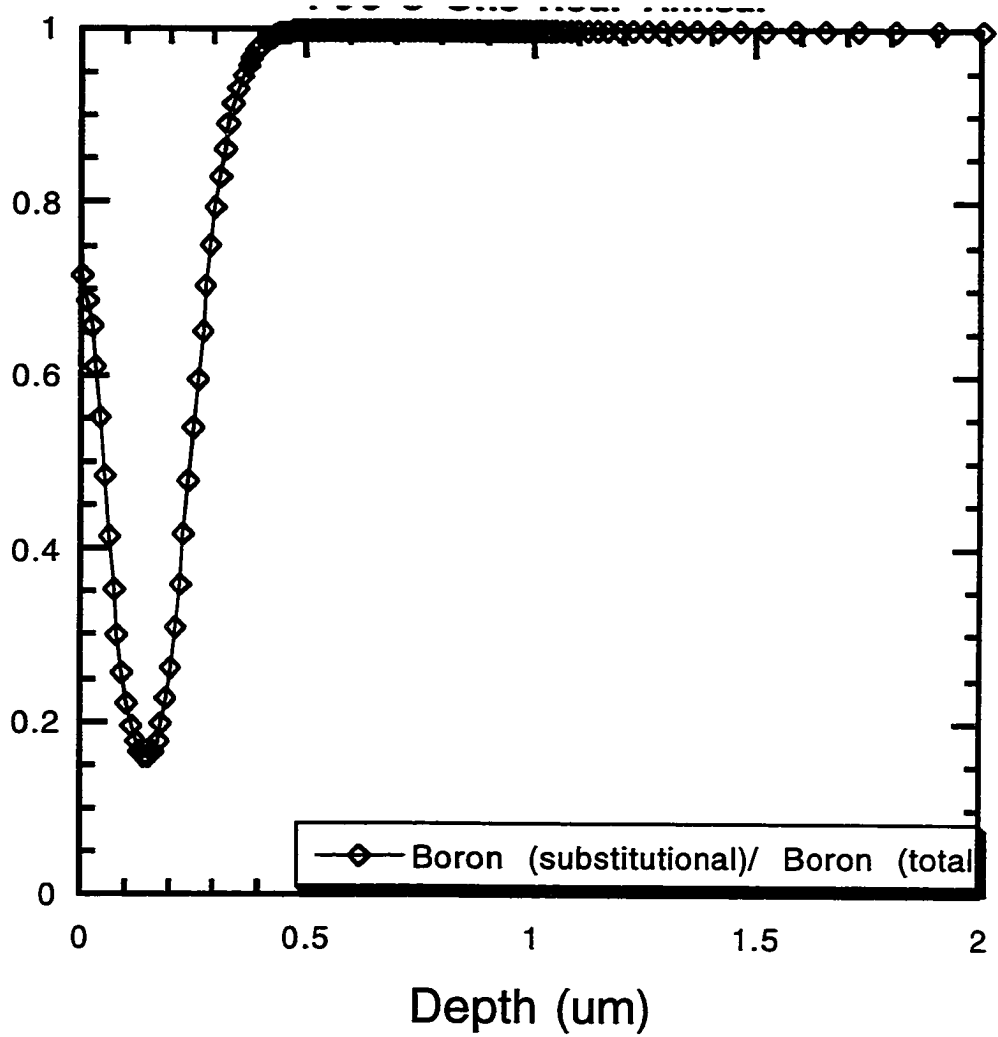


Figure 2-17 Fractional activation of a 40 keV $2 \times 10^{14} \text{ cm}^{-2}$ boron implant following the anneal at 700°C for a time of one hour. Only boron substitutional profile is assumed active.

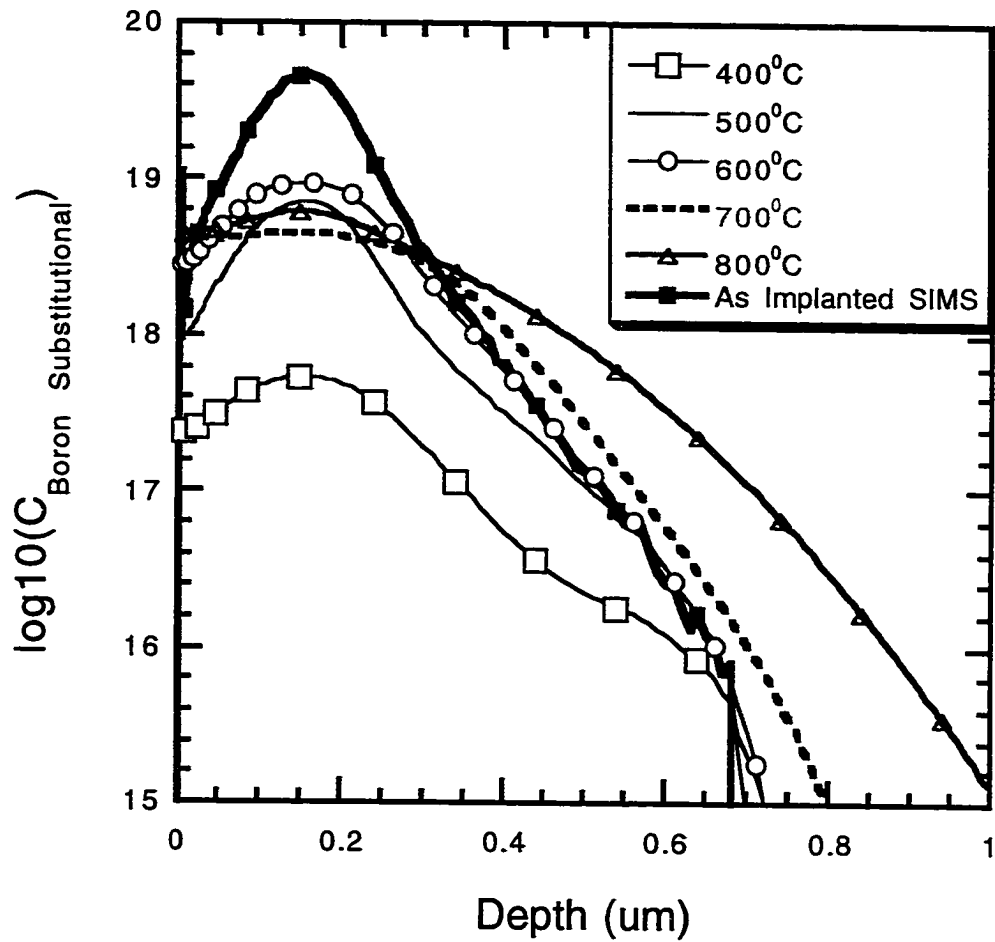


Figure 2-18 Reverse anneal effect as simulated by FLOOPS. A 40keV $6.6 \times 10^{14} \text{ cm}^{-2}$ boron implant is annealed at various temperatures for a duration of one hour. Note that the differential activation is negative from 600°C to 700°C. Plot illustrates the as-implanted profile from SIMS and the simulation of the substitutional boron profile which is assumed electrically active.

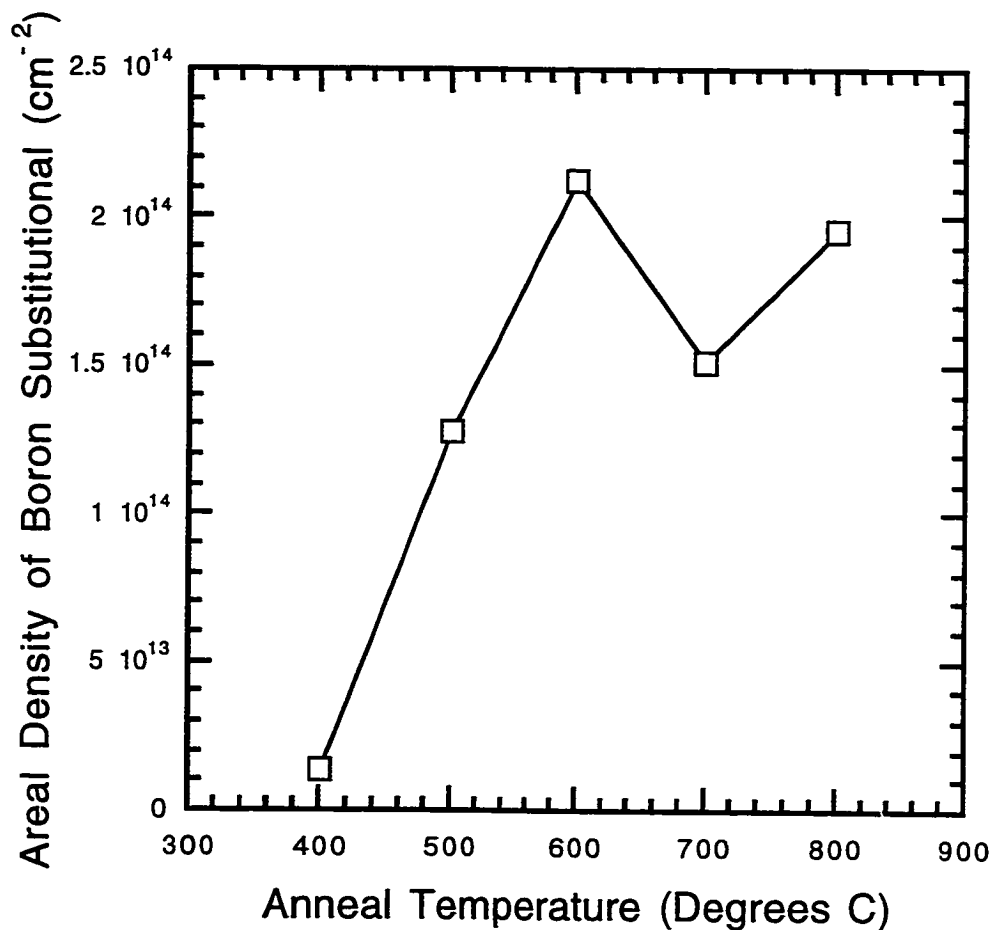


Figure 2-19 Activation of a 40keV $6.6 \times 10^{14} \text{ cm}^{-2}$ boron implant following anneals of 1 hour at various temperatures (as in figure 2-18). Note the negative differential activation between the 600°C and 700°C data point. Again, only the substitutional boron is assumed electrically active in this plot.

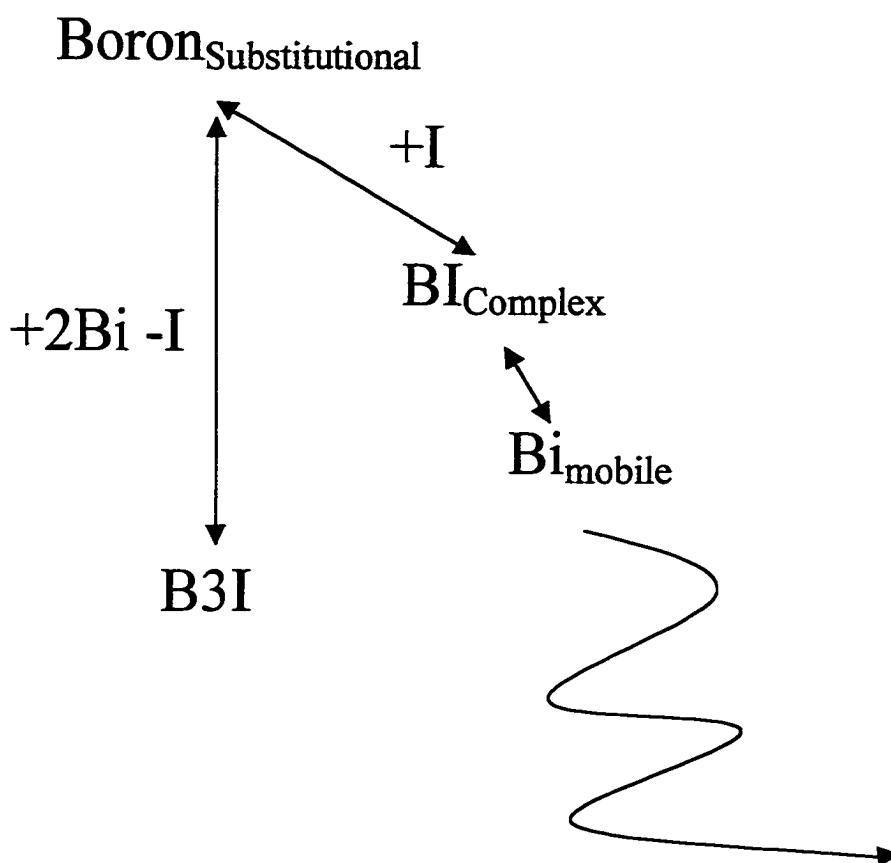


Figure 2-20 Reduced boron cluster model as used in this work. The full cluster model shown in Figure 2-9 has been reduced for computational efficiency.

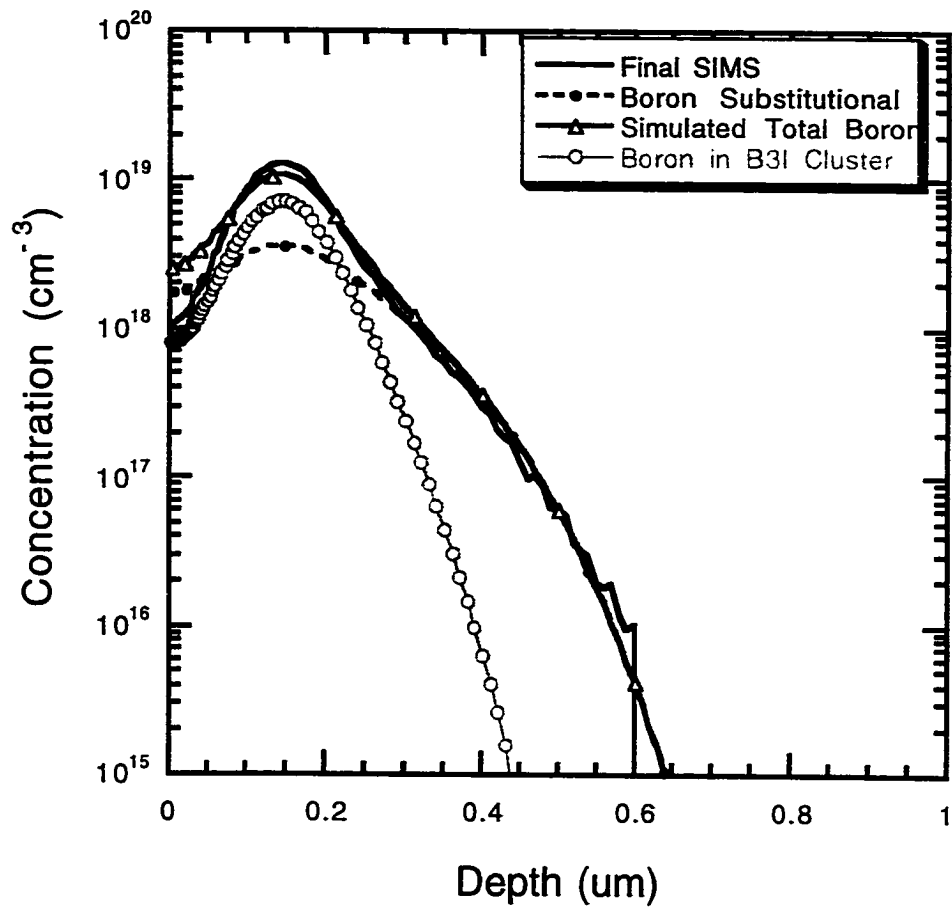


Figure 2-21 Simulation with the reduced cluster model of a $40 \text{ keV } 2 \times 10^{14} \text{ cm}^{-2}$ boron implant following the anneal at 700°C for a time of one hour.

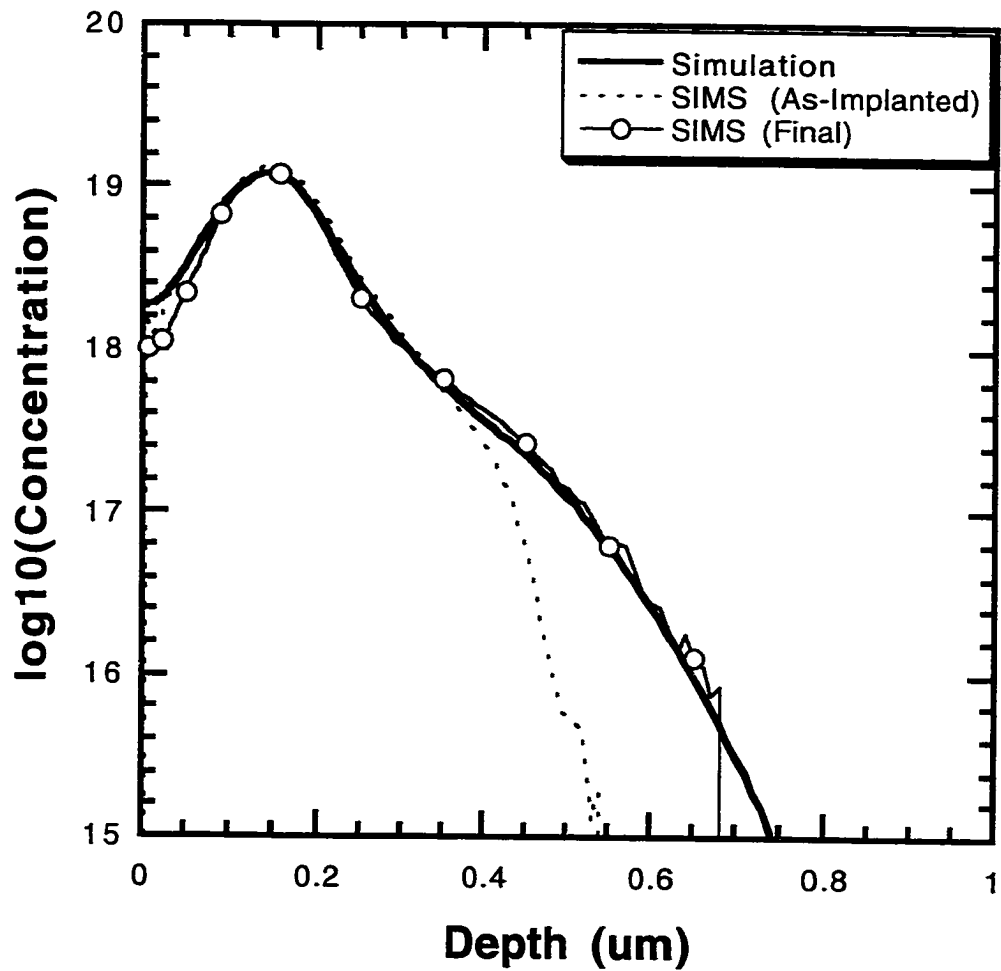


Figure 2-22 Simulation with the reduced cluster model of a 40 keV $2 \times 10^{14} \text{ cm}^{-2}$ boron implant following the anneal at 700°C for a time of two hours.

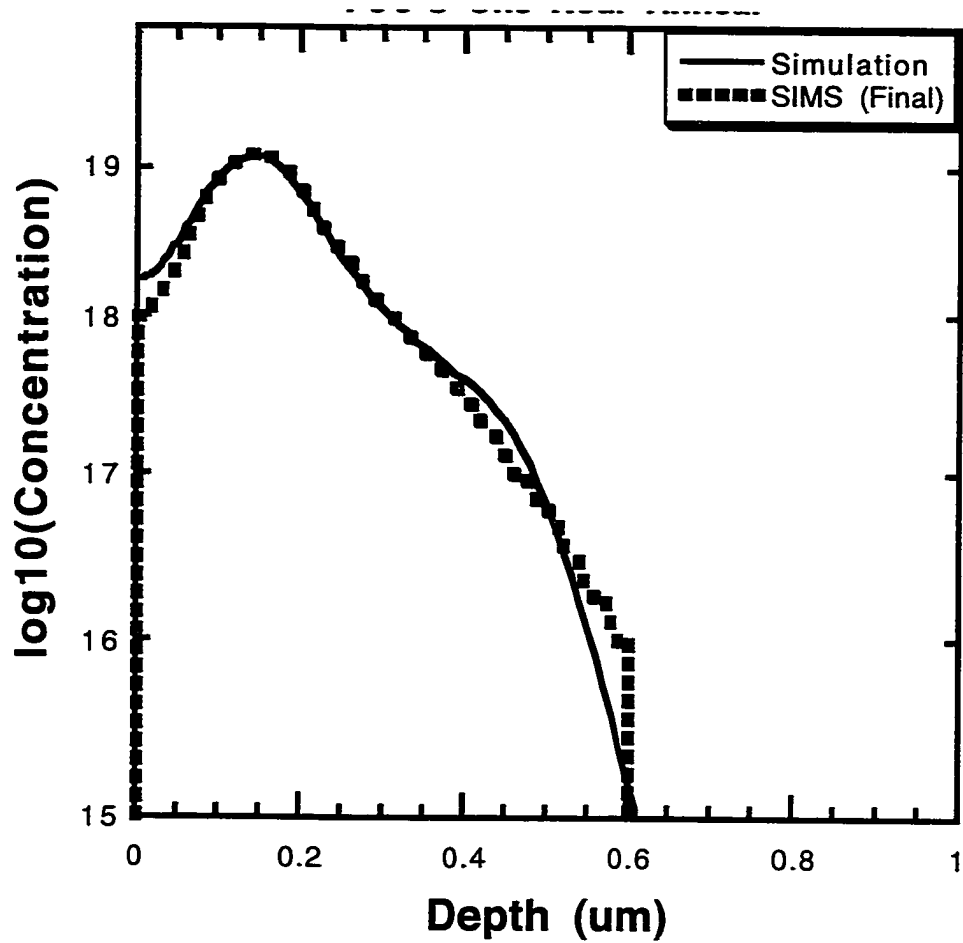


Figure 2-23 Simulation of a 40 keV $2 \times 10^{14} \text{ cm}^{-2}$ boron implant annealed at 700°C for one hour accounting for various concentration dependent effects and differing charge states present in the interstitial system.

CHAPTER 3 EXPERIMENTAL INVESTIGATION OF BORON CLUSTERING KINETICS AND PROCESSES

3.1 Outline of Experiments

The processes and kinetics governing the boron clustering processes have been investigated as part of this work. Two major experiments were conducted. One of these utilizes a silicon self implant to induce damage within boron-doped wells of varying concentration followed by various anneals and structural analysis with PTEM, chemical analysis with SIMS, and electrical analysis with SRP. This experiment yields some insight upon the possible processes leading to boron deactivation. The second experiment is more focussed towards determining the kinetics of the reactivation process. This experiment utilizes a series of wafers implanted with boron at various energies and doses. These wafers were then subjected to a two-stage anneal process in which the first anneal was used to deactivate or cluster the boron and the second was used to reactivate it. This material was then electrically analyzed with SRP and Hall effect, and chemically analyzed with SIMS.

3.2 Boron Well Experiment

Four boron-doped wells were formed by the ion-implantation of boron at 400 keV through 100Å screen oxide into (100) Cz silicon with doses varying from 1×10^{13} to $2 \times 10^{14} \text{ cm}^{-2}$ followed by a 330 minute anneal at 1100°C. This resulted in the formation of four boron-doped wells with concentrations of roughly 5.5×10^{16} , 3×10^{17} , 5×10^{17} , and

$1.2 \times 10^{18} \text{ cm}^{-3}$ to a depth in excess of 1 μm . The boron profile in these well structures was later verified with both SIMS and spreading resistance measurements. The boron-doped wells were then subjected to a silicon self-implant at 40 keV of 1×10^{14} to $2 \times 10^{14} \text{ cm}^{-2}$ dose followed by anneals of 10 to 30 minutes at 740°C , 15 seconds to 35 seconds at 815°C , and 30 minutes to six hours at 670°C in order to nucleate and grow populations of both $\{311\}$ defects and BIC's. The number of residual interstitials trapped in the $\{311\}$ defects following the anneals was then determined by QTEM. Figure 3-1 outlines the process sequence for this experiment.

Figure 3-2 shows a series of TEM micrographs of the residual $\{311\}$ defects for two of the samples from the 740°C study with the $1 \times 10^{14} \text{ cm}^{-2}$ implanted silicon dose which clearly illustrate the trend towards fewer and smaller $\{311\}$ defects at higher boron concentrations for the same anneal conditions. Experimental measurements of those samples annealed at 740°C are plotted in Figure 3-3. These results follow the same trend as a previous study which utilized FZ material, however, we note significant degradation of the residual interstitial concentration in the $\{311\}$ defects at boron concentrations roughly an order of magnitude lower than the previous study. For the 740°C anneals, no quantifiable population of $\{311\}$ defects was observed for the 30 minute anneals for all boron concentrations.

Results from the 670°C study are less clear. For anneal times of 30 minutes to six hours, very few $\{311\}$ defects were observed regardless of boron concentration. It is possible that the boron is influencing the nucleation of the $\{311\}$ defects at these lower temperatures, or that the silicon interstitials are diffusing away or trapped before the $\{311\}$'s can nucleate. A similar self implant of 40 keV $2 \times 10^{14} \text{ cm}^{-2}$ does show

quantifiable populations of $\{311\}$ defects for these anneal conditions, indicating that the additional $1 \times 10^{14} \text{ cm}^{-2}$ implanted silicon ions quench whatever sink was responsible for the lack of $\{311\}$ defects at the lower implant dose.

Those samples subjected to 815°C anneal with the $2 \times 10^{14} \text{ cm}^{-2}$ implanted silicon dose show a population of both $\{311\}$ type defects and dislocation loops. In addition to the trend towards fewer $\{311\}$ defects with increasing boron concentration, we also note fewer of the dislocation loops with increasing boron concentration for the higher fluence silicon implants.

These same samples were then analyzed by spreading resistance profiling (SRP) in order to determine the profile of the boron which is electrically active. By then comparing these results to SIMS profiles of the chemical boron, it is possible to determine the inactive or clustered boron concentration. By comparing the SIMS and SRP, it is possible to determine the fractional activation.

By utilizing the lightest-doped boron well as a control to gauge the intrinsic bimolecular recombination of interstitials and vacancies and account for the surface recombination of interstitials, it is possible to elucidate some of the kinetics of the BIC's. Following the 10 minute anneal at 740°C , the heaviest-doped boron well showed approximately $3.9 \times 10^{13} \text{ cm}^{-2}$ fewer interstitials than the lightest-doped boron well. A comparison of the SIMS and the SRP results indicate that for this same case approximately $3 \times 10^{13} \text{ cm}^{-2}$ boron is deactivated. By attributing all of the missing interstitials to BIC formation, an upper bound of 1.3 can be placed on the ratio of clustered interstitials to clustered boron in the BIC's. A similar analysis following a 20 minute anneal at 740°C , leads to an upper bound of .9 for this fraction. This result

supports previous work utilizing cluster precursors and the progression of the clustered boron toward larger more stable clusters. Both of these ratios are likely high due to the fact the diffusion of the boron from the region subjected to the self implant is neglected. Assuming boron diffusion dominated by a boron-interstitial pair mechanism where each boron atom removed from the implanted region also removes a single interstitial, these ratios are reduced to approximately 1 for the 10 minute anneal and .6 for the 20 minute anneal at 740°C. Accounting for other mechanisms could further lower these ratios.

3.3 Boron Implant Study

A matrix of boron implants were performed as illustrated in table 3.1 at energies of 10 keV to 80 keV and doses of $2 \times 10^{14} \text{ cm}^{-2}$ to $1.6 \times 10^{15} \text{ cm}^{-2}$.

Table 3-1 Implant matrix used in boron implant study. A 'x' indicates that condition was processed.

	$2 \times 10^{14} \text{ cm}^{-2}$	$4 \times 10^{14} \text{ cm}^{-2}$	$8 \times 10^{14} \text{ cm}^{-2}$	$1.6 \times 10^{15} \text{ cm}^{-2}$
10 keV	x	x	x	x
20 keV		x	x	x
40 keV		x	x	x
80 keV		x	x	x

These implants were performed into four inch (100) CZ silicon wafers with a relatively light phosphorus n-type background doping, which enabled electrical measurements to be conducted at a later time. A dicing saw was utilized to cut the wafers into squares of approximately 14.4 mm on each side. The material was then back-side scribed for later identification and pieces from each wafer were subjected to twelve separate anneals as

illustrated in table 3.2. All anneals were conducted in the presence of nitrogen gas and carefully monitored with the temperature recorded prior to the start of the anneal and immediately following the anneal. Push/pull times were negligible for all anneals including those conducted at 1000⁰C. Following the anneals, the samples were subjected to a four step cleaning process which also involves stripping of any oxide which may have reformed during the anneal process to enable high-quality ohmic contacts to be formed with the material. These contacts were deposited with E-beam lithography through a contact mask to produce a Van der Pauw structure. A silicon(3.5%):aluminum(96.5%) alloy was used for the contacts. This contact material has been shown to reduce aluminum spiking to the substrate. These contacts were hardened with a 450⁰C 30 minute anneal. The process sequence for this experiment is outlined in Figure 3-4 and the as-implanted boron profiles are shown in Figures A-1 through A-3 in appendix A.

A MMR Hall effect system was utilized in the analysis of these samples. In addition to this, spreading resistance measurements were also performed upon certain samples following the hall effect analysis. Chemical measurements of boron profiles were conducted with SIMS for the as-implanted wafers and also following several of the anneal steps in order to monitor any potential dose loss, etc..

Table 3-2 Anneal matrix of boron implant study. Wafers in table 3.1 were diced into several pieces with a piece of each wafer being subjected to the twelve anneals as illustrated here. An 'x' indicates given split was subjected to this anneal step.

	Split 1	Split 2	Split 3	Split 4	Split 5	Split 6	Split 7	Split 8	Split 9	Split 10	Split 11	Split 12
750C 10min	X											
750C 30min		X				X	X	X	X	X	X	X
750C 60min			X									
750C 120min				X								
750C 360min					X							
850C 10min						X						
850C 20min							X					
850C 60min								X				
850C 120min									X			
950C 10min										X		
950C 20min											X	
1000C 2min												X
450C 30min	X	X	X	X	X	X	X	X	X	X	X	X

3.3.1 Qualification of Hall Effect Measurements: Comparison to SRP

The data acquired from Hall effect measurements was compared to that obtained from the spreading resistance technique. Ideally, the integrated carrier profile from the spreading resistance analysis should be equivalent to the sheet number provided by the Hall effect analysis. Pooled data from anneals at 750⁰C for times of up to six hours and 850⁰C for times of up to one hour is shown in Figure 3-5. At these temperatures/times,

excellent agreement is obtained between the Hall Effect measurements of the sheet number and the carrier concentration as determined by the spreading resistance technique.

Unfortunately, at longer times at 850°C or anneals at higher temperatures of 950°C or 1000°C, the sheet number was found to exceed the implanted dose by a large margin. Such a condition can not exist unless the vast majority of the implanted boron atoms are multiply ionized. This process requires thermal energy far greater than that provided by these anneals and is, therefore, not possible. A comparison of the Hall effect sheet number measurement and the integrated carrier profile from the spreading resistance technique yields the plot in Figure 3-6. Every sample subjected to anneals at 950°C, 1000°C, and certain samples annealed at 850°C exhibit sheet numbers greater than the implanted dose. Further, as shown in Figure 3-7, these hall effect measurements are neither consistently reproducible or constant with current. In the case of the 80 keV $1.6 \times 10^{15} \text{ cm}^{-2}$ boron implant subjected to the 750°C 30 minute/950°C 20 minute anneal the measured sheet number is observed to vary between approximately $2 \times 10^{15} \text{ cm}^{-2}$ and $8 \times 10^{15} \text{ cm}^{-2}$ while the sheet resistance remains roughly constant. Therefore, for anneals of greater than one hour at 850°C or anneals at 950°C and 1000°C, the Hall Effect data will not be utilized aside from the sheet resistance which is a zero field measurement. The explanation for this observed effect is believed to lie in the increased non-uniformity exhibited in the samples subjected to these anneals at higher temperature. For instance, the aforementioned profile exhibits a marked variation in the hole density as a function of depth at high concentrations, conditions which are not seen by the 750°C and shorter time 850°C annealed samples. If a similar voltage is dropped laterally across this profile, the

holes in regions of lower concentration must travel faster than those at higher concentrations. Recalling that the Hall voltage is proportional to the carrier velocity, it is easy to see how this effect introduces irregularities into the Hall effect measurements. A basic analysis of this system would tend to support the formation of both latitudinal and longitudinal eddy currents in order to equalize the vertical gradient to the hall voltage. These eddy currents serve to both provide an under-estimate of the carrier velocity, and to produce higher order Hall effects which influence the measured voltages and currents. The fact that the Hall effect measurements were observed to vary with forced current provides strong support that such behavior is occurring.

3.3.2 Observed Reactivation Behavior

Immediately following the 750⁰C 30 minute anneal, fractional activities of up to 25% were observed as computed from the ratio of the as-implanted SIMS dose and the measured sheet number. The observed peak carrier density following the 750⁰C 30 minute anneal saturates at a concentration of approximately $3\text{-}4 \times 10^{18} \text{ cm}^{-3}$ independent of the either the implanted boron dose or implantation energy as shown in Figures 3-8 and 3-9. As these samples were subjected to additional anneals, both Hall effect measurements and SRP analysis indicates that the samples are being reactivated. The SRP analysis provides some insight as to where this newly-activated boron is located. Figures 3-10 through 3-13 illustrate the reactivation of a given boron implant at temperatures of 850⁰C and 950⁰C. In general, the reactivation is a uniform process through the peak region of the implanted profile, possibly with a preference towards reactivating from the surface to the bulk as exhibited more strongly by the 20 keV $8 \times 10^{14} \text{ cm}^{-2}$ boron implant annealed at 850⁰C . It is also easy to see that a significant

concentration of boron remains deactivated in the peak region of the implant for all of these cases.

3.3.3 Reactivation of Boron as a Function of Implanted Dose

For a given energy, increasing the implanted dose will lead to a corresponding increase in the density of the boron atoms within the silicon substrate. Figure 3-14, which illustrates the observed spreading resistance profiles observed from the reactivation of 40 keV boron implants at various doses, shows that increasing the boron dose will increase the hole concentration for anneals at 850⁰C. However, it is important to note, that this is not a direct correlation in that the lower dose boron implant will exhibit a higher fractional activation. That is to say, that increasing the boron density leads to a higher fraction of the boron being contained within electrically inactive states.

Figures 3-15 through 3-18 show the change in electrical activity of a boron implant observed as the dose is varied for anneals at 750⁰C. These plots present both the measured sheet resistance values and the fractional activation as determined from the sheet number obtained from the Hall effect analysis. Generally speaking, at fixed implant energy and for all anneal times, increasing the implanted dose leads to reduced fractional activities and lower sheet resistances. Fractional activities of up to 49% are observed following 750⁰C anneals of up to 360 minutes. Increasing the anneal time for a given boron implant also leads to the expected result of a generally monotonically increasing fractional activation and monotonically decreasing sheet resistance. Similar results are obtained and observations apply to those boron implants which are subject to the two-step anneal sequence. The electrical activation of those samples subjected to a 850⁰C secondary anneal to reactivate are shown in Figures 3-19 to 3-22. Plots of the sheet

resistance of the samples subjected to the 950⁰C anneal are shown in Figures 3-23 and 3-24 and in Figure 3-25 for the 1000⁰C 2 minute anneal as a function of the implanted boron dose.

3.3.4 Reactivation as a Function of Implant Energy

For a fixed implant dose, increasing the implant energy will tend to decrease the average density of the implanted boron atoms. Examination of the reactivation of boron implants with fixed dose and varying energy is shown in Figures 3-26 and 3-27 for the two-step anneal sequence terminating with the 850⁰C 10 minute anneal. From these, it can be seen that implanted boron doses of $4 \times 10^{14} \text{ cm}^{-2}$ produce carrier profiles which saturate at roughly $9 \times 10^{18} \text{ cm}^{-3}$ and implanted boron doses of $8 \times 10^{14} \text{ cm}^{-2}$ produce carrier profiles which saturate at approximately $1.2 \times 10^{19} \text{ cm}^{-3}$ carrier concentration both of which are independent of implantation energy over the range studied herein. Figure 3-28 illustrates similar carrier profiles obtained for those two-step anneals which terminate in the 950⁰C 10 minute anneal. These profiles are observed to saturate at carrier concentrations of $5 \times 10^{19} \text{ cm}^{-3}$ for all energies except the 10 keV. It is important to note that the background noise level from the SRP measurement of the 10 keV implant shown in this figure is two orders of magnitude higher than normal which is indicative of extreme lattice distortion and may lead to profile smoothing possibly making this 10 keV carrier profile erroneous.

Figures 3-29 to 3-32 illustrate the reactivation of boron at 750⁰C observed through hall effect. Plots include sheet resistance and the fractional activation as determined from the as-implanted SIMS profiles. Aside from a few slight variations, the observed fractional activation increases with increasing implant energy and anneal time.

Correspondingly, the observed sheet resistance value falls with increased anneal time and increasing implant energy. Similar results are shown in Figures 3-33 to 3-36 for anneals at 850⁰C, Figures 3-37 to 3-38 for anneals and 950⁰C, and in Figure 3-39 for anneals at 1000⁰C. Again, only the sheet resistance is provided for the higher temperature anneals. Fractional activation data may be obtained for the $1.6 \times 10^{15} \text{ cm}^{-2}$ boron implants annealed at 950⁰C from the SRP profiles. This result is shown in Figure 3-40 which illustrates that the 950⁰C 10 minute anneal is sufficient to essentially fully activate the 40 keV and 80 keV boron implant, but not the 20 keV or 10 keV implant.

3.3.5 Reactivation at Similar Chemical Dopant Concentration

The utility of a solubility models for boron activation may be examined by analyzing the reactivation of boron at constant chemical dopant densities. If it is assumed that the projected range of implanted boron is determined largely by the electronic stopping process and channeling effects are neglected, the projected range of the implant will be directly proportional to the implant energy. Therefore, profiles of roughly similar chemical dopant density and peak chemical dopant concentration may be produced by scaling both the implant energy and implant dose by the same factor. The implant matrix we have chosen makes this a very simple task. Figure 3-41 shows how samples with similar chemical dopant densities produce similar activation behavior. From this figure it is possible to see how, for many instances, increasing both the energy and dose by the same factor leads to essentially the same electrical activity. Similar results are shown in Figures 3-42 to 3-43 for temperatures of 750⁰C and 850⁰C.

3.3.6 Mobility Data

Hall effect provides two important pieces of information. One is the carrier sheet number, or number of carriers per unit area, and the other is the mobility of these carriers. The carrier density and clustered boron densities are approximated by dividing the implanted boron dose by twice the projected range of the implant and multiplying by either the fractional activation or the fractional deactivation. By then analyzing the carrier mobility as a function of both the carrier density and as a function of the clustered boron density additional information about the boron clustering process may be obtained. The plot of the hole mobility vs. the carrier density is shown in Figure 3-44. This figure agrees reasonably well with published hole mobility data, although, it must be mentioned that the measured mobility values are higher than the published values. This is possibly due to the inherent error which will exist in our means of approximating the carrier densities.

Figure 3-45 illustrates the hole mobility as a function of the clustered boron density. This plot does not show any clear trend, however, analysis of the same data at fixed values of the carrier density shows a trend towards reduced hole mobility with increasing clustered boron density as shown in Figure 3-46. This result supports the idea of a fractionally active boron complex which would also scatter holes leading to reduced mobility. At higher concentrations of clustered boron, such results are less clear.

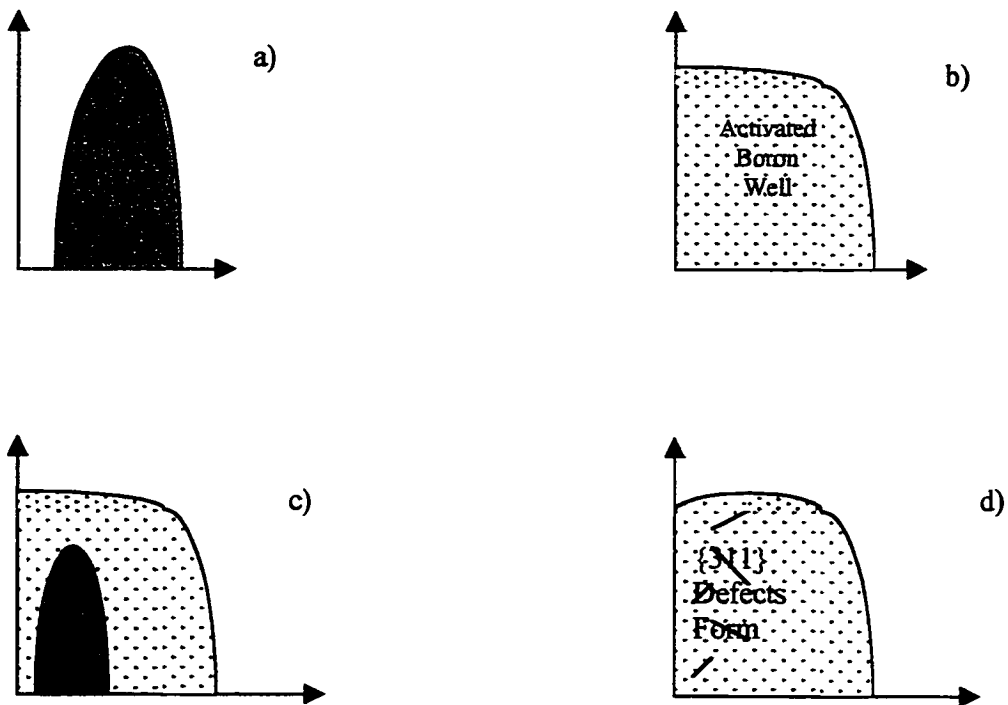


Figure 3-1 Process flow of boron-doped well experiment. a) Boron is implanted at 400 keV and b) annealed at 1100°C for 330 minutes for form a very deep and uniform highly-activated well region c) Silicon is implanted to induce damage and then d) annealed at various times and temperatures to form extended defects and cluster the boron.

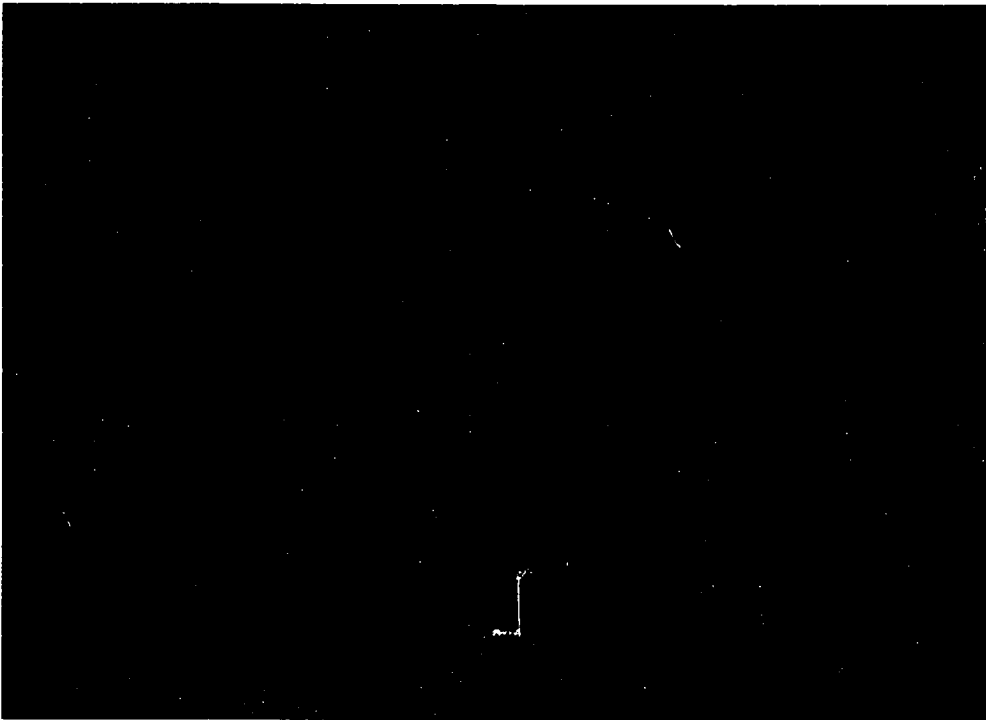


Figure 3-2 Plan view TEM from the boron well experiment following anneals at 740°C for 10 minutes. The micrograph on the left shows the $5 \times 10^{16} \text{ cm}^{-3}$ concentration well and the right micrograph shows the $1.2 \times 10^{18} \text{ cm}^{-3}$ boron-doped well. Both wells received identical 40 keV $1 \times 10^{14} \text{ cm}^{-2}$ silicon implants to induce damage. Note that there are significantly more {311} defects in the more lightly doped sample.

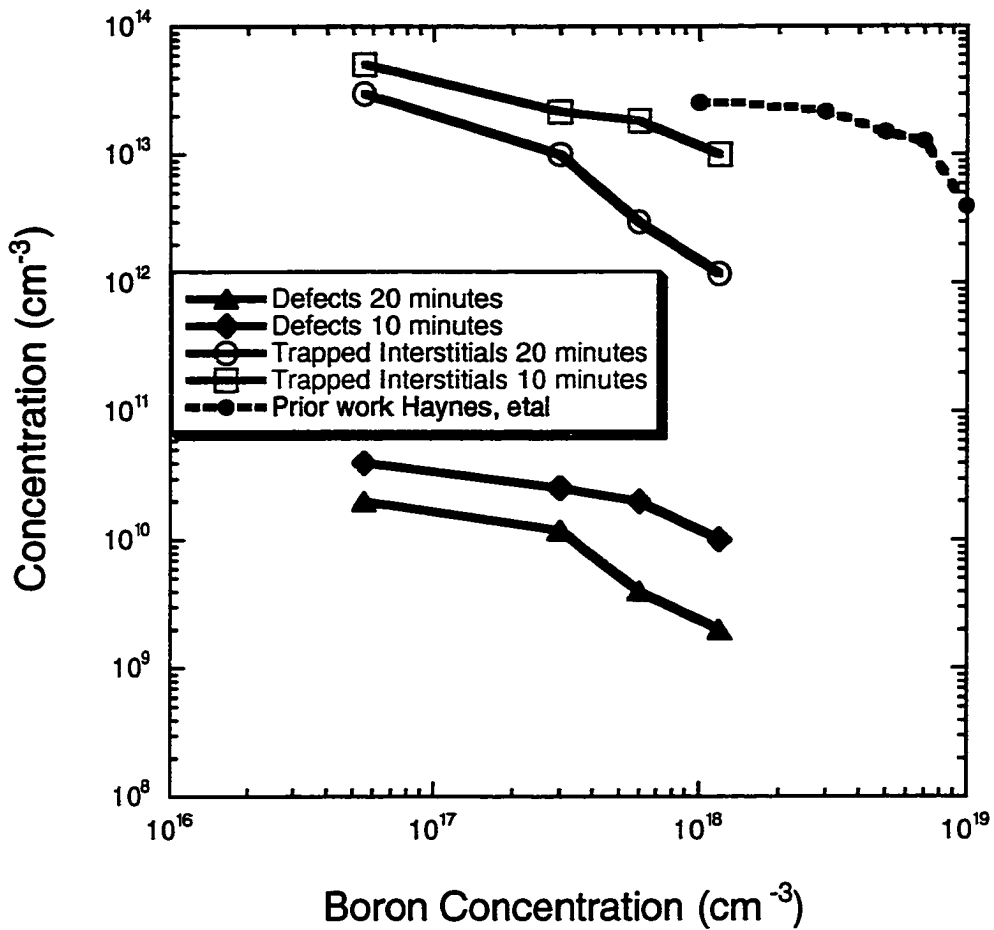


Figure 3-3 Results of defect counts from the boron-doped well experiment. Note that there are both fewer {311} defects and fewer trapped interstitials with increasing boron density. Results shown for a 740°C anneal with a silicon implant of 40 keV at $1 \times 10^{14} \text{ cm}^{-2}$ dose. Shown for reference are the results of a prior study [Hay 96] in which similar structures were formed into float zone material and annealed at 740°C for 15 minutes.

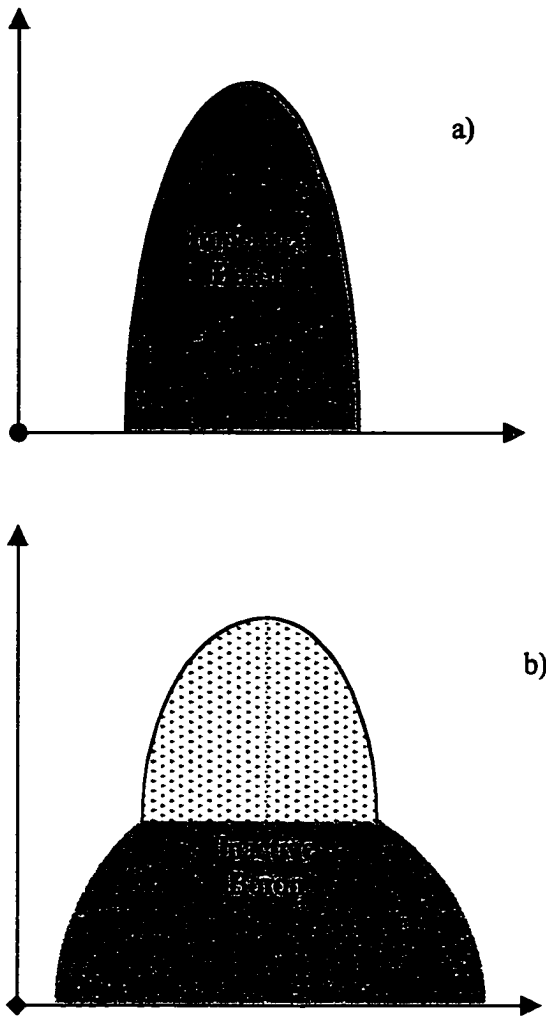


Figure 3-4 Process sequence for boron implant experiment. First a) boron is implanted into lightly n-type silicon wafers at various doses and energies as outlined in table 3-1. Then, b) the material is annealed at various times and temperatures as outlined in table 3-2.

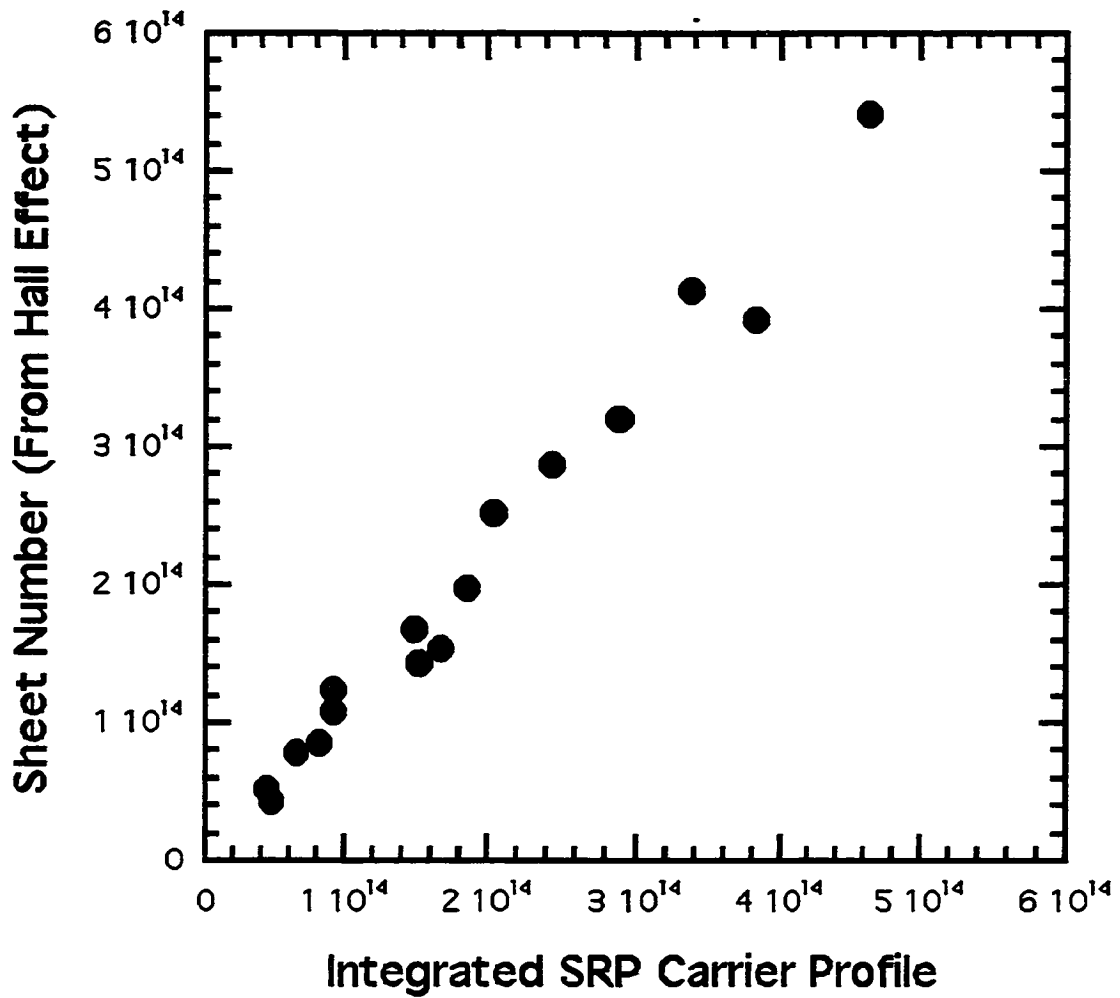


Figure 3-5 Comparison of the integrated spreading resistance profile and sheet number obtained from Hall effect measurement for anneals conducted at 750°C and 850°C for up to one hour. Note that the correlation is nearly 1:1 over the range of carrier densities. This is pooled data (all applicable implants/anneals).

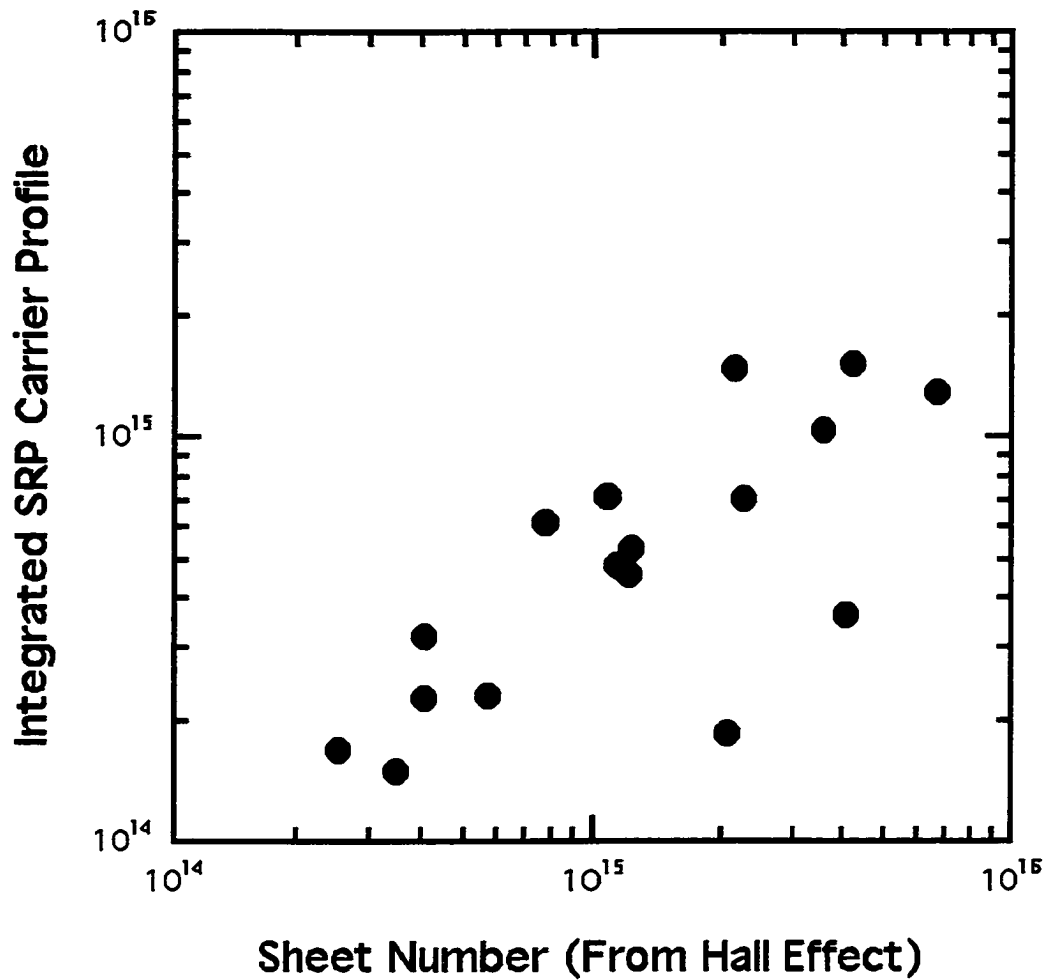


Figure 3-6 Comparison of the integrated spreading resistance carrier profile and the sheet number obtained from Hall effect measurements for anneals at 850°C for times of greater than one hour, at 950°C and 1000°C . Note that there is significant deviation between the two techniques for these samples with the Hall effect measurement always yielding a higher sheet number than the integrated SRP profile. This is pooled data (all applicable implants/anneals).

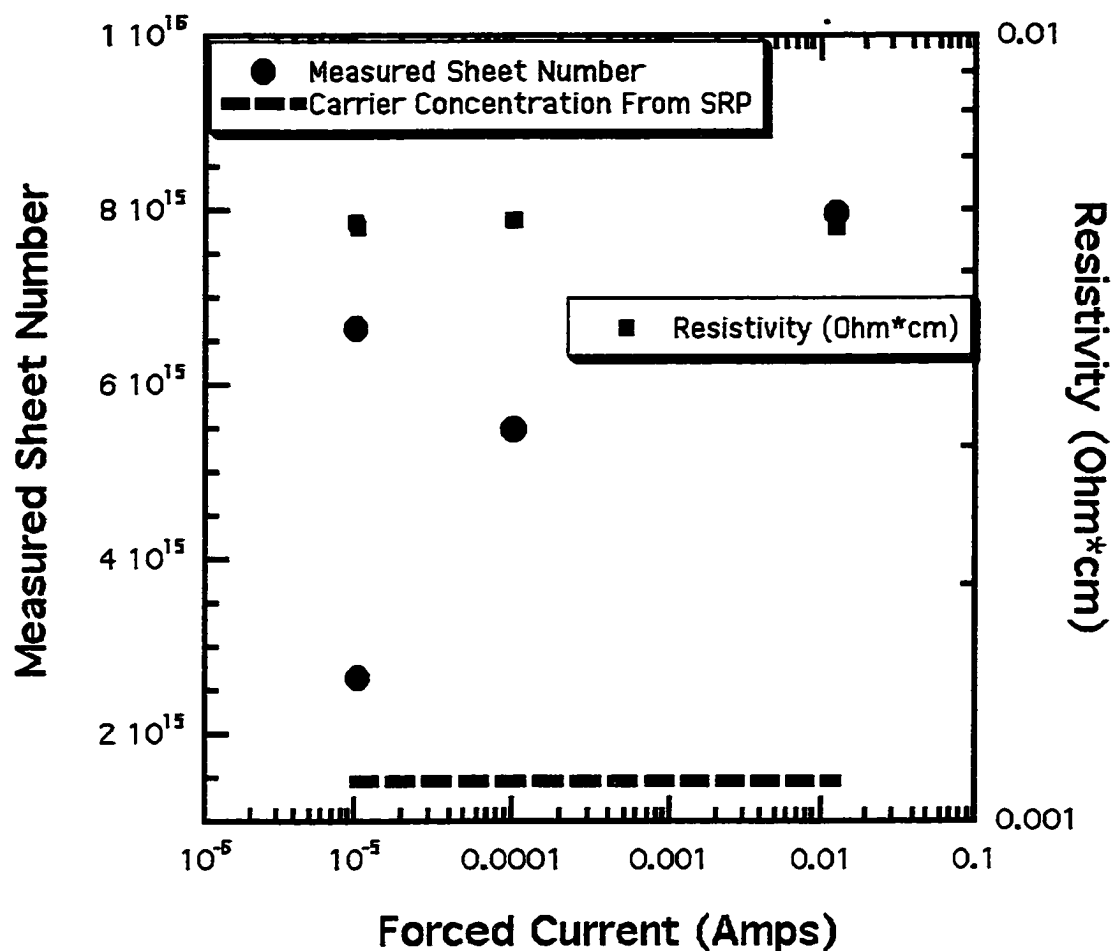


Figure 3-7 Plot showing the variation from run to run in hall effect measurements for samples exhibiting substantial non-uniformity in the carrier profile. Note that the resistivity measurement is nearly constant, while the sheet number measurement is wildly variable. For reference, the integrated SRP value is also plotted on this graph. Also note, that this variation is not necessarily a function of current as exhibited by the two data points at 10 μA current. Sample being analyzed here was a 80 keV $1.6 \times 10^{15} \text{ cm}^{-2}$ boron implant annealed at 750°C for 30 minutes.

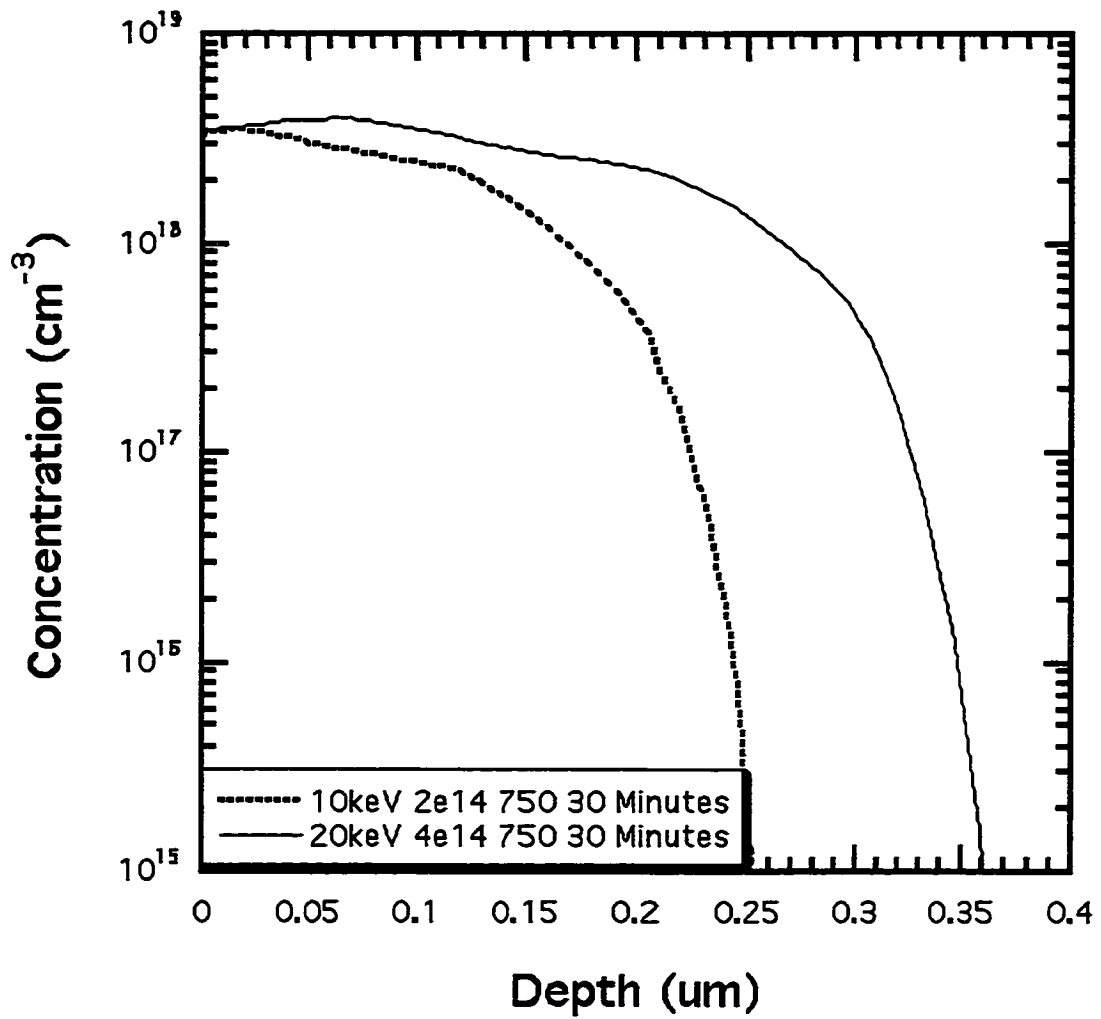


Figure 3-8 Reactivation of a boron implants following a 750°C 30 minute anneal as seen through the spreading resistance profiles. Both samples contain similar dopant densities. Note that the carrier profile saturates at approximately $4 \times 10^{18} \text{ cm}^{-3}$ for both profiles.

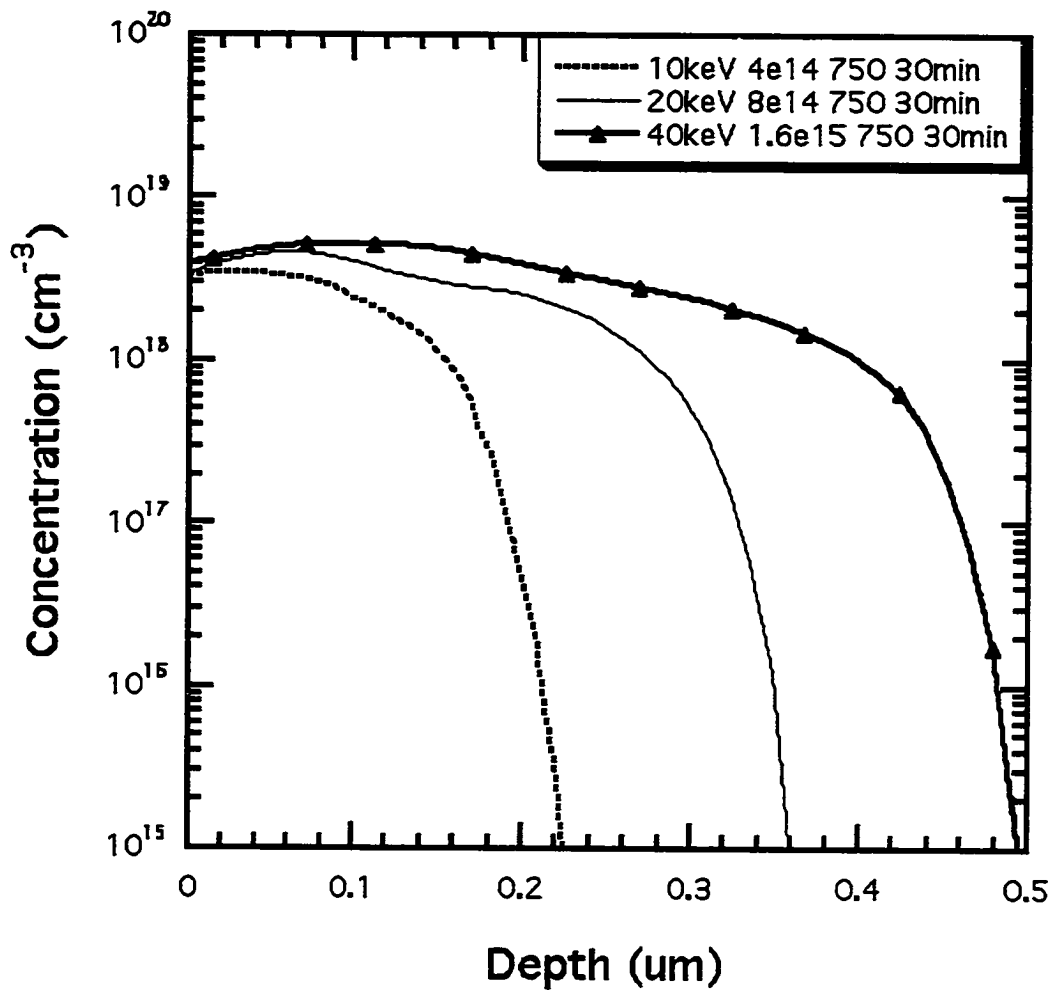


Figure 3-9 Reactivation process at 750°C. Note how the carrier concentration again saturates at approximately $4 \times 10^{18} \text{ cm}^{-3}$ for these 30 minute anneals at 750°C.

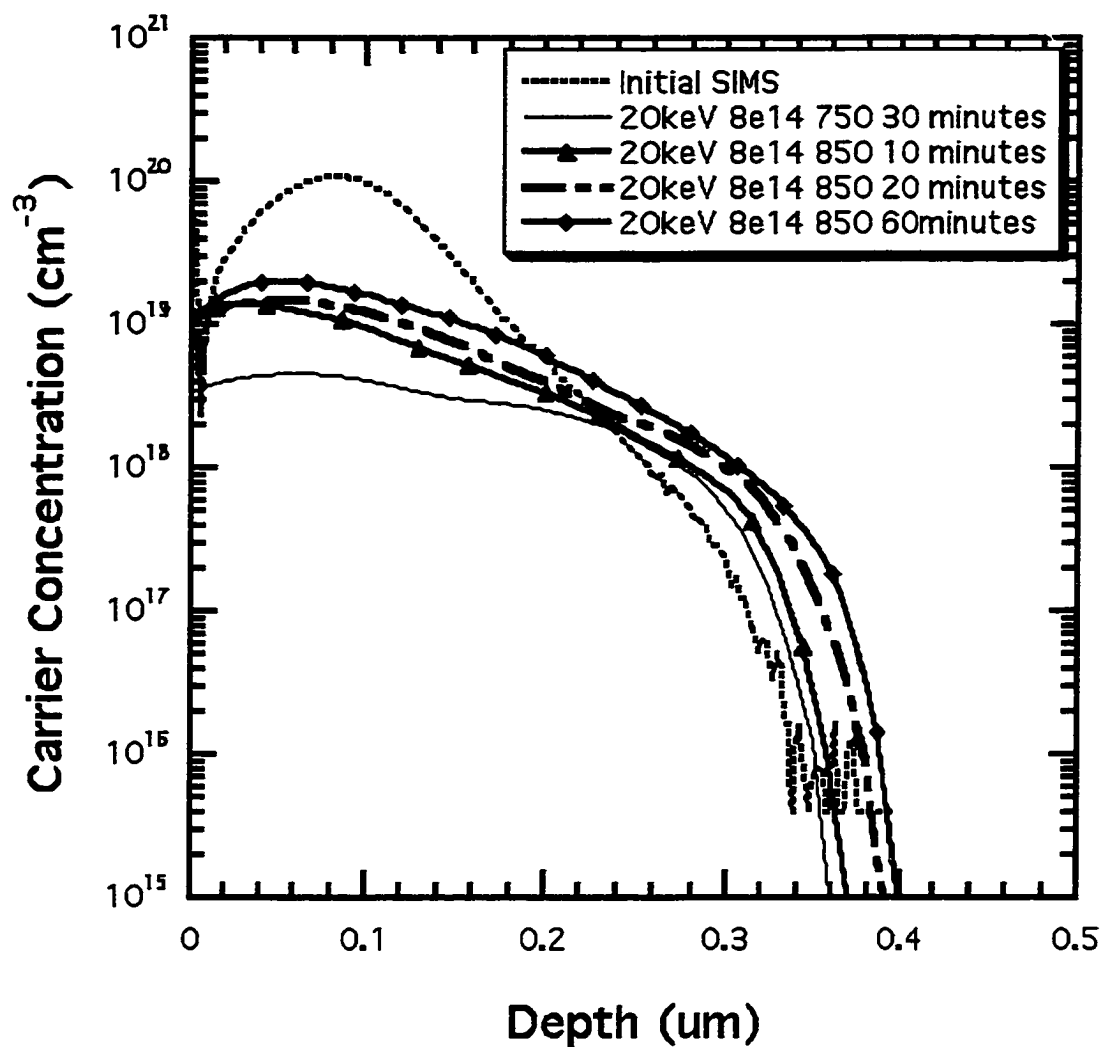


Figure 3-10 Reactivation at 850°C. Note how the carrier profiles saturate at approximately $1-2 \times 10^{19} \text{ cm}^{-3}$ for these anneals at 850°C. There is also a tendency exhibited here for the material to reactivate from the surface to the bulk. All of these anneals are from a clustered state induced by a 750°C 30 minute anneal.

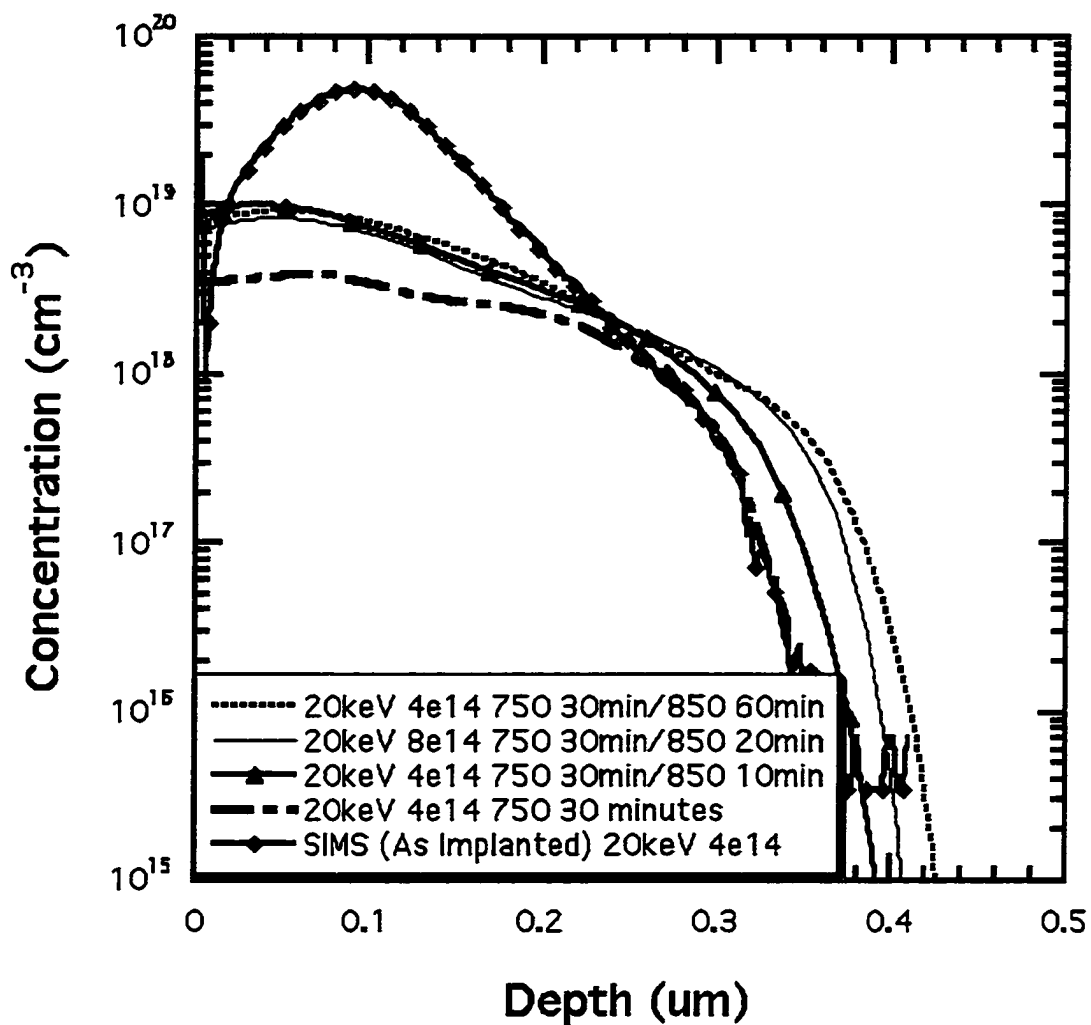


Figure 3-11 SRP profiles of the reactivation process at 850°C for a 20 keV $8 \times 10^{14} \text{ cm}^{-2}$ boron implant reactivated at various times at 850°C. Note the transient enhanced diffusion effects and that the reactivation is mediated by a slight “swelling” of the shorter time profile. All of these anneals are from a clustered state induced by a 750°C 30 minute anneal.

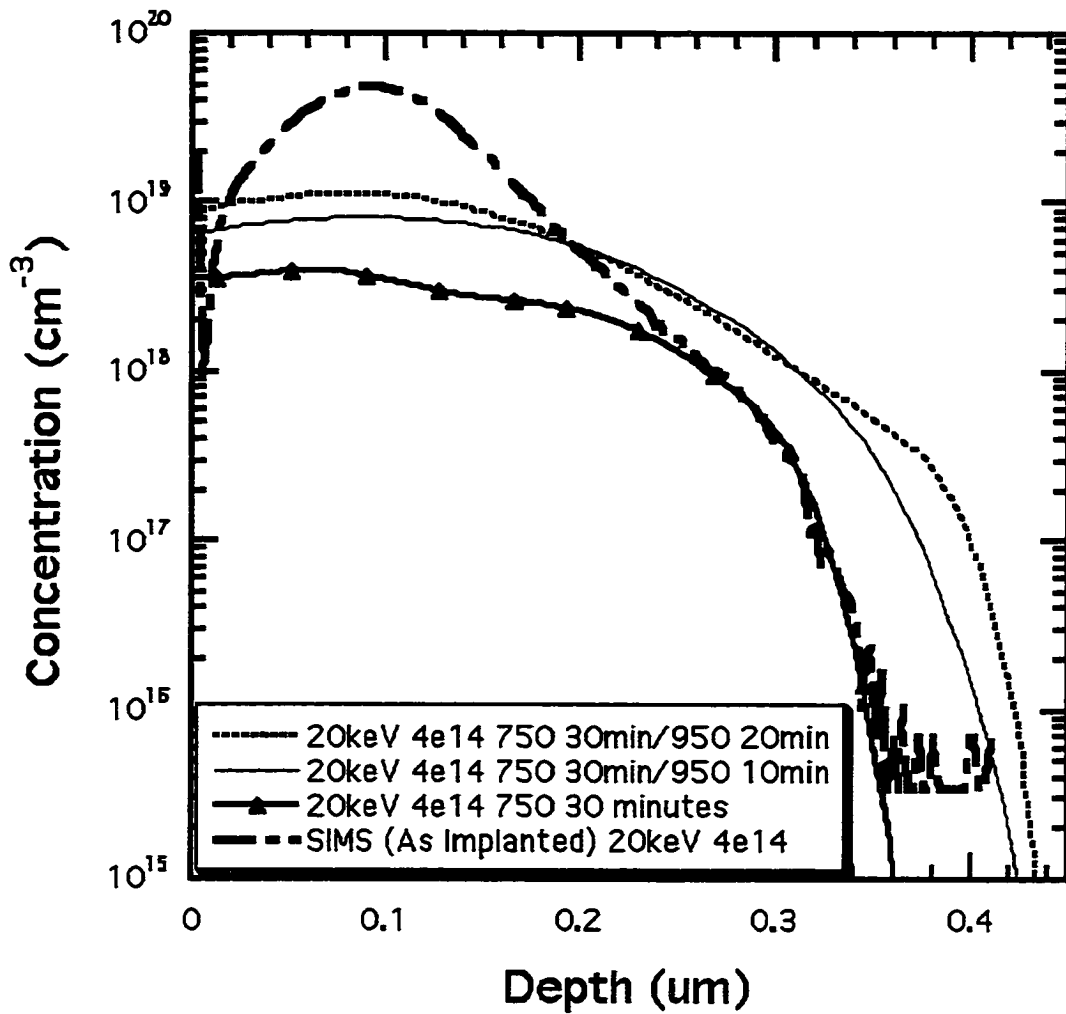


Figure 3-12 Reactivation of a 20 keV $4 \times 10^{14} \text{ cm}^{-2}$ boron implant at 950°C as seen through the spreading resistance profiles. All of these anneals are from a clustered state induced by a 750°C 30 minute anneal.

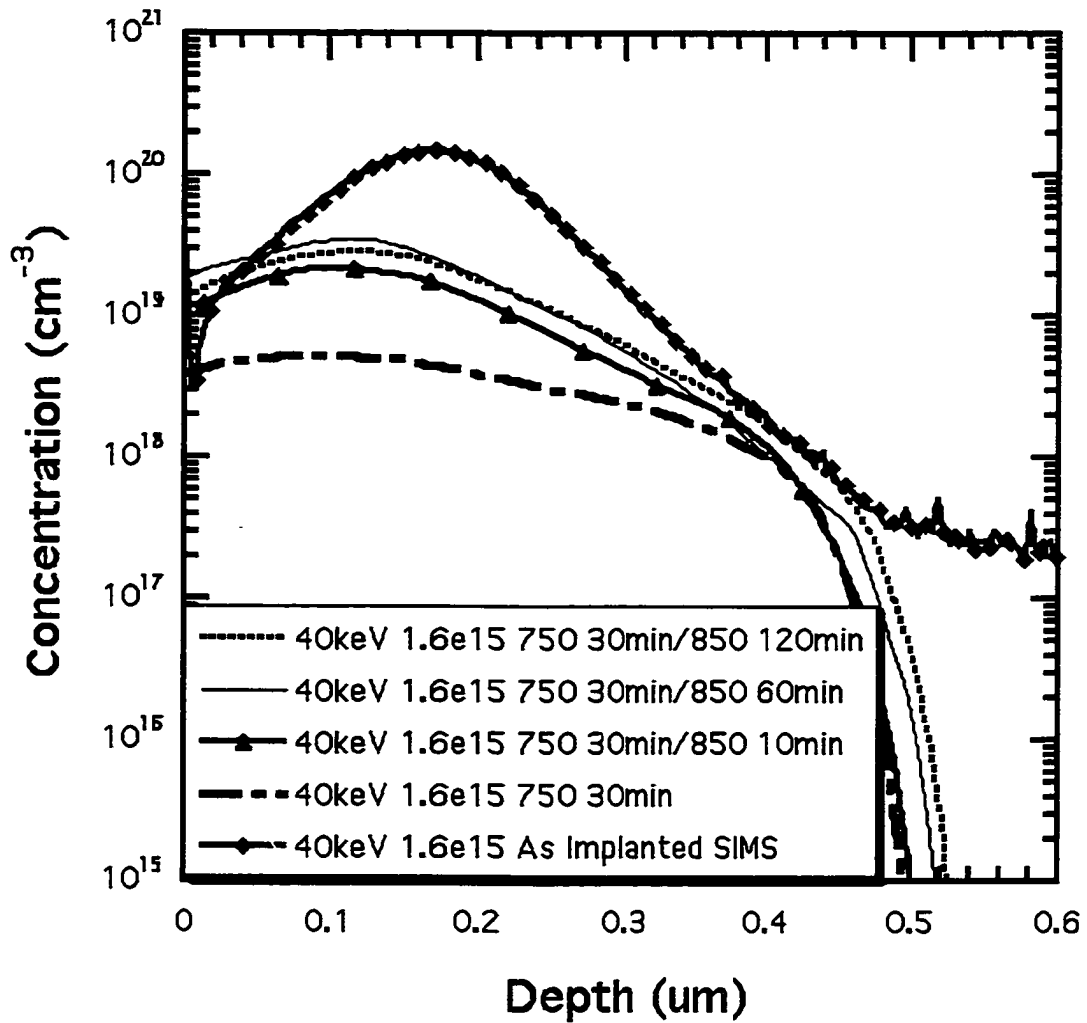


Figure 3-13 Reactivation of a 40 keV $1.6 \times 10^{15} \text{ cm}^{-2}$ boron implant at 850°C as seen through the spreading resistance profiles. All of these anneals are from a clustered state induced by a 750°C 30 minute anneal.

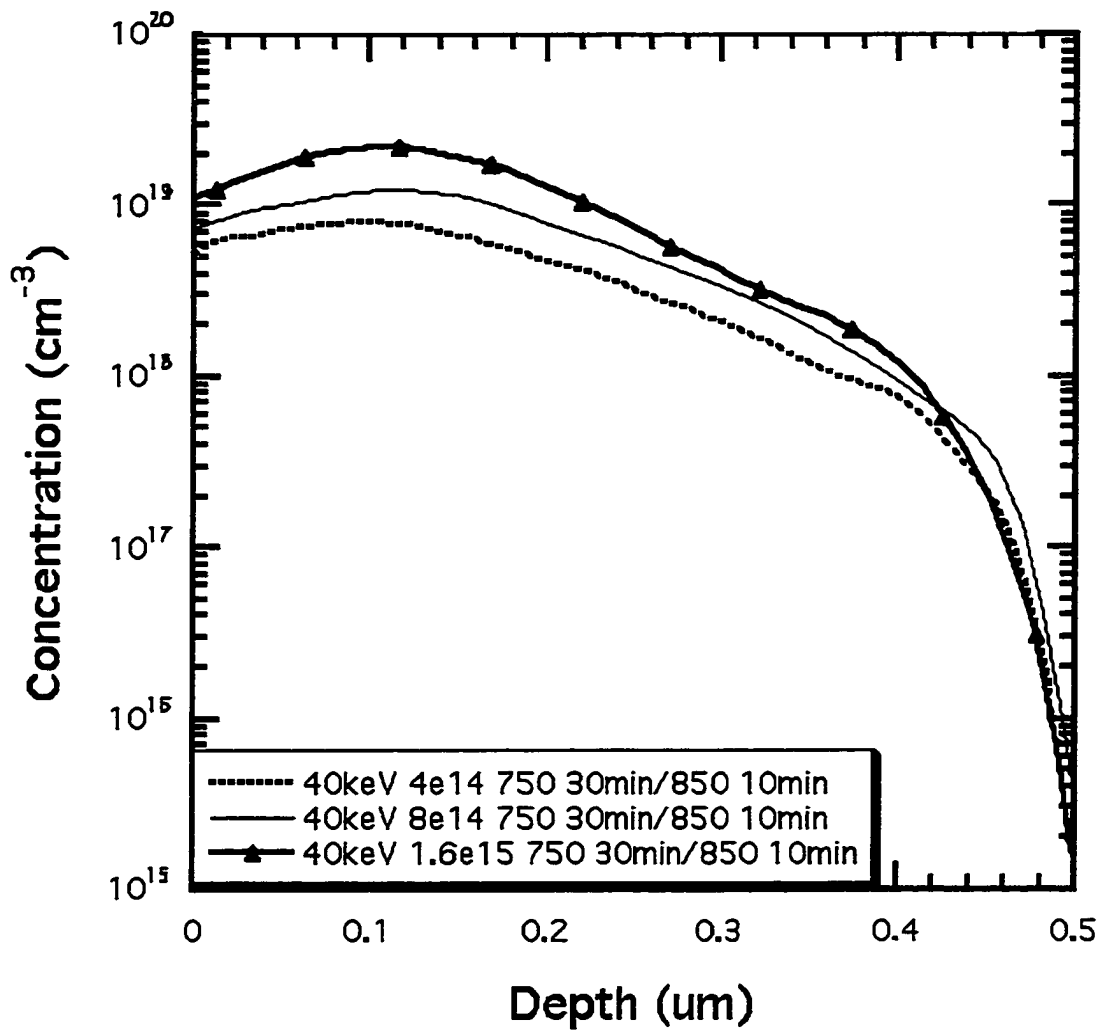


Figure 3-14 Reactivation at 850°C of 40 keV boron implants of various doses. All of these anneals are from a clustered state induced by a 750°C 30 minute anneal.

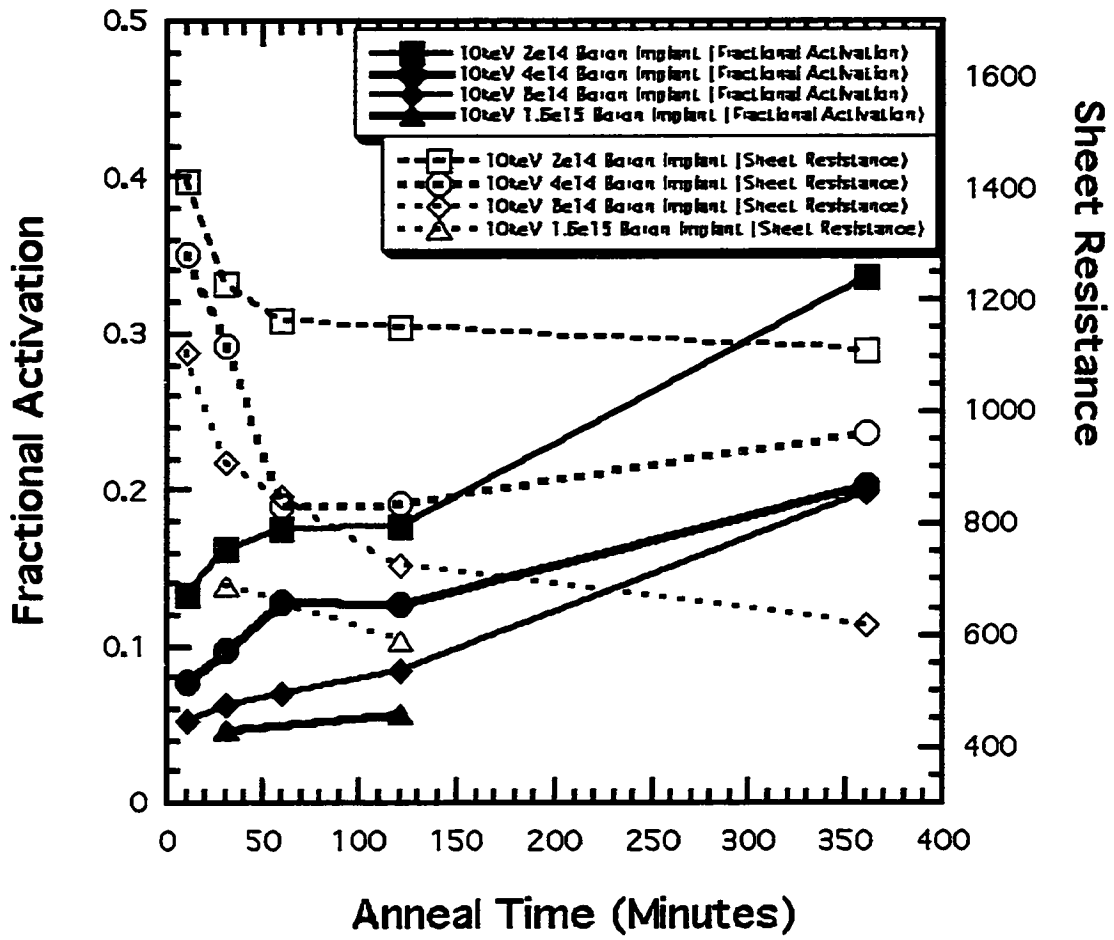


Figure 3-15 Activation of 10 keV boron implants at various doses at 750°C.

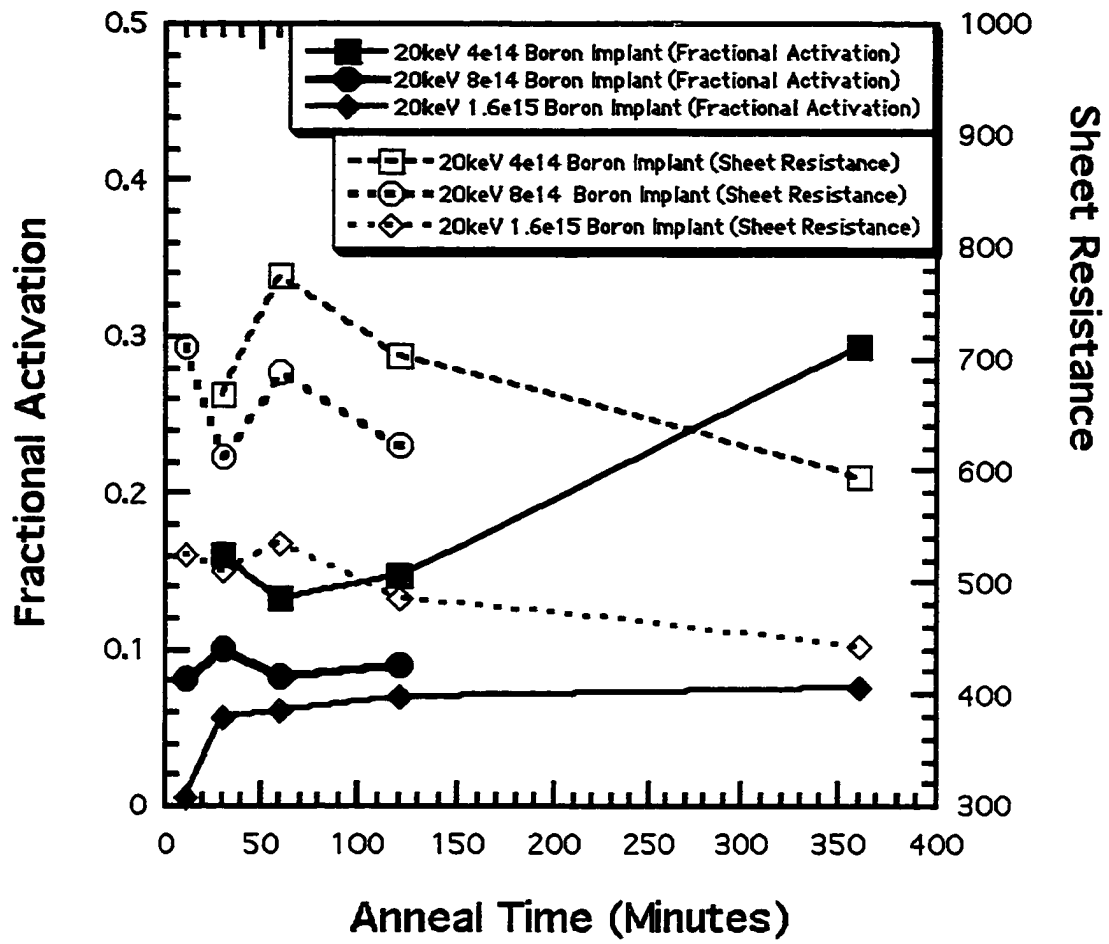


Figure 3-16 Activation of 20 keV boron implants at various doses at 750°C.

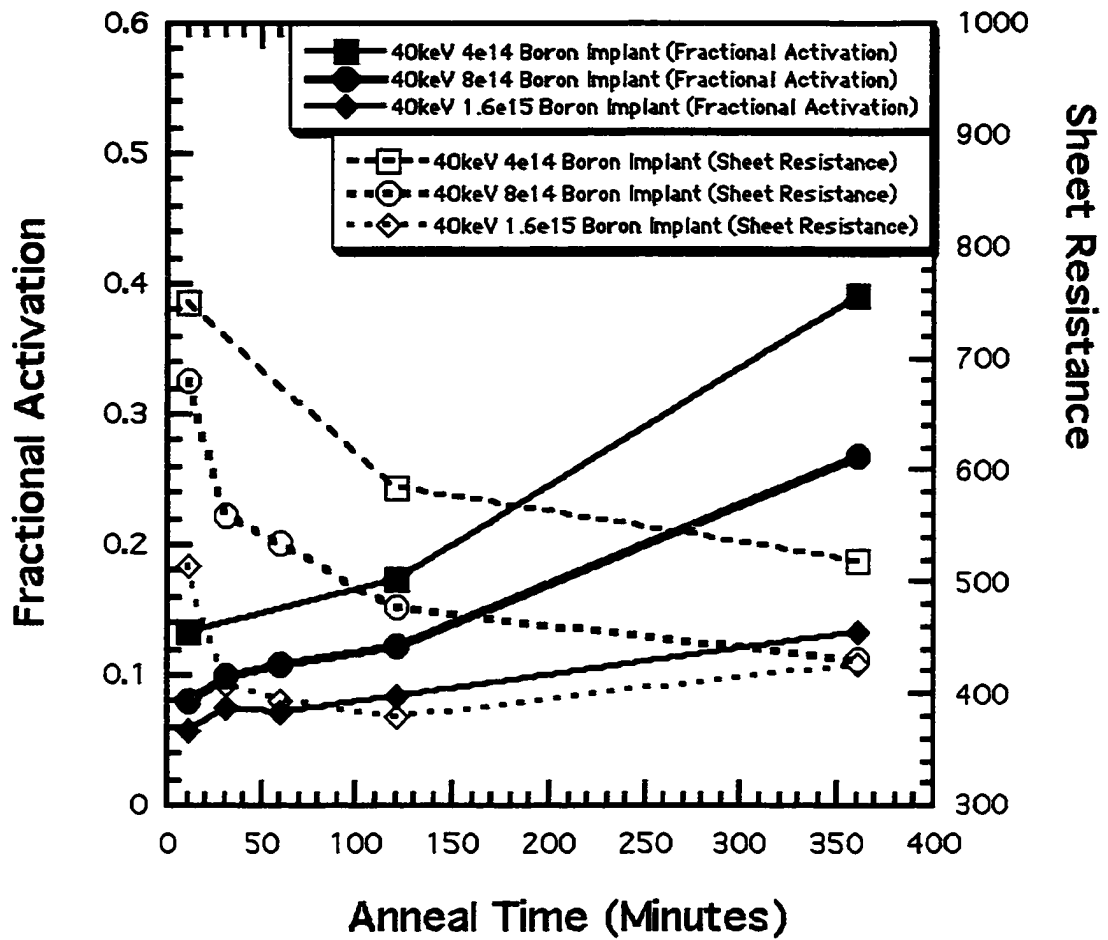


Figure 3-17 Activation of 40 keV boron implants at various doses at 750°C.

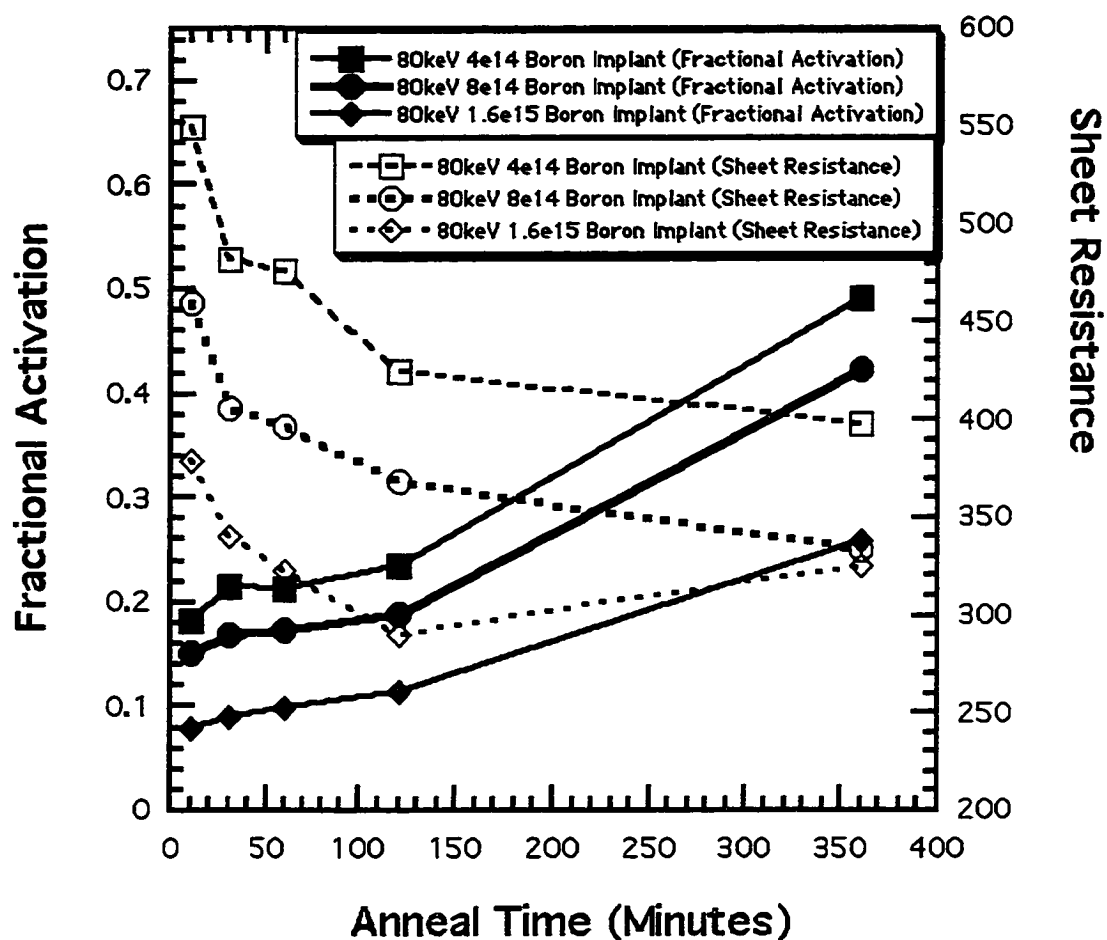


Figure 3-18 Activation of 80 keV boron implants at various doses at 750°C.

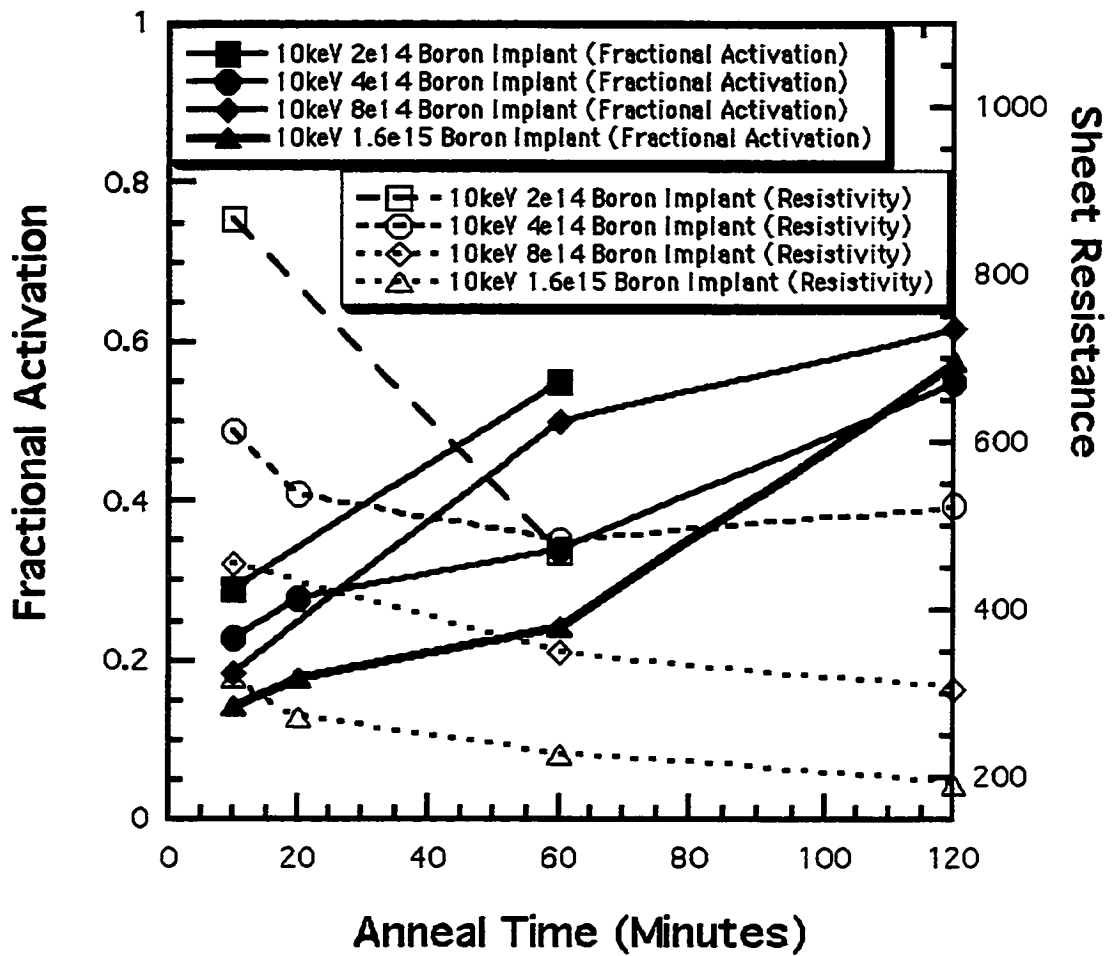


Figure 3-19 Activation of 10 keV boron implants at various doses at 850°C. All of these anneals are from a clustered state induced by a 750°C 30 minute anneal.

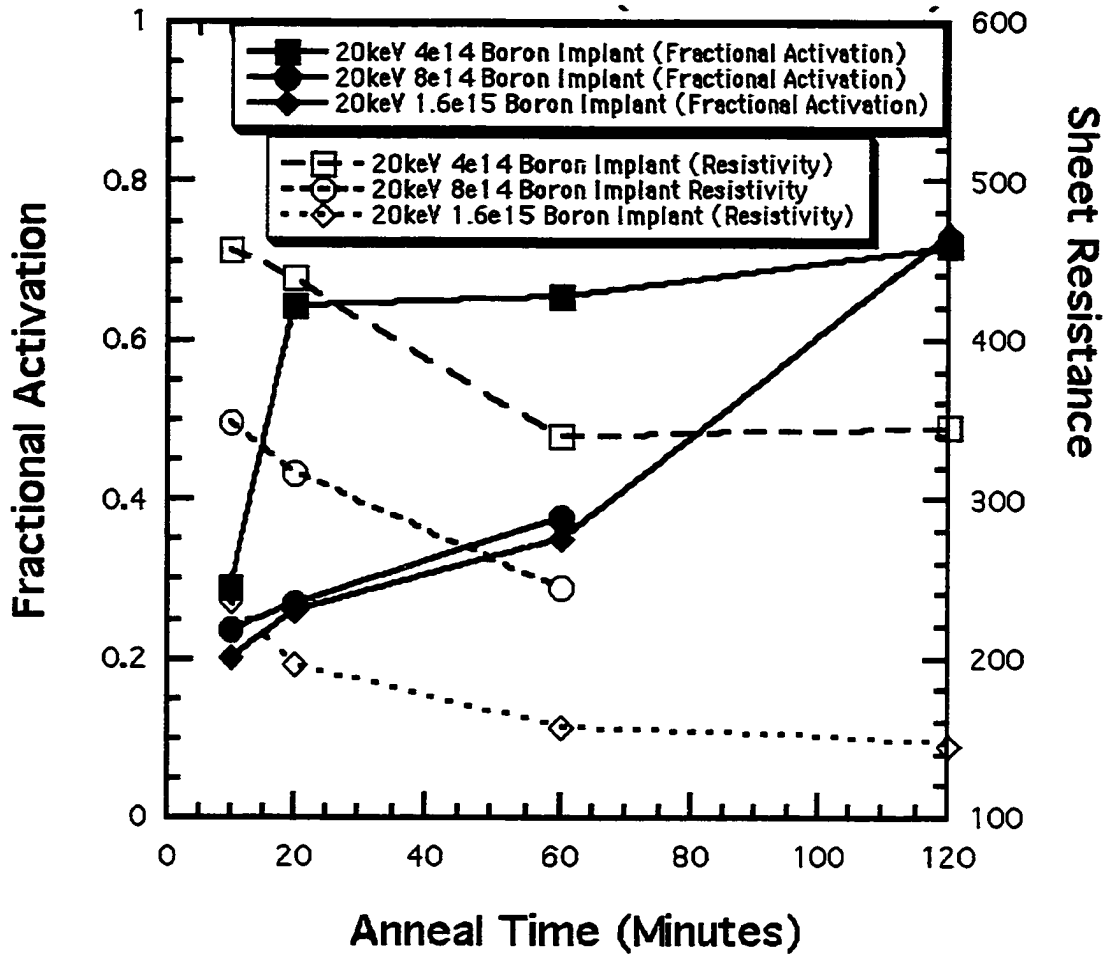


Figure 3-20 Activation of 20 keV boron implants at various doses at 850°C. All of these anneals are from a clustered state induced by a 750°C 30 minute anneal.

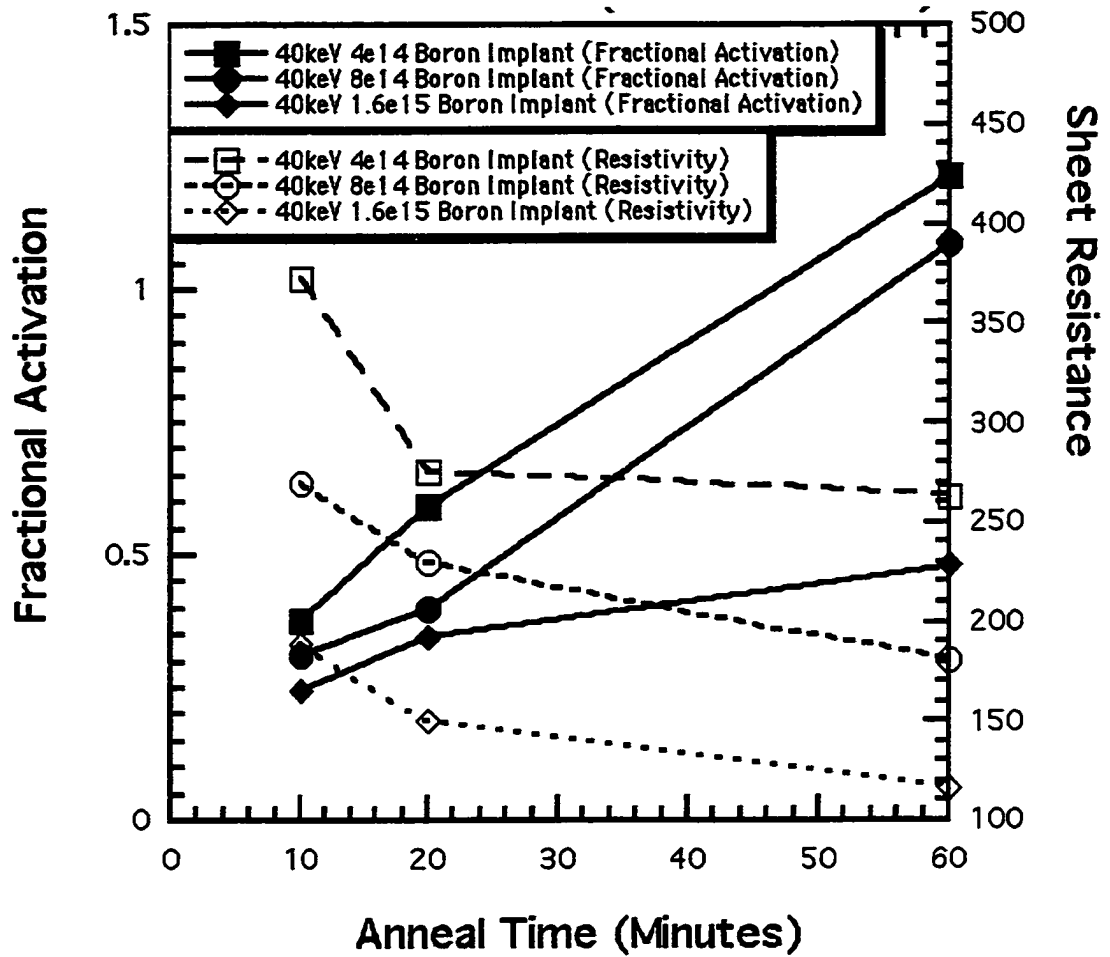


Figure 3-21 Activation of 40 keV boron implants at various doses at 850°C. All of these anneals are from a clustered state induced by a 750°C 30 minute anneal.

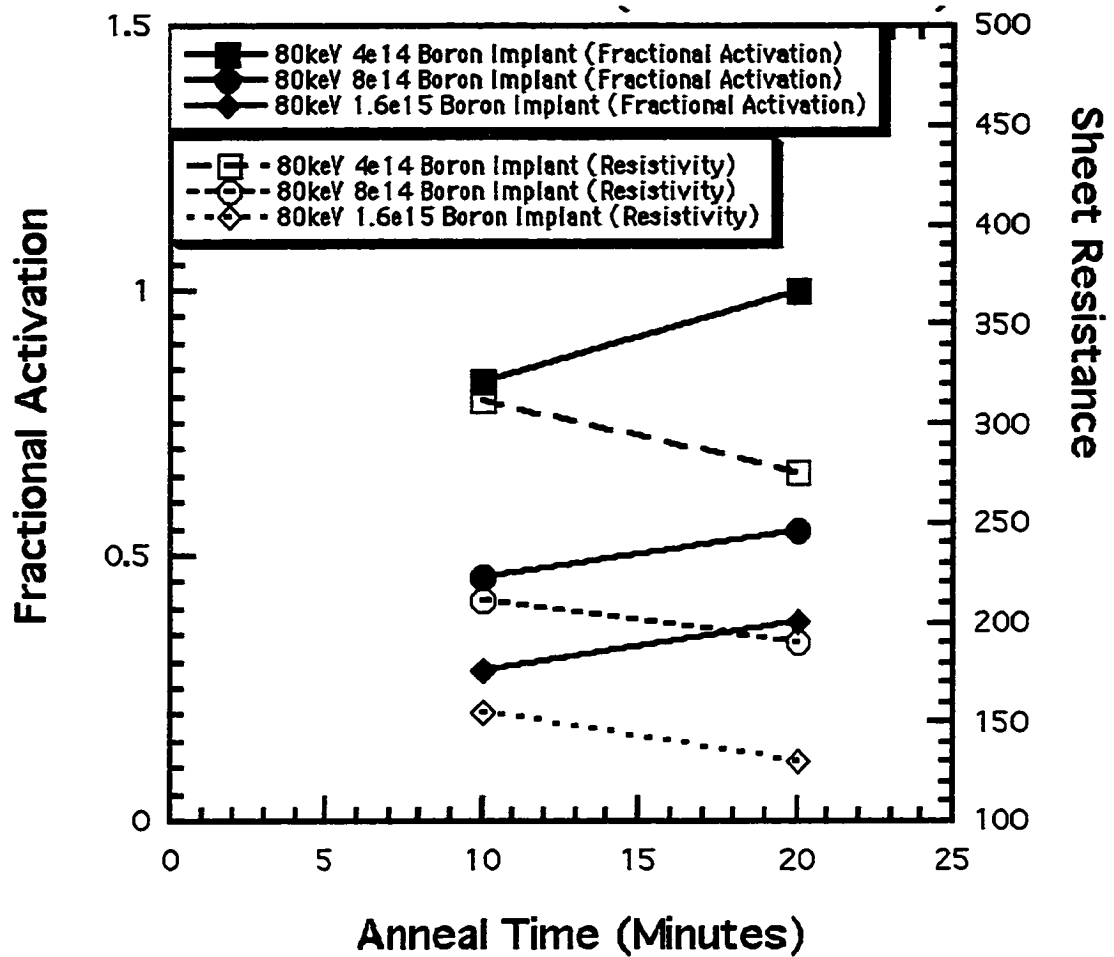


Figure 3-22 Activation of 80 keV boron implants at various doses at 850°C. All of these anneals are from a clustered state induced by a 750°C 30 minute anneal.

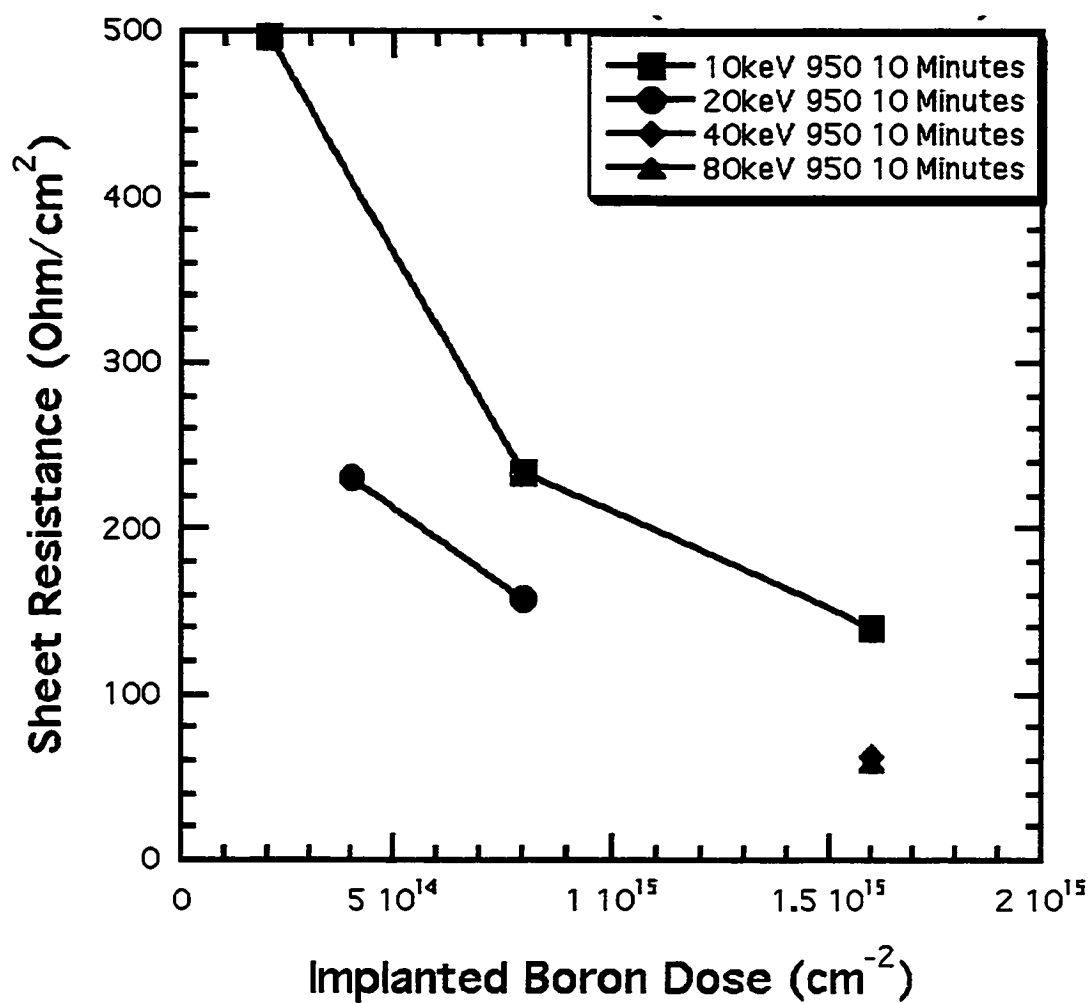


Figure 3-23 Activation of boron implants at various doses following a 10 minute anneal at 950°C. All of these anneals are from a clustered state induced by a 750°C 30 minute anneal.

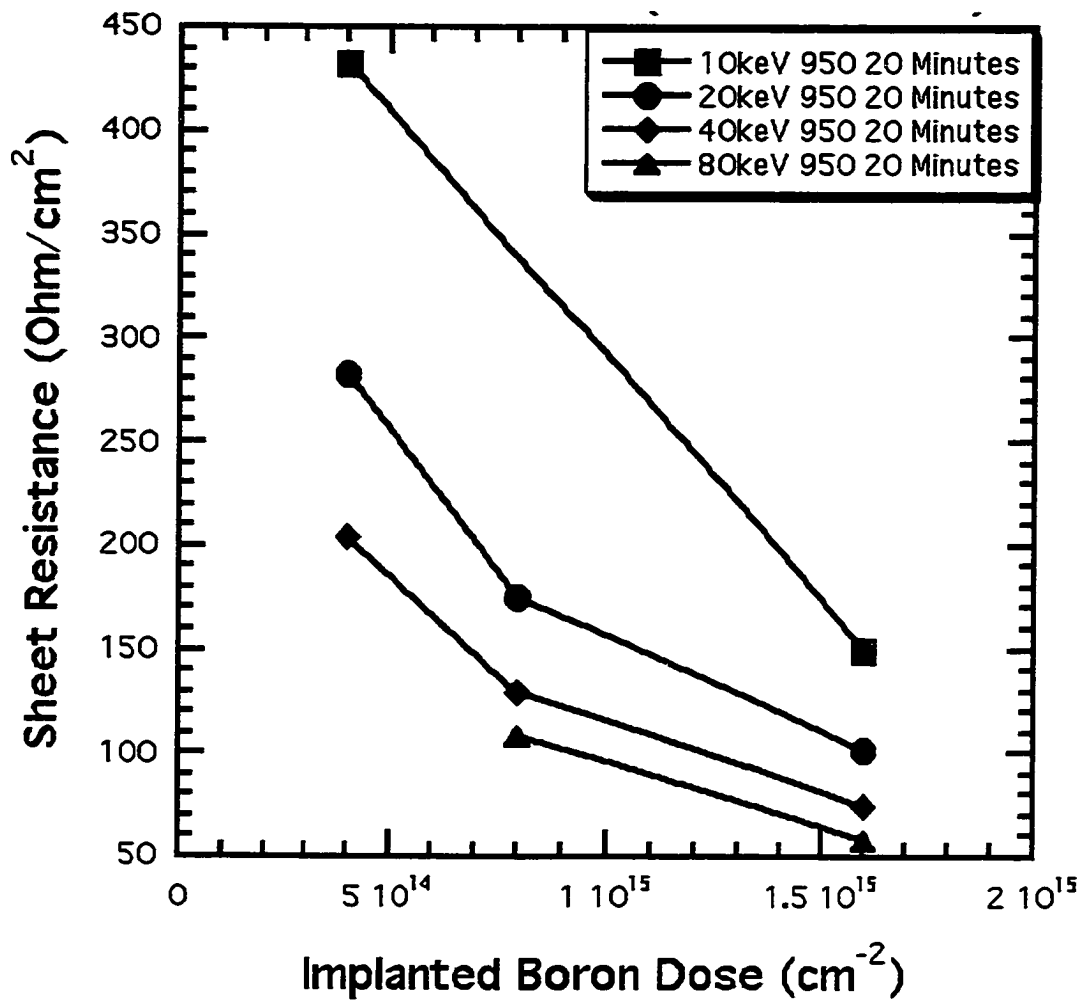


Figure 3-24 Activation of boron implants at various doses following a 20 minute anneal at 950°C. All of these anneals are from a clustered state induced by a 750°C 30 minute anneal.

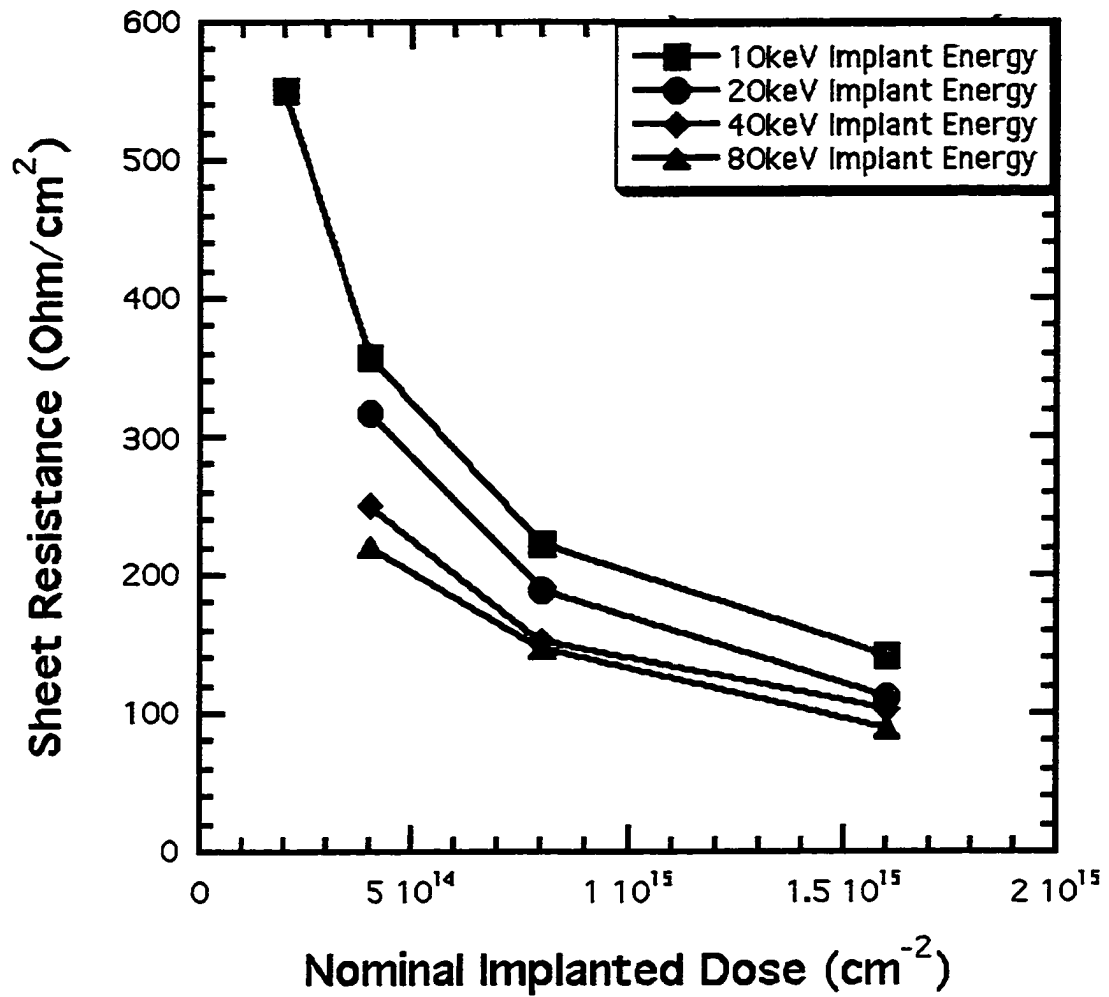


Figure 3-25 Activation of boron implants at various doses following a 2 minute anneal at 1000⁰C. All of these anneals are from a clustered state induced by a 750⁰C 30 minute anneal.

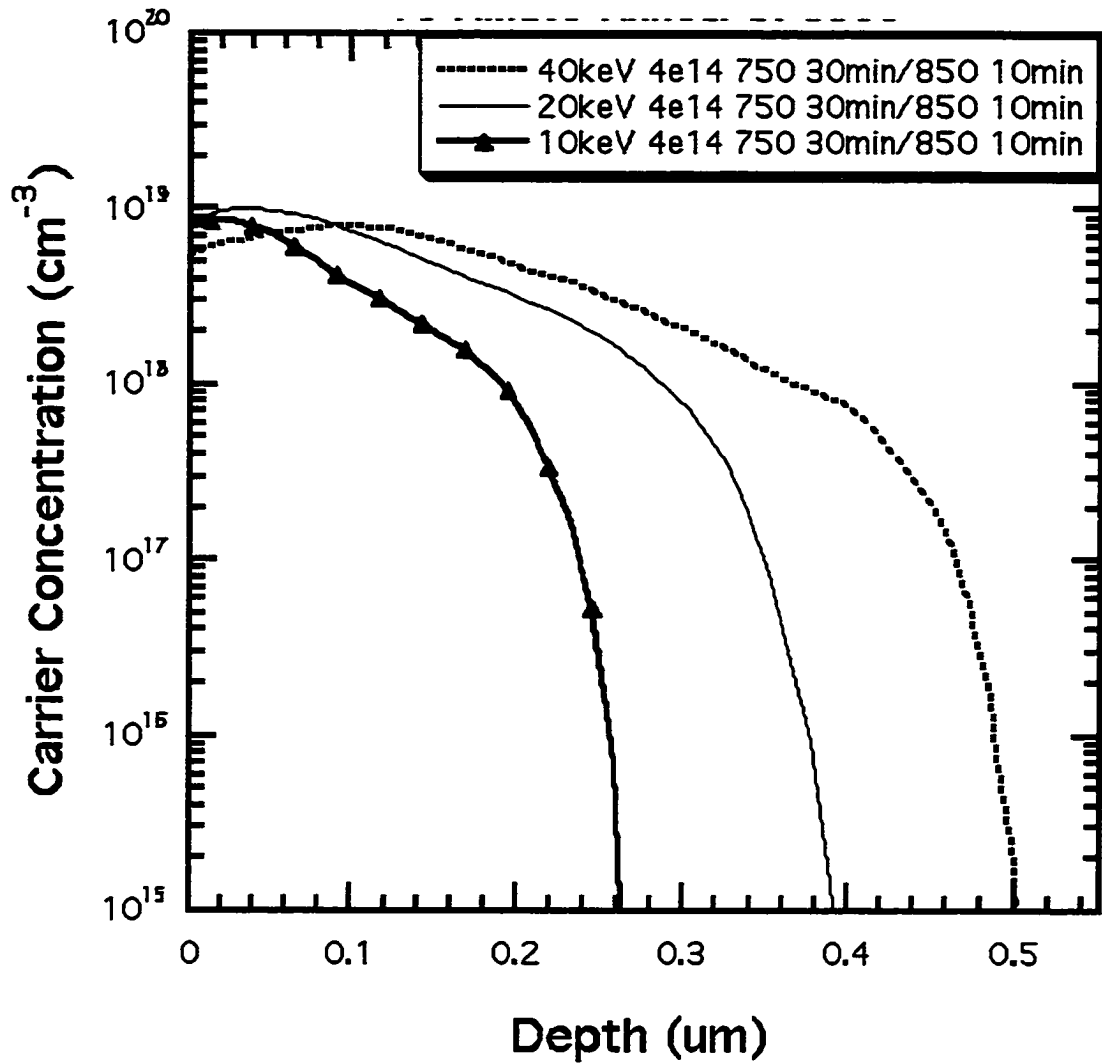


Figure 3-26 Reactivation process of $4 \times 10^{14} \text{ cm}^{-2}$ boron implants as the implant energy is varied. The samples were initially clustered with a 750°C 30 minute and reactivated with the 10 minute anneal at 850°C . Note that the carrier concentrations saturate at $9 \times 10^{18} \text{ cm}^{-3}$ independent of implant energy.

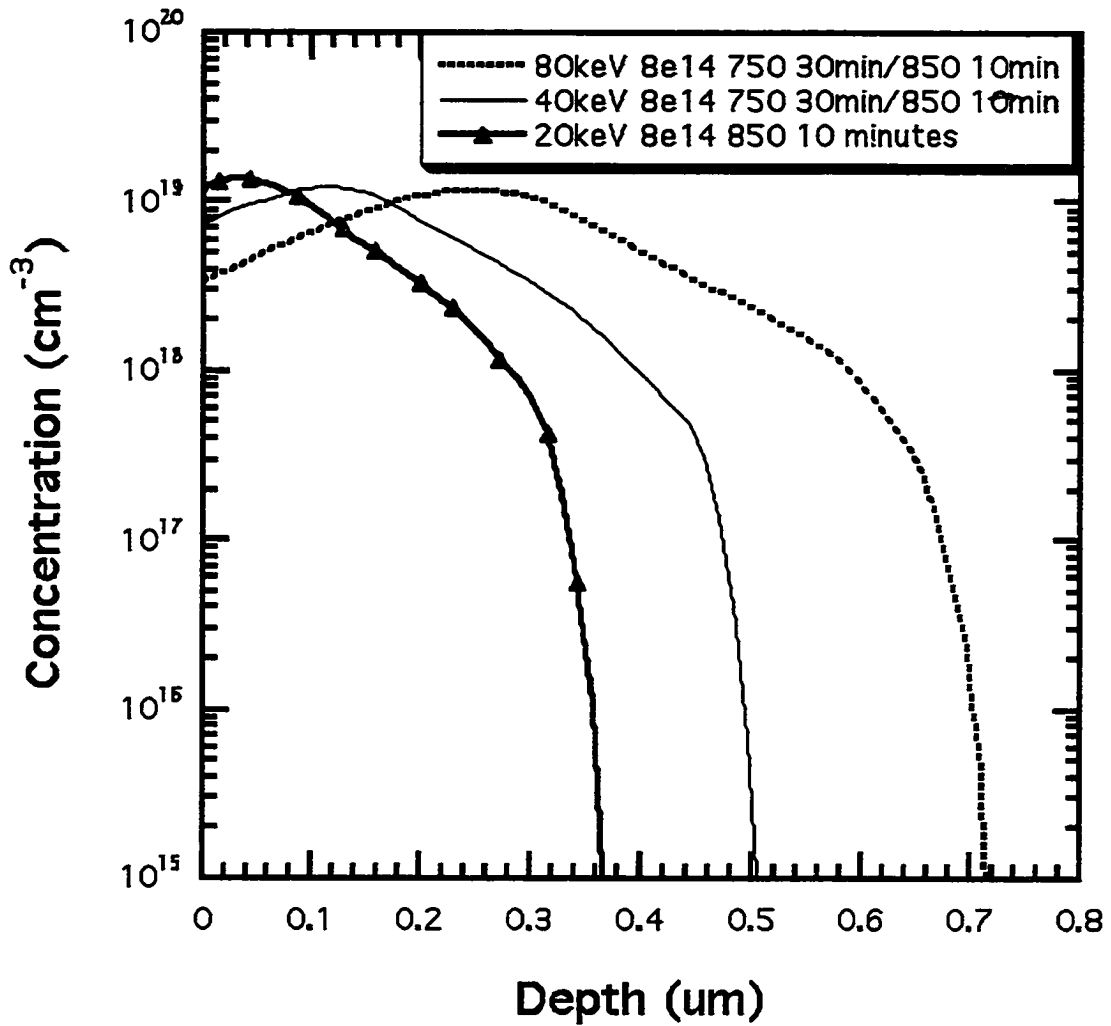


Figure 3-27 Reactivation process of $8 \times 10^{14} \text{ cm}^{-2}$ boron implants as the implant energy is varied. The samples were initially clustered with a 750°C 30 minute and reactivated with the 10 minute anneal at 850°C . Note that the carrier concentrations saturate at $1.2 \times 10^{19} \text{ cm}^{-3}$ independent of implant energy.

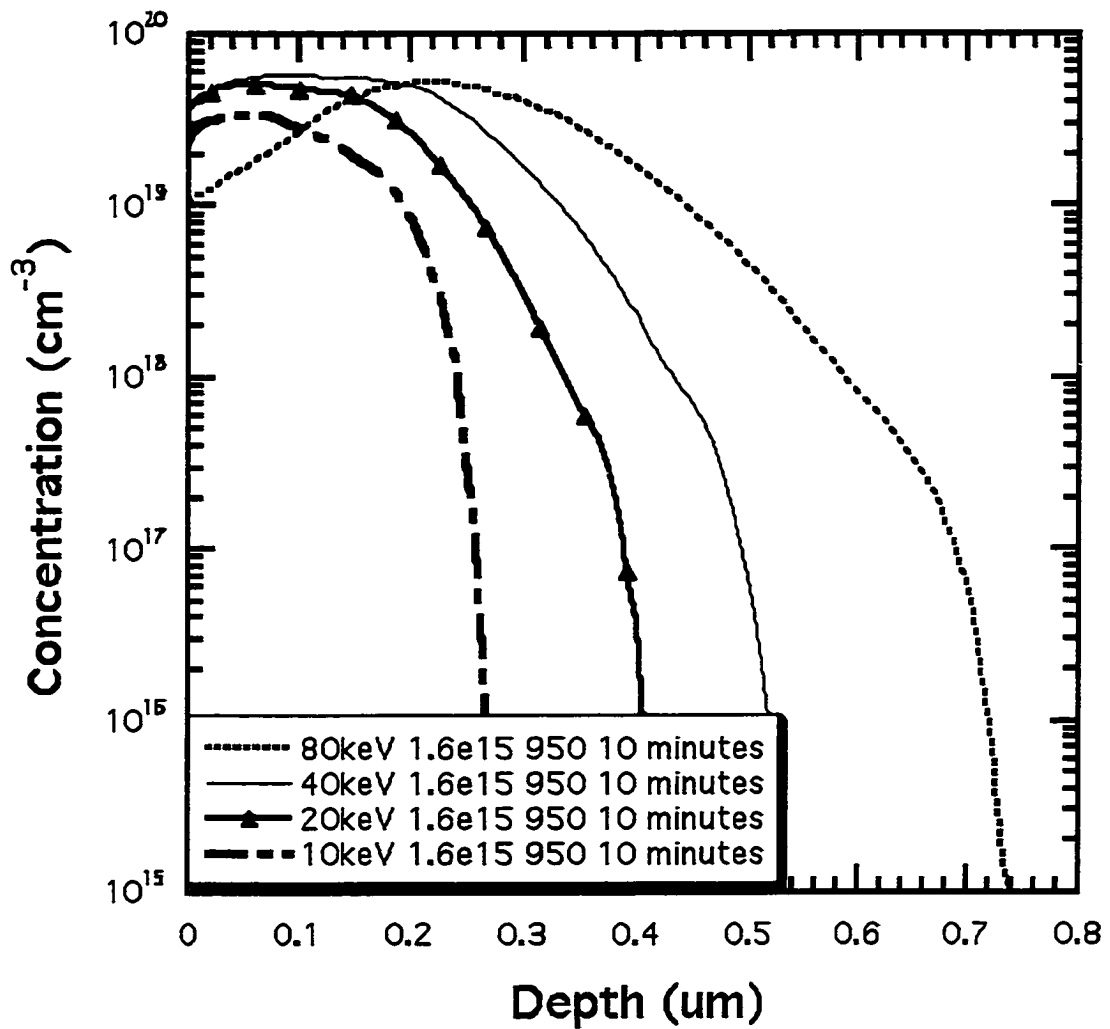


Figure 3-28 Reactivation process of $1.6 \times 10^{15} \text{ cm}^{-2}$ boron implants as the implant energy is varied. The samples were initially clustered with a 750°C 30 minute and reactivated with the 10 minute anneal at 950°C . Note that the carrier concentrations saturate at $5 \times 10^{19} \text{ cm}^{-3}$ independent of implant energy except for the 10 keV sample which is possibly erroneous for reasons discussed.

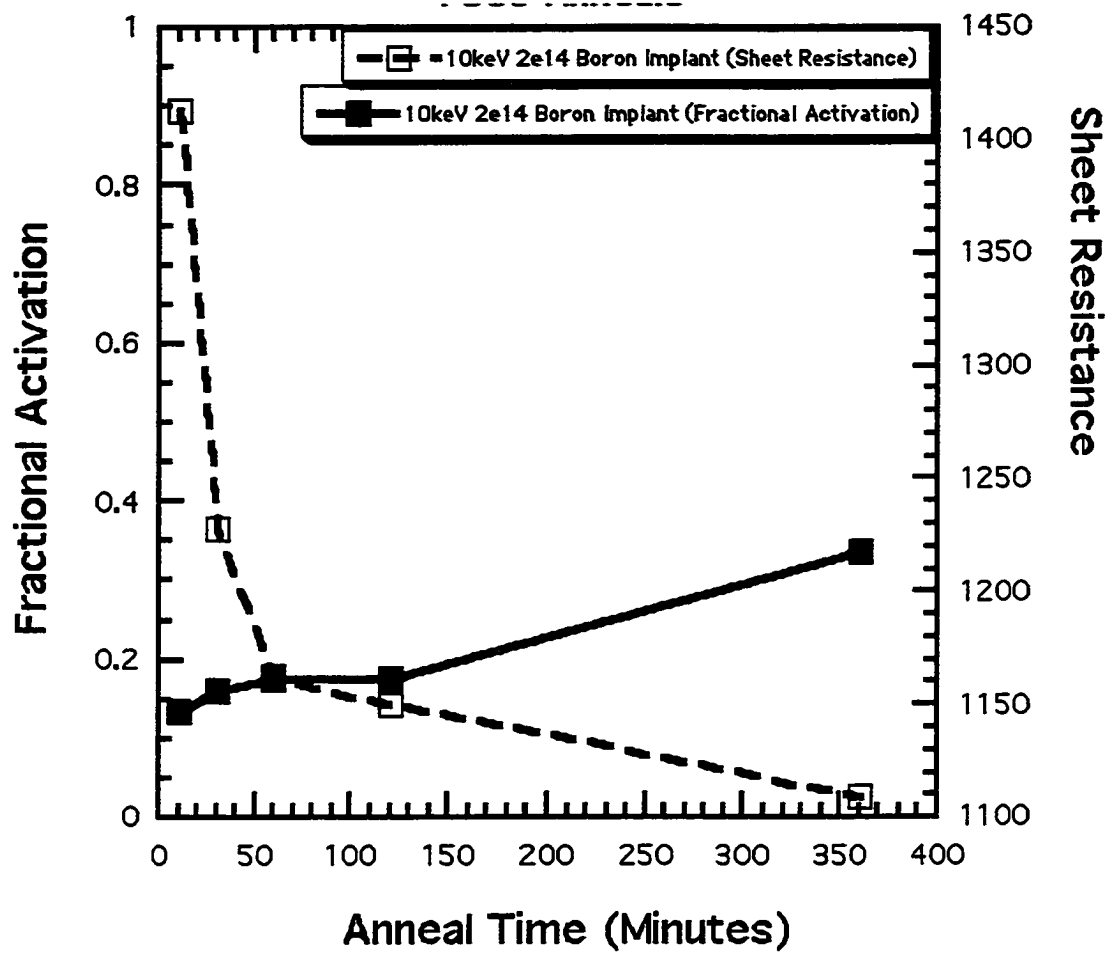


Figure 3-29 Reactivation of $2 \times 10^{14} \text{ cm}^{-2}$ boron implants at 750°C .

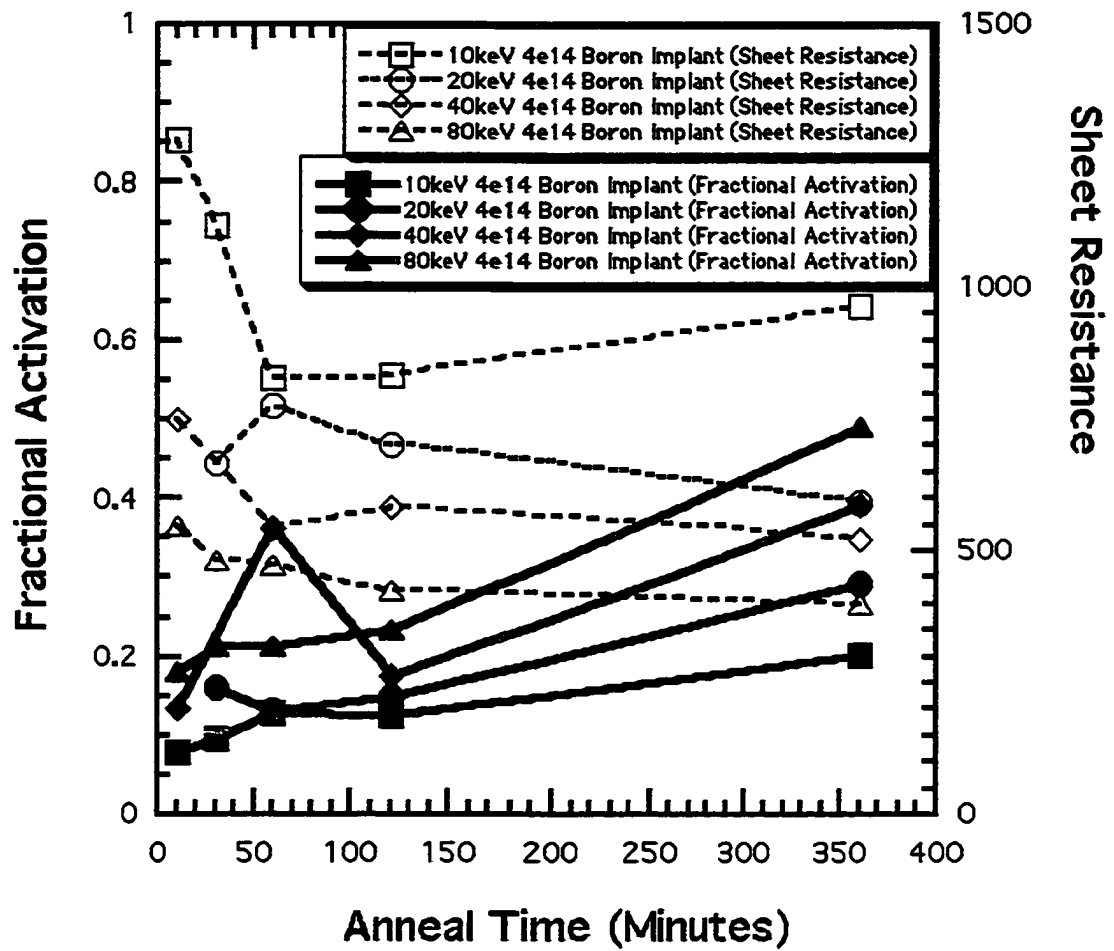


Figure 3-30 Reactivation of $4 \times 10^{14} \text{ cm}^{-2}$ boron implants at 750°C .

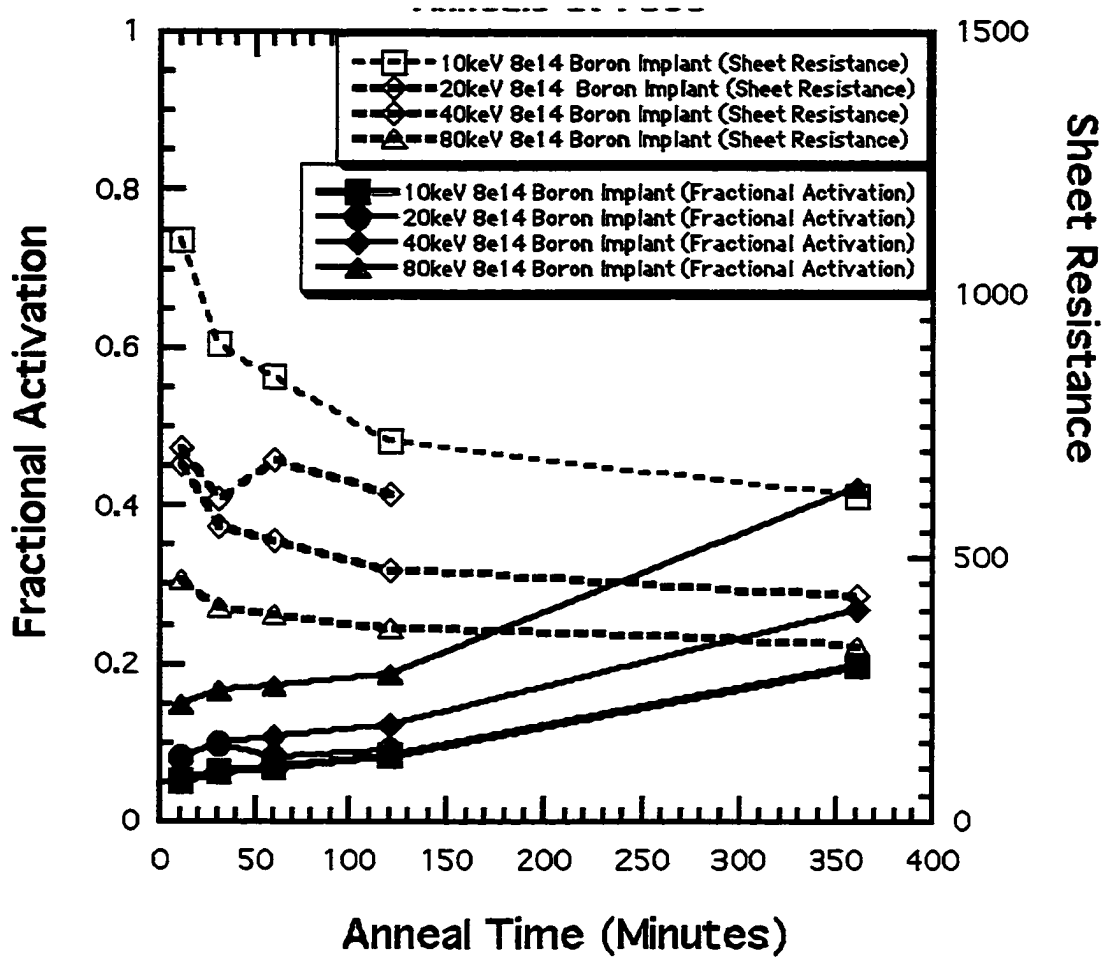


Figure 3-31 Reactivation of $8 \times 10^{14} \text{ cm}^{-2}$ boron implants at 750°C .

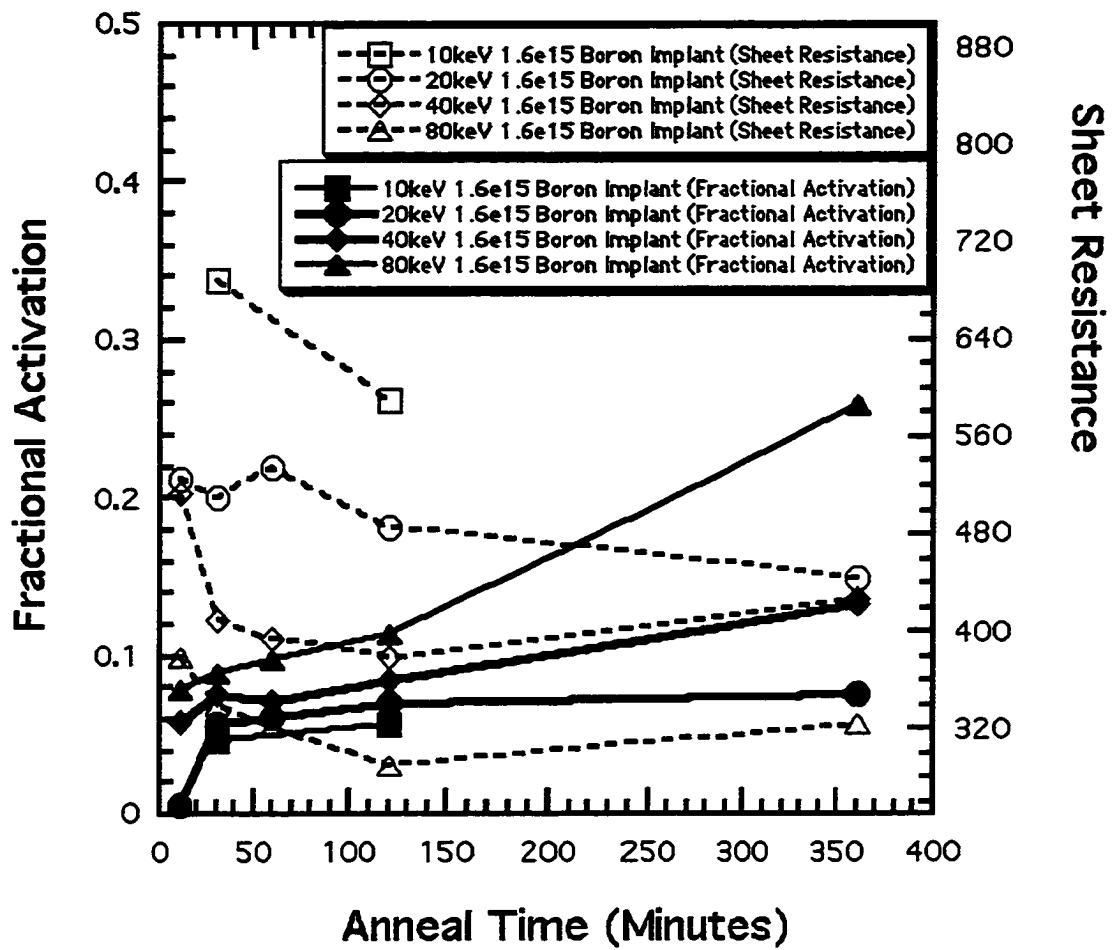


Figure 3-32 Reactivation of $1.6 \times 10^{15} \text{ cm}^{-2}$ boron implants at 750°C .

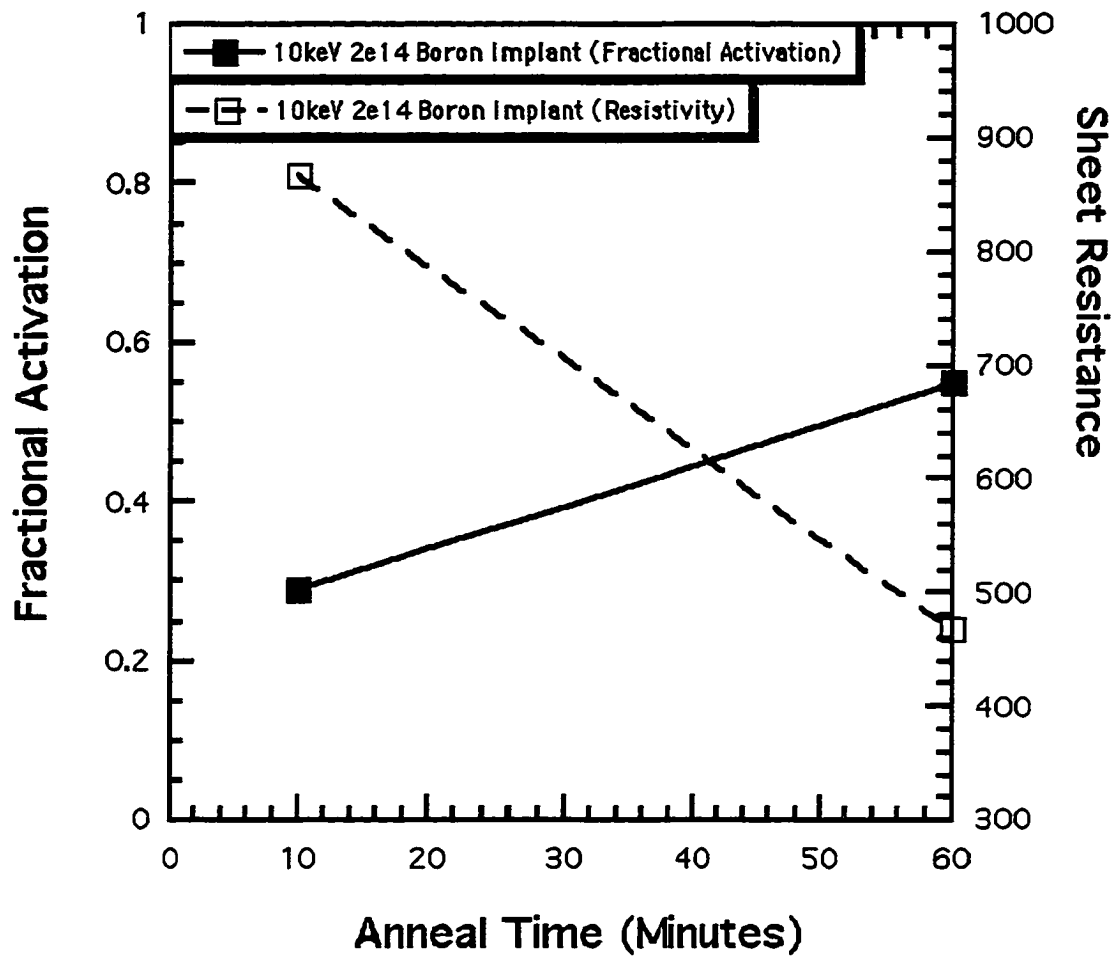


Figure 3-33 Reactivation of $2 \times 10^{14} \text{ cm}^{-2}$ boron implants at 850°C.

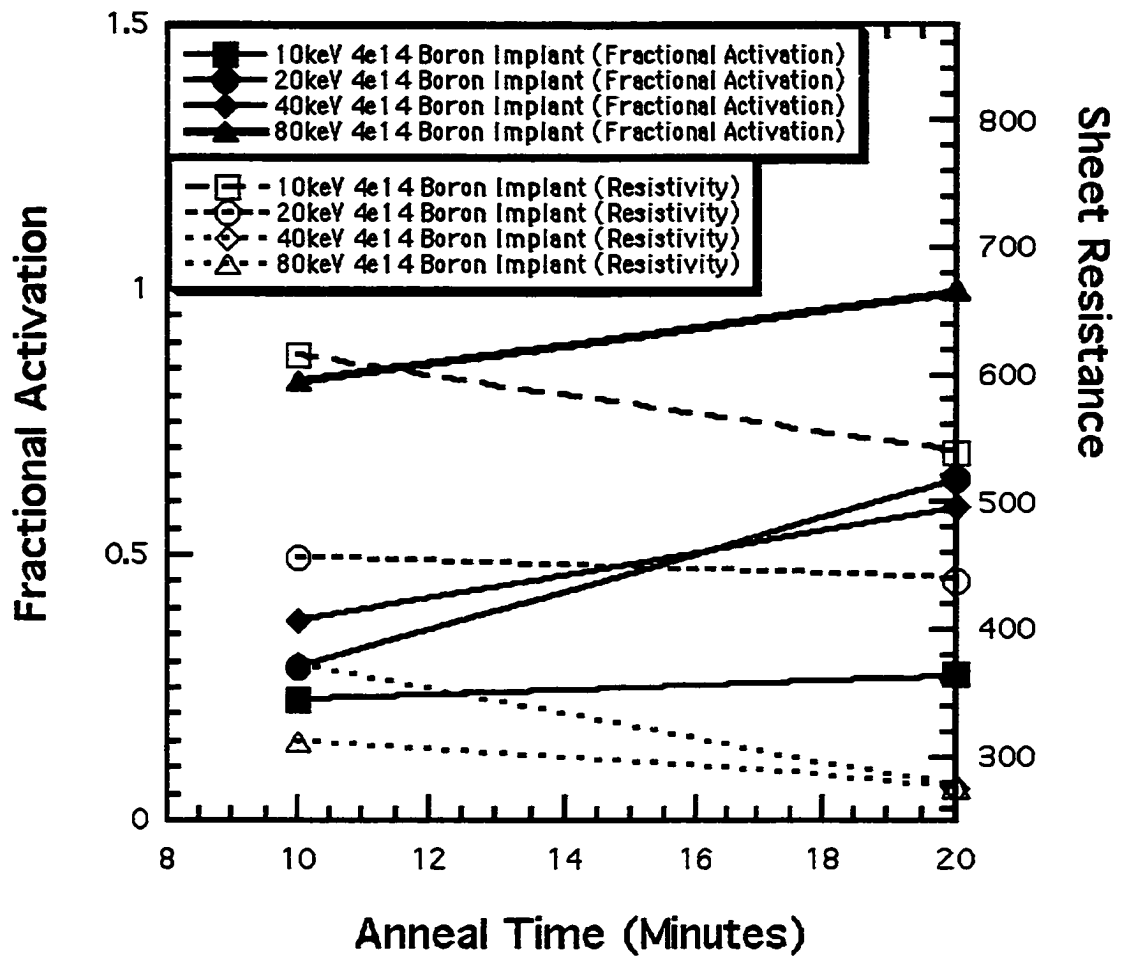


Figure 3-34 Reactivation of $4 \times 10^{14} \text{ cm}^{-2}$ boron implants at 850°C . All of these anneals are from a clustered state induced by a 750°C 30 minute anneal.

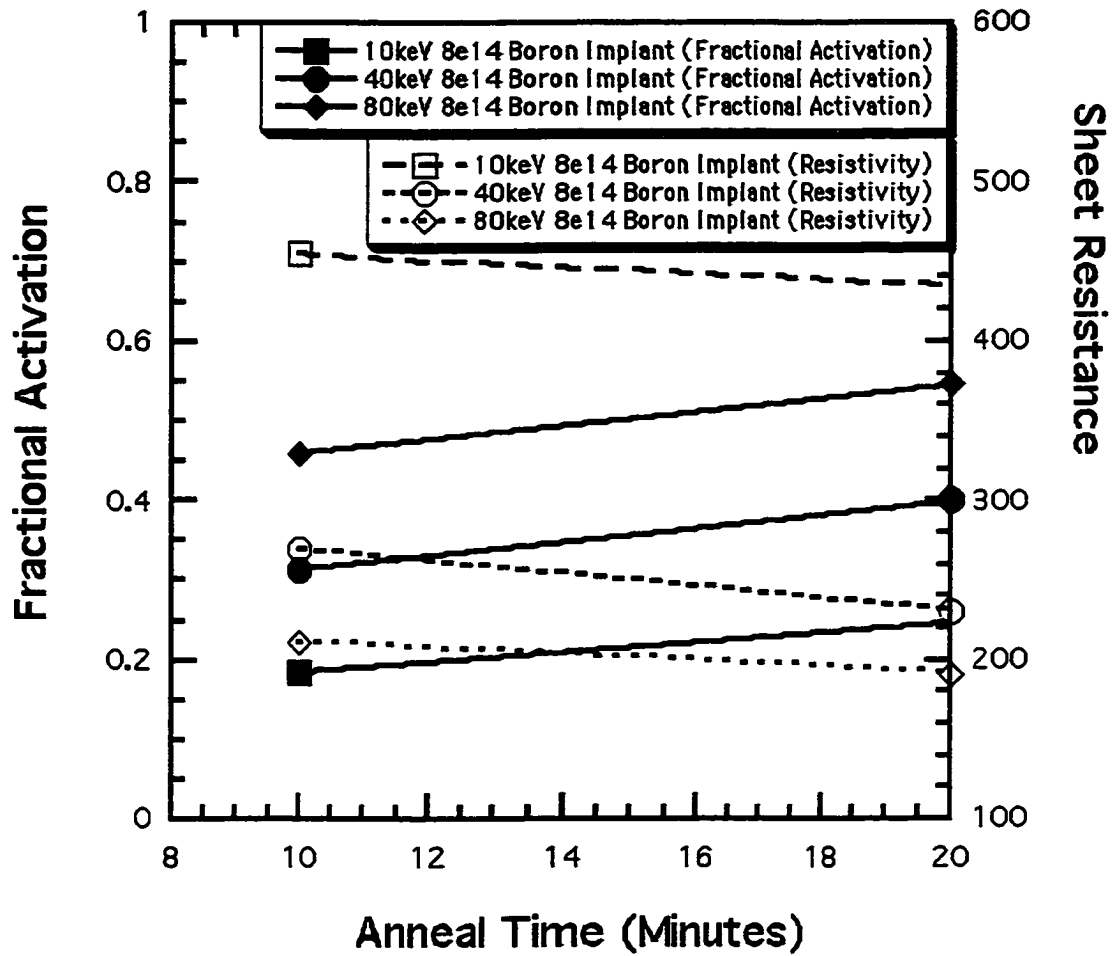


Figure 3-35 Reactivation of $8 \times 10^{14} \text{ cm}^{-2}$ boron implants at 850°C . All of these anneals are from a clustered state induced by a 750°C 30 minute anneal.

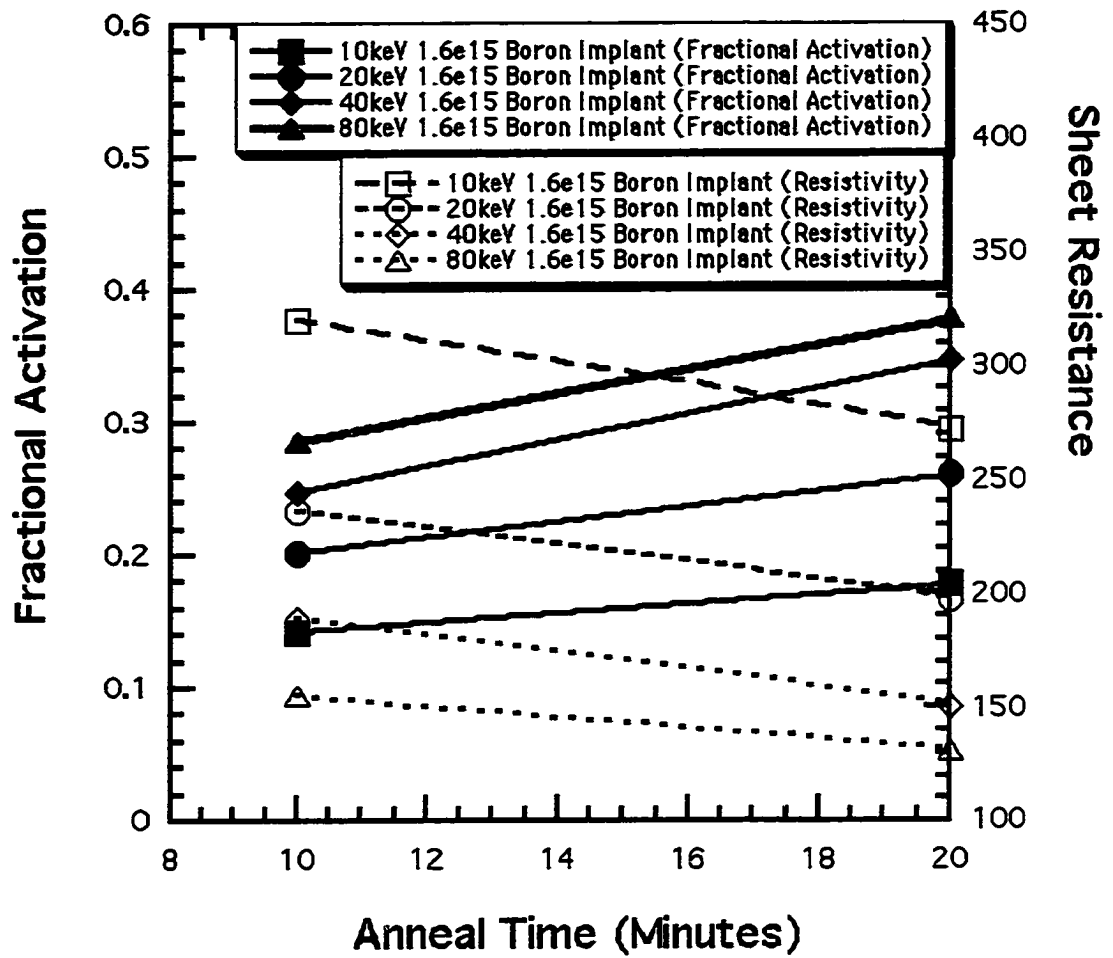


Figure 3-36 Reactivation of $1.6 \times 10^{15} \text{ cm}^{-2}$ boron implants at 850°C . All of these anneals are from a clustered state induced by a 750°C 30 minute anneal.

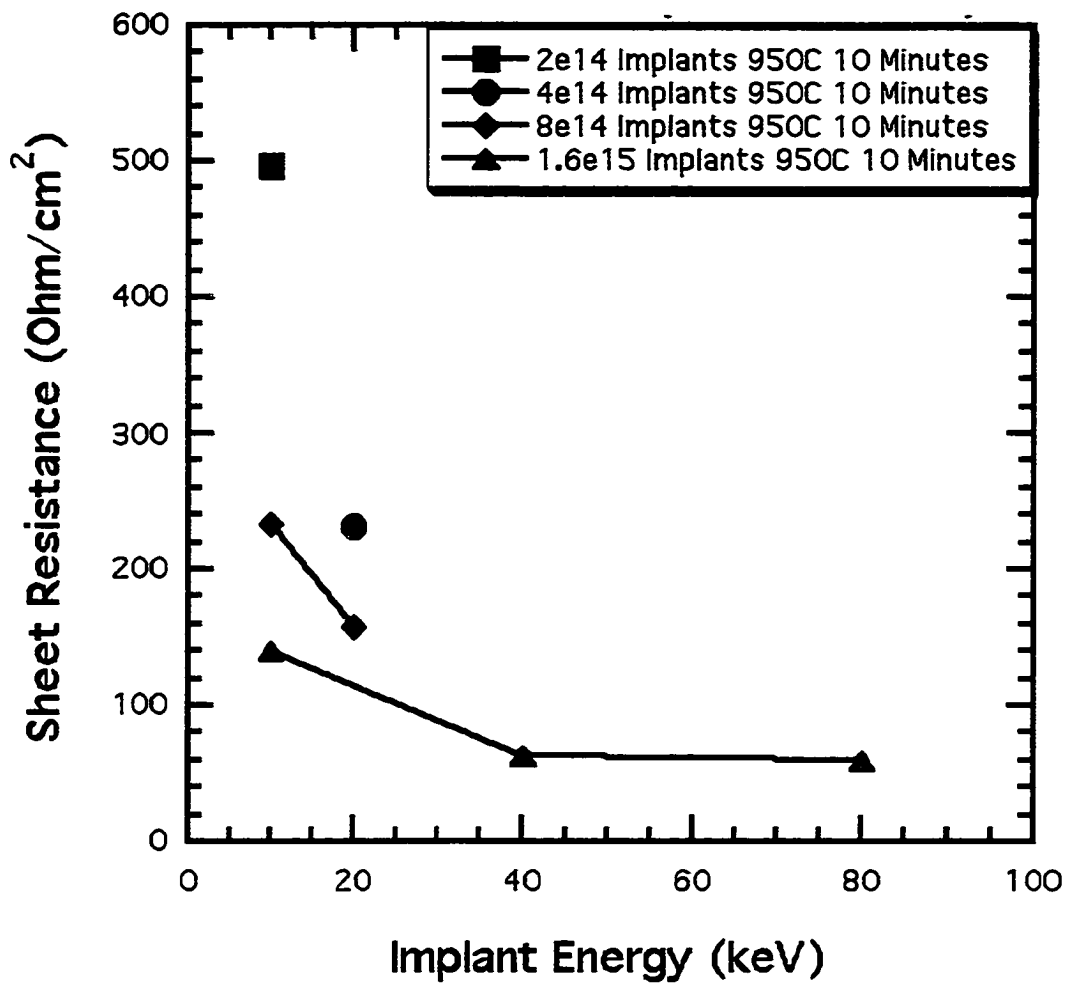


Figure 3-37 Reactivation of boron implants by the 950°C 10 minute anneal from the clustered state as a function of implant energy. All of these anneals are from a clustered state induced by a 750°C 30 minute anneal.

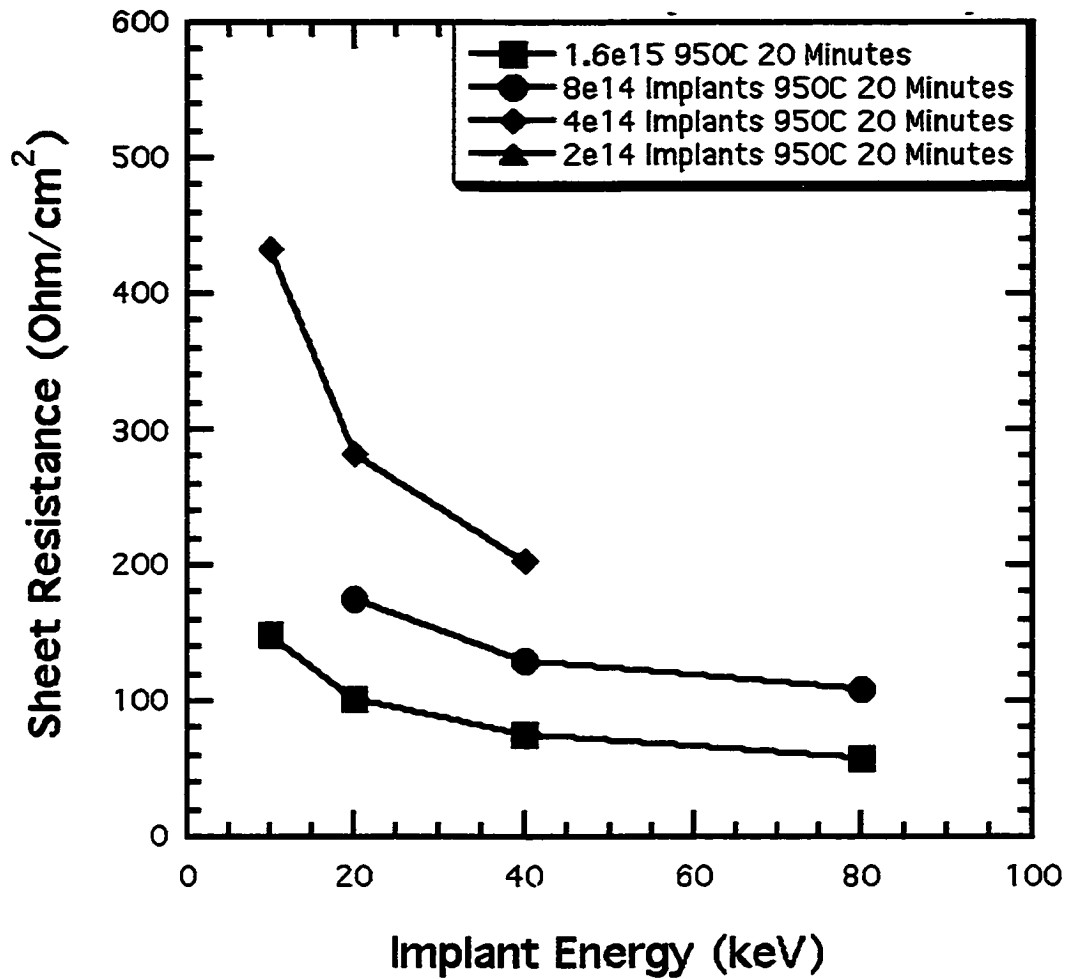


Figure 3-38 Reactivation of boron implants by the 950°C 20 minute anneal from the clustered state as a function of implant energy. All of these anneals are from a clustered state induced by a 750°C 30 minute anneal.

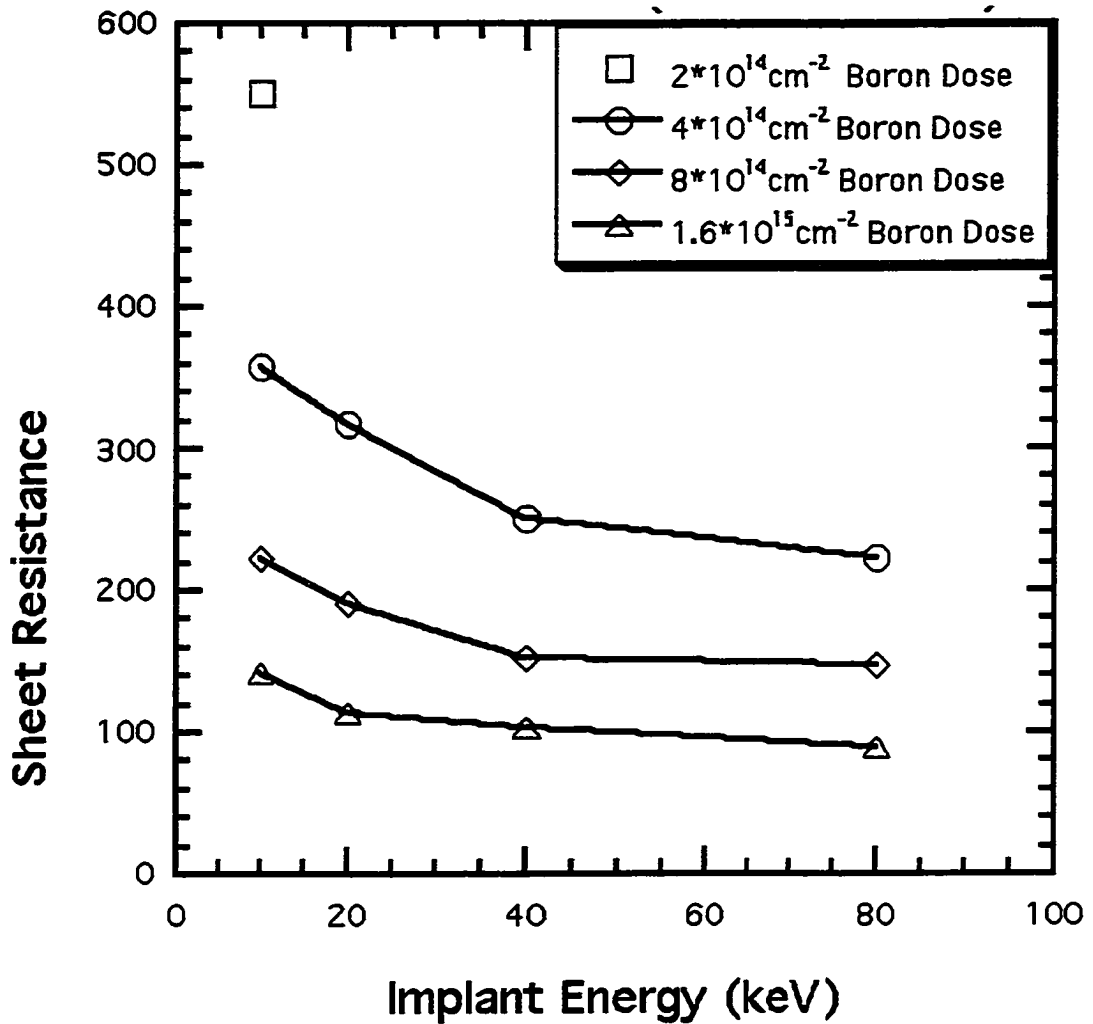


Figure 3-39 Reactivation of boron implants by the 1000°C 2 minute anneal from the clustered state as a function of implant energy. All of these anneals are from a clustered state induced by a 750°C 30 minute anneal.

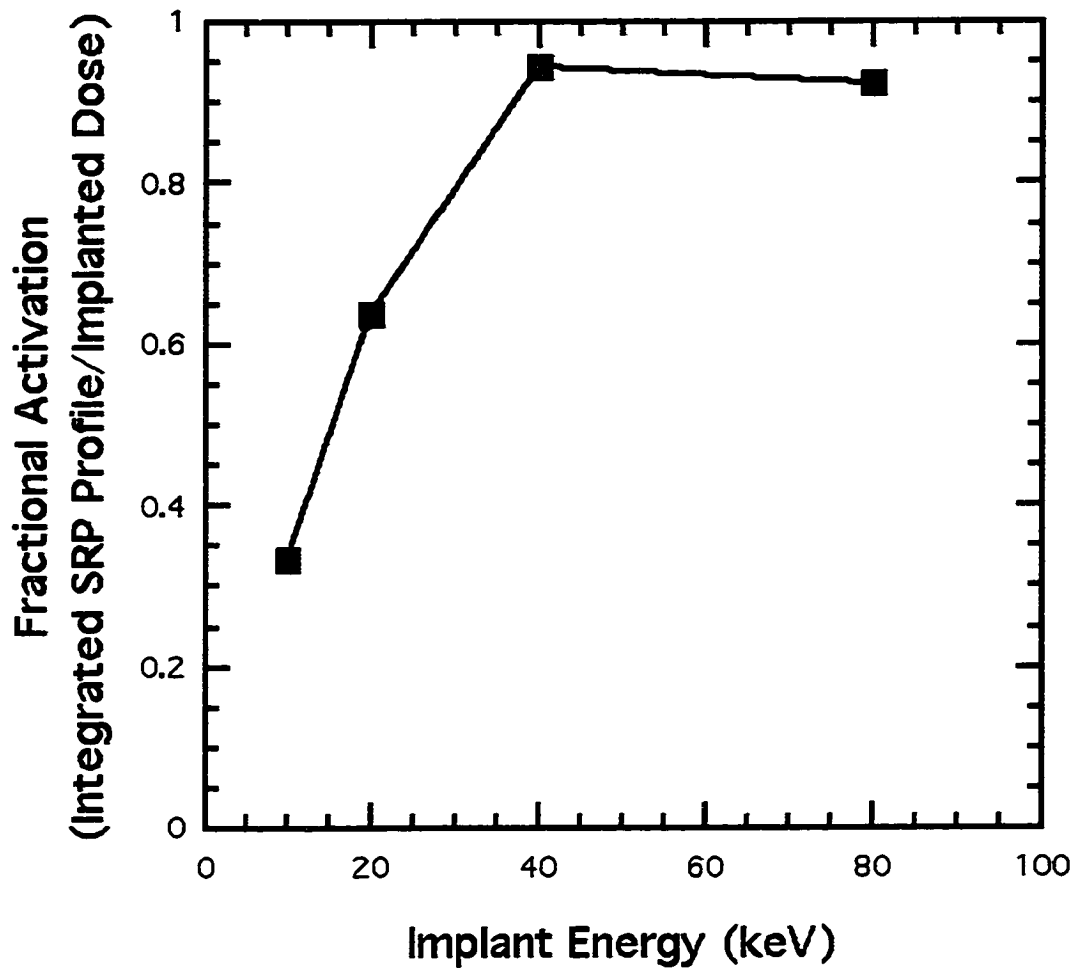


Figure 3-40 Reactivation of the $1.6 \times 10^{15} \text{ cm}^{-2}$ boron implants as a function of implant energy from the clustered state by the 950°C 10 minute anneal. Data is from the integrated SRP profiles. All of these anneals are from a clustered state induced by a 750°C 30 minute anneal.

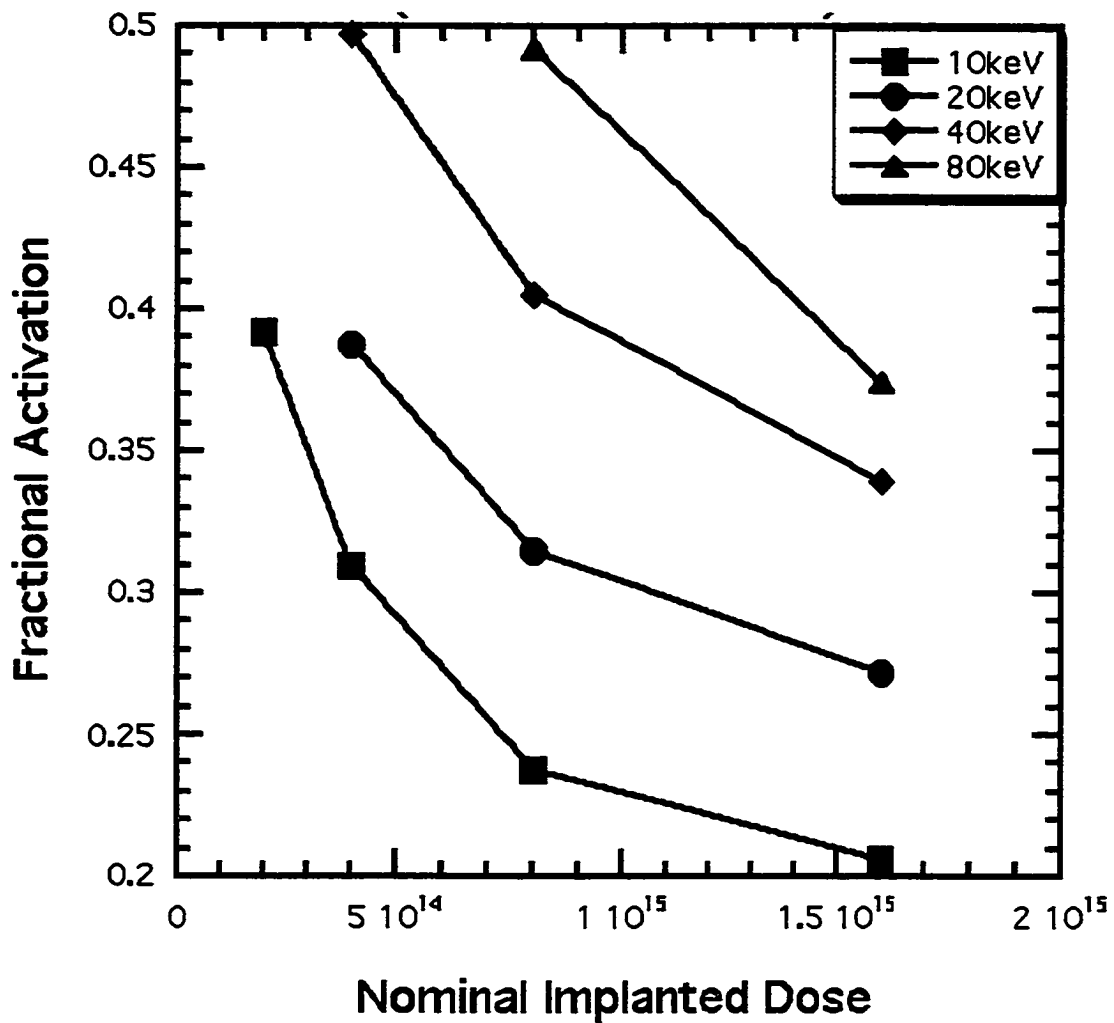


Figure 3-41 Activation of boron from the clustered state by the 850°C 10 minute anneal. Note that similar chemical concentrations of boron yield similar electrical activities. All of these anneals are from a clustered state induced by a 750°C 30 minute anneal.

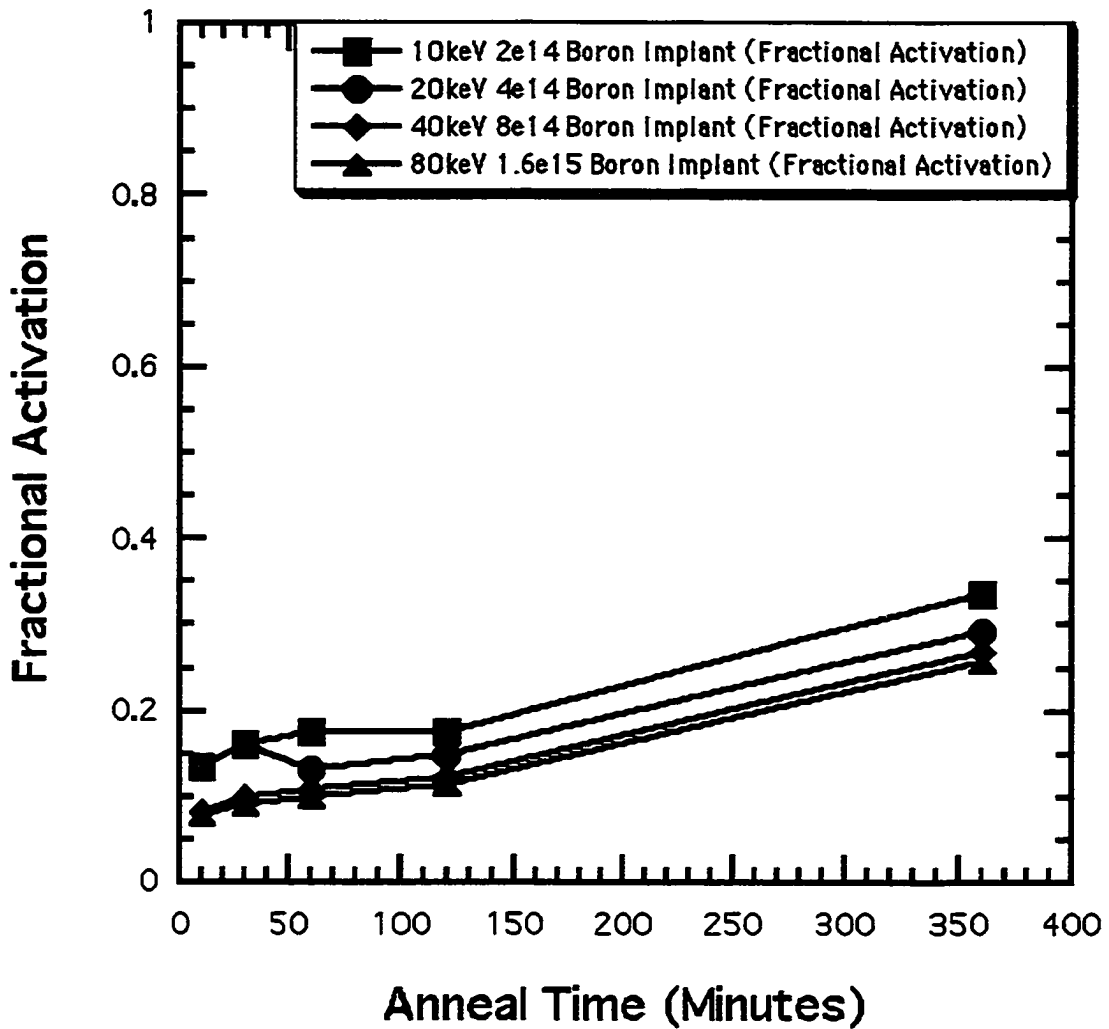


Figure 3-42 Electrical activation of samples with similar chemical boron concentrations. Note the excellent correspondence over the range of anneal times at 750°C.

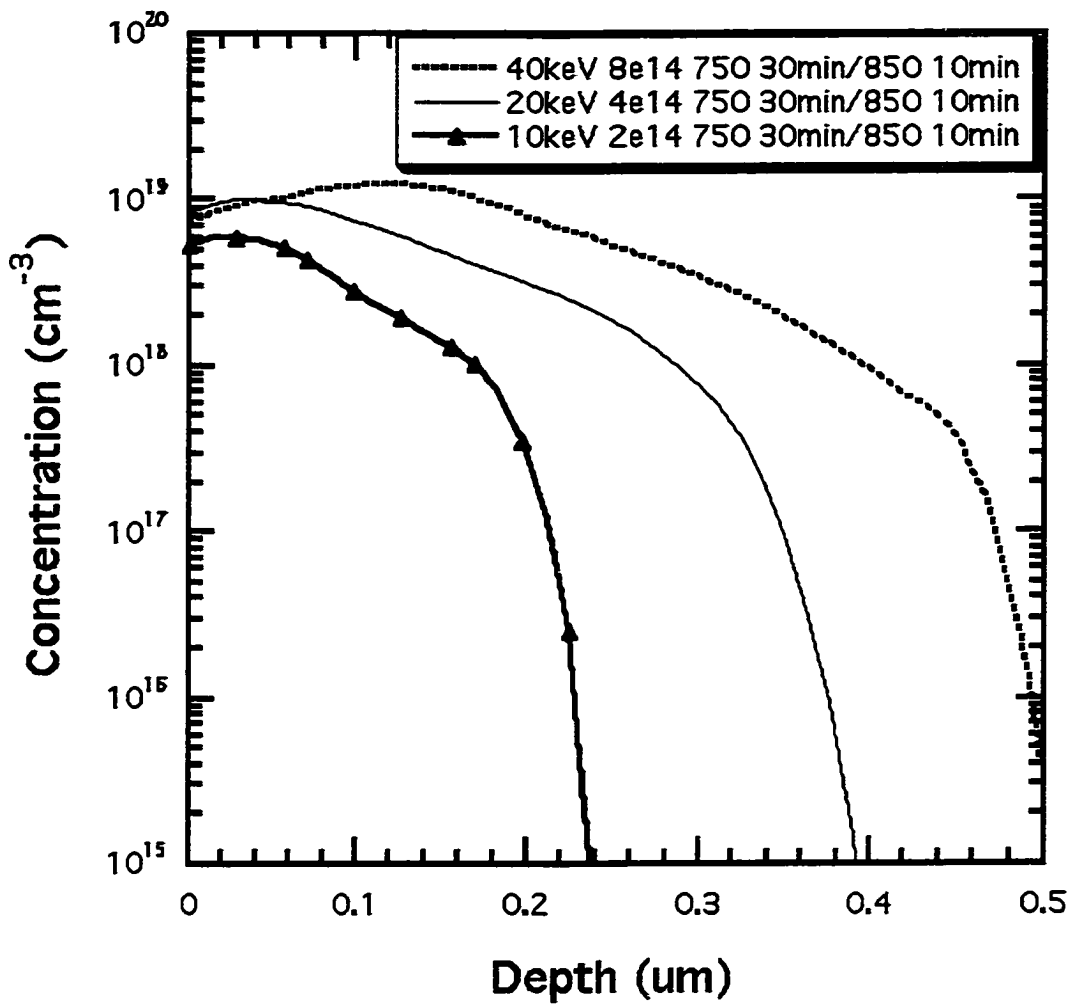


Figure 3-43 Activation of boron samples with similar chemical dopant concentrations from the clustered state by a 850°C 10 minute anneal. Note that there is close correspondence in the peak concentrations with some deviation in the $2 \times 10^{14} \text{ cm}^{-2}$ implant due to the fact that this is essentially fully activated. All of these anneals are from a clustered state induced by a 750°C 30 minute anneal.

•

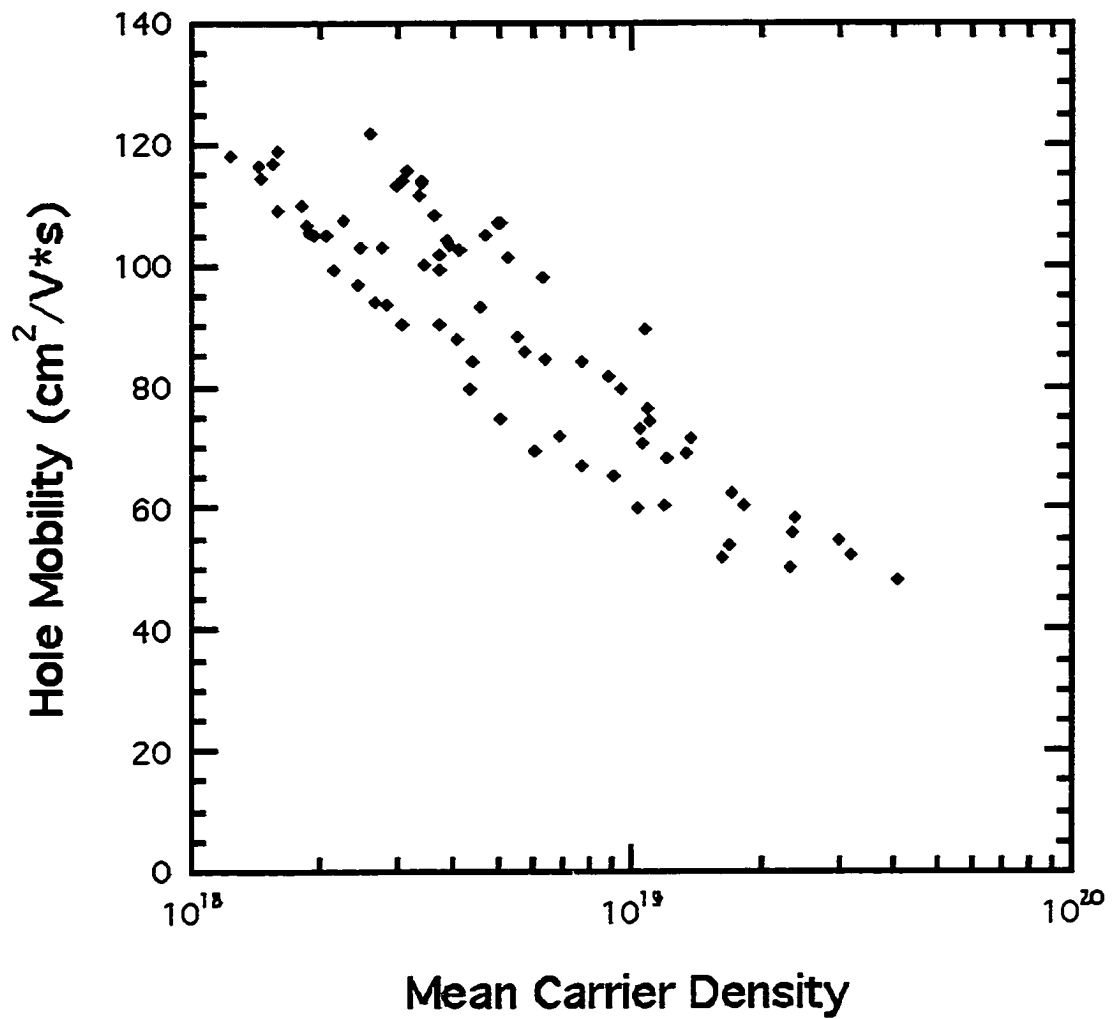


Figure 3-44 Hole mobility as a function of hole density. Note that the hole mobility decreases with increasing hole density due to impurity scattering.

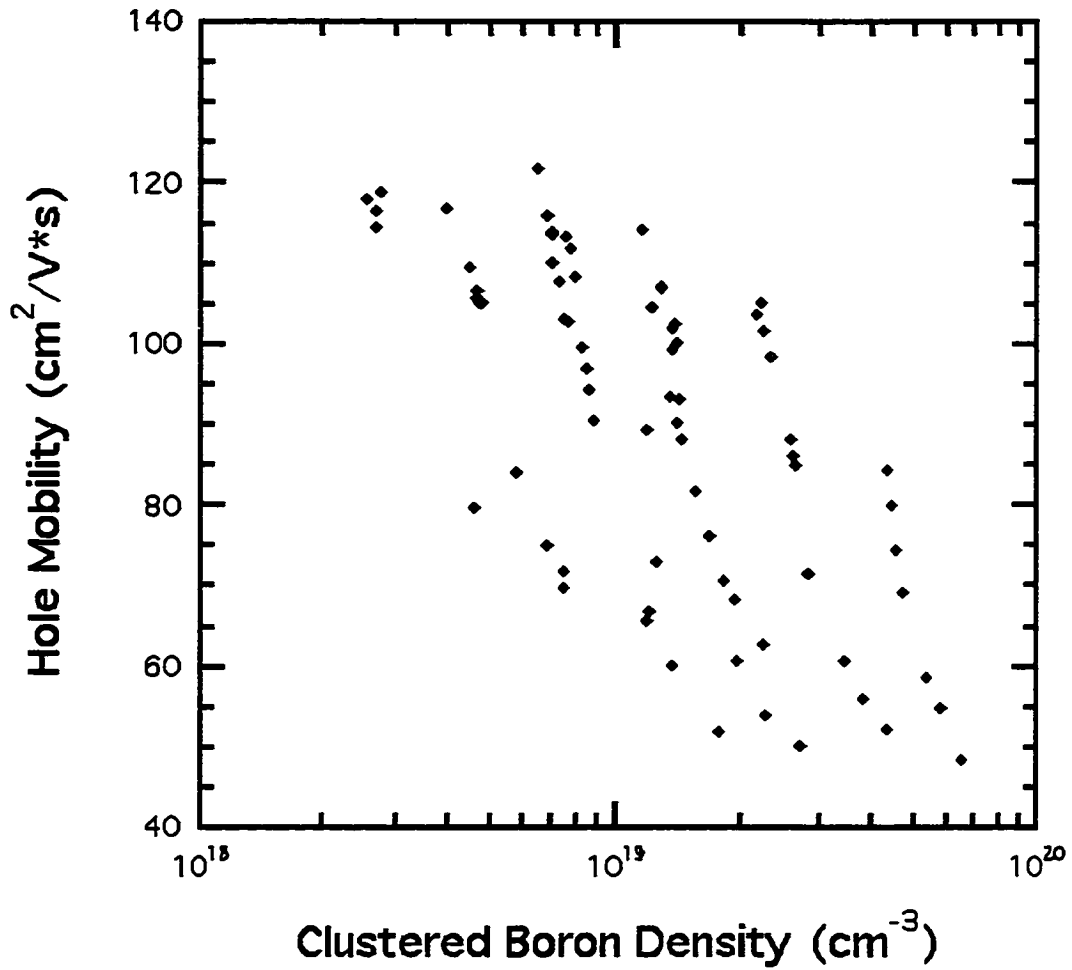


Figure 3-45 Hole mobility as a function of clustered boron density. There is no clear trend directly evident from this plot.

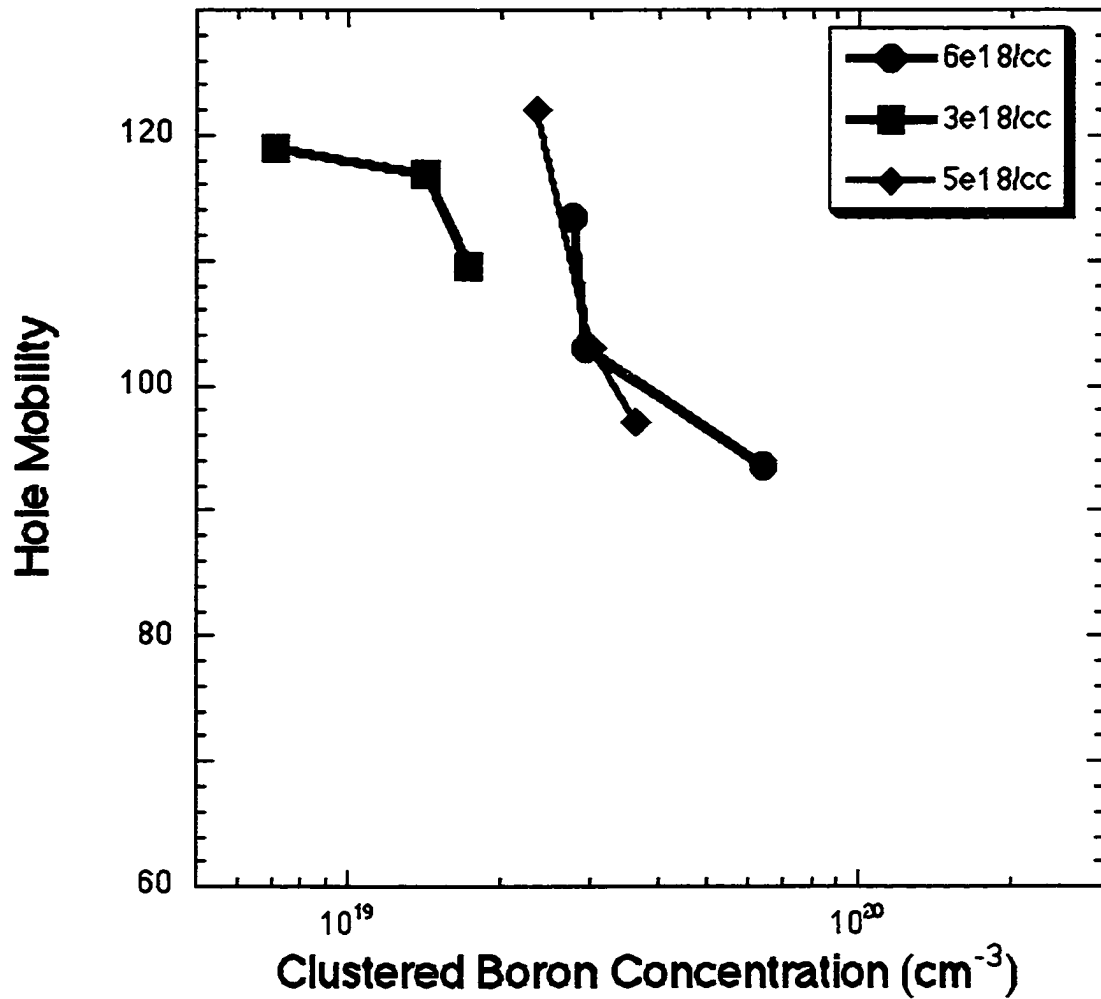


Figure 3-46 Hole mobility as a function of clustered boron concentration. At lower clustered boron densities, the hole mobility appears to decrease with increasing clustered boron density.

CHAPTER 4

ANALYSIS AND SIMULATION OF EXPERIMENTAL FINDINGS

Chapter 3 presents a great deal of new experimental work relating to the boron clustering processes. In this chapter, these experiments are analyzed and simulated in order to validate the model developed in Chapter 2. The ability of this modeling approach to accurately depict the transient enhanced diffusion and intrinsic diffusion of a boron implant has been exhibited in Chapter 2, however, no attempt has yet been made to correlate this model with the activation data which has been obtained. A thorough analysis of the activation data can also help to elucidate some of the kinetics of the boron clustering/declustering processes. Sample FLOOPS scripts along with parameter files are found in appendix B.

4.1 Simulation of Boron Well Experiment

The boron well experiment was simulated as described in Chapter 3. The boron profile was assumed to be uniform and the silicon implant was simulated with the aid of UT Marlowe. The evolution of {311} defects was studied in the presence of a background boron concentration ranging from undoped to $1 \times 10^{20} \text{ cm}^{-3}$. The results of this experiment are in general agreement with the findings obtained as part of this work and prior findings obtained by Haynes, et al. [Hay96]. A plot of the interstitials trapped in {311} defects as a function of boron concentration following the 10 minute and 20 minute anneal at 740°C of a $40 \text{ keV } 1 \times 10^{14} \text{ cm}^{-2}$ silicon implant into a uniformly doped boron well is shown as Figure 4-1. Figures 4-2 and 4-3 illustrate the

differences in the boron activation exhibited by this experiment following the 10 minute anneal at 740°C of a 40 keV $1 \times 10^{14} \text{ cm}^{-2}$ silicon implant into a uniformly doped boron well for the case of 1×10^{16} and a $1 \times 10^{19} \text{ cm}^{-3}$ boron background concentrations, respectively, assuming that the boron activation is wholly due to the substitutional boron component. It is easily seen that a significant amount of the boron in the more heavily-doped boron well is deactivated while the more lightly-doped boron well exhibits very little deactivation. This result is in agreement with the concentration dependent effects noted in Chapter 3.

4.2 Qualitative Comparison to Boron Implant Study

The boron well experiment was next simulated. In general, the results obtained from the simulation agree with the experimental results. The reactivation of the 40 keV $4 \times 10^{14} \text{ cm}^{-2}$ boron implant is shown in Figure 4-4 following a 750°C 30 minute anneal. Spreading resistance analysis of similar structures produced carrier profiles which saturate near the point where the substitutional boron profile saturates in these simulations. The variation of the implanted dose about $4 \times 10^{14} \text{ cm}^{-2}$ produces very little change in the substitutional boron profile as shown in Figure 4-5. This is in agreement with the experimental results shown in Chapter 3. The 40 keV $4 \times 10^{14} \text{ cm}^{-2}$ boron implant, which has been subjected to the 30 minute 750°C anneal, is then further activated with a 10 minute anneal at 850°C. The result is shown in Figure 4-6. Similar results are obtained for other implant conditions.

4.3 Qualitative Correlation to Boron Activation Work

The electrical activation exhibited by the model was next qualitatively compared to experiment. The net level of activation was determined by integrating the profiles of those species which are believed to be ionized. Figure 4-7 illustrates

this for the case of a 40 keV $4 \times 10^{14} \text{ cm}^{-2}$ boron implant annealed at 750°C for a time of 30 minutes which also illustrates the differences in net activation if one accounts for fractionally active boron complexes and does not consider the substitutional boron specie to be the sole contributor to the exhibited boron activation. If only the boron substitutional specie is utilized to account for the boron activation, generally, there is an underestimate of the sheet number for a given implant. Assuming the B3I profile contributes carriers in accordance with a 33% fractional activation leads to an overestimate of the measured carrier profile in this instance.

4.4 Quantitative Comparison of Simulated Results to SRP Profiles

Several of the implant/anneal conditions from the implant study were analyzed with spreading resistance profilometry. This technique, unlike hall analysis, yields a result in the form of a x-y (depth-concentration) profile which is very useful for comparison to simulation. Several examples were run in order to verify the observations of chapter 3 and correct behavior of the model.

Figure 4-8 illustrates the 40 keV $1.6 \times 10^{15} \text{ cm}^{-2}$ boron implant following a 750°C anneal for 30 minutes. The SRP profile saturates at a concentration of $5\text{--}6 \times 10^{18} \text{ cm}^{-3}$ for this condition which is in excellent agreement with the substitutional boron profile for this condition. If one accounted for a 33% fractional activation of the B3I complex, there would be a significant over estimate of the active profile. Figures 4-9 and 4-10 illustrate this same anneal condition subjected to the 750°C 30 minute anneal followed by a 850°C anneal for durations of 10 minutes and 120 minutes, respectively. These anneals further activate the boron in agreement with experiment and the substitutional boron profile is in good agreement with the electrical profile, however, in both cases there is an overestimate of the electrical

concentration in the peak region of the implant by approximately a factor of 1.5.

Figure 4-11 illustrates the comparison of the simulated and measured activation of the 40 keV $4 \times 10^{14} \text{ cm}^{-2}$ boron implant subjected to a 750°C 30 minute anneal with the substitutional boron producing a reasonable estimate of the electrical profile.

Figures 4-12 and 4-13 illustrate a reactivation sequence for the 10 keV $4 \times 10^{14} \text{ cm}^{-2}$ boron implant. Figure 4-12 shows the simulation and electrical profile following a 750°C 30 minute anneal. Figure 4-13 illustrates this implant following the 750°C 30 minute anneal and an additional 850°C anneal for 10 minutes. In both cases, the substitutional boron profile represents an excellent fit to the electrical profile.

Figures 4-14 and 4-15 illustrate another anneal sequence for the 20 keV $8 \times 10^{14} \text{ cm}^{-2}$ boron implant, which is an approximate dual of the 10 keV $4 \times 10^{14} \text{ cm}^{-2}$ implant presented in Figures 4-12 and 4-13. Figure 4-14 shows the simulation and electrical profile following a 750°C 30 minute anneal. Figure 4-15 illustrates this implant following the 750°C 30 minute anneal and an additional 850°C anneal for 10 minutes. In both cases, the substitutional boron profile represents an excellent fit to the electrical profile. It is also interesting to note that the levels of substitutional boron are nearly identical across the anneal sequence for boron profiles of similar concentration.

4.5 Time Constant to Boron Activation and Possible Binding Energies

During the dissolution of the boron clusters, or the reactivation of the boron, the clustered boron concentration is governed by a differential equation of following form:

$$dC_{\text{BIC}}/dt = -K_r \cdot C_{\text{BIC}} \cdot \exp(-E_b/KT) \quad (4.1)$$

Which has the solution of:

$$C_{\text{BIC}}(\text{time}) = C_{\text{BIC}}(t=0) * \exp(-t/\tau) \quad (4.2)$$

$$dC_{\text{BIC}}(\text{time})/dt = -1/\tau * C_{\text{BIC}} \quad (4.3)$$

The experimental value of τ is easily determined by plotting the clustered boron concentration as a function of time. From this, it should be possible to examine the binding energetics limiting the cluster dissolution process. Neglecting any out-diffusion or other dose loss effects during the anneal steps, this may be approximated as the implanted dose determined by SIMS minus the sheet number or integrated SRP profile. Extractions of this nature are shown in Figures A-5 through A-12 in Appendix A as obtained from the data analysis portion of the software tool Kaleidagraph. A summary of these results is shown in table 4-1 for anneals at 750°C and in table 4-2 for anneals at 850°C. The term 'R' is related to the RMS error of the fit with a value of unity being representative of a perfect fit and zero being representative of a poor fit.

An analysis of the time constant to reactivation is shown in Figures A-13 through A-16 of Appendix A at the four different implant energies. In general, we note a trend towards longer time constants to reactivation with increasing implant dose at a fixed energy. Plots of the time constant to reactivation at fixed nominal implanted dose are shown in Figures A-17 through A-19 of Appendix A and show a trend towards longer time constants to reactivation for lower implant energies with fixed implant dose. These observed behaviors are consistent with the idea that there is a concentration dependence to the boron activation.

Table 4-1 Exponential decay fits to the concentration of clustered boron for various implant conditions followed by anneals at 750°C.

	$C_{BIC}(t=0) \text{ (cm}^{-3}\text{)}$	$1/\text{Tau (1/min)}$	R (Error to Fit)
10 keV $2 \times 10^{14} \text{ cm}^{-2}$	2.32e14	.00071	.9738
10 keV $2 \times 10^{14} \text{ cm}^{-2}$	5.00e14	.00040	.9612
10 keV $8 \times 10^{14} \text{ cm}^{-2}$	9.85e14	.00048	.9924
10 keV $1.6 \times 10^{15} \text{ cm}^{-2}$	2.24e15	.00033	.9807
20 keV $4 \times 10^{14} \text{ cm}^{-2}$	4.70e14	.00057	.9334
20 keV $8 \times 10^{14} \text{ cm}^{-2}$	9.88e14	.00060	.6451
20 keV $1.6 \times 10^{15} \text{ cm}^{-2}$	2.02e15	5.63e-5	.7028
40 keV $4 \times 10^{14} \text{ cm}^{-2}$	4.07e14	.00070	.6927
40 keV $8 \times 10^{14} \text{ cm}^{-2}$	9.56e14	.00064	.9894
40 keV $1.6 \times 10^{15} \text{ cm}^{-2}$	2.06e15	.00022	.9851
80 keV $4 \times 10^{14} \text{ cm}^{-2}$	4.43e14	.00134	.9729
80 keV $8 \times 10^{14} \text{ cm}^{-2}$	7.48e14	.00111	.9728
80 keV $1.6 \times 10^{15} \text{ cm}^{-2}$	1.95e15	.00063	.9882

Table 4-2 Exponential decay fits to the concentration of clustered boron for various implant conditions followed by anneals at 850°C.

	$C_{BIC}(t=0) \text{ (cm}^{-3}\text{)}$	$1/\text{Tau (1/min)}$	R (Error to Fit)
10 keV $2 \times 10^{14} \text{ cm}^{-2}$	2.21e14	.01010	.9911
10 keV $2 \times 10^{14} \text{ cm}^{-2}$	4.73e14	.00510	.8942
10 keV $8 \times 10^{14} \text{ cm}^{-2}$	9.49e14	.01020	.9976
10 keV $1.6 \times 10^{15} \text{ cm}^{-2}$	2.11e15	.00330	.9086
20 keV $4 \times 10^{14} \text{ cm}^{-2}$	4.87e14	.04180	.9153
20 keV $8 \times 10^{14} \text{ cm}^{-2}$	9.17e14	.00466	.8916
20 keV $1.6 \times 10^{15} \text{ cm}^{-2}$	1.86e15	.00545	.9103
40 keV $4 \times 10^{14} \text{ cm}^{-2}$	4.2e14	.01950	.9831
40 keV $8 \times 10^{14} \text{ cm}^{-2}$	8.90e14	.01630	.9316
40 keV $1.6 \times 10^{15} \text{ cm}^{-2}$	1.80e15	.00409	.7101
80 keV $4 \times 10^{14} \text{ cm}^{-2}$	4.65e14	.18600	.9976
80 keV $8 \times 10^{14} \text{ cm}^{-2}$	6.85e14	.03170	.9813
80 keV $1.6 \times 10^{15} \text{ cm}^{-2}$	1.85e15	.01670	.9705

It is likely that the boron dissolution process is time-limited by the dissolution of a single cluster complex. Two possible means of cluster dissolution are:

- a) Dissolution of a cluster by dissociation of a boron interstitialcy.



For example:



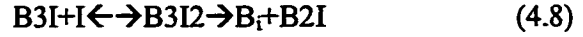
In this case the reverse prefactor, k_r , is given by:

$$K_r = 4\pi D_{Bi} a_{silicon} C_{silicon} \exp(-E_b/KT) \quad (4.6)$$

b) Dissolution by capture of an interstitial to form an unstable complex which then dissociates a boron interstitialcy.



For example:



If dissolution in this case is assumed to take place under small saturations of interstitials, the reverse prefactor is given by:

$$K_r = 4\pi D_I a_{silicon} C_{istar} \exp(-E_b/KT) \quad (4.9)$$

For both cases, the clusters are assumed to be electrically inactive. If clusters are assumed to be fractionally electrically active the value of K_r should be scaled by the fractional inactivity. Equation 4.6 would then be modified to form of equation 4.10 and equation 4.9 would be modified to form of equation 4.11.

$$K_r = 4\pi D_{Bi} a_{silicon} C_{silicon} \exp(-E_b/KT) * (1-FA) \quad (4.10)$$

$$K_r = 4\pi D_I a_{silicon} C_{istar} \exp(-E_b/KT) * (1-FA) \quad (4.11)$$

Utilizing these equations, the value of the average binding energy to net release of a single boron interstitialcy is shown in table 4-3 under the assumed cases mentioned above for fractional activations of 0 at temperatures of 750°C and 850°C. For the case of the interstitial capture mechanism it is assumed that the captured interstitial is of a neutral charge state with a migrational energy of .9 eV. Modification of the system to account for a singly positive or doubly positively charged interstitial may introduce a small barrier of less than .9 eV. This was also based on assumption that dissolution takes place under the intrinsic value of C_{istar} ,

which does not account for any charge effects which may greatly enhance the intrinsic interstitial population. The term 'rxn limited' refers to the barrier being zero or negative.

Table 4-3 Calculated barriers to hypothetical BIC cluster dissolution reactions from experimental dissolution data.

	750°C Anneal $B_n I_m \rightarrow B_{n-1} I_{m-1} + B_i$	750°C Anneal $B_n I_m + I \rightarrow B_{n-1} I_m + B_i$	850°C Anneal $B_n I_m \rightarrow B_{n-1} I_{m-1} + B_i$	850°C Anneal $B_n I_m + I \rightarrow B_{n-1} I_m + B_i$
10 keV $2 \times 10^{14} \text{ cm}^{-2}$	2.63 eV	~rxn limited	2.63 eV	~rxn limited
10 keV $4 \times 10^{14} \text{ cm}^{-2}$	2.68 eV	~rxn limited	2.70 eV	~rxn limited
10 keV $8 \times 10^{14} \text{ cm}^{-2}$	2.66 eV	~rxn limited	2.63 eV	~rxn limited
10 keV $1.6 \times 10^{15} \text{ cm}^{-2}$	2.70 eV	~rxn limited	2.74 eV	~rxn limited
20 keV $4 \times 10^{14} \text{ cm}^{-2}$	2.65 eV	~rxn limited	2.49 eV	~rxn limited
20 keV $8 \times 10^{14} \text{ cm}^{-2}$	2.65 eV	~rxn limited	2.70 eV	~rxn limited
20 keV $1.6 \times 10^{15} \text{ cm}^{-2}$	2.85 eV	~rxn limited	2.69 eV	~rxn limited
40 keV $4 \times 10^{14} \text{ cm}^{-2}$	2.63 eV	~rxn limited	2.57 eV	~rxn limited
40 keV $8 \times 10^{14} \text{ cm}^{-2}$	2.64 eV	~rxn limited	2.58 eV	~rxn limited
40 keV $1.6 \times 10^{15} \text{ cm}^{-2}$	2.74 eV	~rxn limited	2.72 eV	~rxn limited
80 keV $4 \times 10^{14} \text{ cm}^{-2}$	2.58 eV	~rxn limited	2.35 eV	~rxn limited
80 keV $8 \times 10^{14} \text{ cm}^{-2}$	2.59 eV	~rxn limited	2.52 eV	~rxn limited
80 keV $1.6 \times 10^{15} \text{ cm}^{-2}$	2.64 eV	~rxn limited	2.58 eV	~rxn limited

It is interesting to note that in the case of the direct dissociation of the BIC complex, the net energy to reactivation is approximately 3 eV (~2.7 eV binding energy and .3 eV migrational energy of boron interstitialcy) for all the cases

considered. There is, however, a trend towards higher binding energies with increasing boron dose and decreasing boron implant energies. This is, in effect, the concentration dependence which has been previously discussed. The binding energy for the reactivation process which involves the dissociation of the boron interstitialcy is plotted as a function of the implant energy in Figures 4-16 and 4-17 and as a function of the implanted dose in Figures 4-18 and 4-19 for the anneals performed at temperatures of 750°C and 850°C, respectively.

4.6 Correlating Observed Dissolution Kinetics to Cluster System

The cluster system of figure 1-17 shows the full boron system along with the theoretical binding energies. It is immediately obvious that, in order for the observed reactivation behavior to be correlated to the dissolution of boron clusters, a significant number of the clusters must have initially existed. It is also now apparent that this behavior occurs with a limiting energy of approximately 2.7 eV for the dissolution of a boron interstitialcy.

The only cluster which forms in significant enough concentration to account for the reactivation behavior according to our modeling work and first principles calculations is the B3I complex. This cluster has two possible dissolution mechanisms, one which involves the dissociation of a boron interstitialcy and the other which involves the capture of an interstitial to form the unstable B3I2 complex which then may dissociate to the B2I complex or back to the B3I complex. Our observations are most consistent with the dissociation of the B3I cluster to the B2 cluster which has a 3.0 eV reverse barrier which is in excellent agreement with the extracted ~2.7 eV binding energy.

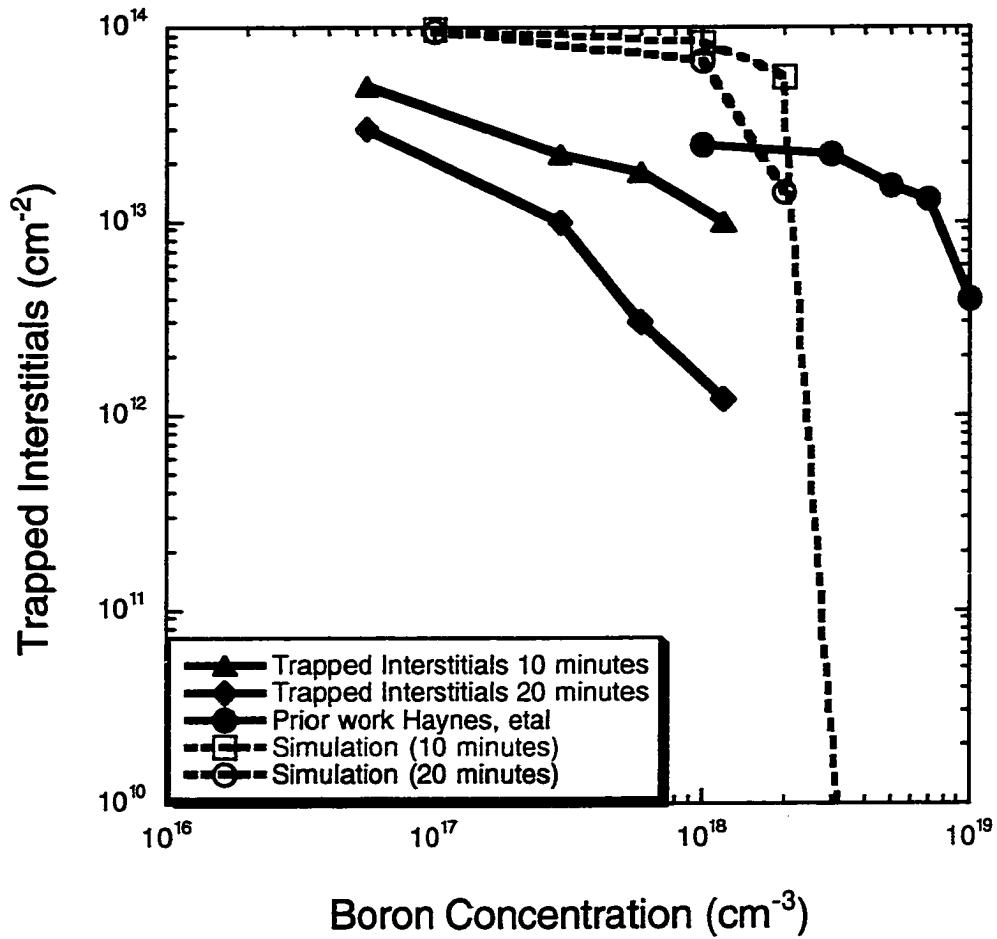


Figure 4-1 Simulation of boron well experiment following anneals at 740°C with a silicon implant of $1 \times 10^{14} \text{ cm}^{-2}$ at 40 keV. Plotted is the residual trapped interstitials in {311} defects as a function of the boron well concentration simulated at 10 minutes and 20 minutes. Also shown are the experimental results of this study and those of a prior experiment which utilized a 15 minute anneal.

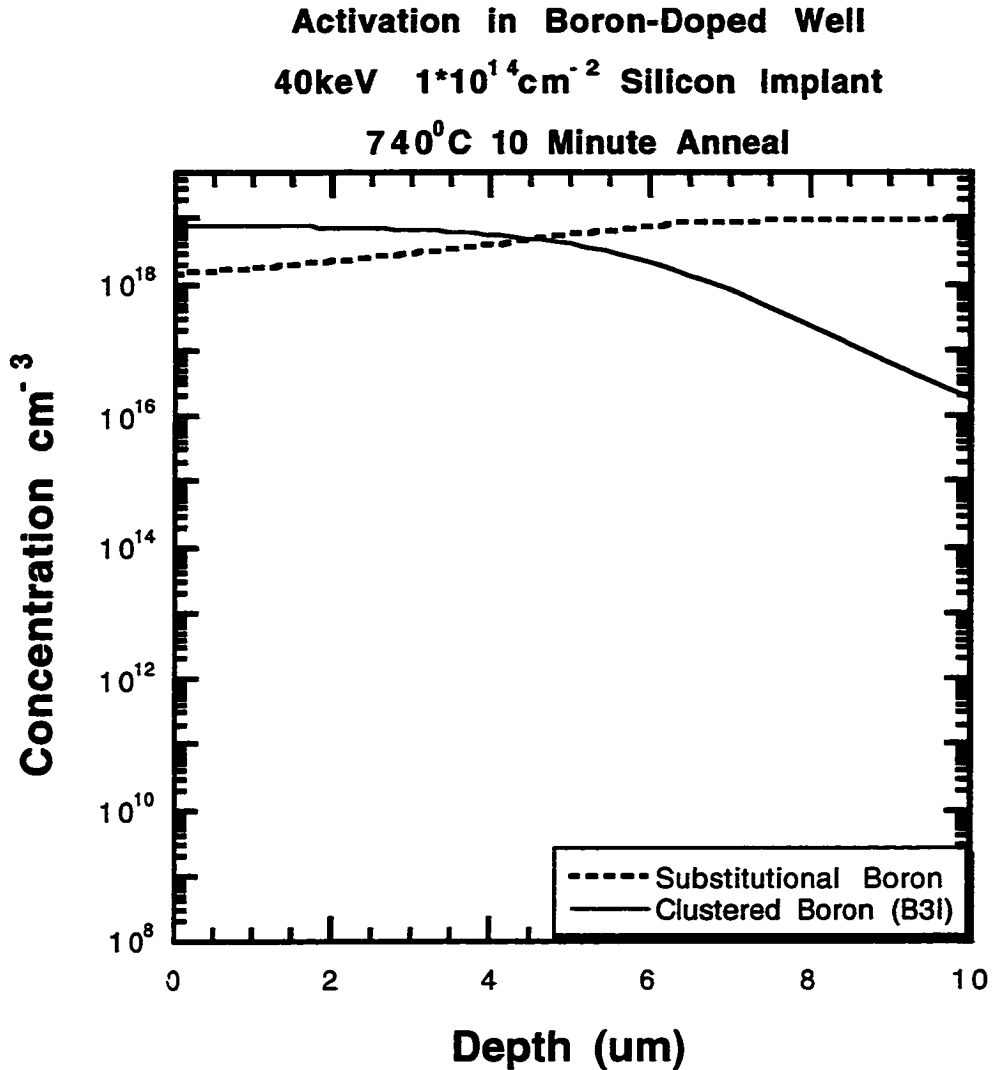


Figure 4-2 Simulation of a 10 minute anneal at 740⁰C of a 40 keV $1 \times 10^{14} \text{ cm}^{-2}$ silicon implant into a boron-doped well of $1 \times 10^{19} \text{ cm}^{-3}$ concentration. A significant fraction of the boron is deactivated.

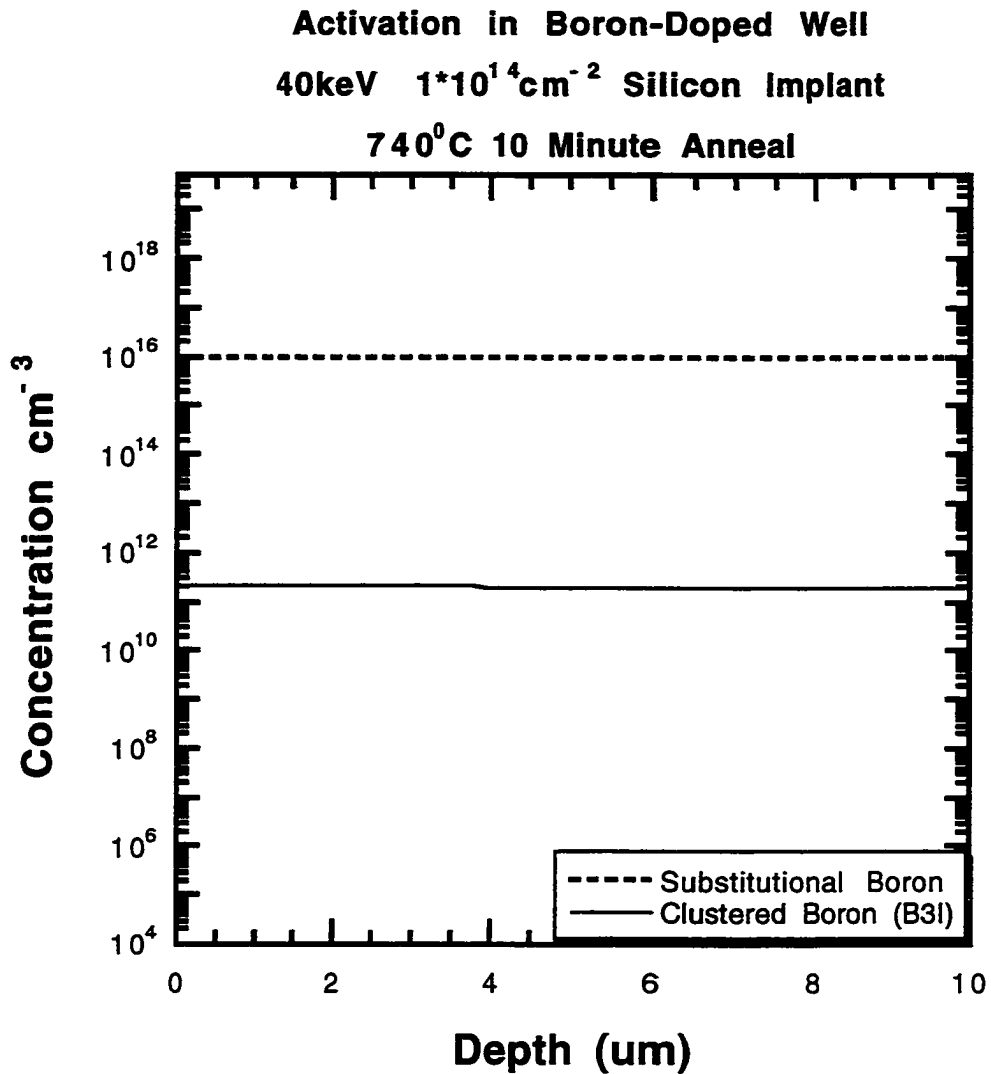


Figure 4-3 Simulation of a 10 minute anneal at 740⁰C of a 40 keV $4 \times 10^{14} \text{ cm}^{-2}$ silicon implant into a boron-doped well of $1 \times 10^{16} \text{ cm}^{-3}$ concentration. Very little of the boron is deactivated.

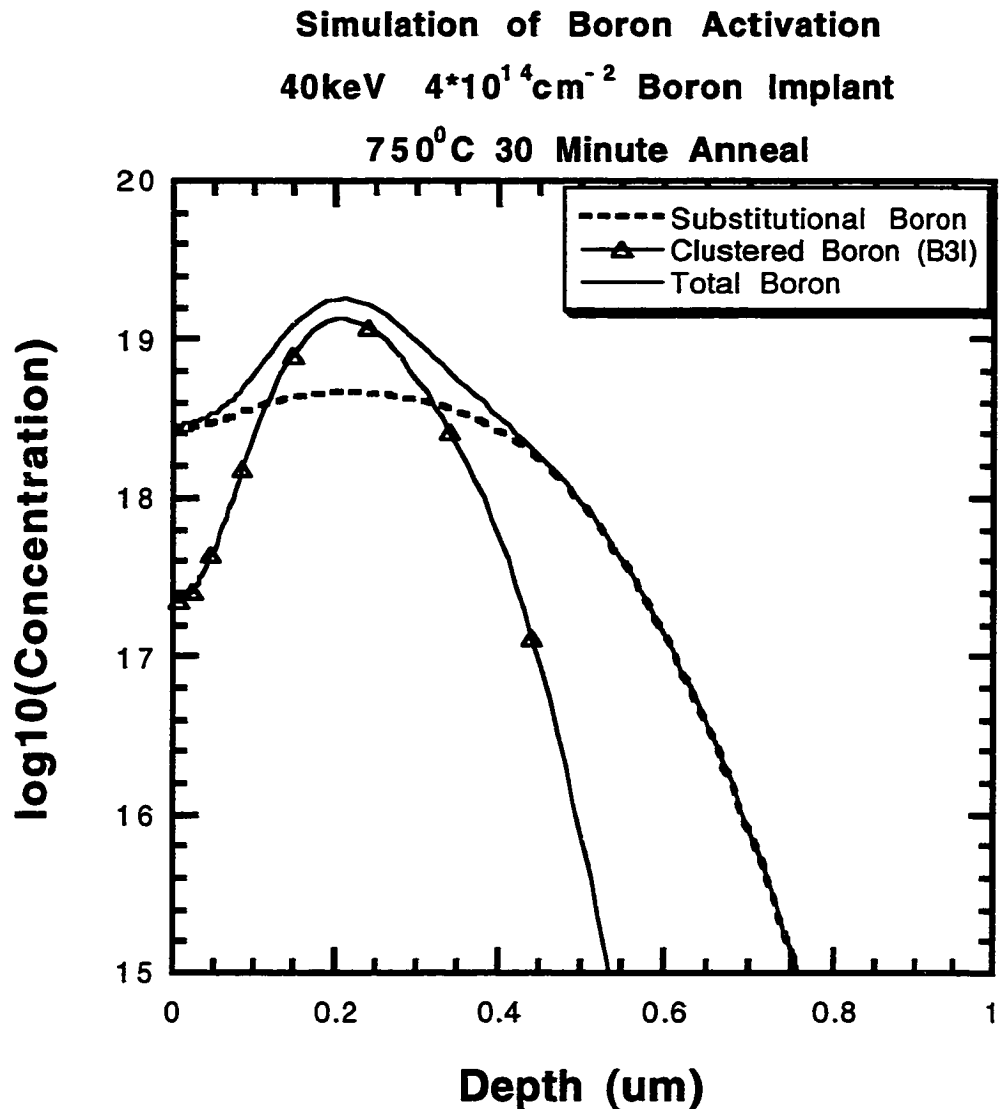


Figure 4-4 Simulation of a 40 keV $4 \times 10^{14} \text{cm}^{-2}$ boron implant annealed for 30 minutes at a temperature of 750⁰C. Note that the substitutional boron concentration saturates at similar concentrations to those determined through this work.

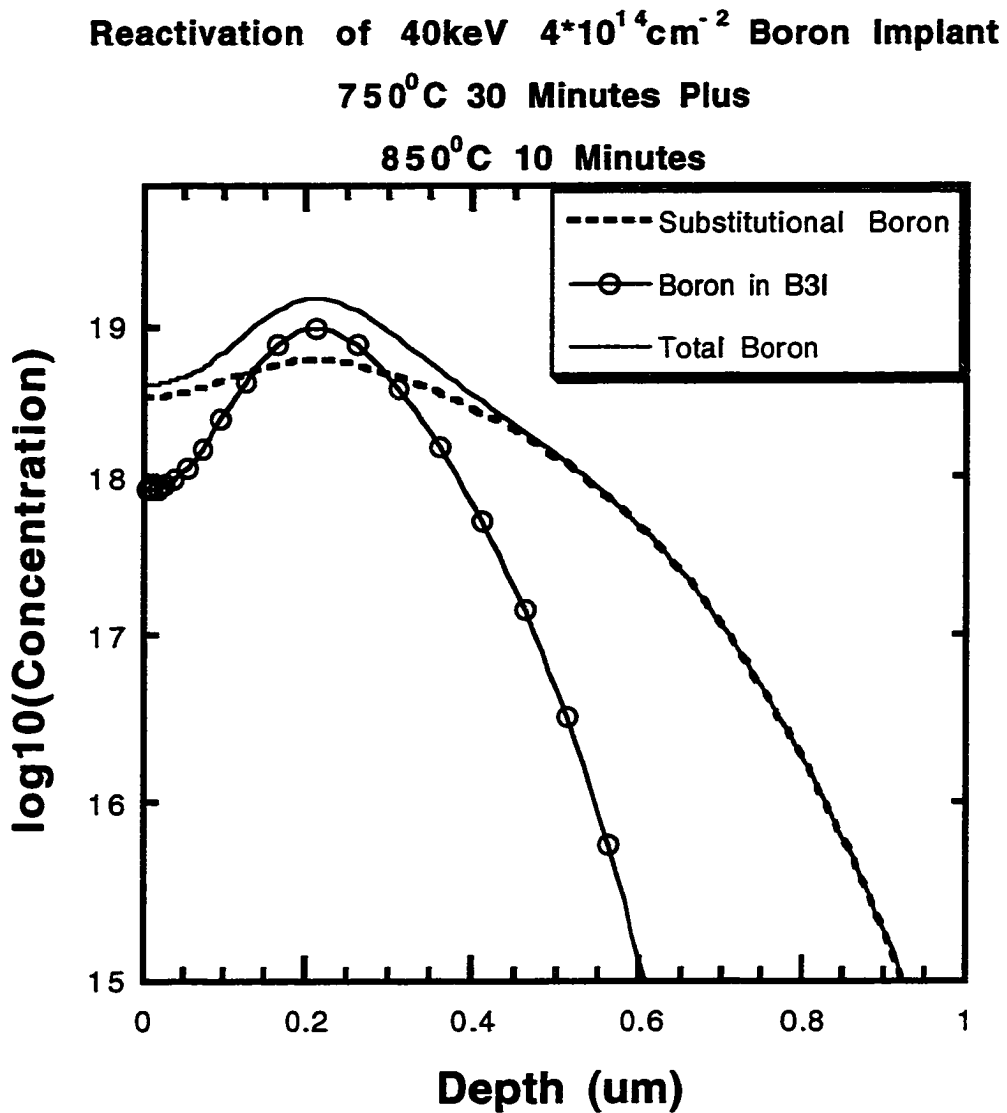


Figure 4-5 Simulation of a 40 keV $4 \times 10^{14} \text{ cm}^{-2}$ boron implant annealed for 30 minutes at a temperature of 750°C (state of Figure 4-4) with an additional 10 minute anneal at 850°C.

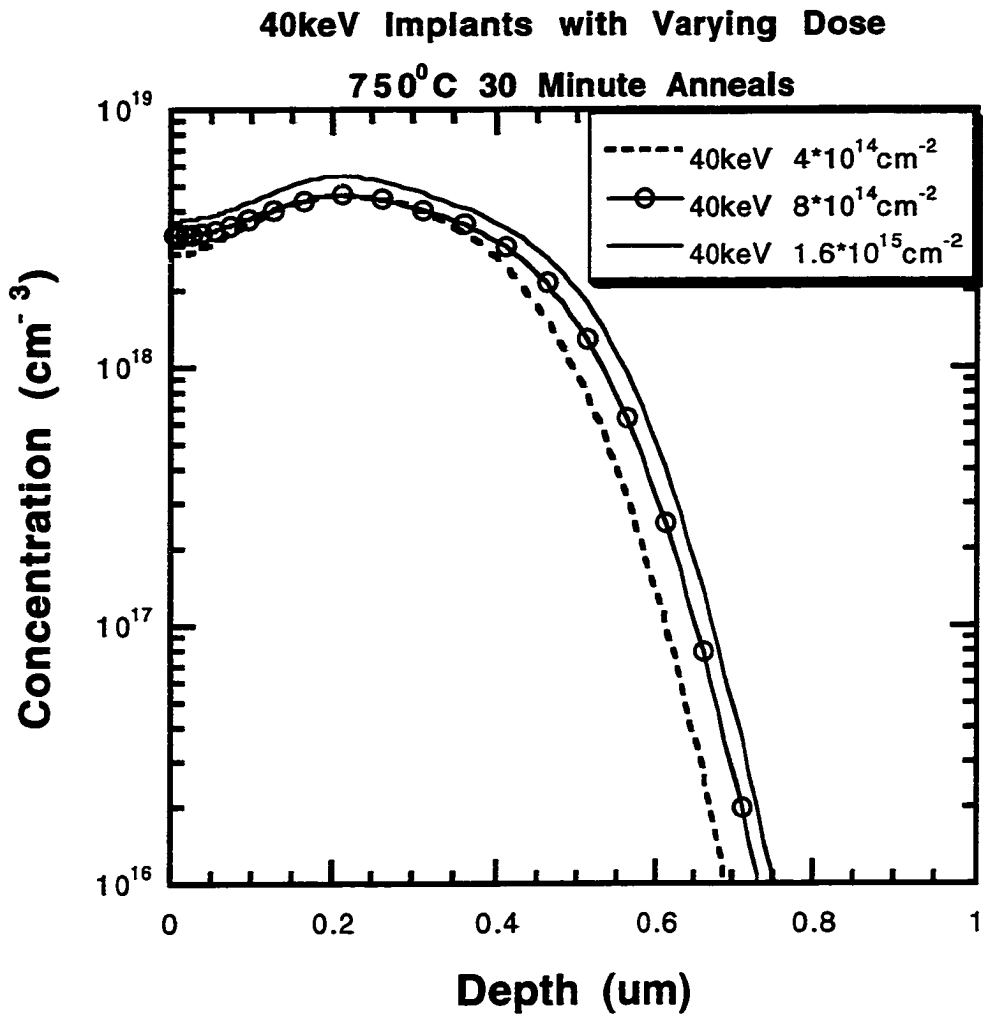


Figure 4-6 Simulation illustrating the levels of boron substitutionality following a 750⁰C anneal for 30 minutes of a 40 keV boron implant of varying dose. Note the boron substitutional level saturates in the mid 10^{18} cm^{-3} concentrations with very little change over a significant dose range.

Fractional Activation Accounting for Fractional Activation

40keV $4 \times 10^{14} \text{ cm}^{-2}$ Boron Implant

750°C 30 Minute Anneal

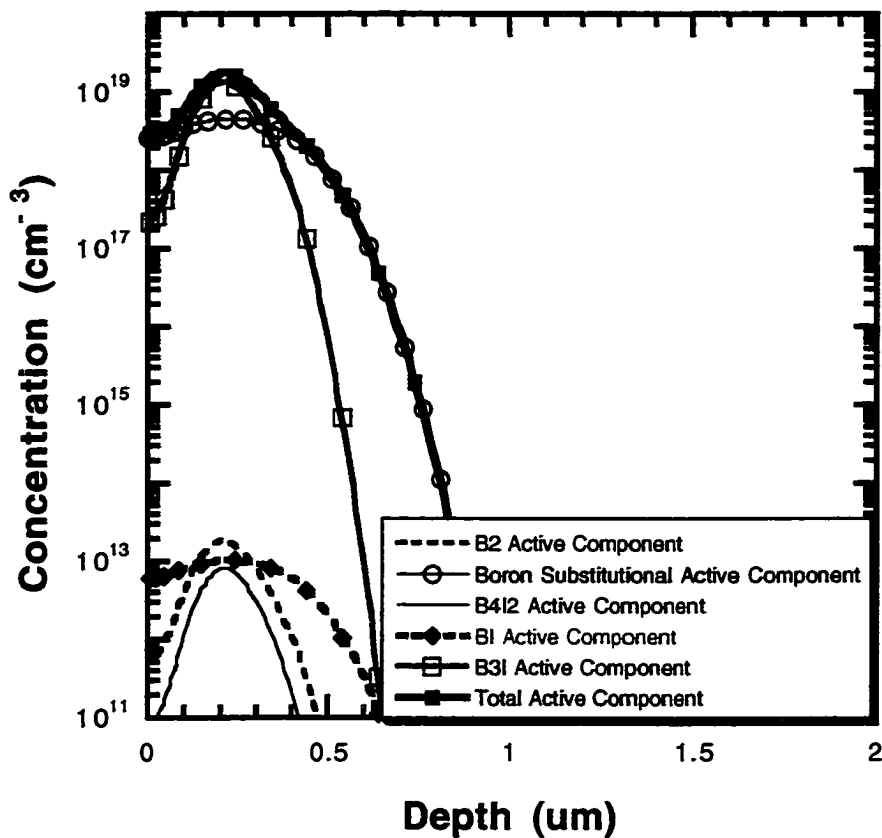


Figure 4-7 Simulation of the boron activation from a 40 keV $4 \times 10^{14} \text{ cm}^{-2}$ boron implant annealed at 750°C for 30 minutes. Including the fractional activation of the B3I cluster leads to an over estimate of the sheet number. For this condition, the SRP profile saturates at approximately $5 \times 10^{18} \text{ cm}^{-3}$ concentration.

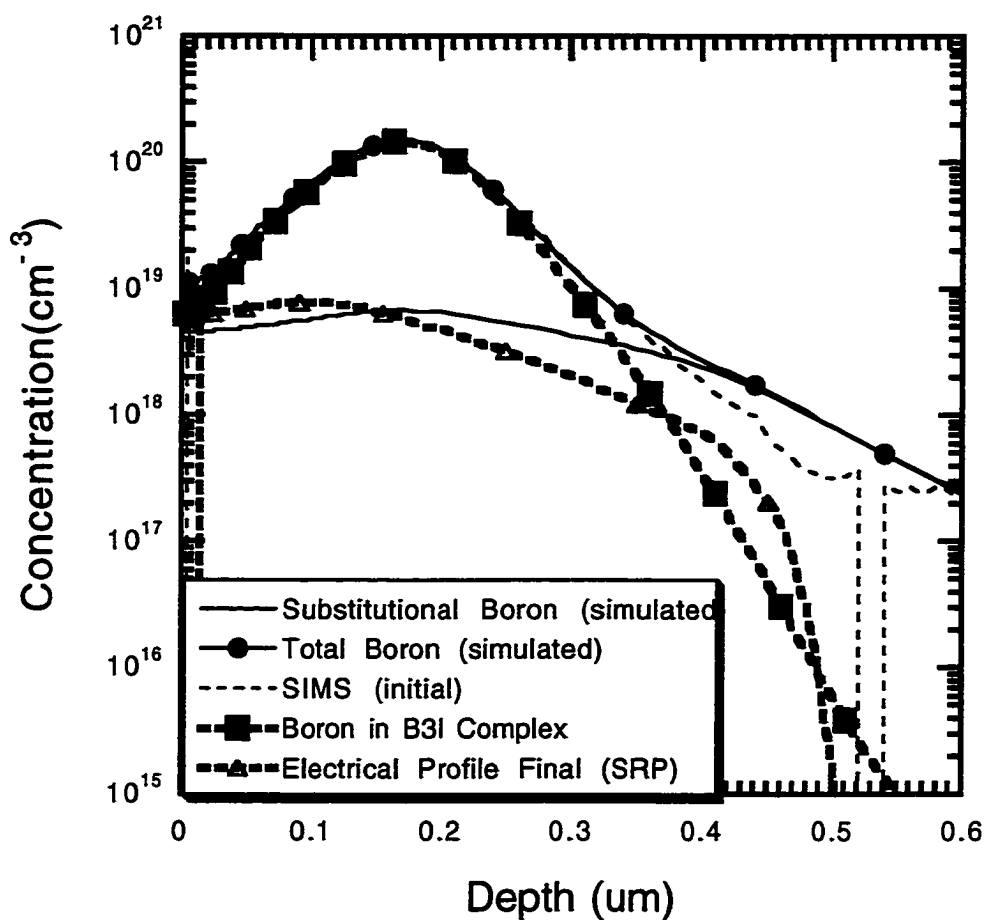


Figure 4-8 Direct comparison of the activation exhibited by the model developed through this work and electrical measurement from SRP. A 40 keV $1.6 \times 10^{15} \text{ cm}^{-2}$ boron implant was subjected to a 30 minute 750°C Anneal.

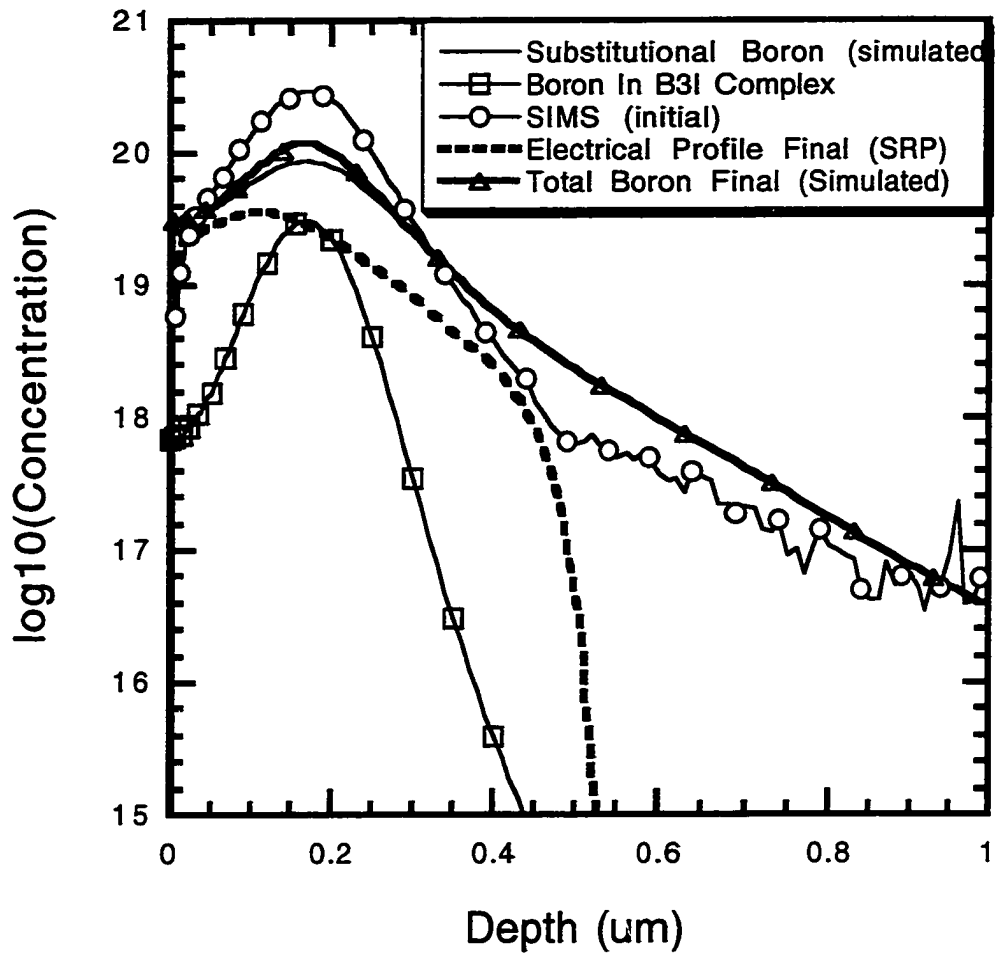


Figure 4-9 Direct comparison of the activation exhibited by the model developed through this work and electrical measurement from SRP. A 40 keV $1.6 \times 10^{15} \text{ cm}^{-2}$ boron implant was subjected to a 30 minute 750°C Anneal (state of Figure 4-8) followed by a 10 minute anneal at 850°C.

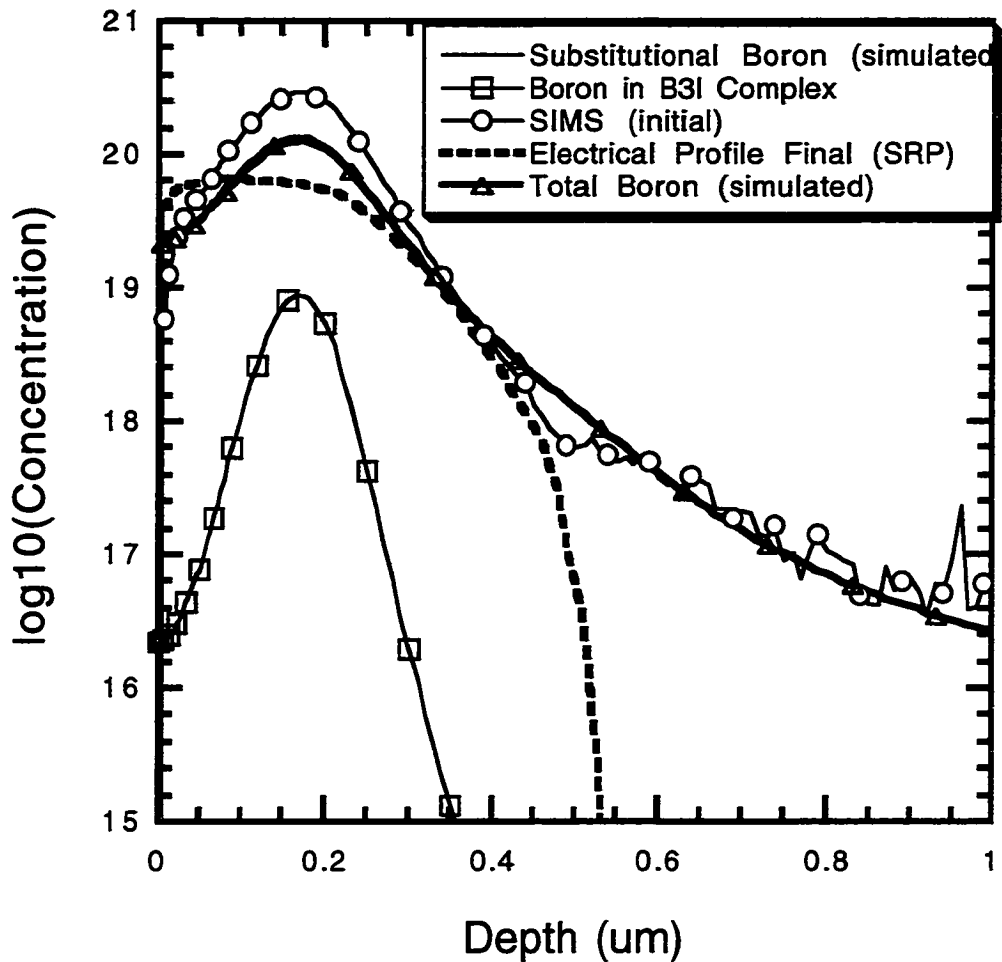


Figure 4-10 Direct comparison of the activation exhibited by the model developed through this work and electrical measurement from SRP. A 40 keV $1.6 \times 10^{15} \text{ cm}^{-2}$ boron implant was subjected to a 30 minute 750°C Anneal (state of Figure 4-8) followed by a 120 minute anneal at 850°C . At this time, the boron is essentially fully substitutional in the simulated result and essentially fully active in the electrical profile.

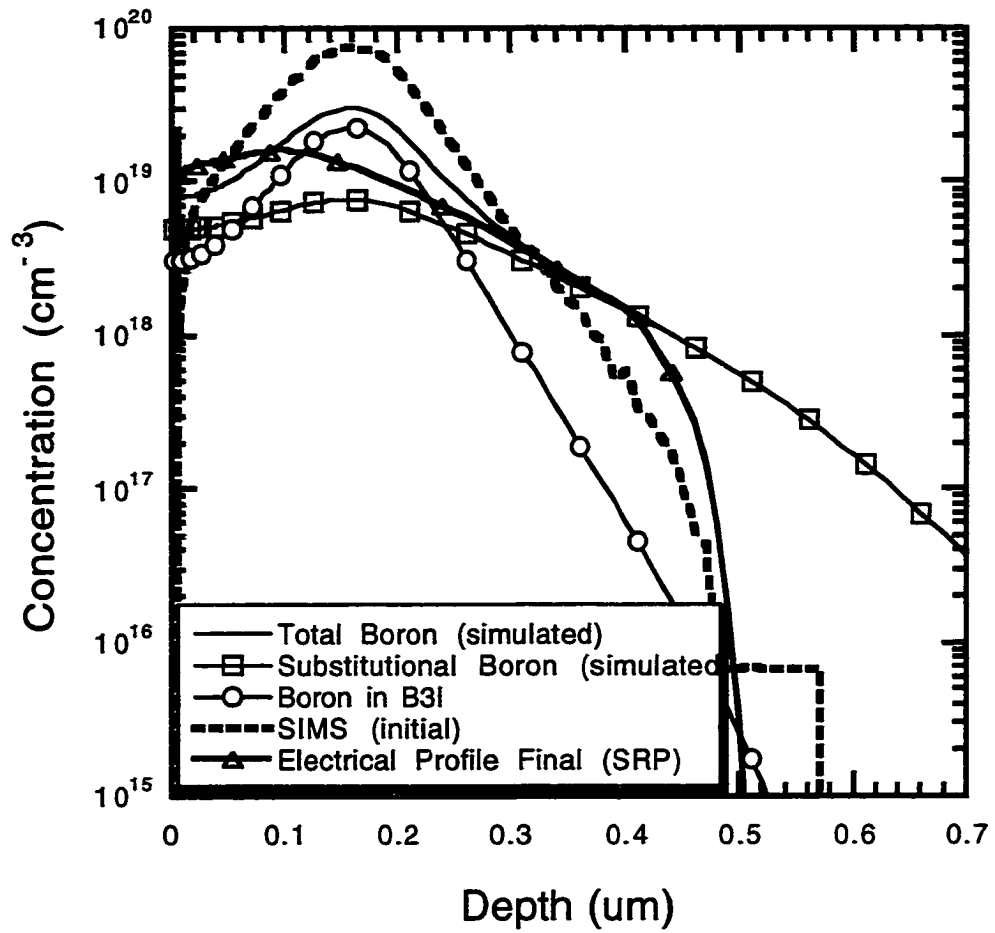


Figure 4-11 Direct comparison of the activation exhibited by the model developed through this work and electrical measurement from SRP. A 40 keV $4 \times 10^{14} \text{ cm}^{-2}$ boron implant was subjected to a 30 minute 750°C anneal.

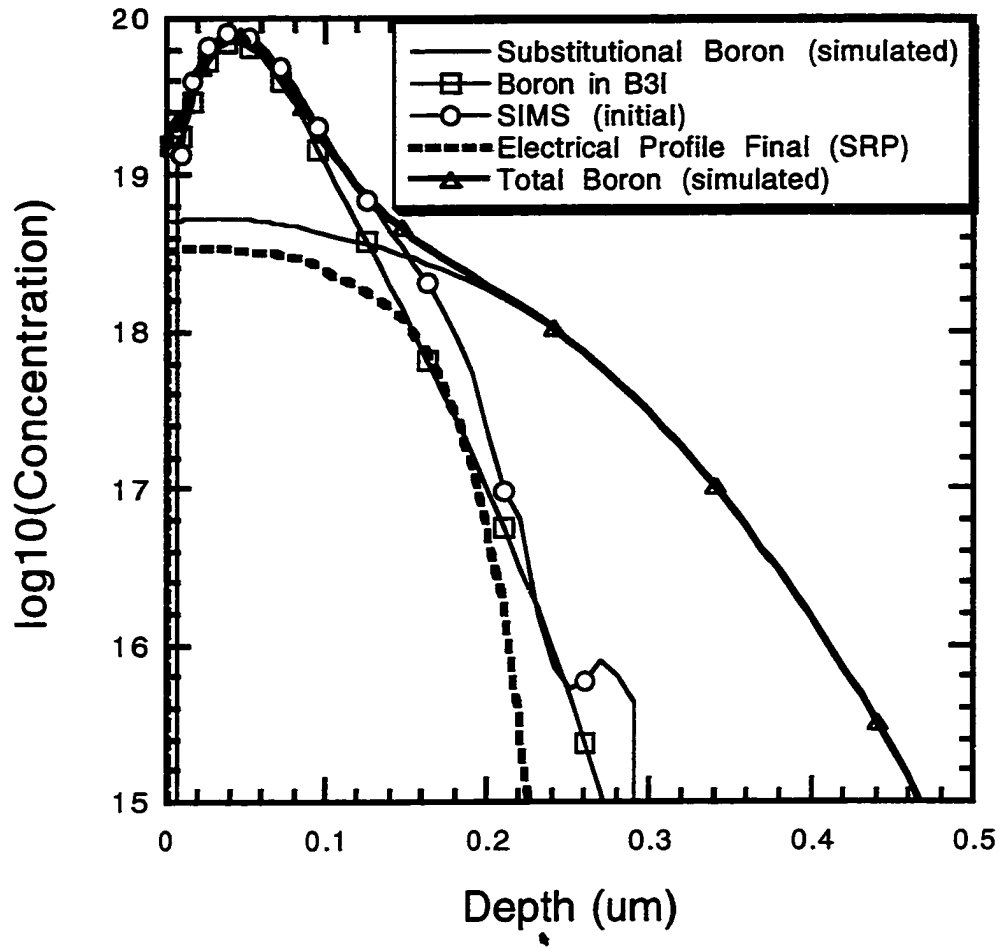


Figure 4-12 Direct comparison of the activation exhibited by the model developed through this work and electrical measurement from SRP. A 10 keV $4 \times 10^{14} \text{ cm}^{-2}$ boron implant was subjected to a 30 minute 750°C anneal.

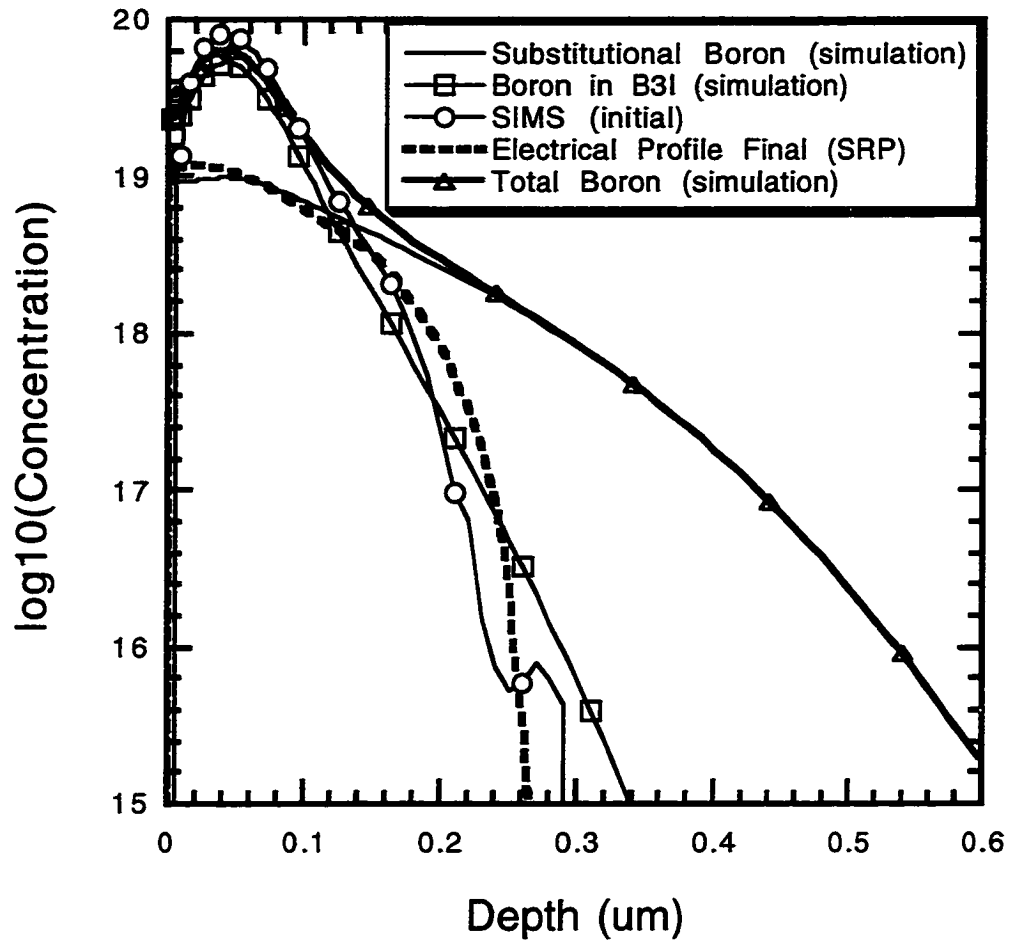


Figure 4-13 Direct comparison of the activation exhibited by the model developed through this work and electrical measurement from SRP. A 10 keV $4 \times 10^{14} \text{ cm}^{-2}$ boron implant was subjected to a 30 minute 750°C anneal (state of Figure 4-12) followed by a 850°C anneal for a time of 10 minutes.

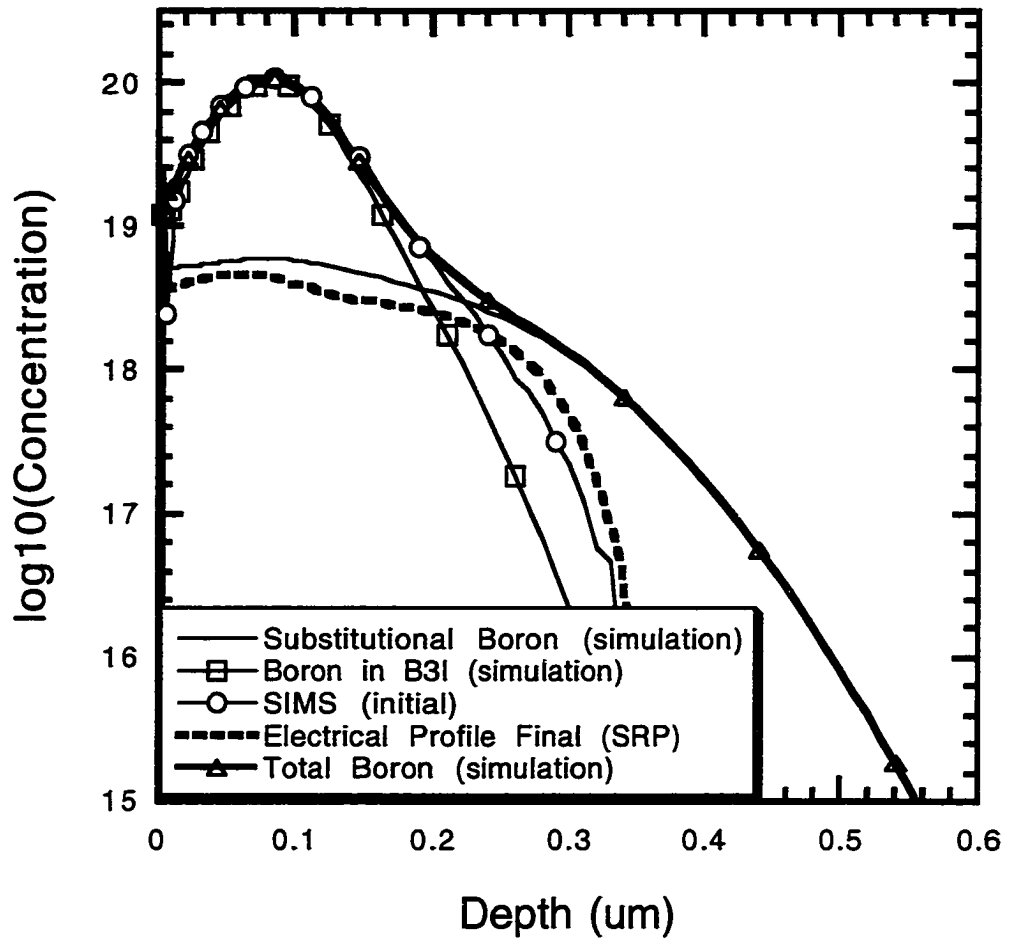


Figure 4-14 Direct comparison of the activation exhibited by the model developed through this work and electrical measurement from SRP. A 20 keV $8 \times 10^{14} \text{ cm}^{-2}$ boron implant was subjected to a 30 minute 750°C anneal.

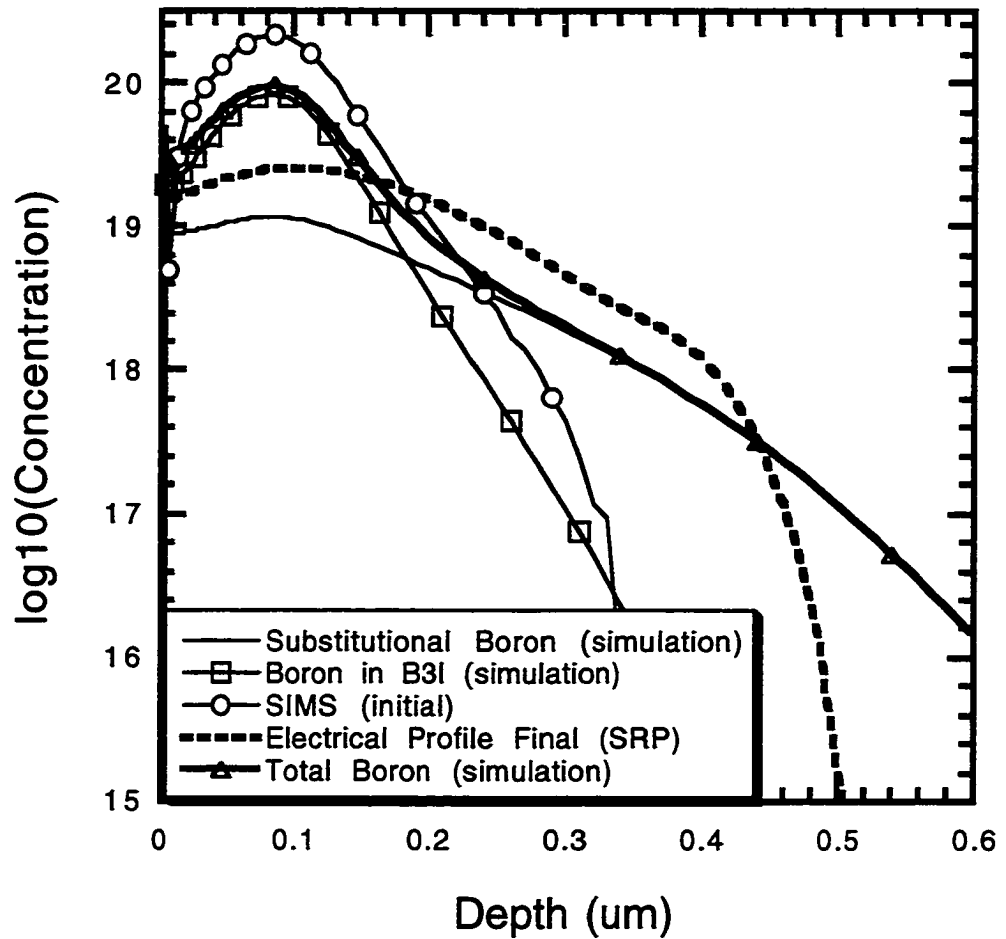


Figure 4-15 Direct comparison of the activation exhibited by the model developed through this work and electrical measurement from SRP. A 20 keV $8 \times 10^{14} \text{ cm}^{-2}$ boron implant was subjected to a 30 minute 750°C anneal (state of Figure 4-14) followed by a 850°C anneal for a time of 10 minutes.

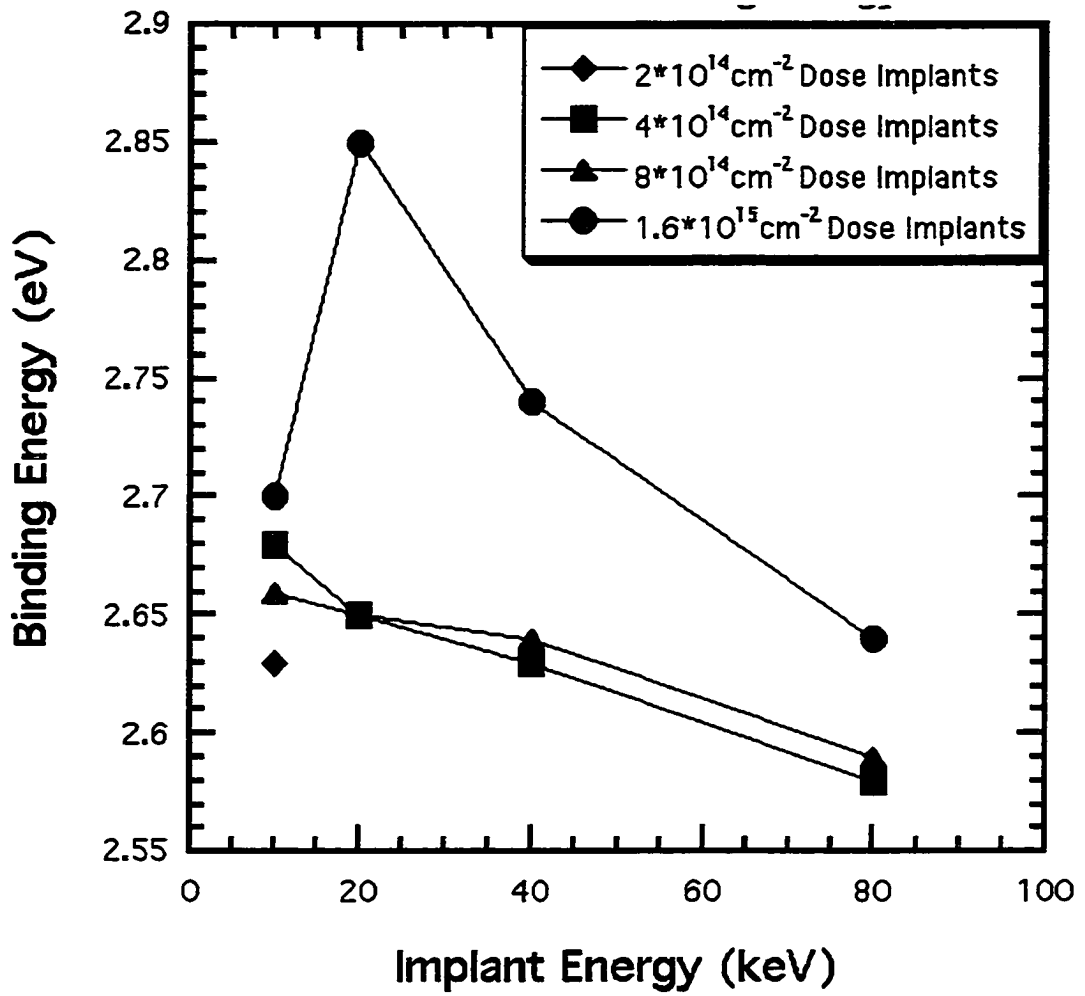


Figure 4-16 Calculated binding energy to dissociation of a boron interstitialcy from a BIC-like cluster as calculated from anneals at 750°C as a function of implant energy.

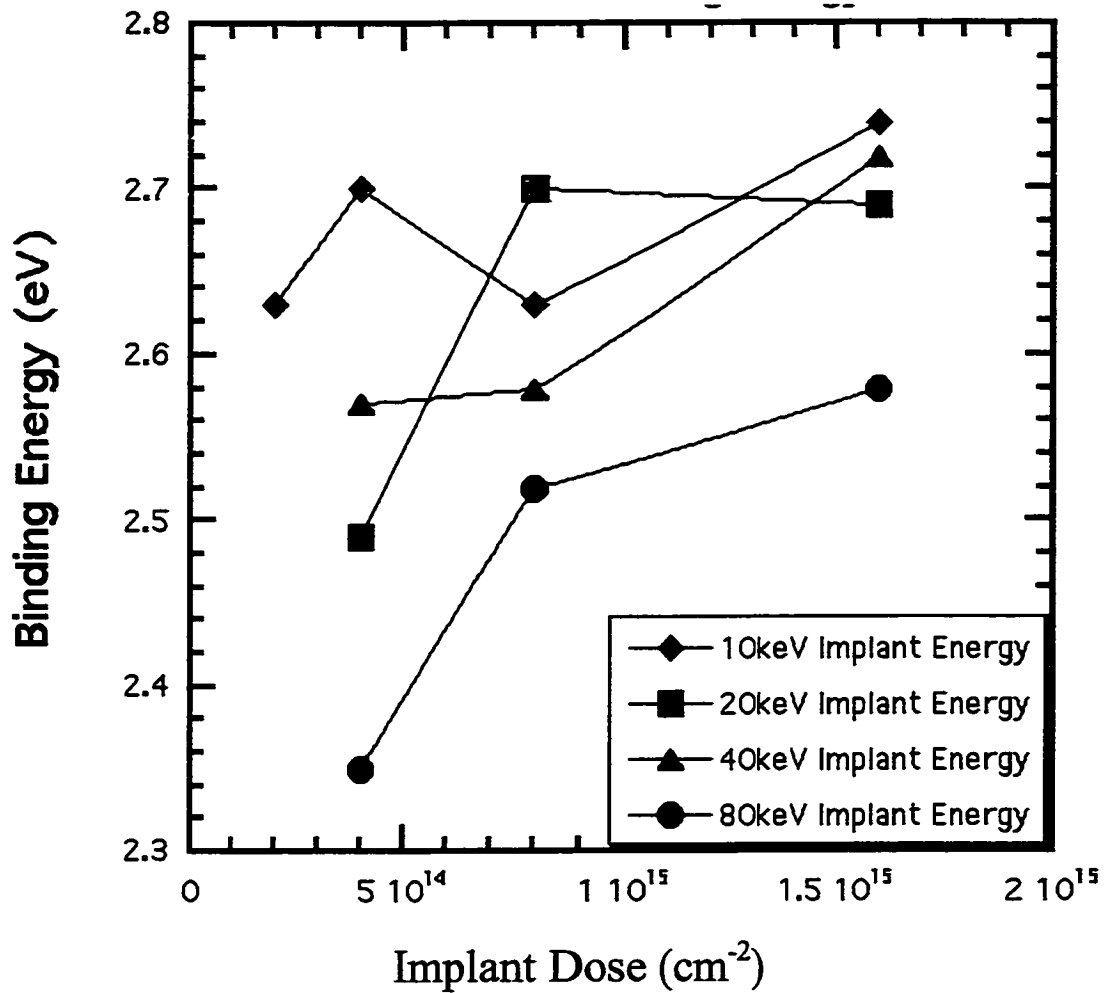


Figure 4-17 Calculated binding energy to dissociation of a boron interstitialcy from a BIC-like cluster as calculated from anneals at 850°C as a function of implant energy.

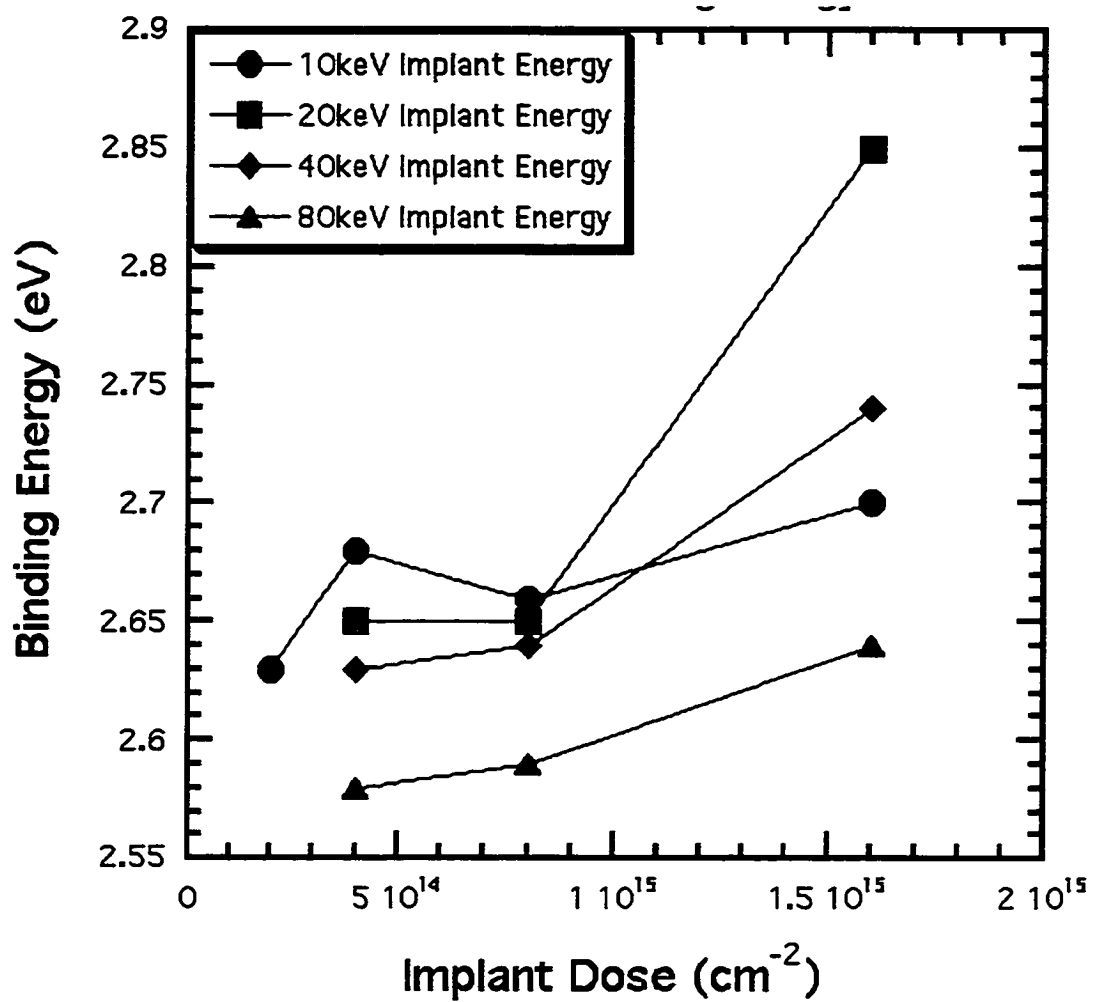


Figure 4-18 Calculated binding energy to dissociation of a boron interstitialcy from a BIC-like cluster as calculated from anneals at 750°C as a function of implant dose.

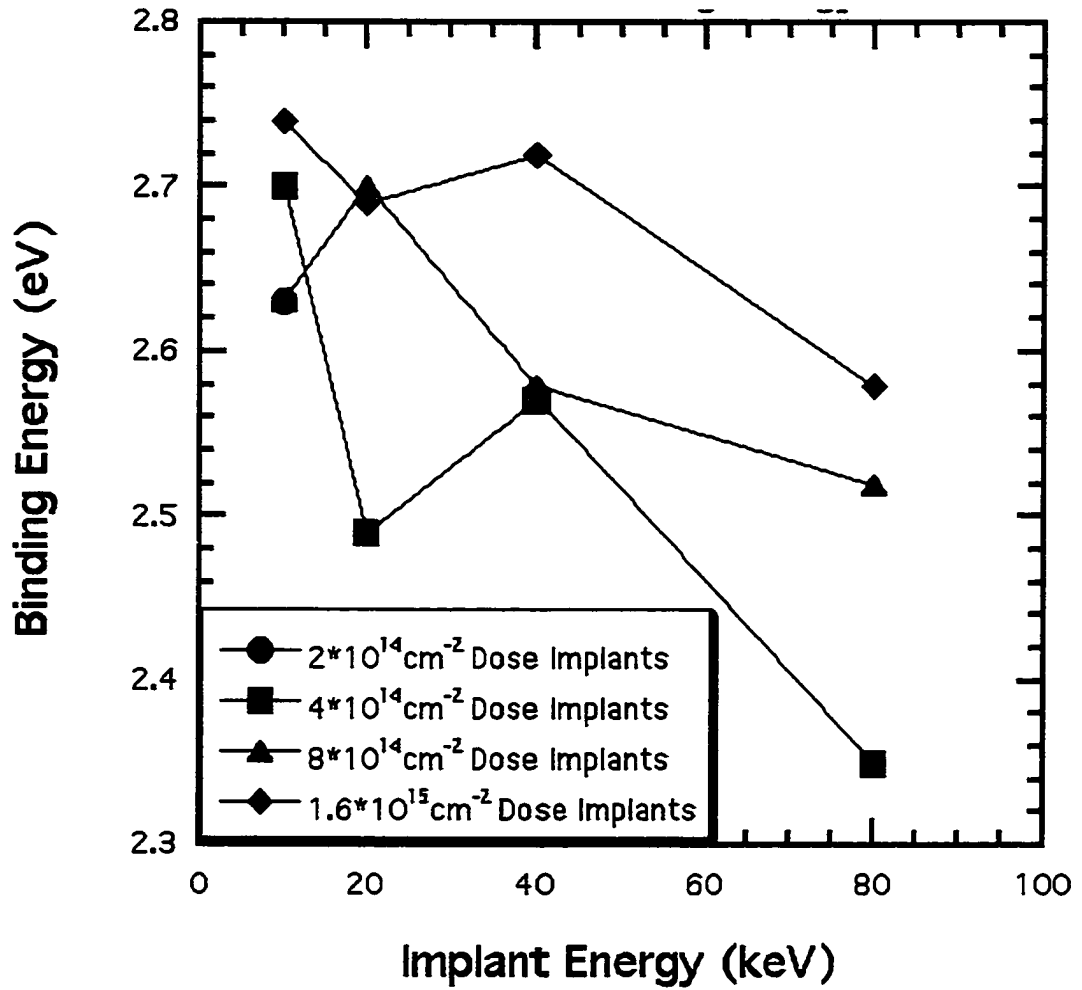


Figure 4-19 Calculated binding energy to dissociation of a boron interstitialcy from a BIC-like cluster as calculated from anneals at 850°C as a function of implant dose.

CHAPTER 5 SUMMARY OF FINDINGS AND FUTURE WORK

5.1 Summary

Transient phenomena are inherent to the use of boron as a dopant in silicon CMOS technologies. If an effort is to be made to minimize these effects, it is first necessary that a thorough physical understanding of their causes and mechanisms be developed. This work represents an effort towards meeting this goal in which experimental results are obtained, analyzed, and implemented within a TCAD simulation software tool. A summary of this work and brief discussion of key results follows.

First-principles calculations have been utilized in the development of a predictive model for boron diffusion and activation. Excellent agreement has been found to exist between the continuum modeling approach we have pursued and the kinetic monte carlo approach performed by Lawrence Livermore National Labs. While a typical KMC simulation may run in a period of 2-3 days on a powerful computer, the continuum model can often provide results in a few minutes. Both models have also validated the utility of first principles calculations to TCAD modeling. Excellent results have been obtained in applying this model to the simulation of transient enhanced diffusion effects, clustering of boron in a uniformly-doped region, and predicting the $\{311\}$ evolution in the presence of high concentrations of boron.

An experiment has been performed in which silicon was implanted into a boron-doped well structure. Following low temperature anneals and QTEM counts of the interstitials trapped in the $\{311\}$ defects it is possible to estimate the number of interstitials which have been removed to form BIC clusters. Analysis with SRP and SIMS can then also be used to determine the number of boron atoms which have been electrically removed from the well structure and an estimate to the ratio of the trapped interstitials to the trapped boron has been established.

A large matrix of activation data as functions of anneal time, implant energy and implant dose has been developed and is presented herein. Spreading resistance measurements indicate that it is often appropriate to utilize a solubility model to boron activation at low temperatures for deeper implants, but also indicate that this may not be appropriate for shallow implants annealed at high temperatures. Analysis of the activation data has also provided time constants to boron reactivation as a function of anneal temperature, implant dose, implant energy and peak boron concentration. We have utilized these time constants to show that the dissolution of boron clusters is approximately consistent with the presumed energetics of the B3I complex. We have also shown that the reactivation process is strongly concentration dependent.

Comparison of the spreading resistance profiles to the results obtained from our simulations of active boron are favorable. In both simulation and experiment, a solubility model may be appropriate to describe the boron activation behavior in many instances. In general, our simulations of the substitutional boron profile are a very good fit to the carrier profile provided by SRP, however, it is not possible to eliminate the possibility

that certain BIC clusters are fractionally active as predicted by Lawrence Livermore National Laboratories.

5.2 Future Work

There is still a significant amount of research to be done in the area of examining boron activation behavior. The following are some suggestions.

- Study boron activation at lower implant energies. Implant energies of 20 keV to 80 keV are well above what is currently utilized in the formation of source/drain regions of the device. These are the regions where transient phenomena are of particular concern. At lower implant energies, other transient phenomena such as boron enhanced diffusion are more prevalent and the surface would have a much more significant effect upon the diffusion and activation behavior. Implants at lower energies would also resolve some of the Hall effect issues we experienced during this work as the profiles would be much more uniform.
- Study boron activation exhibited by spike, RTA, and laser anneals. The anneal sequence we have used in this study would represent a “worst case” scenario in terms of minimizing transient phenomena. Current CMOS processes utilize short, high-temperature anneals in order to rapidly activate the implant while minimizing the diffusion.
- Study the boron cluster through the use of X-ray diffraction or deep level transient spectroscopy (DLTS). Preliminary studies through this work indicated that it may be possible to use x-ray diffraction to directly monitor the progression of boron clusters through the strain they induce within the crystal. There is currently some

disagreement on the mechanisms involved in boron clustering. Such work would go a long ways towards resolving these issues.

- Study boron activation in the presence of impurity species. Experimental work is performed on material grown by many different techniques. These different growth techniques may introduce concentrations of impurity atoms which may serve to trap interstitials and minimize diffusion and clustering. It may not always be valid to correlate the results of experiments performed on different material.
- Develop a model for boron enhanced diffusion and implement within existing framework. Boron enhanced diffusion, whether it be caused by a cluster, surface or intrinsic charge effects, is a major concern to the formation of ultra-shallow p+/n junctions.
- Develop a modeling approach which better captures the initial state of the system. It is likely that the “plus 1” treatment of the initial damage profile will fail in many instances. Cascade recombinations of the interstitial and vacancy profiles have been attempted and could be used in future. Kinetic monte carlo simulations are also capable of determining the “as-implanted” state of the system. This includes not only the initial damage profile, but also the initial substitutional boron and interstitial boron residual from the implant self-heating. Such deviations from the “plus 1” approach utilized in this work will likely become more severe.
- Update the model as new energetic parameters become available. To date, there has been some variability in these parameters. It is also likely that clusters larger than B3I are important in higher concentration regions.

APPENDIX A

SUPPLEMENTAL DATA FROM BORON IMPLANT STUDY

Chapter 3 illustrates the boron implant/activation study performed as part of this work. For purposes of clarity, some plots were intentionally omitted from this chapter and appear in this appendix. Figures A-1 through A-4 show the as-implanted boron profiles grouped by the implant energy. Figures A-5 through A-8 illustrate the exponential best fits to the boron cluster dissolution data at 750⁰C grouped by the implant energy. Figures A-9 through A-12 illustrate the exponential best fits to the boron cluster dissolution data at 850⁰C grouped by the implant energy. Figures A-13 through A-16 illustrate the time constant to boron cluster dissolution at temperatures of 750⁰C and 850⁰C grouped by the implant energy. Figures A-17 through A-19 illustrate the time constant to boron cluster dissolution at temperatures of 750⁰C and 850⁰C grouped by the implant dose.

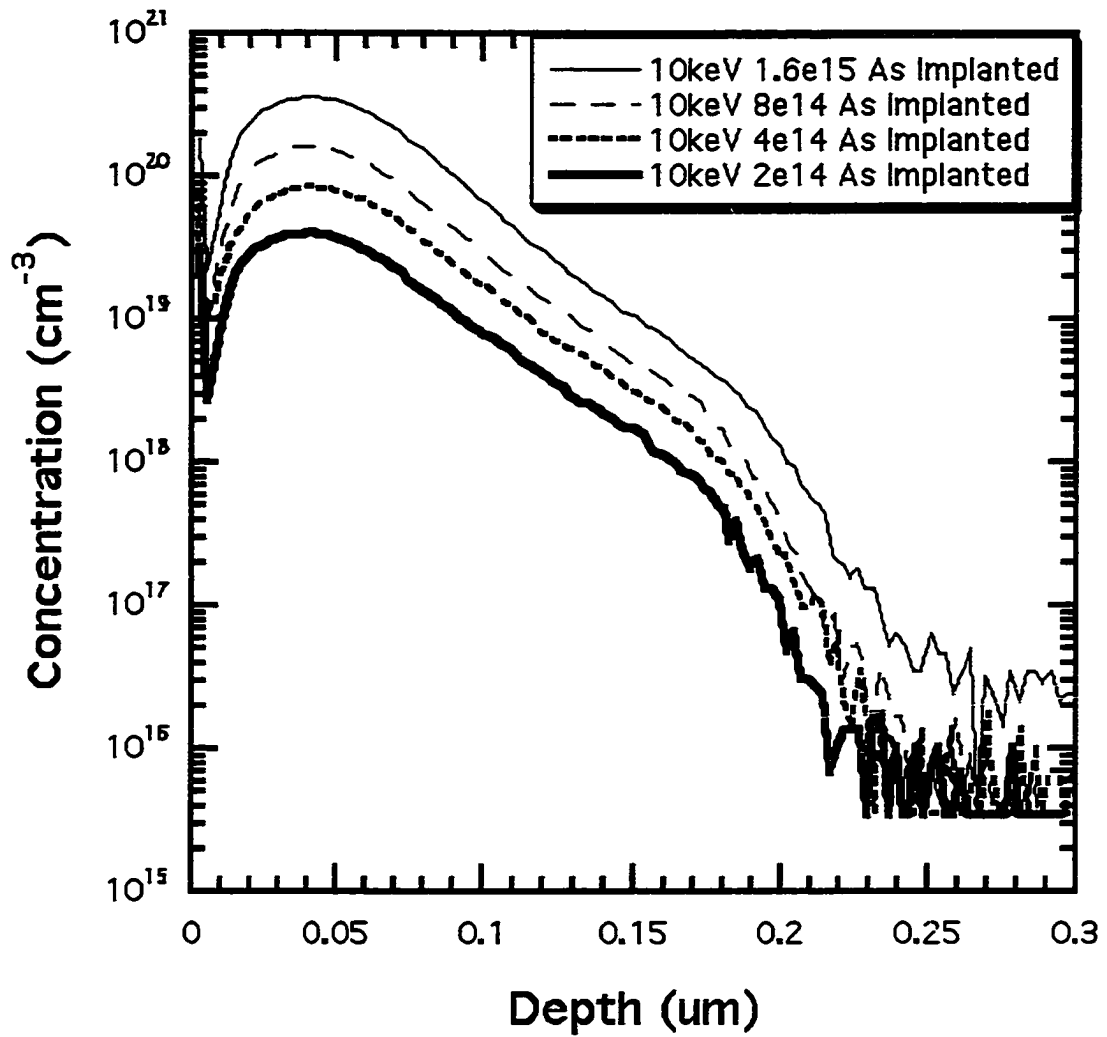


Figure A-1 10 keV as-implanted profiles from SIMS.

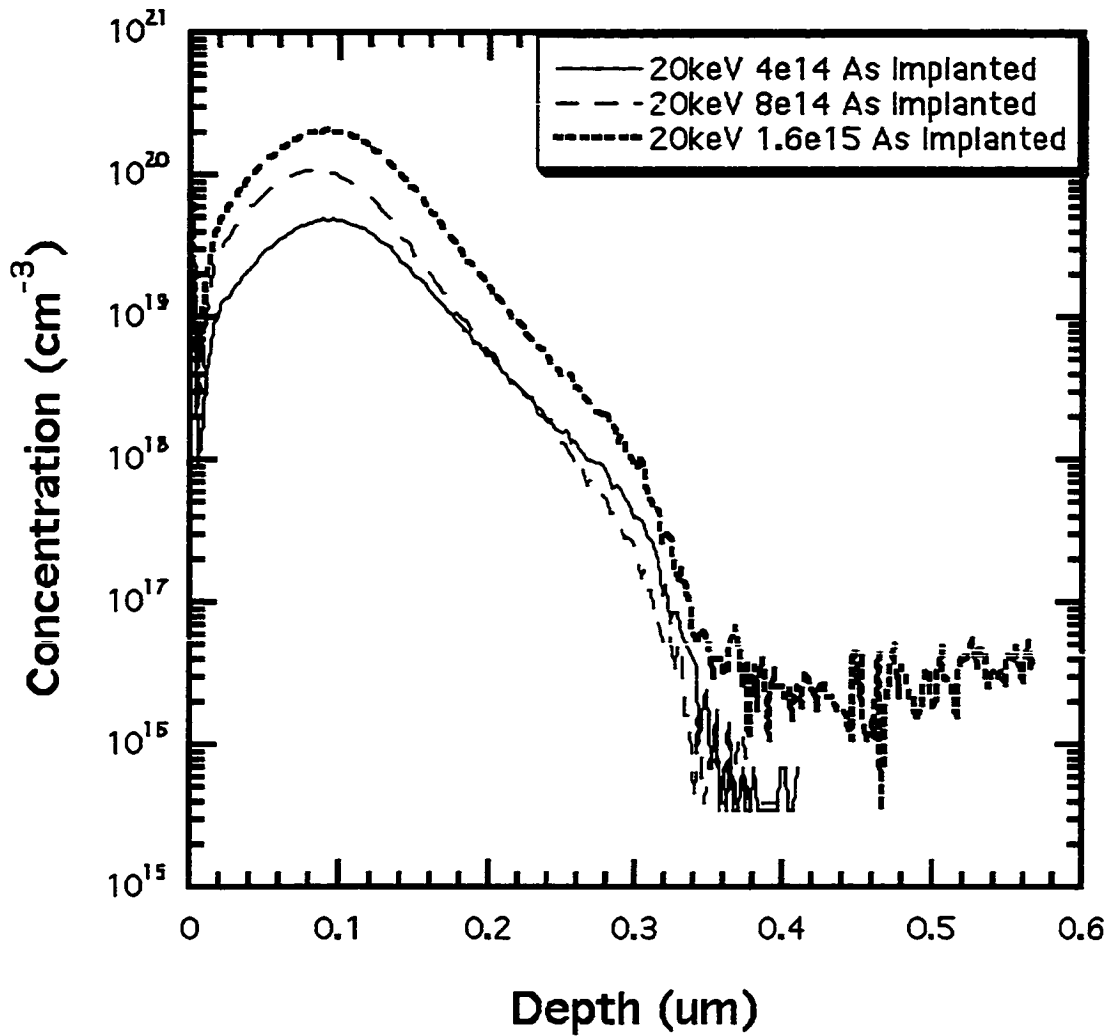


Figure A-2 20 keV as-implanted profiles from SIMS.

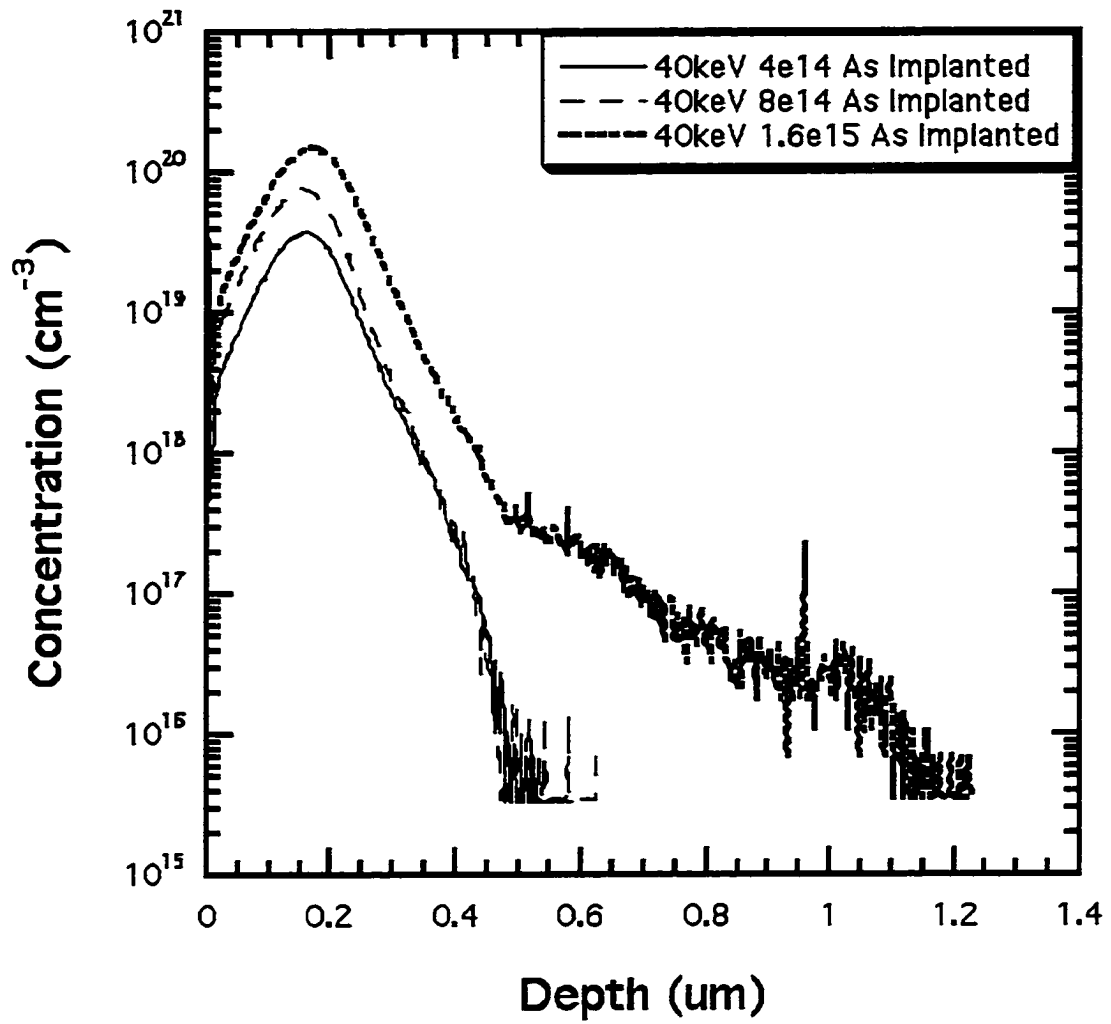


Figure A-3 40 keV as-implanted profiles from SIMS.

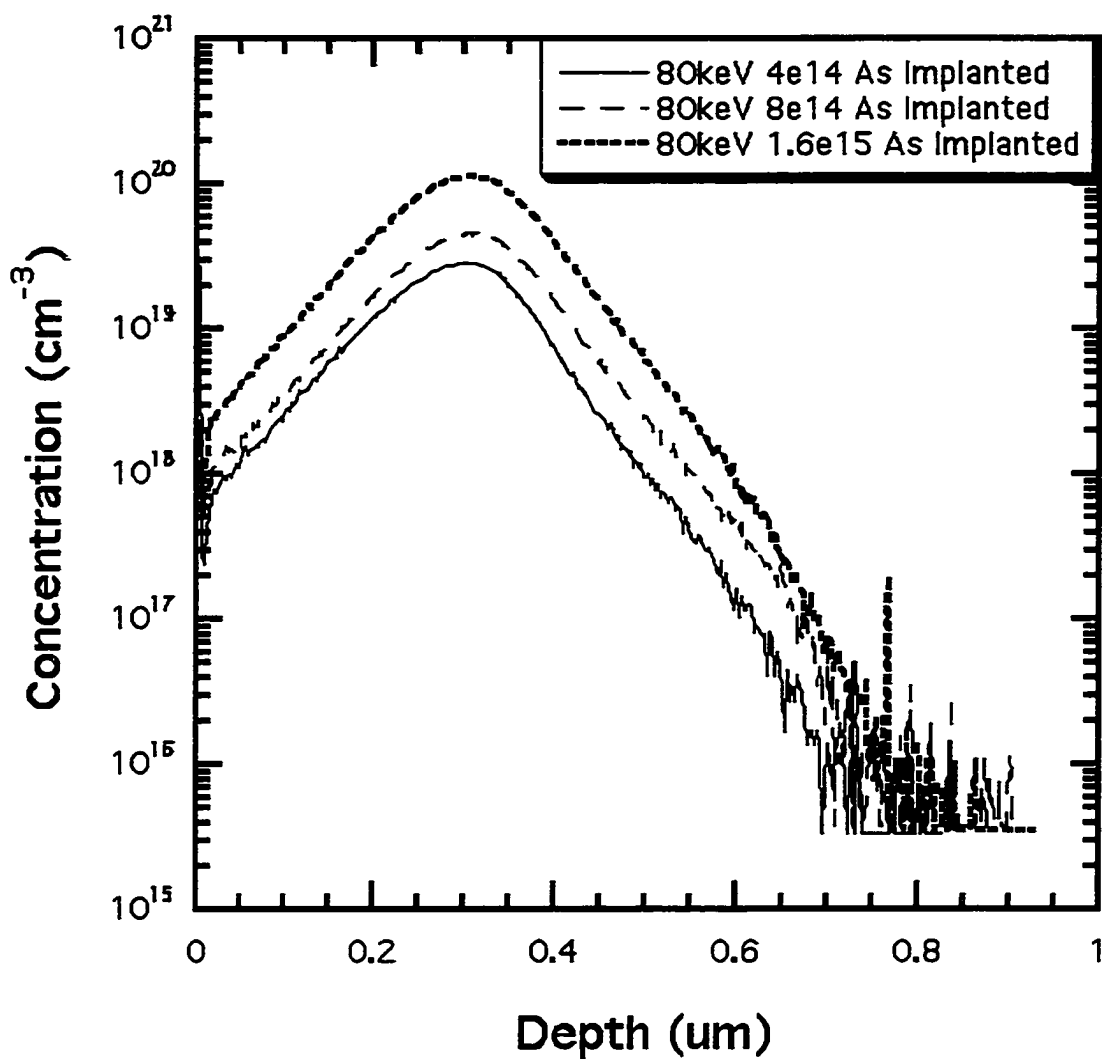


Figure A-4 80 keV as-implanted profiles from SIMS.

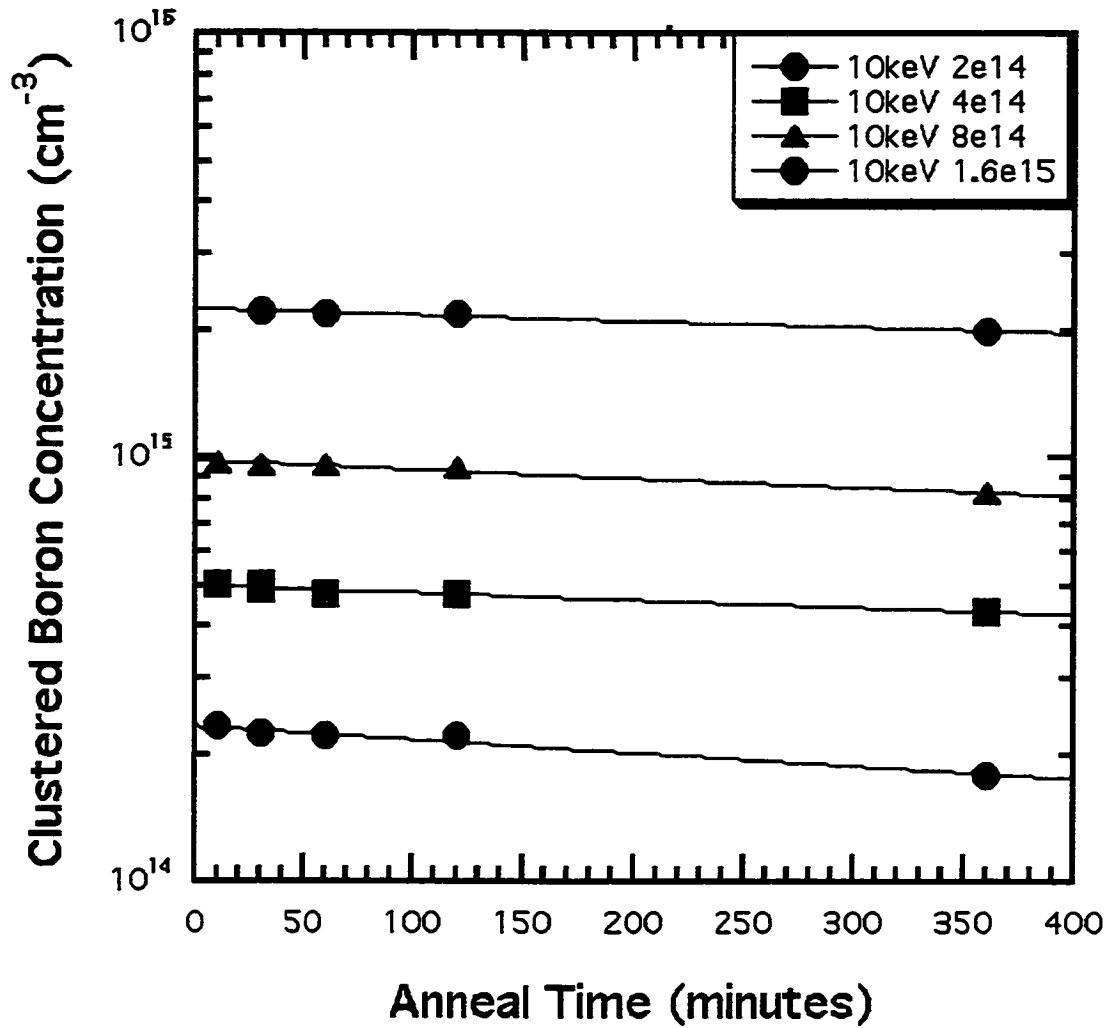


Figure A-5 Exponential best fits to the 750°C BIC cluster dissolution observed from implants performed at 10 keV.

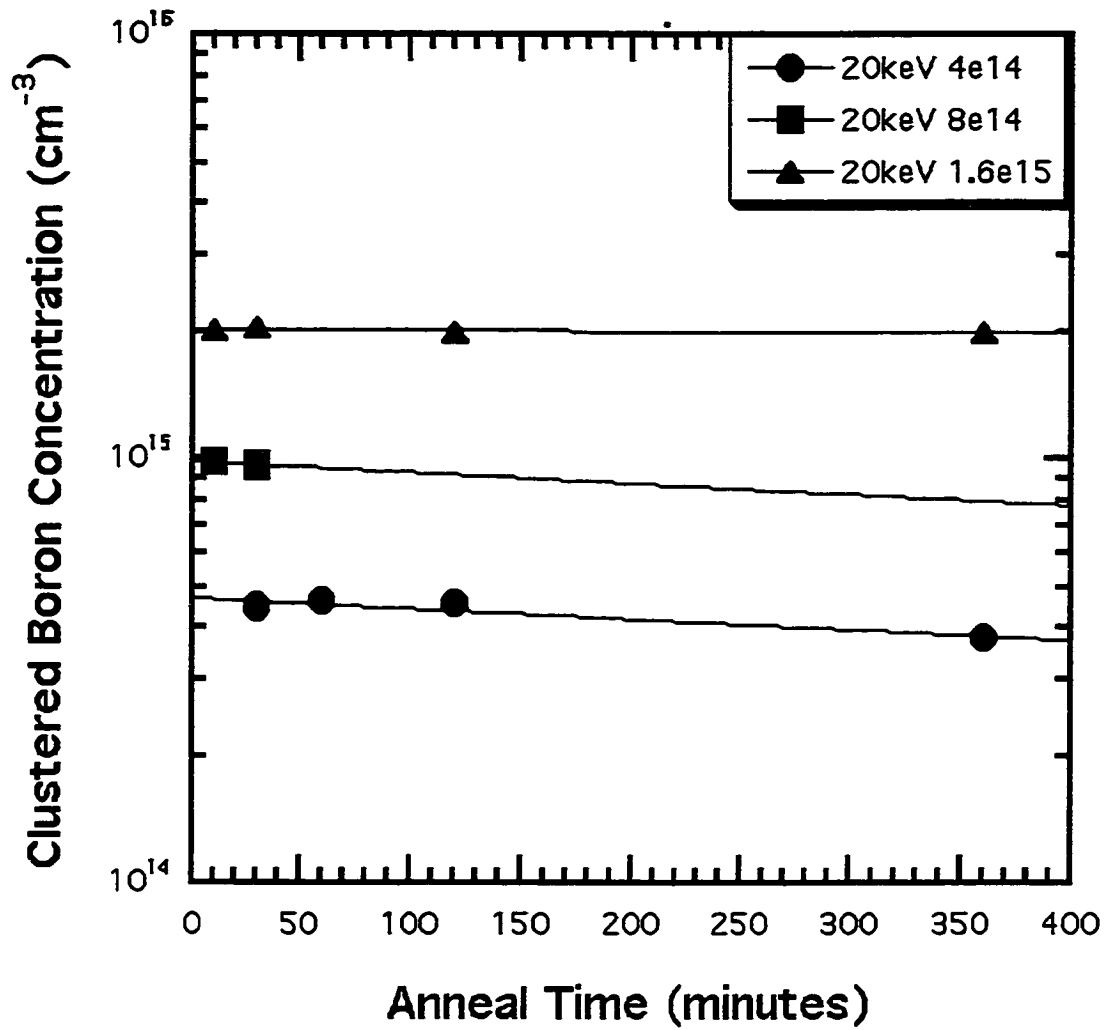


Figure A-6 Exponential best fits to the 750°C BIC cluster dissolution observed from implants performed at 20 keV.

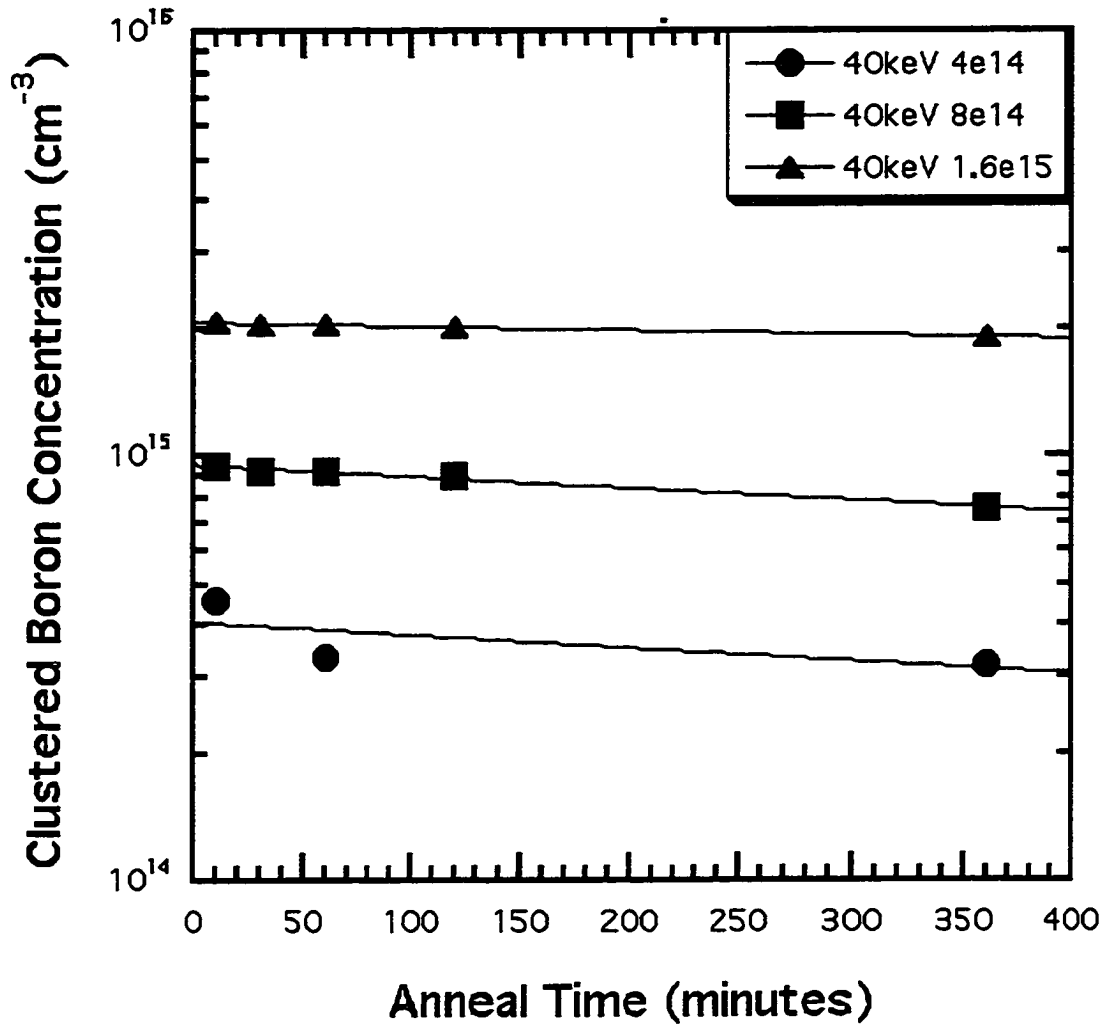


Figure A-7 Exponential best fits to the 750°C BIC cluster dissolution observed from implants performed at 40 keV.

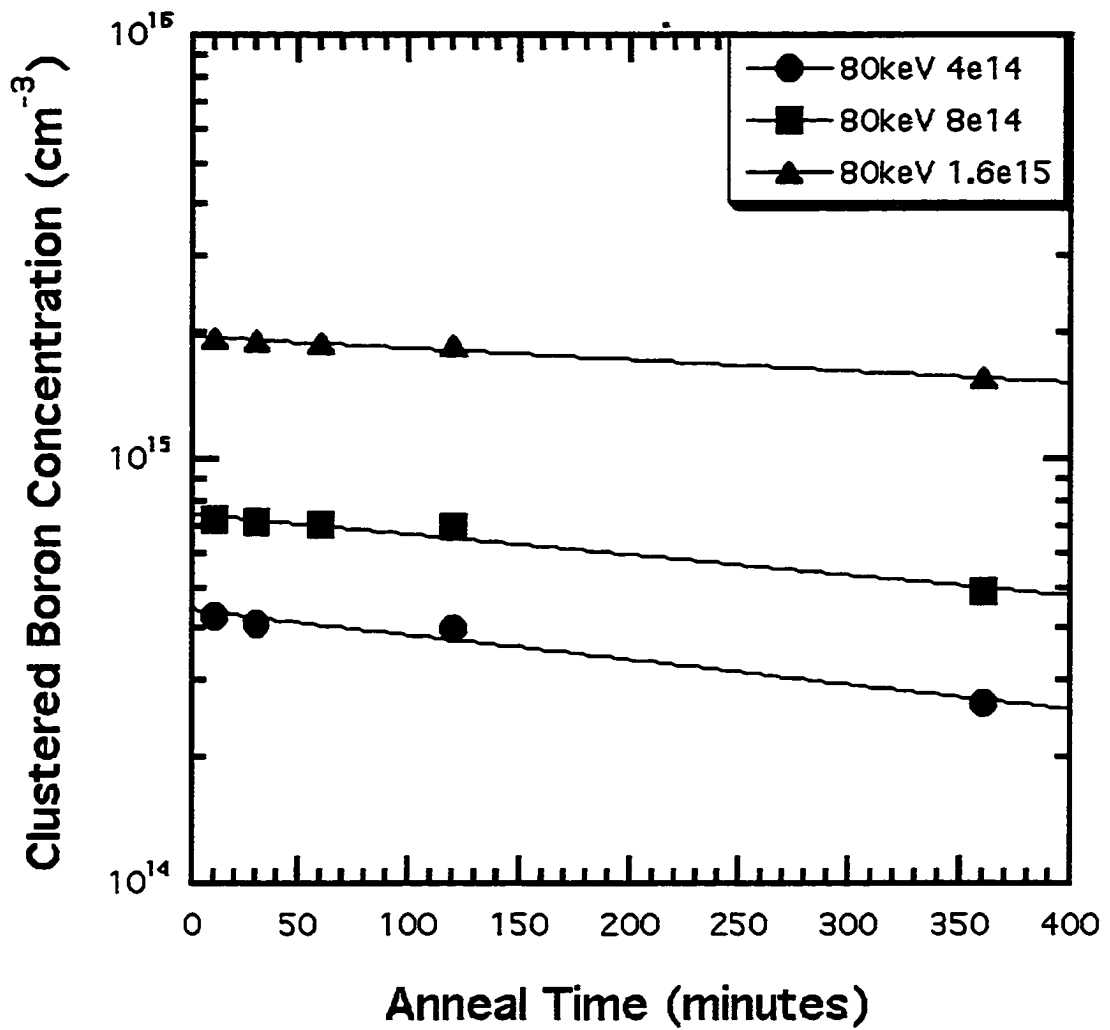


Figure A-8 Exponential best fits to the 750°C BIC cluster dissolution observed from implants performed at 80 keV.

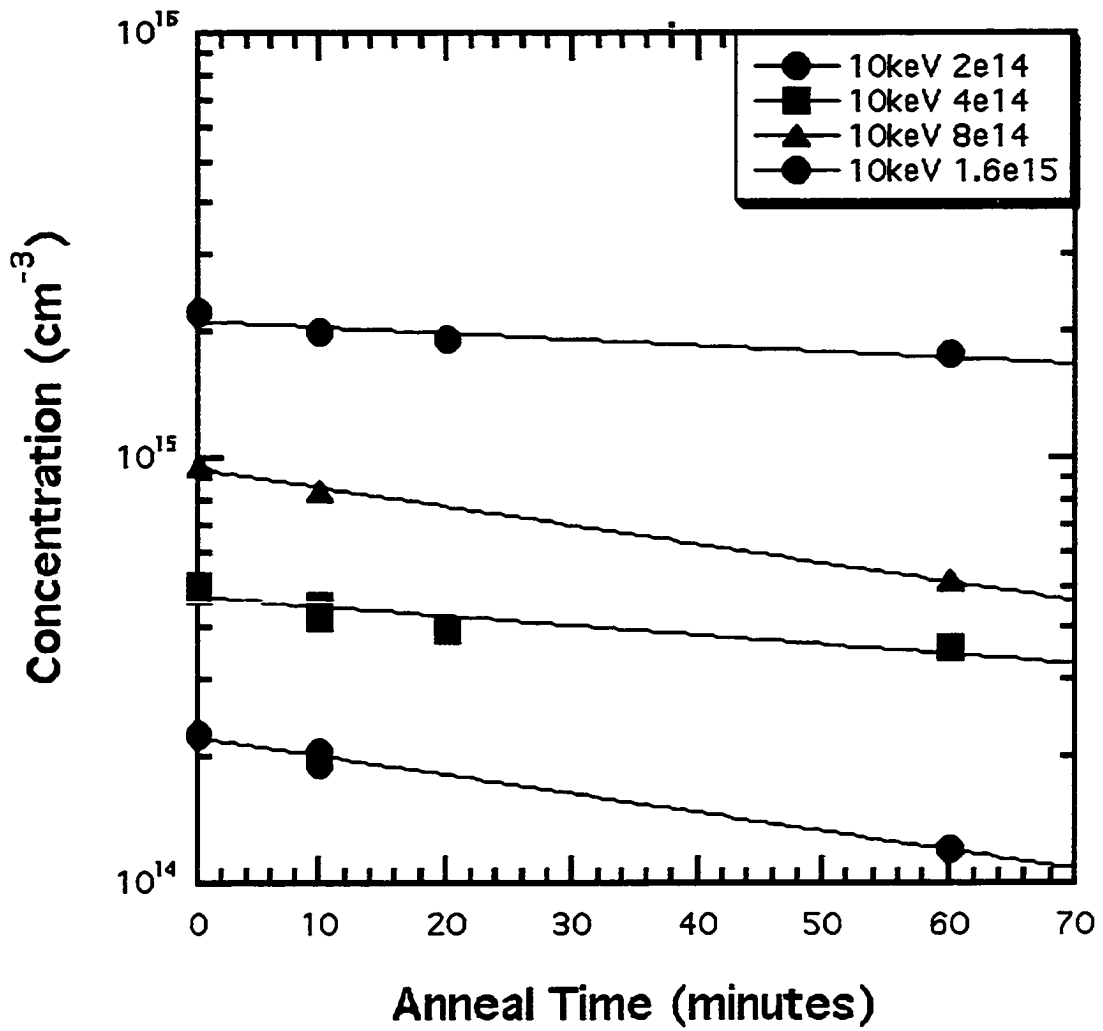


Figure A-9 Exponential best fits to the 850°C BIC cluster dissolution observed from implants performed at 10 keV.

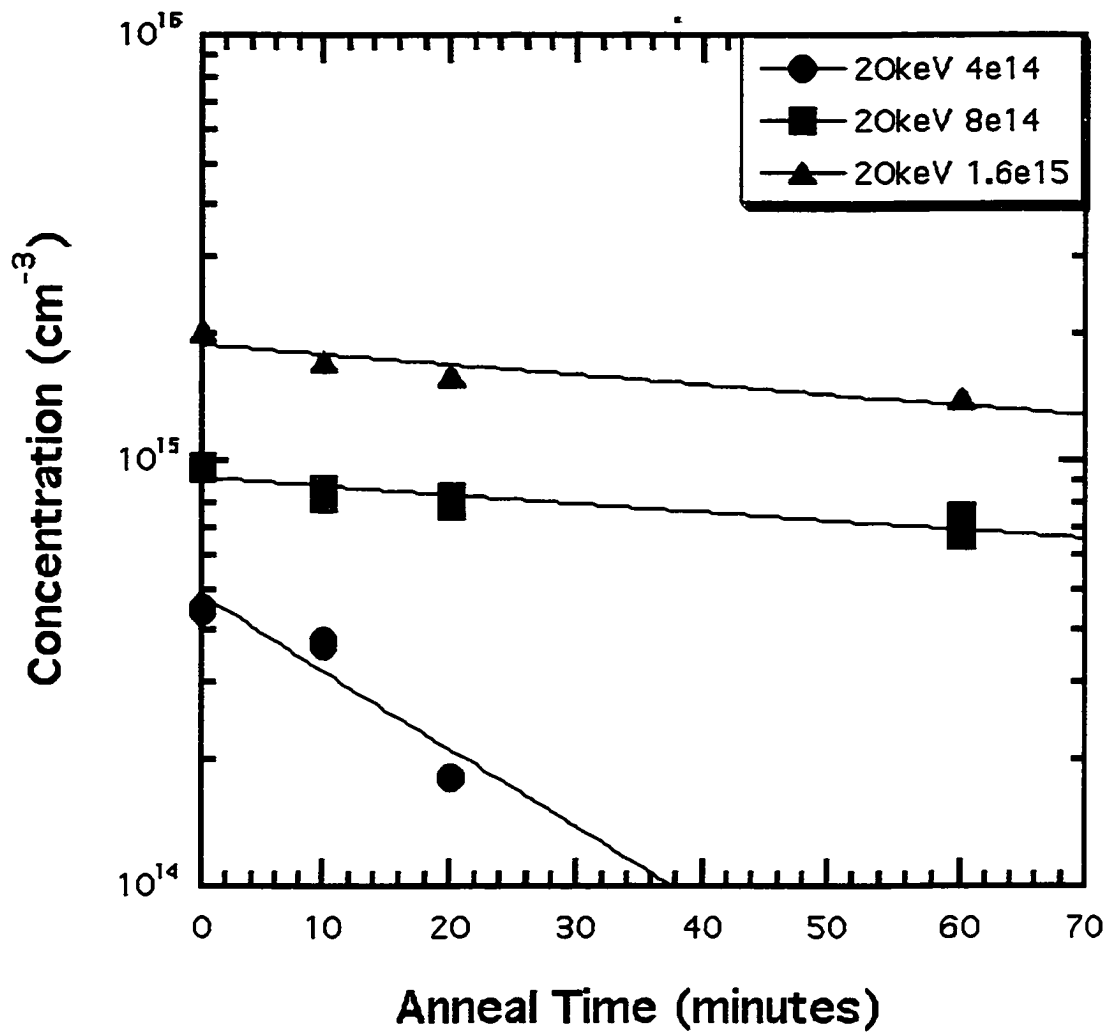


Figure A-10 Exponential best fits to the 850°C BIC cluster dissolution observed from implants performed at 20 keV.

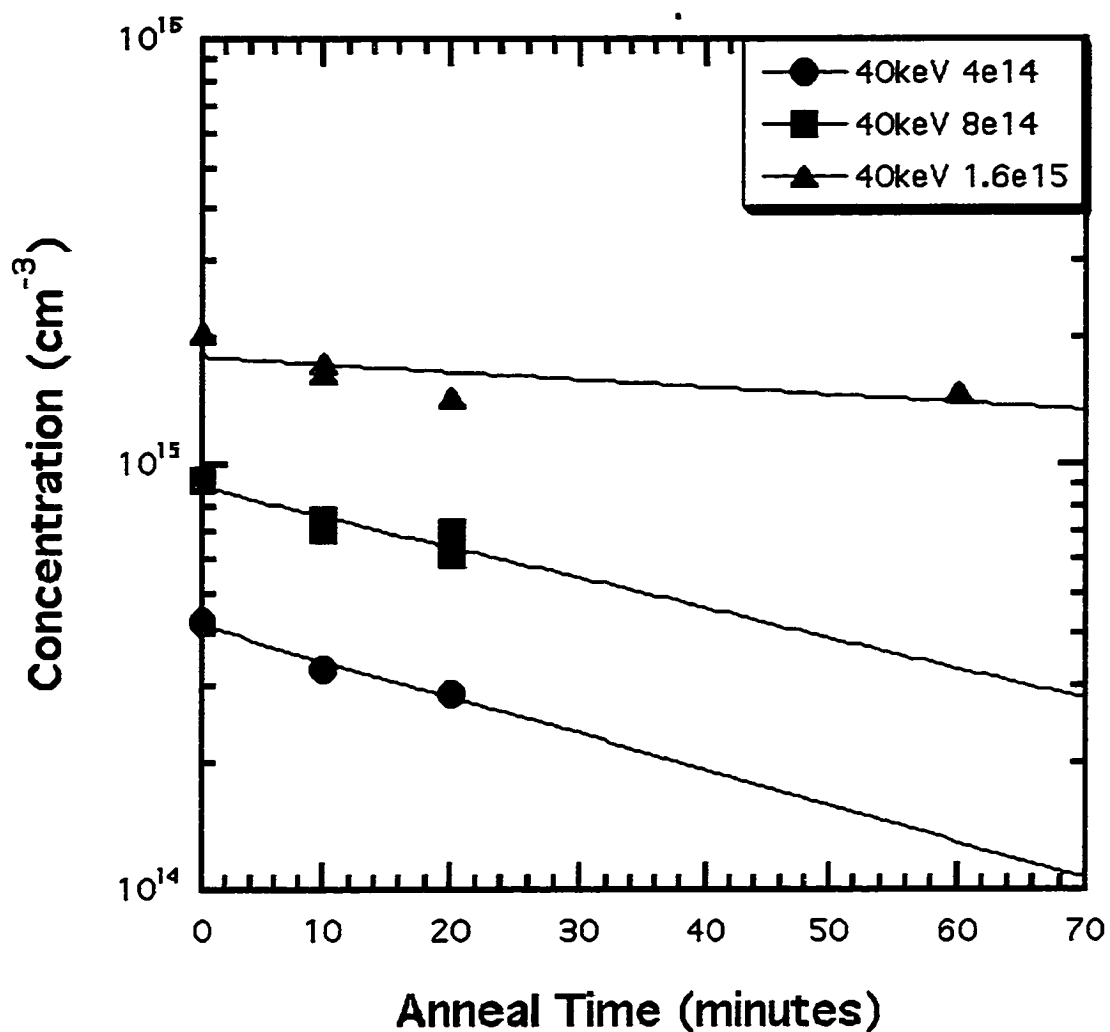


Figure A-11 Exponential best fits to the 850°C BIC cluster dissolution observed from implants performed at 40 keV.

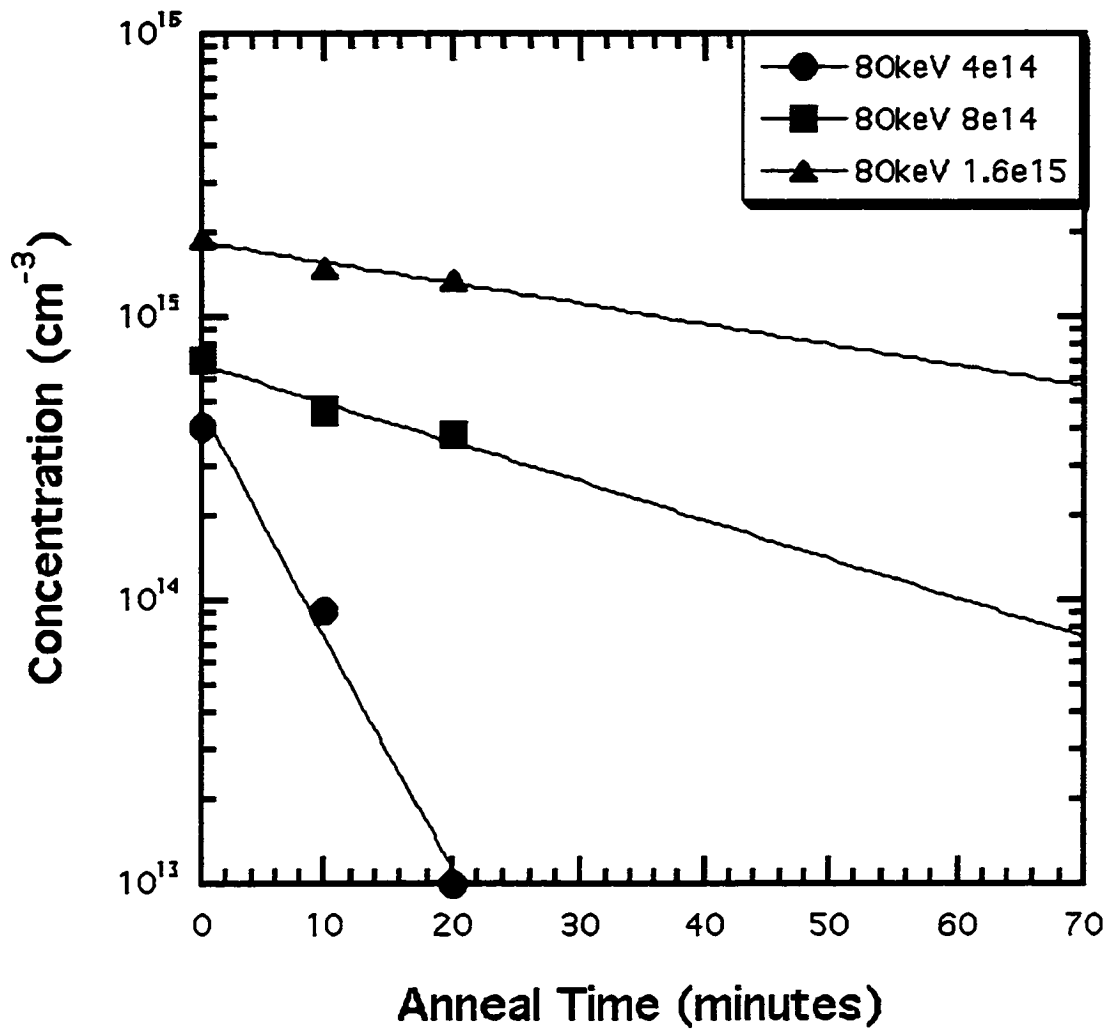


Figure A-12 Exponential best fits to the 850°C BIC cluster dissolution observed from implants performed at 80 keV.

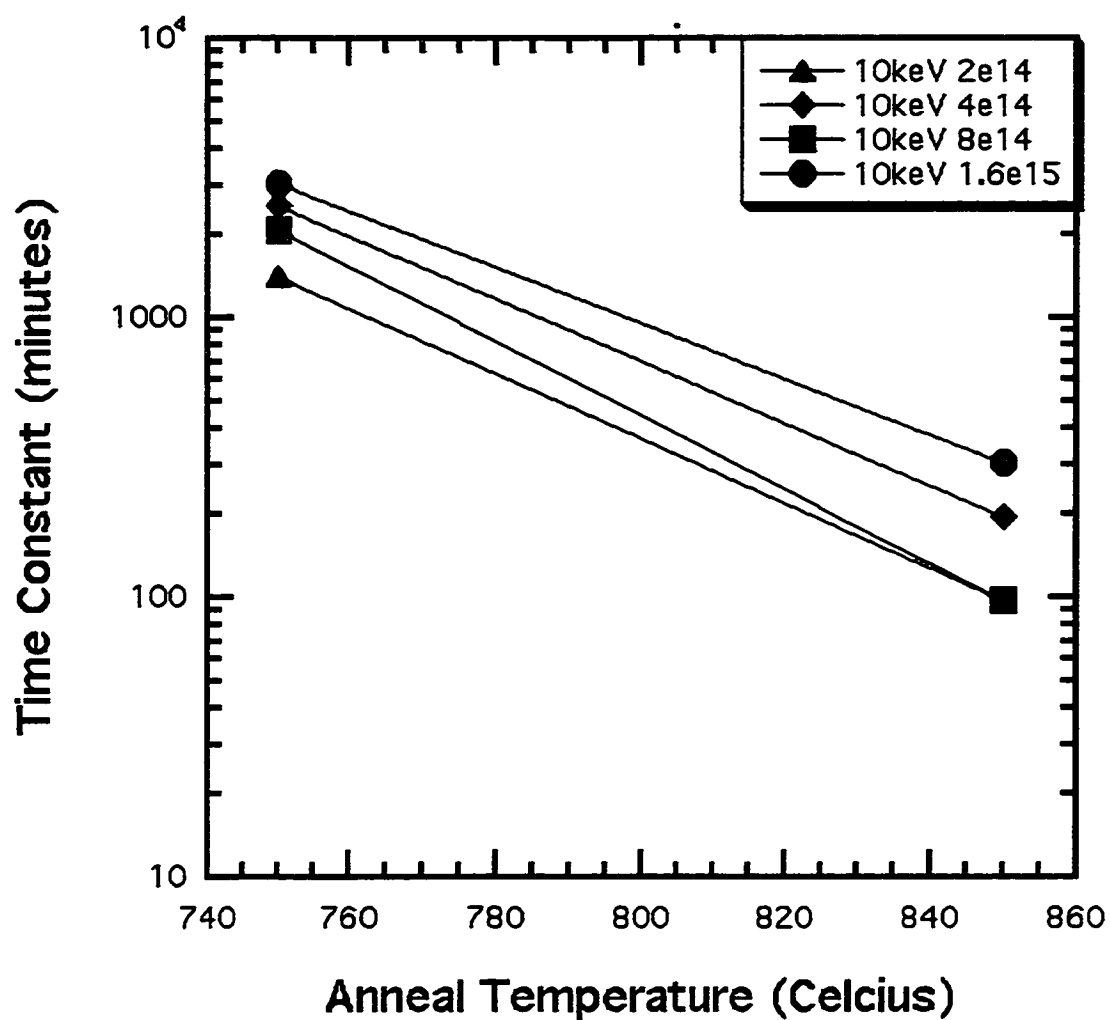


Figure A-13 Time constant to boron reactivation from clustered state following 10 keV implants at temperatures of 750°C and 850°C.

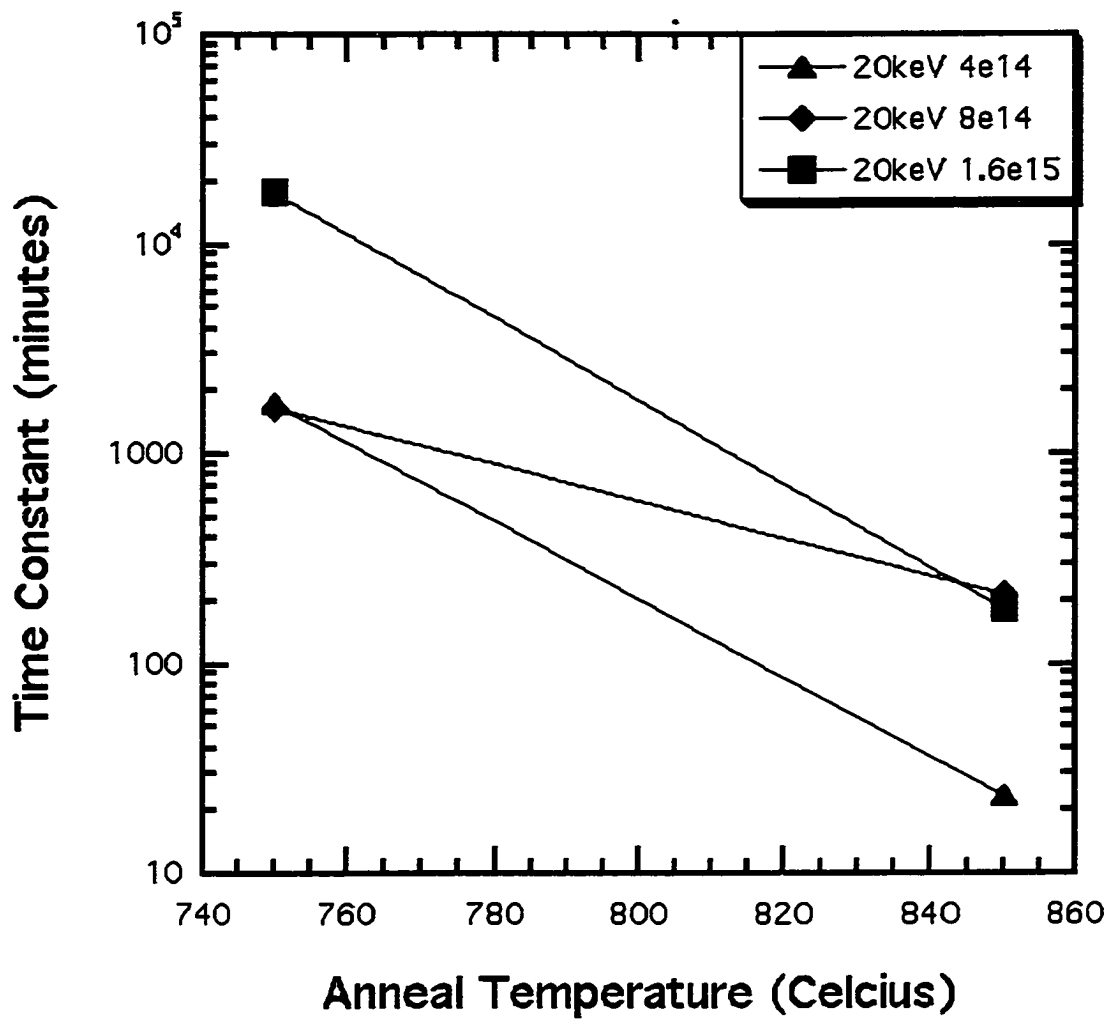


Figure A-14 Time constant to boron reactivation from clustered state following 20 keV implants at temperatures of 750°C and 850°C.

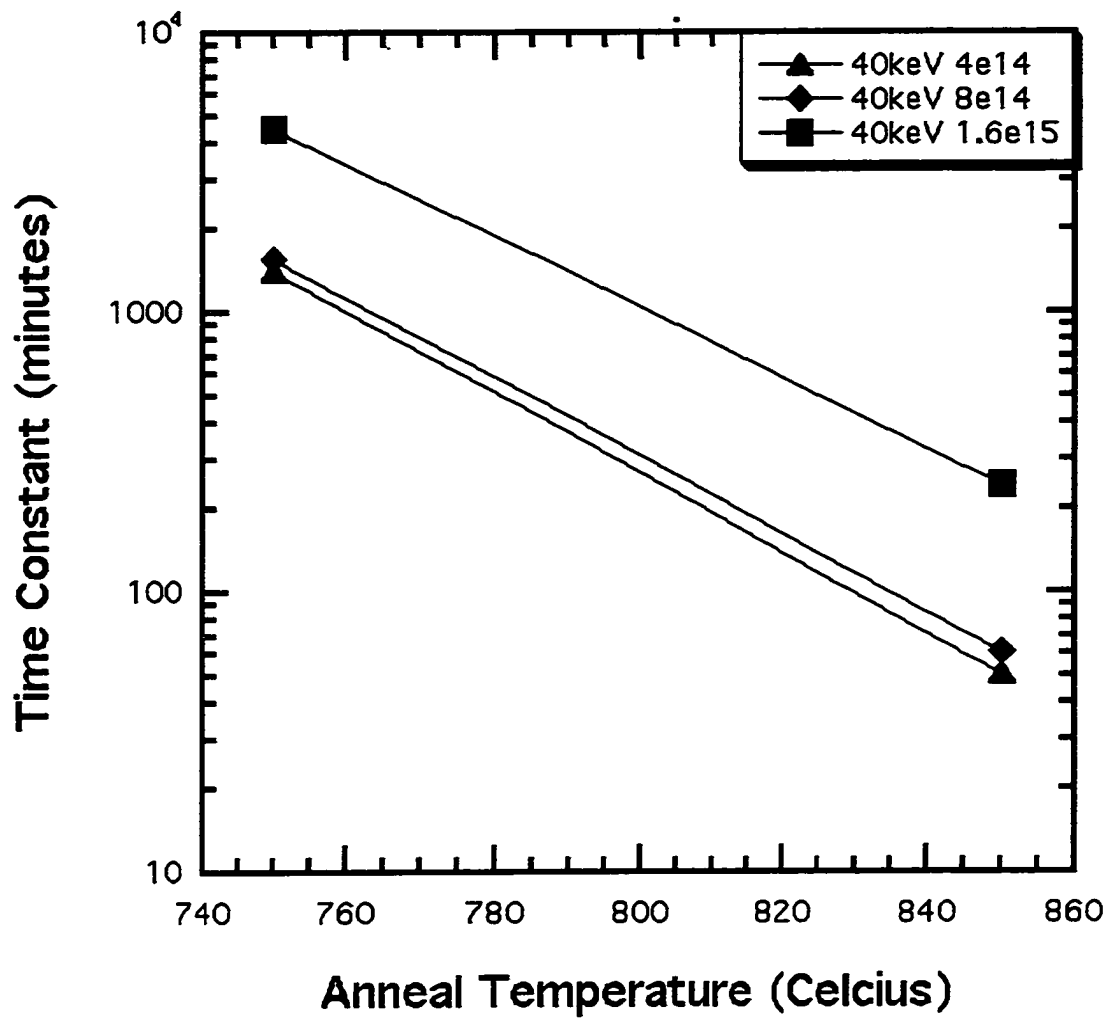


Figure A-15 Time constant to boron reactivation from clustered state following 40 keV implants at temperatures of 750°C and 850°C.

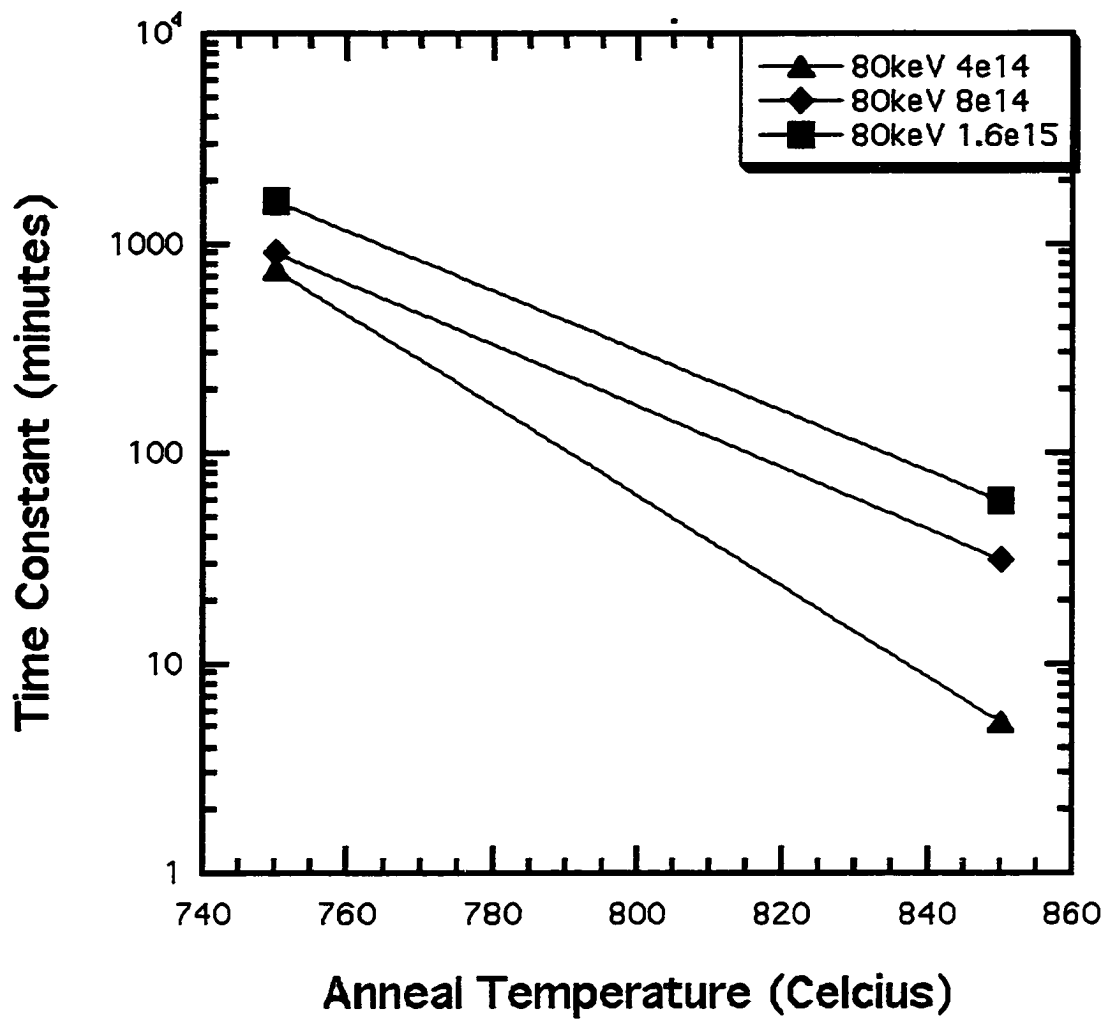


Figure A-16 Time constant to boron reactivation from clustered state following 80 keV implants at temperatures of 750°C and 850°C.

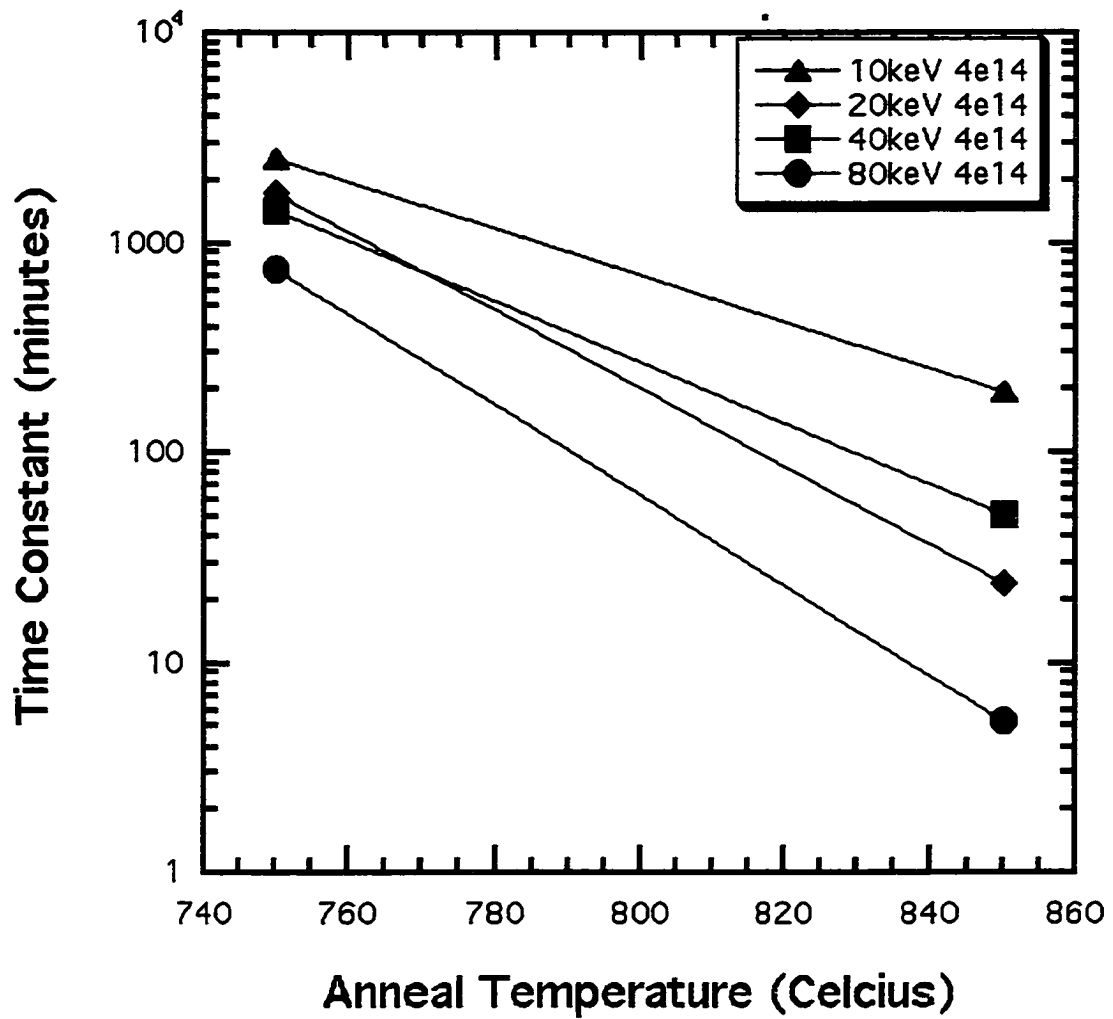


Figure A-17 Time constant to boron activation for $4 \times 10^{14} \text{ cm}^{-2}$ boron implants.

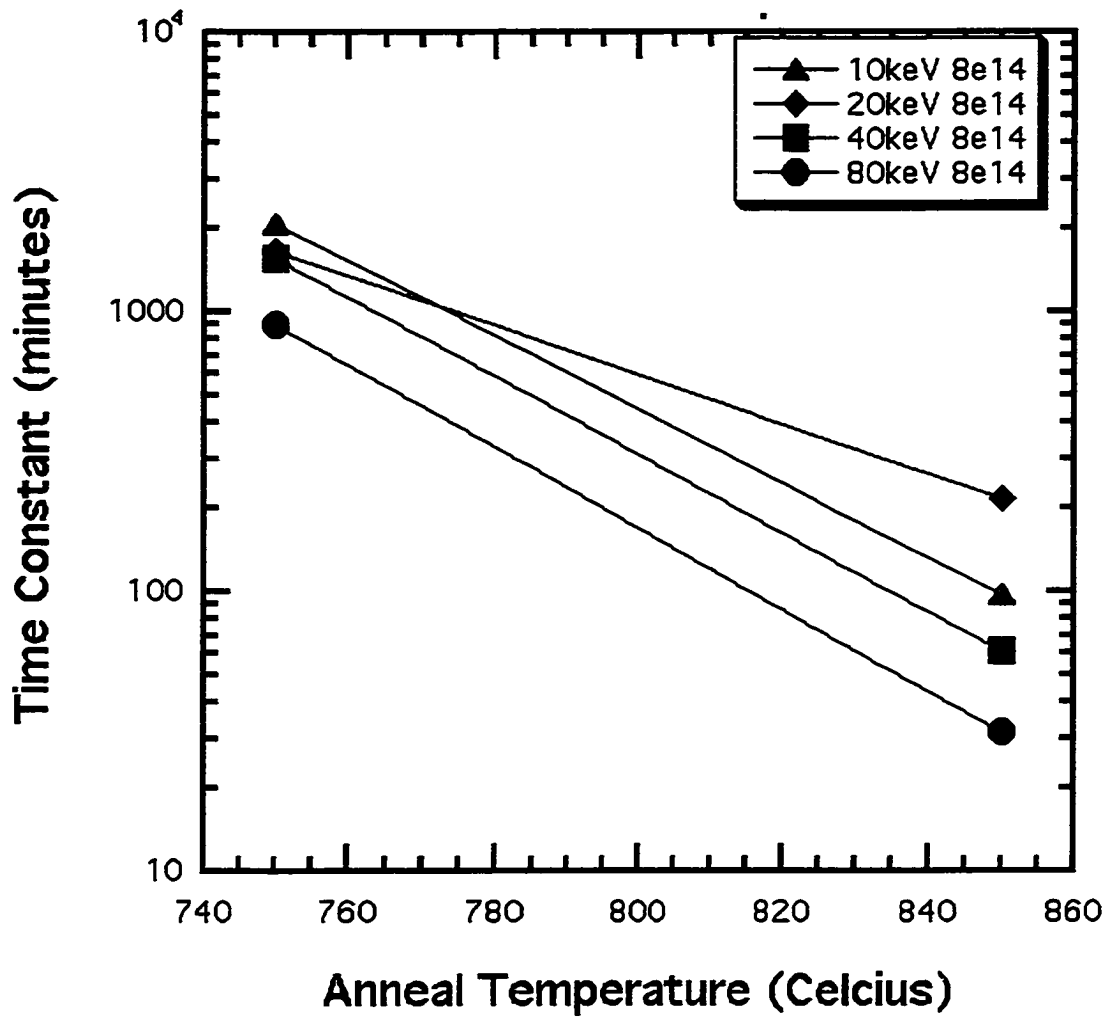


Figure A-18 Time constant to boron activation for $8 \times 10^{14} \text{ cm}^{-2}$ boron implants.

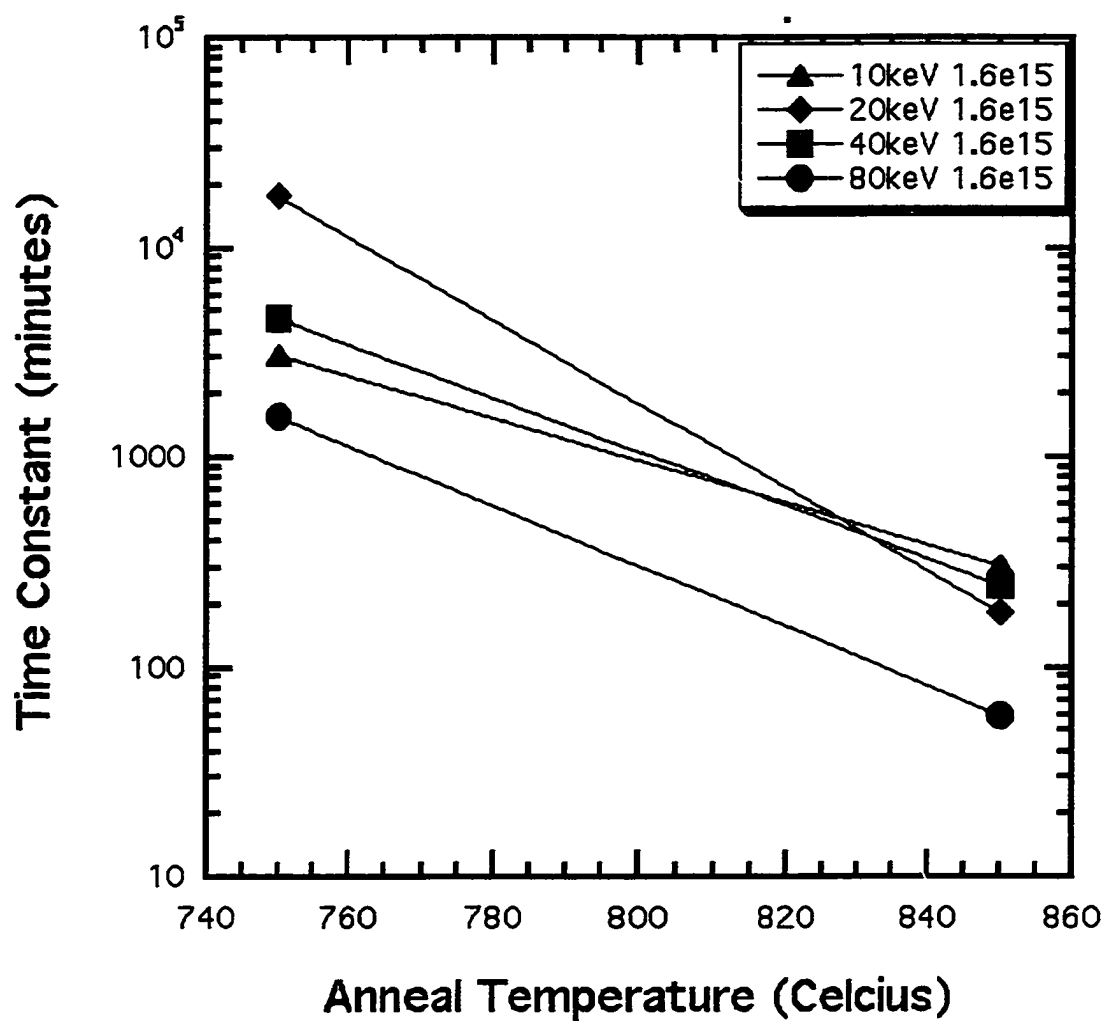


Figure A-19 Time constant to boron activation for $1.6 \times 10^{15} \text{ cm}^{-2}$ boron implants.

APPENDIX B SAMPLE INPUT SCRIPTS

Chapter 2 of this work presents the development of a predictive model capable of accurately describing several transient phenomena in boron-doped silicon. Chapter 4 then utilizes this model in order to simulate experiments similar to those presented in Chapter 2. Contained in this appendix are scripts illustrating the formulation of the equations governing the system. The parameters are presented previously in this work.

B.1 Full Model Equation Set

term name=B1rxn add silicon eqn= "\$KB1f * (Bsub) * (Int) - \$KB1r * (B1)"

term name=Bimobrxn add silicon eqn= "\$KB1r * (B1) - \$KB1f * (Bimob)"

term name=I2crxn add silicon eqn= "(Int) * (Int) * \$KI2cf - \$KI2cr * (I2c)"

term name=B2Irxn add silicon eqn= "\$KBiBsf * (Bimob) * (Bsub) - \$KBiBsr * (B2I)"

term name=B3Irxn add silicon eqn= "(B2I) * (Bimob) * \$KB3I2f"

term name=I3crxn add silicon eqn= "(Int) * (I2c) * \$KI3cf - \$KI3cr * (I3c)"

term name=D3rxn add silicon eqn= "(I3c) * (Int) * \$K311n"

term name=D3rxf add silicon eqn= "(D3) * (Int) * \$K311f - (D3) * \$K311r"

term name=B2I2rxn add silicon eqn= "(B1) * (Bimob) * \$KB2I2f - (B2I2) * \$KB2I2r"

term name=B2I2rx2 add silicon eqn= "(B2I2) * (Bimob) * \$KBiB2I2r"

term name=B12rxn add silicon eqn= "(B1) * (Int) * \$KB12f2 - (B12) * \$KB12r2"

term name=B12rx2 add silicon eqn= "(Bimob) * (Int) * \$KB12f - (B12) * \$KB12r"

term name=Isurf add eqn= " $((Int) - \$Cistar) * \$Kisurf$ "

term name=Vsurf add eqn= " $((Vac) - \$Cvstar) * \$Kvsurf$ "

term name=IVRCC add eqn= " $(Int) * (Vac) * \$Kr - (\$Cistar) * (\$Cvstar) * \Kr "

term name=B4I2rxn add eqn= " $(Bimob) * (B3I) * \$KB4I2f - (B4I2) * \$KB4I2r$ "

term name=B3Irx2 add eqn= " $(B2) * (Bimob) * \$KB3If - (B3I) * \$KB3Ir$ "

term name=B2Irx2 add eqn= " $(B2) * (Int) * \$KIB2f - (B2I) * \$KIB2r$ "

solution name=BI2 !damp !negative ifpresent=BI2 add

pdbSetString Silicon BI2 Equation " $ddt(BI2) - BI2rxn - BI2rx2 + B2I2rx2$ "

solution name=B2I2 !damp !negative ifpresent=B2I2 add

pdbSetString Silicon B2I2 Equation " $ddt(B2I2) - B2I2rxn - B2I2rx2$ "

solution name=Bsub !damp !negative ifpresent=Bsub add

pdbSetString Silicon Bsub Equation " $ddt(Bsub) + B1rxn + B2Irxn$ "

solution name=Bimob !damp !negative ifpresent=Bimob add

pdbSetString Silicon Bimob Equation " $ddt(Bimob) - Bimobrxn - grad(Bimob) * \$DBi + B2Irxn + B3Irxn + B2I2rxn + B2I2rx2 + BI2rx2 + B4I2rxn + B3Irx2$ "

#pdbSetString Silicon_Oxide Bimob Equation_Silicon " $ddt(Bimob) + \$KBimobsurf * Bimob$ "

use above form for OED conditions

```
#pdbSetString Silicon_Oxide Bsub Equation_Silicon "ddt(Bsub) - $KBimobsurf *
Bimob"
```

```
#above accounts for surface dose loss
```

```
solution name=BI !damp !negative ifpresent=BI add
```

```
pdbSetString Silicon BI Equation "ddt(BI) - B1rxn + Bimobrxn + B2I2rxn + BI2rxn"
```

```
solution name=Int !damp !negative ifpresent=Int add
```

```
pdbSetString Silicon Int Equation "ddt(Int) + B1rxn - $Di * grad(Int) + IVRCC + I2crxn
+ I2crxn + I3crxn + D3rxn + D3rxf + BI2rx2 + BI2rxn - B2I2rx2 + B2Irx2"
```

```
pdbSetString Silicon_Oxide Int Equation_Silicon "ddt(Int) + Isurf"
```

```
solution name=Vac !damp !negative ifpresent=Vac add
```

```
pdbSetString Silicon Vac Equation "ddt(Vac) - $Dv * grad(Vac) + IVRCC"
```

```
pdbSetString Silicon_Oxide Vac Equation_Silicon "ddt(Vac) + Vsurf"
```

```
solution name=I2c !damp !negative ifpresent=I2c add
```

```
pdbSetString Silicon I2c Equation "ddt(I2c) - I2crxn + I3crxn"
```

```
solution name=B2I !damp !negative ifpresent=B2I add
```

pdbSetString Silicon B2I Equation "ddt(B2I) - B2Irxn + B3Irxn - B2Irx2"

solution name=B3I !damp !negative ifpresent=B3I add

pdbSetString Silicon B3I Equation "ddt(B3I) - B3Irxn + B4I2rxn - B3Irx2"

solution name=I3c !damp !negative ifpresent=I3c add

pdbSetString Silicon I3c Equation "ddt(I3c) - I3crxn + D3rxn"

solution name=D3 !damp !negative ifpresent=D3 add

pdbSetString Silicon D3 Equation "ddt(D3) - D3rxn - D3rxn - D3rxn - D3rxn - D3rxn"

solution name=B4I2 !damp !negative ifpresent=B4I2 add

pdbSetString Silicon B4I2 Equation "ddt(B4I2) - B4I2rxn"

solution name=B2 !damp !negative ifpresent=B2 add

pdbSetString Silicon B2 Equation "ddt(B2) + B3Irx2 + B2Irx2"

B.2 Reduced Model Equation Set

term name=B1rxn add silicon eqn= "\$KBIf * (Bsub) * (Int) - \$KBIr * (BI)"

term name=Bimobrxn add silicon eqn= "\$KBir * (BI) - \$KBif * (Bimob)"

term name=I2crxn add silicon eqn= "(Int) * (Int) * \$KI2cf - \$KI2cr * (I2c)"

term name=B2Irxn add silicon eqn= "\$KBiBsf * (Bimob) * (Bsub) - \$KBiBsr * (B2I)"

term name=I3crxn add silicon eqn= "(Int) * (I2c) * \$KI3cf - \$KI3cr * (I3c)"

term name=D3rxn add silicon eqn= "(I3c) * (Int) * \$K311n"

```

term name=D3rx add silicon eqn= "(D3) * (Int) * $K311f - (D3) * $K311r"

term name=B2I2rxn add silicon eqn= "(BI) * (Bimob) * $KB2I2f - (B2I2) * $KB2I2r"

term name=B2I2rx2 add silicon eqn= "(BI2) * (Bimob) * $KBiBI2r"

term name=BI2rxn add silicon eqn= "(BI) * (Int) * $KBi2f2 - (BI2) * $KBi2r2"

term name=BI2rx2 add silicon eqn= "(Bimob) * (Int) * $KBi2f - (BI2) * $KBi2r"

term name=Isurf add eqn= "((Int) - $Cistar) * $Kisurf"

term name=Vsurf add eqn= "((Vac) - $Cvstar) * $Kvsurf"

term name=IVRCC add eqn= "(Int) * (Vac) * $Kr - ($Cistar) * ($Cvstar) * $Kr"

term name=B3Iredrxn add eqn= "(.1 * (Bsub) * (Bimob) * (Bimob) * $KBiBsf /
$KBiBsr * $KB3I2f / $KB3I2r / (Int) - (B3Ired)) * .005 * $KBiBsf * $KB3I2f /
($KBiBsf + $KB3I2f) - (B3Ired) * 40 * $KBiBsr * $KB3I2r / ($KBiBsr + $KB3I2r) *
(Int)"

#term name=B3Iredrxn add eqn= "((Bsub) * (Bimob) * (Bimob) * $KBiBsf * $KB3I2f /
($KBiBsf + $KB3I2f) - (B3Ired) * $KBiBsr * $KB3I2r / ($KBiBsr + $KB3I2r) * (Int))"

#default form and fitted form

solution name=Bsub !damp !negative ifpresent=Bsub add

pdbSetString Silicon Bsub Equation "ddt(Bsub) + BIrxn + B3Iredrxn"

solution name=Bimob !damp !negative ifpresent=Bimob add

pdbSetString Silicon Bimob Equation "ddt(Bimob) - Bimobrxn - grad(Bimob) * $DBi +
B3Iredrxn + B3Iredrxn"

```

pdbSetString Silicon_Oxide Bimob Equation_Silicon "ddt(Bimob) + \$KBimobsurf *
Bimob"

pdbSetString Silicon_Oxide Bsub Equation_Silicon "ddt(Bsub) - \$KBimobsurf * Bimob"

solution name=BI !damp !negative ifpresent=BI add

pdbSetString Silicon BI Equation "ddt(BI) - BIr_{rxn} + Bimob_{rxn}"

solution name=Int !damp !negative ifpresent=Int add

pdbSetString Silicon Int Equation "ddt(Int) + BIr_{rxn} - \$Di * grad(Int) + IVRCC + I2_{crxn}
+ I2_{crxn} + I3_{crxn} + D3_{rxn} + D3_{rxn} - B3Ired_{rxn}"

pdbSetString Silicon_Oxide Int Equation_Silicon "ddt(Int) + Isurf"

solution name=Vac !damp !negative ifpresent=Vac add

pdbSetString Silicon Vac Equation "ddt(Vac) - \$Dv * grad(Vac) + IVRCC"

pdbSetString Silicon_Oxide Vac Equation_Silicon "ddt(Vac) + Vsurf"

solution name=I2c !damp !negative ifpresent=I2c add

pdbSetString Silicon I2c Equation "ddt(I2c) - I2_{crxn} + I3_{crxn}"

solution name=B3Ired !damp !negative ifpresent=B3Ired add

pdbSetString Silicon B3Ired Equation "ddt(B3Ired) - B3Iredrxn"

solution name=I3c !damp !negative ifpresent=I3c add

pdbSetString Silicon I3c Equation "ddt(I3c) - I3crxn + D3rxn"

solution name=D3 !damp !negative ifpresent=D3 add

pdbSetString Silicon D3 Equation "ddt(D3) - D3rxn - D3rxn - D3rxn - D3rxn - D3rxf"

LIST OF REFERENCES

- Aga97 Agarwal, A., Gossman, H.-J., Eaglesham, D.J., Pelaz, L., Jacobson, D.C., Haynes, T.E., & Erokhin, Y.E., *Appl. Phys. Lett.* 71, 3141 (1997).
- Aga98 Agarwal, A., Gossman, H.-J., Eaglesham, D.J., Pelaz, L., Herner, S.B., Jacobson, D.C., Haynes, T.E., & Simonton, R., *Materials Science in Semiconductor Processing* 1, 17 (1998).
- Aga99 Agarwal, A., Gossman, H.-J., & Fiory, A.T., *Mat. Res. Soc. Symp. Proc.* 568, 19 (1999).
- Aga99a Agarwal, A., Gossman, H.-J., & Eaglesham, D.J., *Mat. Res. Soc. Symp.* 568, 3 (1999).
- Aga99b Agarwal, A., Gossman, H.-J., Eaglesham, D.J., Herner, S.B., Fiory, T., & Haynes, T.E., *Appl. Phys. Lett.* 74, 2435 (1999).
- Ame Am. Soc. Test. Mat., ASTM Standard, F84, Part 43.
- Ari88 Arienzo, W.A.O., Glang, R., Lever, R.F., Lewis, R.K., & Morehead, F.F., *J. Appl. Phys.* 63, 116 (1988).
- Bar69 Baron, R., Shifrin, G.A., Marsh, O.J., & Mayer, J.W., *J. Appl. Phys.* 40, 3702 (1969).
- Ben97 Benton, J.L., Libertino, S., Kringhoj, P., Eaglesham, D.J., & Poate, J.M., *J. Appl. Phys.* 82, 120 (1997).
- Ben98 Benton, J.L., Halliburton, K., Libertino, S., Eaglesham, D.J., & Coffa, S., *J. Appl. Phys.* 84, 4749 (1998).
- Bri99 Brindos, R., Keys, P., Jones, K.S., & Law, M.E., *Appl. Phys. Lett.* 75, 229 (1999).
- Cas99 Castell, M.R., Simpson, T.W., Mitchell, I.V., Perovic, D.D., Baribeau, J.-M., *Appl. Phys. Lett.* 74, 2304 (1999).
- Cat98 Caturla, M.J., Johnson, M.D., & de la Rubia, T.D., *Appl. Phys. Lett.* 72, 2736 (1998).

- Cha96 Chao, H.S., Griffin, P.B., & Plummer, J.D., *Appl. Phys. Lett.* 68, 3570 (1996).
- Che96 Cheng, J.Y., Eaglesham, D.C., Jacobson, D.C., Stolk, P.A., Benton, J.L., & Poate, J.M., *J. Appl. Phys.* 80, 2105 (1996).
- Cof00 Coffa, S., Libertino, S., & Spinella, C., *Appl. Phys. Lett.* 76, 321 (2000).
- Col00 Collart, E.J.H., Murrell, A.J., Foad, M.A., Van den Berg, J.A., Zhang, S., Armour, D., Goldberg, R.D., Wang, T.S., Cullis, A.G., Clarysse, T., & Vandervorst, W., *J. Vac. Sci. Technol. B* 18, 435 (2000).
- Cow90 Cowern, N.E.B., Janssen, K.T.F., & Jos, H.F.F., *J. Appl. Phys.* 68, 6191 (1990).
- Cow94 Cowern, N.E.B., van de Walle, G.F.A., Zalm, P.C., & Vandenhout, D.W.E., *Appl. Phys. Lett.* 65, 2981 (1994).
- Cow99 Cowern, N.E.B., Mannino, G., Stolk, P.A., Roozeboom, F., Huizing, H.G.A., & van Berkum, J.G.M., *Phys. Rev. Lett.* 82, 4460 (1999).
- Cow00 Cowern, N., & Rafferty, C., *MRS Bulletin*, 39 (2000).
- Cur97 Current, M.I., in *Technology Roadmaps for Doping of Semiconductor Transistors*, (1997).
- Eag94 Eaglesham, D.J., Stolk, P.A., Gossman, H.-J., & Poate, J.M., *Appl. Phys. Lett.* 65, 2305 (1994).
- Eag95 Eaglesham, D.J., Stolk, P.A., Gossman, H.-J., Haynes, T.E., & Poate, J.M., *Nucl. Inst. & Meth. in Phys. Res. B* 106, 191 (1995).
- Eag97 Eaglesham, D.J., Haynes, T.E., Gossman, H.-J., Jacobson, D.C., Stolk, P.A., & Poate, J.M., *Appl. Phys. Lett.* 70, 3281 (1997).
- Fai77 Fair, R.B., & Tsai, C.C., *J. Electrochem. Soc.* 124, 1107 (1977).
- Fai90 Fair, R.B., *J. Electrochem. Soc.* 137, 667 (1990).
- Fio99 Fiory, A.T., Bourdelle, K.K., Agarwal, A., Gossman, H.-J., & Rafferty, C.S., *Mat. Res. Soc. Symp. Proc.* 568, 31 (1999).
- Foa99 Foad, M.A., Murrell, A.J., Collart, J.H., Cock G., Jennings, D., & Current, M.I., *Mat. Res. Soc. Symp. Proc.* 568, 55 (1999).
- Foa00 Foad, M.A., Webb, R., Smith, R., Matsuo, J., Al-Bayati, A., Wang, T.S., & Cullis, T., *J. Vac. Sci. Tech. B* 18, 445 (2000).

- Gil89 Giles, M.D., IEEE Transactions on Computer-Aided Design 8, 460 (1989).
- Gil91 Giles, M.D., J. Electrochem. Soc. 138, 1160 (1991).
- Gos95 Gossman, H.-J., Gilmer, G.H., Rafferty, C.S., Unterwald, F.C., Boone, T., Luftman, H.S., & Frank, W., J. Appl. Phys 77, 1948 (1995).
- Gre90 Green, M.A., J. Appl. Phys. 67, 2944 (1990).
- Hay96 Haynes, T.E., Eaglesham, D.J., Stolk, P.A., Gossman, H.-J., Jacobson, D.C., & Poate, J.M., Appl. Phys. Lett. 69, 1376 (1996).
- Hob99 Hobler, G. & Rafferty, C.S., Mat. Res. Soc. Symp. Proc. 568, 123 (1999).
- Hu97 Hu, S.M., Mat. Sci. and Engr. R13, 105 (1997).
- Hua97 Huang, M.B., Simpson, T.W., & Mitchall, I.V., Appl. Phys. Lett. 70, 1146 (1997).
- Hui96 Huizing, H.G.A., Visser, C.C.G., Cowern, N.E.B., Stolk, P.A., & de Kruif, R.C.M., Appl. Phys. Lett 69, 1211 (1996).
- Jar96 Jaraiz, M., Gilmer, G.H., Poate, J.M., & de la Rubia, T.D., Appl. Phys. Lett. 68, 409 (1996).
- Joh98 Johnson, M.D., Caturla, M.-J., & de la Rubia, T.D., J. Appl. Phys. 84, 1963 (1998).
- Jon88 Jones, K.S., Prussin, S., & Weber, E.R., Appl. Phys. A. 45, 1 (1988).
- Jon96 Jones, K.S., Zhang, L.H., Krishnamoorthy, V., Simons, D.S., Chi, P., Rubin, L., & Elliman, R.G., Appl. Phys. Lett. 68, 2672 (1996).
- Jon97 Jones, K.S., Moller, K., Chen, J., Puga-Lambers, M., Freer, B., Berstein, J., & Rubin, L., J. Appl. Phys. 81, 6051 (1997).
- Kim97 Kim, J., Wilkins, J.W., Khan, F.S., & Canning, A., Phys. Rev. B 55, 16186 (1997).
- Lam99 Lampin, E., Senez, V., & Claverie, A., J. Appl. Phys. 85, 8137 (1999).
- Law88 Law, M.E., Ph.D. Dissertation, Stanford University, 1988.
- Law96 Law, M.E., FLOOPS User's Manual, (University of Florida, Gainesville, FL, 1996).

- Law00 Law, M.E., Gilmer, G.H., & Jaraiz, M., MRS Bulletin, 45 (2000).
- Len00 Lenosky, T.J., Sadigh, B., Theiss, S.K., Caturla, M.J., & de la Rubia, T.D., Appl. Phys. Lett. 77, 1834 (2000).
- Ler99 Lerch, W., Gluck, M., Stolwijk, N.A., Walk, H., Schafer, M., Marcus, S.D., Downey, D.F., & Chow, J.W., J. Electrochem. Soc. 146, 2670 (1999).
- Li00 Li, H.-J., Kohli, P., Ganguly, S., Kirichenko, T.A., Banerjee, S., & Zeitzoff, P., Appl. Phys. Lett. 77, 2683 (2000).
- Lil97 Lilak, A.D., Earles, S.K., Jones, K.S., Law, M.E., & Giles, M.A., Tech. Dig. Int. Electron Devices Meet., 493 (1997).
- Lil99 Lilak, A.D., Earles, S.K., Law, M.E., & Jones, K.S., Appl. Phys. Lett. 74, 2038 (1999).
- Liu96 Liu, J., Ph.D. Dissertation, University of Florida, (1996).
- Liu00 Liu, X.Y., Windl, W., & Masquillier, M., Appl. Phys. Lett. 77, 2018 (2000).
- Luo98 Luo, W., Rasband, P.B., Clancy, P., & Roberts, B.W., J. Appl. Phys. 84, 2476 (1998).
- Moo65 Moore, G.E., Electronics 38, 114 (1965).
- Nap99 Napolitani, E., Carner, A., Privitera, V., Magna, A.L., Shroer, E., Priolo, F., Mannino, G., & Moffatt, S., Mat. Res. Symp. Proc. 568, 43 (1999).
- Osb96 Osburn, C., Downey, D., Felch, S.B., & Lee, B.S., Proc. 11th Intl. Conf. on Ion Implant Tech., 1 (1996).
- Pac91 Packan, P.A., PhD Dissertation, Stanford University, 1991.
- Par94 Park, H., Robinson, H., Jones, K.S., & Law, M.E., Appl. Phys. Lett. 65, 436 (1994).
- Pel97 Pelaz, L., Jaraiz, M., Gilmer, G.H., Gossman, H.-J., Rafferty, C.S., Eaglesham, D.J., & Poate, J.M., Appl. Phys. Lett. 70, 2285 (1997).
- Pel98 Pelaz, L., Gilmer, G.H., Jaraiz, M., Herner, S.B., Gossman, H.-J., Eaglesham, D.J., Hobler, G., Rafferty, C.S., & Barbolla, J., Appl. Phys. Lett. 73, 1421 (1998).

- Pel99 Pelaz, L., Gilmer, G.H., Gossman, H.-J., & Rafferty, C.S., *Appl. Phys. Lett.* 74, 3657 (1999).
- Pen86 Pennycook, S.J., Culbertson, R.J., & Narayan, J., *J. Mater. Res.* 1, 476 (1986).
- Poa95 Poate, J.M., Eaglesham, D.J., Gilmer, G.H., Gossman, H.-J., Jaraiz, M., Rafferty, C.S., & Stolk, P.A., *Tech. Dig. Int. Electron Devices Meet.*, 77 (1995).
- Raf96 Rafferty, C.S., Gilmer, G.H., Jaraiz, M., Eaglesham, D., & Gossman, H.-J., *Appl. Phys. Lett.* 68, 2395 (1996).
- Ras98 Rasband, P.B., Clancy, P., Roberts, B.W., *J. Appl. Phys.* 84, 2472 (1998).
- Sch99 Schroer, E., Privitera, V., Priolo, F., Napolitani, E., & Carnera, A., *Appl. Phys. Lett.* 74, 3396 (1999).
- Smi98 Smith, R., Shaw, M., Webb, R., & Foad, M.A., *J. Appl. Phys.* 83, 3148 (1998).
- Sol90 Solmi, S., Landi, E., & Baruffaldi, F., *J. Appl. Phys.* 68, 3250 (1990).
- Sto95 Stolk, P.A., Gossman, H.-J., Eaglesham, D.J., Jacobson, D.C., Luftman, H.S., & Poate, J.M., *Mat. Res. Soc. Symp. Proc.* 354, 307 (1995).
- Sto95a Stolk, P.A., Eaglesham, D.C., Gossman, H.-J., & Poate, J.M., *Appl. Phys. Lett.* 66, 1370 (1995).
- Sto97 Stolk, P.A., Gossman, H.-J., Eaglesham, D.J., Jacobson, D.C., & Poate, J.M., *J. Appl. Phys.* 81, 6031 (1997).
- Sze81 Sze, S.M., *Physics of Semiconductor Devices*, 2nd Edition, John Wiley and Sons (1981).
- Tas89 Tasch, A.F., Shin, H., Park, C., Alvis, J., & Novak, S., *J. Electrochem. Soc.* 136, 810 (1989).
- The00 Theiss, S.K., Caturla, M.J., Johnson, M.D., Zhu, J., Lenosky, T., Sadigh, B., & de la Rubia, T.D., *Thin Solid Films* 365, 219 (2000).
- Tho98 Thompson, S., Packan, P., & Bohr, M., *Intel Technology Journal* Q3, 1 (1998).
- Tru205 Trumbore, F.A., *Bell System Technical Journal*, 205 (1960).
- Uem97 Uematsu, M., *J. Appl. Phys.* 82, 2228 (1997).

- Uem98 Uematsu, M., J. Appl. Phys., J. Appl. Phys. 84, 4781 (1998).
- Vai99 Vailionis, A., Glass, G., Desjardins, P., Cahill, D., & Greene, J.E., Phys. Rev. Lett. 82, 4464 (1999).
- Vuo00 Vuong, H.H., Rafferty, C.S., Eshraghi, S.A., Ning, J., McMacken, J.R., & Stevie, F.A., J. Vac. Sci. Technol. B 18, 428 (2000).
- Wol86 Wolf, S., Tauber, R.N., in Silicon Processing for the VLSI Era Volume 1- Process Technology, Vol 1, (Lattice Press 1986).
- Wan97 Wang, L.Z., Luo, M.S.-C., Tseng, H.-H., & Ajuria, S.A., J. Electrochem. Soc. 144, 299 (1997).
- Wan00 Wang, T.-S., Cullis, A.G., Collart, E.J.H., Murrell, A.J., & Foad, M.A., Appl. Phys. Lett., Appl. Phys. Lett. 77, 3586 (2000).
- Wat97 Watkins, G.D., Mat. Res. Soc. Symp. Proc. 469, 139 (1997).
- Web69 Webber, R.F., Thorn, R.S., & Large, L.N., Int. J. Electronics 26, 163 (1969).
- Wil86 Willoughby, A.F.W., Evans, A.G.R., Champ, P., Yallup, K.J., Godfrey, D.J., & Dowsett, M.G., J. Appl. Phys. 59, 2392 (1986).
- Zhu97 Zhu, J. Mat. Res. Soc. Symp. Proc. 469, 151 (1997).

BIOGRAPHICAL SKETCH

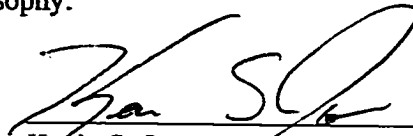
The author was born on September 13, 1973, in Dearborn, Michigan. After attending high school in Merrill, Wisconsin he attended Michigan Technological University in Houghton, Michigan and was awarded the Bachelor of Science degree in electrical engineering in May of 1995. In August of 1995 he began graduate education at the University of Florida and was awarded the Masters of Science degree in 1998 and completed his Ph.D. studies in May of 2001. He was advised by Dr. Mark E. Law during his graduate education.

I certify that I have read this study and that in my opinion it conforms to acceptable standards of scholarly presentation and is fully adequate, in scope and quality, as a thesis for the degree of Doctor of Philosophy.



Mark E. Law, Chairman
Professor of Electrical and Computer
Engineering

I certify that I have read this study and that in my opinion it conforms to acceptable standards of scholarly presentation and is fully adequate, in scope and quality, as a thesis for the degree of Doctor of Philosophy.



Kevin S. Jones
Professor of Electrical and Computer
Engineering

I certify that I have read this study and that in my opinion it conforms to acceptable standards of scholarly presentation and is fully adequate, in scope and quality, as a thesis for the degree of Doctor of Philosophy.



Gijs Bosman
Professor of Electrical and Computer
Engineering


I certify that I have read this study and that in my opinion it conforms to acceptable standards of scholarly presentation and is fully adequate, in scope and quality, as a thesis for the degree of Doctor of Philosophy.




Stephen Pearson
Professor of Materials Science and
Engineering

This thesis was submitted to the Graduate Faculty of the College of Engineering and to the Graduate School and was accepted as partial fulfillment of the requirements for the degree of Doctor of Philosophy.

August 2001


for Pramod B. Khargonekar
Dean, College of Engineering


Winfred M. Phillips
Dean, Graduate School